UNIVERSITY OF SOUTHAMPTON

Faculty of Engineering and the Environment

Computational Engineering Design Group

Implications for Leaflet Behaviour in Heavily Calcified Patient-Specific Aortic Roots: Simulation of Transcatheter Aortic Valve Implantation.

by

Jonathon M. Bailey

Thesis for the degree of Doctor of Philosophy

September 2015

UNIVERSITY OF SOUTHAMPTON

FACULTY OF ENGINEERING AND THE ENVIRONMENT

Thesis for the degree of Doctor of Philosophy

IMPLICATIONS FOR LEAFLET BEHAVIOUR IN HEAVILY CALCIFIED PATIENT-SPECIFIC SIMULATION OF TRANSCATHETER AORTIC VALVE IMPLANTATION

Jonathon M. Bailey

As life expectancy increases, there are more and more cases of age-related disease presenting to medical attention. Aortic stenosis (AS) is a common age-related heart condition in which there is a thickening and distortion of the valve leaflets together with calcium deposition in the aortic root and valve. Surgical valve replacement (SVR) of the calcified valve is the current default treatment for AS. However, due to the invasive nature of the procedure, a large population of patients are deemed too high risk to undergo SVR. Transcatheter aortic valve implantation (TAVI) was developed as a percutaneous alternative to SVR.

TAVI is a purely mechanical process beyond the initial positioning of the device, that is, there is no decision making. As a result it can be computationally modelled using finite element analysis (FEA). This thesis describes how FEA has been used to analyse the stresses within the prosthetic leaflets during and post-deployment. Further, the application of patient-specific deployment simulation for predicting adverse effects post TAVI was explored.

FEA simulation of TAVI deployment is challenging as a realistic aortic root model must be developed. This was accomplished by extracting data from patient specific medical images. The TAVI device itself, in particular the leaflets, are subjected to elevated stresses and deformation during deployment. Creating an FEA model robust enough to withstand the deployment process was achieved by modelling the leaflets in a planar orientation, then using a preliminary simulation to manipulate the leaflets into a functional position while maintaining a highly regular mesh.

The key findings in this thesis concern device orientation and how it influences the operating stress of the valve. Sub-optimal device orientation can result in an average stress increase of 25%, which could potentially reduce the lifespan of the device. Patient-specific deployment simulations were also shown to have application outside of device orientation assessment as regions of potential paravalvular aortic regurgitation were identifiable.

Table of Contents

List of Tables

List of Figures

Declaration of Authorship

I, Jonathon Bailey, declare that this thesis and the work presented in it are my own and has been generated by me as the result of my own original research.

Implications for Leaflet Behaviour in Heavily Calcified Patient-Specific Aortic Roots: Simulation of Transcatheter Aortic Valve Implantation

I confirm that:

1. This work was done wholly or mainly while in candidature for a research degree at this University;
2. Where any part of this thesis has previously been submitted for a degree or any other qualification at this University or any other institution, this has been clearly stated;
3. Where I have consulted the published work of others, this is always clearly attributed;
4. Where I have quoted from the work of others, the source is always given. With the exception of such quotations, this thesis is entirely my own work;
5. I have acknowledged all main sources of help;
6. Where the thesis is based on work done by myself jointly with others, I have made clear exactly what was done by others and what I have contributed myself;

Signed: .....

Date:.....

Acknowledgements

I would like to thank my friends and colleagues for the help and support I received during my PhD, I couldn't have finished without you.

Special mention is warranted for my supervisors, Nick Curzen and Neil Bressloff, thank you so much for making my PhD an incredible and unforgettable period of my life, and most importantly, putting up with me.

Through good fortune I had the pleasure of meeting, and working with, David Walker, Ian Sinclair and Stephen Hardon who selflessly aided me in my PhD by allowing me access to laboratories, equipment and data. Without kind gestures such as these, my research would never have progressed in to the thesis it did.

Most of all, I would like to thank my Mother and Father, who have always supported my endeavours, for this I am eternally grateful.

Definitions and Abbreviations

ζ_i – Damping ratio

μCT – Micro computer tomography

σ_{DPC} – Standard deviation from a perfect circle

σ_{vM} – Standard deviation of von Mises stress

ANPD – Average nodal position discrepancy

AS – Aortic stenosis

BE – Balloon-expandable

CAD – Computer aided design

CEL – Coupled Eulerian Lagrangian

CFD – Computational fluid dynamics

CT – Computer tomography

DUS – Doppler ultrasound system

DW-MRI – Diffusion weighted magnetic resonance imaging

EOS – Equation of state

FEA – Finite element analysis

Fr – French

FSI – Fluid structure interaction

LVOT – Left ventricular outflow tract

MRI – Magnetic resonance imaging

MRS – Modified Rankin scale

MSCT – Multi slice computer tomography

PAR – Paravalvular aortic regurgitation

PET – Polyethylene terephthalate

PPM – Patient prosthetic mismatch

SE – Self-expandable

SEM – Scanning electron microscopy

SHGM – Second harmonic generation microscopy

SVR – Surgical valve replacement

TAVI – Transcatheter aortic valve implantation

TOE – Trans-oesophageal echocardiography

UHST – University Hospital Southampton Trust

ViV – Valve in valve

Chapter 1: Introduction

The human cardiovascular system is one of the most intriguing collection of organs and has been the focus of discussion for millennia. Leonardo da Vinci spent many years studying the cardiovascular system and it is claimed he dissected up to ten cadavers during his research, recording his findings in detailed drawings. One such drawing of a heart is shown in Figure 1 (Shoja et al. 2012, Keele 1983). The heart is a double pump lying in the centre of the circulatory system, driving blood around the arteries and veins, which make up an elaborate network, feeding all of the tissue within the body. Unfortunately, in the western world, heart disease is a common ailment affecting an increasingly ageing population.

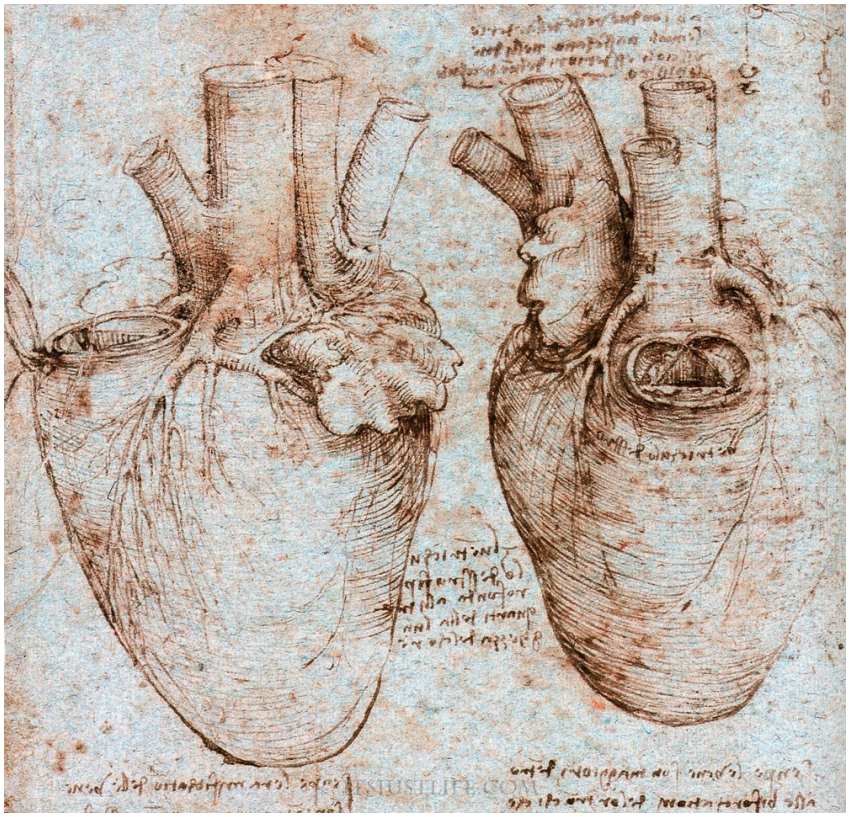

Figure 1. Anatomical drawings of an Ox heart by Leonardo de Vinci. These images are part of the Windsor collection. The aortic valve, with its triplet of leaflets is visible in both drawings of the heart (Shoja et al. 2012).

One of the most common cardiovascular diseases is aortic stenosis (AS) in which the aortic valve becomes calcified and ineffective. If left untreated AS will result in patient death. The standard treatment to eligible patients is surgical valve replacement (SVR). However, as SVR is unfavourably invasive, many patients are deemed too frail for the procedure to be attempted. In order to reduce the

annual mortality associated with AS, a minimally invasive treatment was developed: transcatheter aortic valve implantation (TAVI).

The first TAVI device was deployed in a human in 2002. Despite the young age of the technology, it has started to replace the current standard procedure of SVR (Eggebrecht and Mehta 2016). Unfortunately, TAVI is not free from adverse outcomes. Blood can flow backwards around the valve, something which has been linked to early mortality (Tamburino et al. 2011). TAVI has also been linked to an increased incidence of stroke in patients (Smith et al. 2011). Finally, when in situ for long enough, all prosthetic valves will likely to fail, the leaflets are particularly vulnerable to restenosis. However, for the case of TAVI, there is not enough data to predict device life expectancy or to identify the factors associated with reduced life expectancy.

Due to the rapid adoption of TAVI in the western world, it is important to develop a comprehensive understanding of device lifespan and potential adverse outcomes post TAVI. This thesis aims to shed light into these uncertainties through computational finite element methods. This enhanced understanding will support patient selection and procedural planning resulting in safer treatment of AS.

1.1 Introduction to This Work

For the case of balloon expandable devices (BE), the deployment procedure of a TAVI device involves a clinician positioning the device and deployment apparatus within the aortic root. In order to perform TAVI, the clinician rapidly increases the pressure within the balloon, which expands the device. This procedure is therefore predominantly mechanical in nature, that is, there is no decision making after the initial orientating of the device. As a result, it is possible to simulate the procedure through finite element analysis (FEA). FEA simulation of TAVI devices has been limited, advancements upon these initial simulations will allow stresses and displacements within the device and surrounding tissue to be analysed.

All TAVI devices will fail through restenosis, provided the recipient does not first pass away. If the device becomes stenosed, a second prosthetic valve must be implanted, which increases the risk to the patient and cost. Decreasing the operational stress will reduce the incidence of restenosis, and therefore increase the device life span. The focus of this research is the leaflet performance within an Edwards Lifesciences SAPIEN XT, with the aim of finding any implications the leaflets may suffer, if the device frame is not circular.

The secondary aim of this thesis is to determine if patient-specific deployment simulations are reaching the sophistication required to accurately identify areas within the patient's aortic root which are susceptible to valvular leakage. The simulations may also offer insight into the stresses within

the calcified plaque yielding information surrounding the possibility of rupture and debris release. In the future, clinicians may consult computational patient-specific deployment simulations in order to determine if the patient is suitable for TAVI or even find the optimal deployment zone. A review of patient-specific deployment simulations is presented within this work.

To realise these aims, the following objectives were developed.

A computer aided design (CAD) model of the TAVI device was produced. The computational components required to accurately represent an actual device was also explored. Furthermore, a balloon and support components were also developed in CAD, resulting in a functional deployment system.

A geometric model of the aortic root was extracted from medical images, as opposed to a parameterised CAD model. Although a parameterised CAD model of an aortic root would have offered the ability to intricately alter the aortic root, it would not have allowed for patient specific procedural planning.

Once all of the geometries had been produced, a deployment simulation was developed. The simulation involved the device being crimped to a suitable diameter before being deployed into the aortic root model. The software package used was Abaqus CAE v6.12. The contact definitions associated with a balloon inflating (which is present in this analysis) are extremely difficult to model, as a result Explicit analysis was used which has superior contact modelling abilities in comparison to Implicit analysis (SIMULIA 2013c).

The deployment simulation was repeated with the device in different orientations to identify any implication to the device function associated with the device orientation. Variation in the stresses experienced by the prosthetic valve was monitored in order to find any complication that may compromise the device lifespan.

Furthermore, attempts to identify areas that are vulnerable to paravalvular aortic regurgitation (PAR) were also made. Finally, the stress levels within the calcified plaques were monitored in order to offer further insight into embolism.

This research will hopefully help push towards patient-specific deployment simulations, which could potentially be used to predict adverse outcomes of TAVI and become standard procedure.

1.2 Thesis Outline

This thesis contains nine chapters, a summary of each is presented below.

Chapter 1. The introduction to this thesis.

Chapter 2. The background information to this thesis is contained in this chapter. A description of the circulatory system and its anatomy is first presented. The symptoms, incidence, and treatment of AS is then described. TAVI, a modern treatment of AS is further detailed, including the procedural options, devices and a summary of associated complications.

Chapter 3. In this chapter the three main complications associated with TAVI are further discussed: PAR, embolism and reduced device lifespan associated with improperly implanted devices.

Chapter 4. This chapter contains a summary of computational simulation of TAVI found in the literature. The simulations are partitioned into two categories: device deployment and valvular function simulations.

Chapter 5. The methods used to produce the TAVI device models are described in this chapter. Each component is detailed in turn, as well as brief computational analysis of the functionality of the leaflet model.

Chapter 6. A chronological description of the efforts to produce a detailed patient specific aortic root model is presented in this chapter.

Chapter 7. This is the first of two chapters that focus on TAVI simulation. Within this chapter, the requirement of each component of the TAVI device, for accurate deployment simulation was explored. Using this knowledge, efficient analysis of both PAR and emboli release is performed.

Chapter 8. Chapter 8 presents the primary research of this thesis, focusing on calculating the leaflet operating stress, and identifying any event that may compromise the leaflets. The simulations initially examine the device preparation and deployment procedure, before turning to the operating stress.

Chapter 9. This chapter is the conclusion in which the results and impact of this work will be described.

Chapter 2: Transcatheter Aortic Valve Implantation

2.1 The Human Circulatory System

The human circulatory system comprises three components that work in harmony to supply the body with nutrients: the heart, pulmonary system (lungs) and the systemic system (arteries and veins). Each of these components is critical, if any of these three falters, the result is often mortality. Unfortunately, in the western world, cardiovascular disease is a common occurrence in the elderly population (Nkomo et al. 2006).

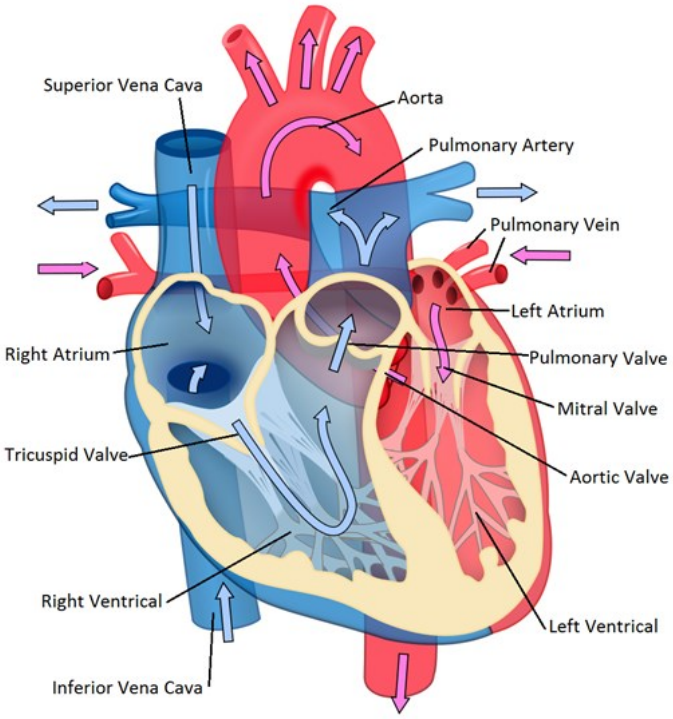

Figure 2. Gross anatomy of the human heart. Blue arrows represent flow of deoxygenated blood, while red arrows represent flow of oxygenated blood (Foundation 2013).

The heart is a large muscular structure with four chambers (Figure 2); the upper two are the atria, while the lower two are the ventricles. Deoxygenated blood flows from the body through the superior and inferior vena cava into the right atrium. The right ventricle relaxes in order to fill with blood, which is aided by the right atrium contracting. The right ventricle then contracts closing the tricuspid valve and pushing blood through the pulmonary valve towards the lungs (where it is oxygenated). The blood then returns to the heart through the pulmonary vein and into the left atrium. Similarly to the right side of the heart, the left ventricle will then relax in order to fill with blood which is aided

by the left atrial contraction. The left ventricle contracts closing the mitral valve and pushing the blood through the aortic valve into the aorta. The left ventricle then expands; this opens the mitral valve and closes the aortic valve. The blood flows throughout the body delivering the oxygen it has absorbed in the lungs.

The aortic root is a short length of tubular tissue that houses the aortic valve and connects the aorta to the left ventricle (Figure 3). The aortic valve within the root comprises three leaflets (visible in Figure 3), each of which has its own sinus that bulges out creating the widest point of the aortic root. The two coronary arteries originate from the sinuses in the aortic root and are visible in Figure 3. The coronary arteries can be used to identify the sinuses: left coronary sinus, right coronary sinus and non-coronary sinus. The aortic root is not necessarily circular above and below the sinuses, rather it is common for the aortic root to be elliptical (Hayashida et al. 2013).

Although the aortic valve conventionally has three leaflets, disorders exist where the number of leaflets varies from one to four (Russo et al. 2008, Sievers and Schmidtke 2007, Roberts and Ko 2005). A bicuspid aortic valve (two leaflets) is the most frequent congenital defect and is present in 1-2% of the population (Fedak et al. 2002).

The tissues that comprise the aortic root and valve are fibrous, and therefore neither isotropic nor homogeneous (Hokken et al. 1997). Furthermore the distribution of fibres throughout the leaflets is irregular, and inversely proportional to the fibril diameter (Balguid et al. 2008). As a result the material properties of the aortic root are difficult to model. Computational analysis of the aortic root and leaflets has often adopted a modified *Fung* (Fung 1993) material model which is non-linear, hyperelastic, anisotropic and inhomogeneous (Sun, Abad, and Sacks 2005).

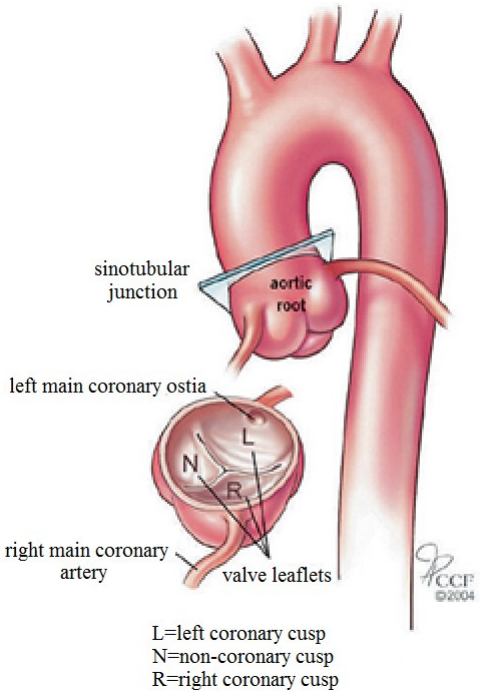

Figure 3. The relationship between the aorta, aortic root and aortic valve (Foundation 2014).

2.2 Aortic Stenosis

Throughout life, the human body slowly deposits calcified plaques around the cardiovascular system. These plaques often cause the tissue to be uncharacteristically stiff, or hard, a condition known as sclerosis (Ngo, Sverdlov, and Horowitz 2012). If the plaque deposition becomes severe, and the lumen of the vessel is narrowed, the condition is known as stenosis. Stenosis is potentially very serious as it can inhibit blood from flowing effectively around the body. If a coronary artery is stenosed (through calcium deposition or otherwise), cardiac arrest can occur. Figure 4 shows a reproduced image from a micro computer tomographic (μCT) scan. Figure 4A shows the tissue of the heart, while Figure 4(B) depicts the calcified plaques within the coronary arteries and aortic root (as well as an elastic band used to hold a plastic bag over the heart during the scan).

The aortic valve can succumb to stenosis (aortic stenosis - AS). AS both stiffens and distorts the leaflets reducing the ability of the leaflets to fully close, as well as reducing the effective orifice area while open (Otto et al. 1999). If AS is not treated, either the heart has to work harder, or the tissue dependent on the circulatory system will become malnourished. AS can result in further disorders including angina, embolism, stroke and sudden death (Keeley and Grines 1998, Bertrand et al. 1981, Smucker et al. 1988, Webb et al. 2009, Daneault et al. 2011).

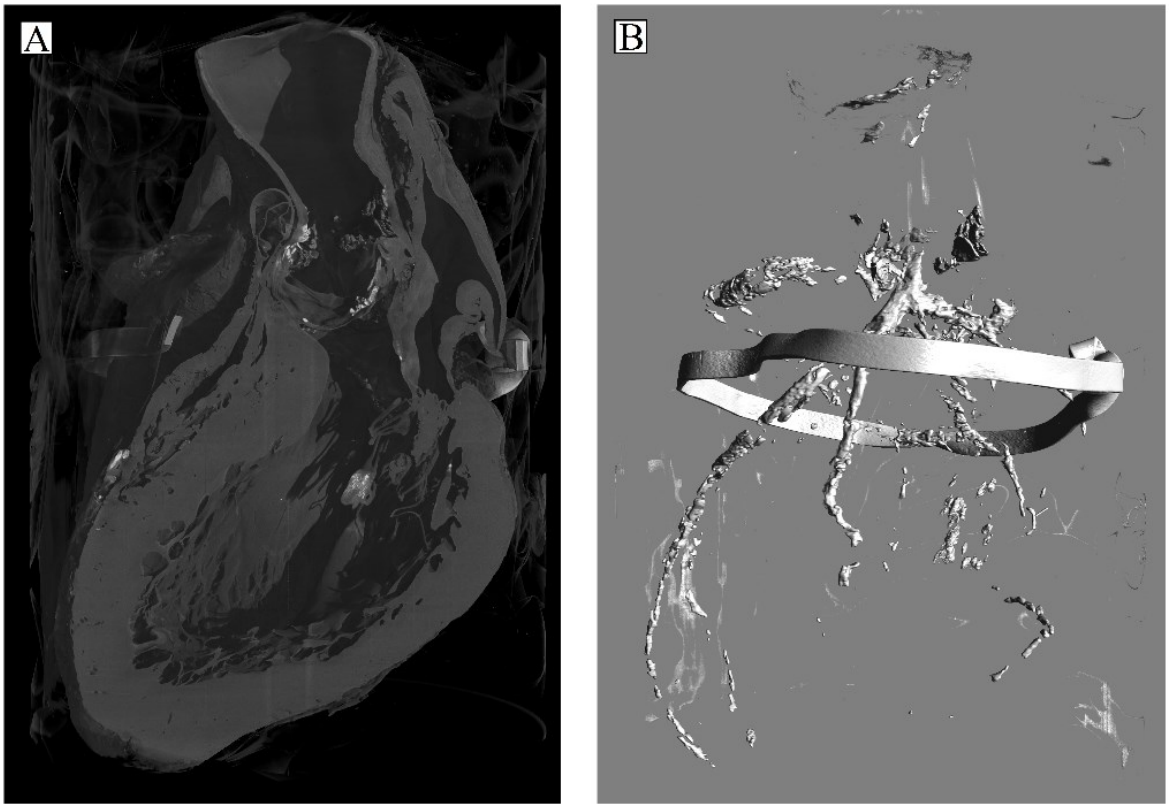

Figure 4. μCT scan of a human heart with a section cut away (A), the same scan displaying the calcified plaques present in the heart, as well as an elastic band (B).

The incidence of aortic stenosis in the elderly population (greater than the age of 65) is 2%. Risk factors that are associated with AS include, age, gender, smoking, obesity and congenital heart defects. (Stewart et al. 1997, Otto et al. 1999, Lindroos et al. 1993, Nkomo et al. 2006, Calle et al. 1999, Fenoglio Jr et al. 1977, Roberts 1970).

A study of 11,911 patients' echocardiography data demonstrated that the incidence of AS is age related. The youngest age bracket was 18 to 44 years of age, in which the incidence of AS was 0.02%, whereas the incidence of AS in patients over the age of 75 was 2.8%. A summary of the data is shown in Table 1 (Nkomo et al. 2006).

Age (years)	Sample size	Incidence of AS	Incidence of any valve disease
18 – 44	4351	0.02%	0.7%
45 – 54	696	0.1%	0.4%
55 – 64	1240	0.2%	1.9%
65 – 74	3879	1.3%	8.5%
> 74	1745	2.8%	13.2%

Table 1. The incidence of aortic stenosis with reference to age.

Aortic stenosis is associated with increased stress on the aortic valve (Otto 2008, Schoen and Levy 2005). Similarly, bicuspid aortic valves are less efficient than tricuspid aortic valves which increases the stress in the valve. This could be the cause of an increased incidence of AS in individuals with a bicuspid aortic valve. It has been reported that up to 73% of individuals with bicuspid valves also had some form of aortic stenosis at the time of death (Fenoglio Jr et al. 1977, Roberts 1970).

2.3 Treatment of Aortic Stenosis

The standard procedure to treat aortic stenosis is SVR. Aortic valve prosthetic replacements are implanted into, above or below the aortic root annulus and can be either bioprosthetic or non-bioprosthetic with mechanical leaflets. An example of a bioprosthetic SVR prosthesis is the Edwards Lifesciences Magna valve (Figure 5).

Figure 5. The Edwards Lifesciences Magna SVR device (Edwards Lifesciences 2014b).

The first steps of the implantation process involve opening the sternum in order to reveal the heart. Then an extracorporeal circulation machine is installed and the aortic root is sealed by means of cannulas. A *T* shaped incision is made in the aortic root before the aortic leaflets are removed and the root decalcified. The prosthetic valve is then implanted in place of the native aortic valve (see Figure 6). The aortic root is then sutured closed, the extracorporeal circulation machine is detached and the sternum is closed. The one year survival rate of SVR can be as high as 96%; however, in high risk patients, the one year survival rate can be as low as 74.8% (Mohr et al. 1995, Smith et al. 2011).

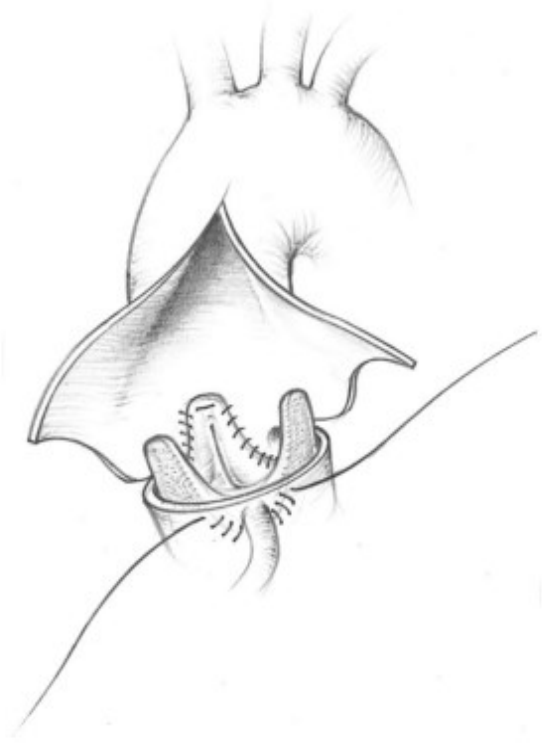

Figure 6. SVR involves opening the aorta to insert the prosthetic valve (Siebenmann Md 1997).

Mechanical valve replacements such as the Carbomedics Bileaflet prosthesis are implanted in the same manner as bioprosthetic valves (Rödler et al. 1997). Most modern mechanical valves feature a hinge which can be a source of thromboembolisms due to high shear stress and as a result are used less frequently than their biological counterparts (Yun et al. 2012).

Despite the extremely invasive nature of SVR, a procedural success rate (at one year) as high as 96% can be achieved (Mohr et al. 1995). However, in order to maintain such a high success rate, patient selection must be extremely stringent. Data collected on 5001 patients (collected before 2001) showed that 31.8% of patients were deemed too high risk to undergo cardiac intervention (Iung et al. 2003). As a result, a new valve replacement procedure was developed called trans-catheter aortic valve implantation (TAVI) in which the prosthetic device is delivered percutaneously (through a needle puncture in the skin). This type of procedure is minimally invasive, making it more suitable for frail patients. One of the first TAVI devices that was shown to be capable of undergoing balloon expansion into an anaesthetised porcine is shown in Figure 7 (Webb and Binder 2012).

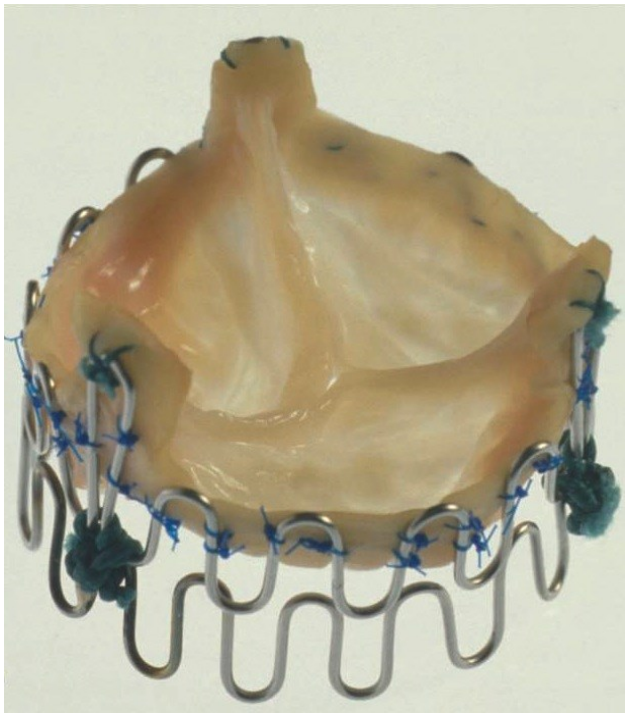

Figure 7. The Anderson valve, the first implanted TAVI device (Webb and Binder 2012).

The most common access site is the femoral artery. Trans-femoral TAVI involves anaesthetising the patient, and creating a small incision in the inner leg to access the femoral artery. The device is then fed through the femoral artery, through the aorta and into the aortic root. After being carefully positioned within the native aortic valve, the device is deployed. A detailed description of the deployment procedure can be found in section 2.6.

There have been many large studies to verify whether TAVI is superior to the traditional SVR. This includes an Italian study in which 2108 patients were reviewed, 1383 underwent surgical replacement whereas 725 patients underwent TAVI. It was found that the 30 day mortality was 3.8% for both techniques and the incidence of stroke was statistically similar between the two procedures (D'Errigo et al. 2012).

Edwards Lifesciences performed a study in which SVR and TAVI were randomly allocated to 699 patients with severe symptomatic aortic stenosis. This random allocation makes the study more credible than others as TAVI is often considered a *backup* option for frail patients. The results showed that the TAVI device had a lower incidence of mortality at 30 days, and a statistically similar one year mortality (table 2) (Smith et al. 2011).

End Point	TAVI (%)	SVR (%)
30 day mortality	3.4	6.5
1 year mortality	24.2	26.8

Table 2. Comparison of mortality rates between TAVI and SVR

An alternative study focused on the benefits of TAVI against no treatment. 358 patients who were deemed too frail for SVR, were randomly assigned either TAVI or standard therapy (comprising drug courses, and potentially balloon angioplasty, which was performed in 84.8% of the patients). It was shown that TAVI is significantly safer than standard therapy as the one year mortality rates were 30.7% and 49.7% respectively.

In the previous studies discussed, the incidence of mortality at one year was relatively high as the patients undergoing treatment were high risk. During 2010 and 2011, 1416 patients underwent TAVI. 806 patients had a device from the Edwards Lifesciences SAPIEN range (SAPIEN 2 or SAPIEN XT), while 610 patients received a Medtronic CoreValve. The mortality rate at one year for both groups was 14% and 16% respectively. This is a significant decrease in the mortality rates previously discussed (24.2% and 30.7%) as the patients are in a lower risk group (Sabaté et al. 2013). TAVI has always been considered an alternative treatment to SVR; as time goes by it will likely become the primary treatment for AS, in which case, the risk factor associated with each patient will decrease, as will the mortality rate.

2.4 Introduction to Transcatheter Aortic Valve Implantation

TAVI is a relatively new medical procedure, and there is still a broad variety of devices and deployment methods being developed. There are two main options for deploying a TAVI device: self-expandable (SE) and balloon-expandable (BE). SE devices rely on the superelastic material properties of the frame to expand, as opposed to BE devices which are deployed using balloon inflation (de Buhr et al. 2012). There are advantages to both types of devices. The BE devices are guaranteed to reach full expansion while SE devices generally have a lower delivery profile allowing for safer delivery of the device. Furthermore, SE devices can be retracted after being semi-deployed if the device is incorrectly positioned during deployment (Meredith et al. 2012, Meredith et al. 2013). This thesis focuses on BE devices as the local hospital (Southampton General Hospital – NHS 2014) specializes in BE devices.

Since the size of the aortic root and valve vary between patients, a small number of different sizes of each valve are available. Guidelines matching aortic root sizes with TAVI sizes are issued by the manufacturer (Leber et al. 2013). The aortic root diameters and corresponding device diameters are listed in Table 3 for the Edwards Lifesciences SAPIEN XT. It is important to note that there are grey areas that fall between valve sizes and require patient-specific consideration. If the prosthetic valve chosen is too small, the resultant orifice area is much smaller than the natural orifice area; this is a condition known as patient prosthetic mismatch (PPM). Severe PPM occurs in approximately 7.6% of cases and increases the three month mortality rates from 4% to 9.5% (Kukucka et al. 2012).

SAPIEN XT diameter	Recommended annulus diameter
20 mm	15-17 mm
23 mm	18-21 mm
26 mm	22-24 mm
29 mm	25-28 mm

Table 3. Recommended device and aortic annulus diameter pairings.

Interestingly, TAVI devices such as the SAPIEN XT can also be deployed in the mitral valve. *Cheung et al. (2011)* performed transapical TAVI deployment in the mitral valve on 11 patients with a one year mortality rate of 18%. Other deployment techniques for mitral valve replacement have also been developed including transfemoral-transseptal and transjugular-transseptal both with positive results (Schaefer et al. 2012b, Schaefer et al. 2012a).

2.5 Transcatheter Aortic Valve Implantation Devices

There are only four companies selling TAVI devices commercially in the UK (CE mark approved): Medtronic, Edwards Lifesciences, Boston Scientific and Direct Flow. There are also a multitude of smaller companies developing valves through clinical trials, attempting to gain a foot-hold in a very dynamic and lucrative market. A brief description of the main devices, as well as a selection of less conventional devices, is presented in this section.

2.5.1 Edwards Lifesciences SAPIEN XT

The SAPIEN XT is a second generation TAVI valve designed and manufactured by Edwards Lifesciences. It features bioprosthetic leaflets manufactured from bovine pericardium, a cobalt chromium alloy frame and a polyethylene terephthalate (PET) cuff. The SAPIEN XT is deployed through balloon-expansion. The delivery catheter size is 24 Fr[1] (using the Edwards Lifesciences NovaFlex+ delivery system - Edwards Lifesciences 2014a). Some patients may not have suitable femoral arteries to support such a catheter. In order to broaden the market for its device, Edwards Lifesciences developed the transapical delivery method (Edwards LifeSciences 2013b). The SAPIEN XT is available in four sizes: 20 mm, 23 mm, 26 mm and 29 mm diameter. The 29 mm device is unique as it has additional cells, as seen in Figure 8.

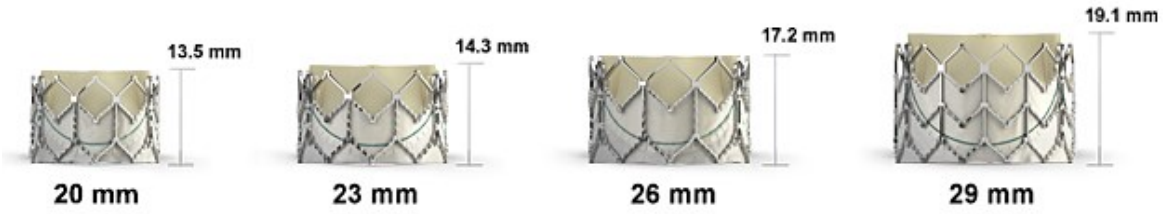

Figure 8. All available Edwards SAPIEN XT TAVI valves with dimensions (Edwards LifeSciences 2013b)

2.5.2 Edwards Lifesciences SAPIEN 3

The Edwards Lifesciences SAPIEN 3 (Figure 9) is the next iteration in the SAPIEN range to the SAPIEN XT. The design has been modified specifically to reduce PAR. The cuff is significantly larger and features on the exterior of the frame as well as the interior. The larger cuff could potentially aid in reducing PAR by plugging any gaps between the frame and the native tissue. The second

[1] Fr is the abbreviation of *French*, the unit used to measure the diameter of a catheter. 1Fr is 0.33mm.

notable area of improvement is the frame geometry which has been optimised to reduce PAR. Finally the delivery system has been redeveloped. The new eSheath incorporates a dynamic expansion mechanism in which the diameter of the sheath can be temporarily and locally increased to allow the TAVI device to be transported along the catheter. This reduces the minimal sheath diameter required to deploy the SAPIEN 3 to 14 Fr. The SAPIEN 3 is available in 23 mm, 26 mm and 29 mm sizes. In the future, a 20 mm device will also be released (Edwards LifeSciences 2013a, Ronald K. Binder 2012).

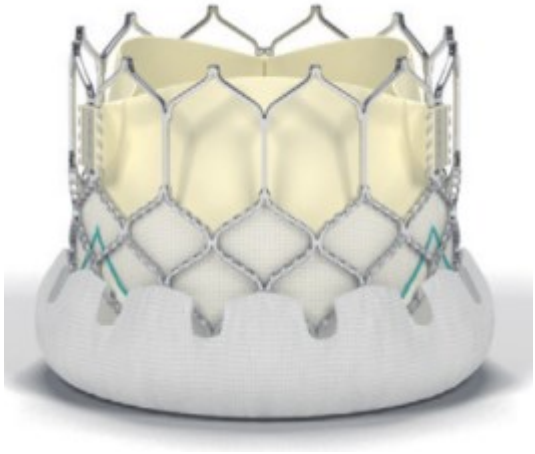

Figure 9. Edwards LifeSciences SAPIEN 3 (Ronald K. Binder 2012).

2.5.3 Medtronic CoreValve

The Medtronic CoreValve (Figure 10(A)) is a self-expanding device made from a nickel titanium alloy. The delivery diameter of the CoreValve is 18 Fr. If the femoral artery cannot support a 18 Fr catheter, the CoreValve can be implanted by means of the subclavian artery (Medtronic 2013a). The leaflets are manufactured from porcine pericardium as opposed to bovine. The CoreValve features a large cuff (larger than the SAPIEN XT) which is hypothesised to reduce PAR and create a superior seal. The device has an inconsistent radius in order to increase the axial traction and reduce migration of the device. The device is available in four sizes: 23 mm, 26 mm, 29 mm and 31 mm diameters (Medtronic 2013a, Nijhoff et al.).

2.5.4 Medtronic CoreVlave Evolut-R

The CoreValve Evolut-R (Figure 10(B)) is the latest device from Medtronic. The CoreValve Evolut-R is available in 23 mm, 26 mm, 29 mm and 31 mm sizes. The device has improved the deployment performance, compared to its predecessor (CoreValve), as well as the ability to be resheathed if deployment is not satisfactory. The deployment diameter of the Evolut-R has been further reduced to 16Fr allowing it to be deployed through narrower vessels. Finally the frame height has been reduced by approximately 10%, possibly to allow easier access (Sinning et al. 2013).

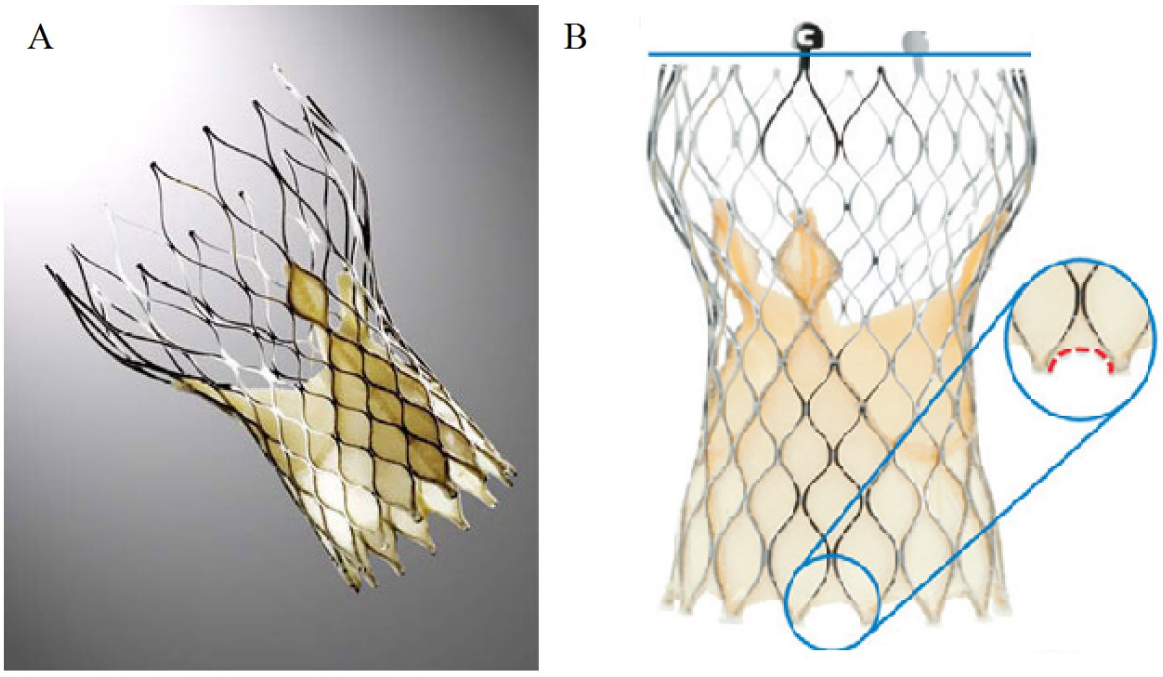

Figure 10. Medtronic CoreValve (A) and CoreValve Evolut-R (B) (Medtronic 2013b, Sinning et al. 2013)

2.5.5 Direct Flow Medical Valve

The Direct Flow Medical Valve (Figure 12(A)**)** is a novel valve as it does not have a metal frame. Rather, a series of inflatable chambers are filled with a radio opaque solution during deployment. The device can be repositioned by deflating then re-inflating the chambers. The device is also flexible pre-deployment as it comprises thin walled chambers. The solution within the chambers must cure, a 90 minute process, effectively doubling the procedural time. The device is available in both 25 mm and 27 mm diameter devices and is deployed on an 18 Fr catheter (Klaudija Bijuklic and Joachim Schofer 2012).

2.5.6 Boston Scientific Lotus Valve

The Lotus valve is a unique device with respect to delivery as it employs a deployment system that uses a nitinol frame that initially expands to a sub-deployed diameter. After which the axial length of the device is shortened in order to increase the diameter of the device to the full deployment diameter. Finally, the catheter is disconnected from the valve, up to this point the device is repositionable and retrievable. The device itself with the delivery apparatus is pictured in Figure 11. The device is available in three sizes: 25 mm, 27 mm and 29 mm diameters (Scientific 2016).

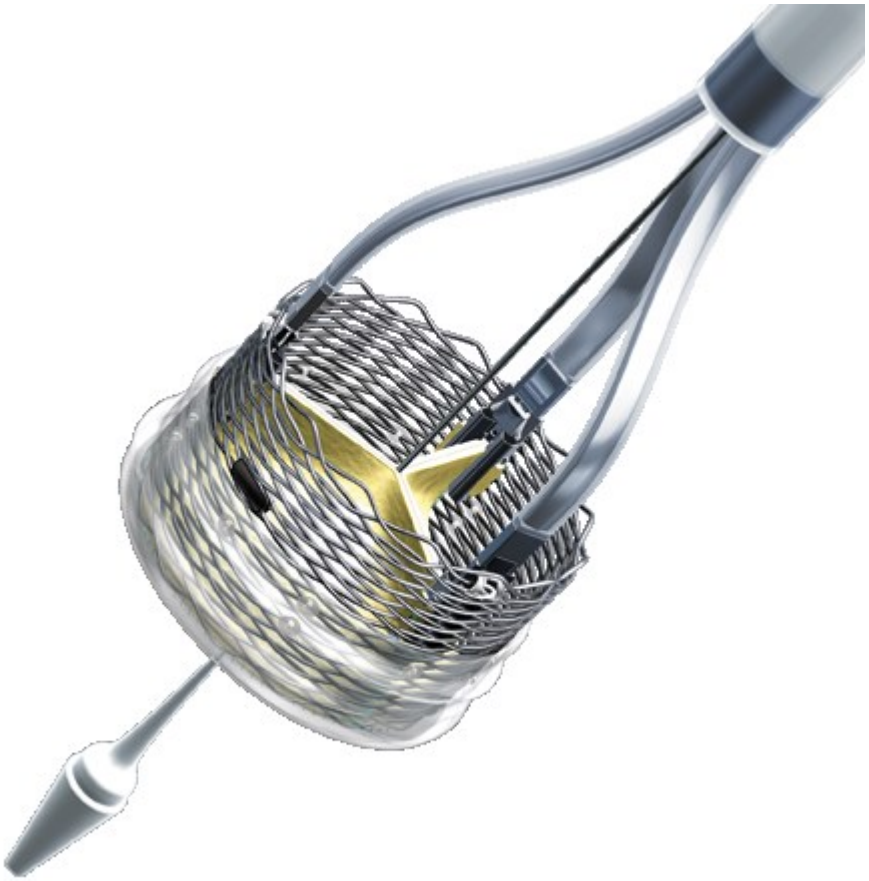

Figure 11. The Boston Scientific Lotus valve (Scientific 2016).

2.5.7 JenaValve

JenaValve Technology is a relatively small company that developed the JenaValve (DICardiology 2013), which is a self-expanding device with porcine bioprosthetic leaflets (Figure 12(B)). The device has been developed to ease the deployment process with a novel positioning system. Three fixation clips slide into the native valves sinuses, and guide the device through deployment into a location specified by the clip length. This deployment procedure also ensures the prosthetic leaflet is in phase with the native leaflet. Furthermore, rapid pacing is not required for deployment which reduces patient stress. The device requires a 32 Fr catheter which is relatively large and can only be deployed transapically. It is available in three sizes: 23 mm, 25 mm and 27 mm diameter (Hendrik Treede and Hans-Reiner Figulla 2012)

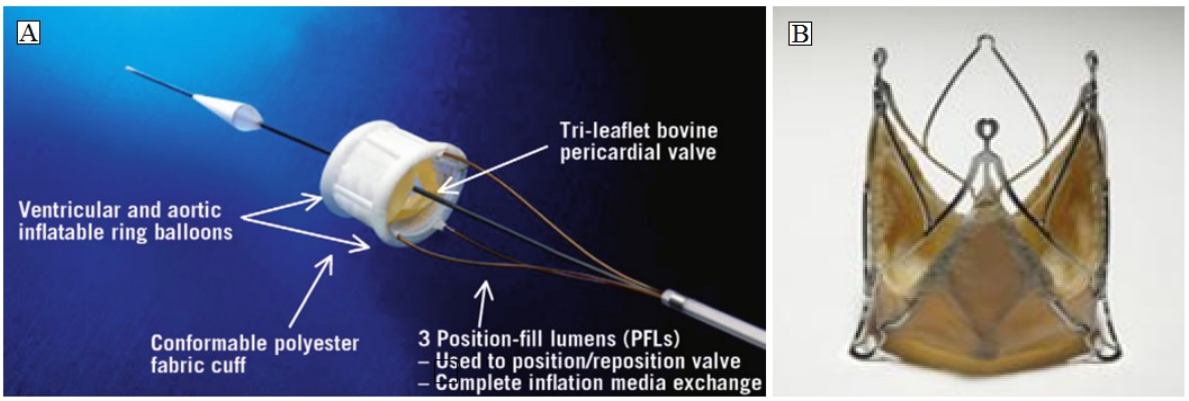

Figure 12. Direct flow Medical Valve with delivery catheter (A) and the JenaValve (B) (DICardiology 2013, Klaudija Bijuklic and Joachim Schofer 2012).

This is not a complete review of current TAVI devices. Further devices include, but is not limited to: Myval by Meril, Acurate neo by Symetis, Trinity by Transcatheter Technologies and the BIOVALVE by Biotronik.

2.6 Transcatheter Aortic Valve Implantation Procedure

There are multiple methods of deploying TAVI devices, as this thesis focuses on BE devices, the most common methods for delivering BE devices will be explained only. There are two main deployment methods for TAVI: transfemoral and transapical. Each deployment method relies on the same imaging techniques for positioning the TAVI device: trans-oesophagus echocardiogram (TOE) and angioplastic fluoroscopy (Bagur et al. 2011, Rodes-Cabau 2010). A transvenous pacing wire is required to stall the heart during deployment and is implanted trans-femorally, although internal trans-jugular is also possible. Pig tail angioplasty catheters are used in all techniques and can again

be delivered by means of the femoral or jugular arteries. Angioplasty is common practice in all three methods. Devices such as the Ascendra (Edwards LifeSciences 2015) angioplasty kit are used in which an Ascendra introducer is inserted over the guide wire. An angioplasty balloon is then advanced to the deployment position and gauged with the aid of radio opaque markers. Generally, under rapid pacing the angioplasty balloon is inflated. The balloon is then deflated and sheathed before being removed from the patient. The delivery of the balloon is also normally the same delivery route as the TAVI device.

2.6.1 Transfemoral Deployment

Transfemoral is the preferred access site to the heart during TAVI. A small incision in the groin is made, where access to the femoral artery is achieved. The TAVI device then travels up the femoral artery and to the aorta where the TAVI device is pushed through the aortic valve. The catheter delivery system has a shunted nose to aid passage through the native valve. When a preferable position is found the device is expanded under pacing to stall the heart and reduce the blood pressure. After deployment all the catheters are removed and the incision in the groin is sutured (Webb et al. 2006, Cribier et al. 2006).

2.6.2 Transapical Deployment

Unfortunately, elderly patients with poor circulation frequently have unsuitable femoral arteries for transfemoral access (stenotic femoral arteries can result in a lumen that is smaller than the delivery catheter). As a result the transapical approach was developed. An incision is made in the chest in-between the 5^{th} and 6^{th} intercostal space where a soft tissue retractor retains easy access. An incision is then made in the pericardium revealing the apex of the heart; the pericardium is kept open with stitches. Purse string sutures are then stitched to the apex and are used to secure the apex and consequently close the hole. A needle is pushed through the centre of the purse string sutures towards the right shoulder. A catheter is then pushed through the hole and delivered through the aortic valve into the aorta. A catheter is inserted along the initial guide wire which is retracted, only for a stiffer guide wire to be inserted in its place followed by the valve loader containing the valve which is advanced into the aortic root. The valve is then advanced into deployment position guided by radio opaque markers. Rapid pacing is then administered to stall the heart. After the pressure has dropped sufficiently, the balloon inside the valve should be deployed forcefully. After deployment all the catheters and sheath are removed from the patient and the purse strings are tightened closing the

incision in the heart. The rest of the tissue is closed in layers (Ben-Gal and Williams 2011, Walther et al. 2011, Pasic, Dreysse, et al. 2010).

2.6.3 Transaortic Deployment

Transaortic implantation is a technique that is very occasionally used when the patient meets three requirements 1) the aorta is not calcified, 2) the anatomy allows the sheath to be inserted in a direct line to the deployment zone, 3) the aorta is long enough to allow the balloon to expand without interference (Bapat and Attia 2012). In order to gain access to the aorta, a mini *J-shaped* sternotomy is performed through the right third intercostal spacing. The sternum can then be divided by means of an automatic sternal saw, revealing the pericardium which is incised to give a direct route to the aorta. Purse string sutures are used to secure the aorta for the catheter. A needle punctures the aorta and a soft guide wire and catheter are inserted. The initial guide wire is removed for a stiffer wire to be inserted in its place followed by the valve loader containing the valve which is advanced into the aortic root. The valve is then advanced into deployment position guided by radio opaque markers. Rapid pacing is administered to stall the heart. After the blood pressure has dropped, the balloon inside the valve should be deployed. The catheters are removed and the aorta is closed by means of the purse strings. The pericardium is left open while the sternum is closed with sternum wires (Bapat and Attia 2012, Ihlberg et al. 2012, Clarke et al. 2013, Bapat, Attia, and Thomas 2012).

2.7 Complications Following Treatment of Aortic Stenosis

SVR is an extremely invasive procedure which involves extensive trauma to the patient. There are a series of procedural complications that are associated with an increased mortality rate. The most common is bleeding within the chest cavity after the procedure. This requires a second operation to correct and occurs in 3.4% of patients. Despite all efforts to ensure sterility in the operating room, infection still occurs in 2% of SVR patients. If the intima (inner lining of the aorta) is perforated, blood can enter the aortic wall and delaminate the tissue; this is known as aortic dissection and occurs in 0.6% of SVR patients. If untreated, all of these conditions will result in mortality (Smith et al. 2011).

Many of the complications observed in SVR also occur in TAVI. Both post-operative bleeding and infection occur in 0.6% and 2% of patients respectively. However, these complications within TAVI are less severe because both occur at the access site: the inner leg, as opposed to the sternum. Aortic dissection also occurs in TAVI patients and is reported in as many as 0.9% procedures, which, if untreated, will result in mortality (Smith et al. 2011).

A major complication of both TAVI and SVR is stroke. The exact process is unclear, but it is believed that the frame in some manner interacts with the plaques, dislodging them in the process, at which point the plaques can potentially migrate to the brain before causing cerebral lesions. In a randomised study, in which high risk patients were allocated either TAVI or SVR, the relative incidence of major stroke one year after the procedure was 5.1% and 2.4% respectively (Smith et al. 2011).

Both TAVI and SVR have a further complication; valve failure. Calcified plaques can be redeposited onto the prosthetic leaflets inhibiting proper function, this process is known as restenosis. A TAVI device suffering from extreme restenosis is shown in Figure 13. As TAVI is a relatively new procedure, it is predominantly only applied to high risk patients who frequently die of other complications before restenosis can occur. Due to limited data, the life span of TAVI devices is not known. A study following 353 patients who received a Medtronic CoreValve over a five year period found two instances of restenosis (restenosis was detected 1465 and 1693 days after the patient underwent TAVI - Barbanti et al. 2015. The life expectancy of SVR prosthetic devices have been well documented, normally surviving 7-15 years (Butchart et al. 2001).

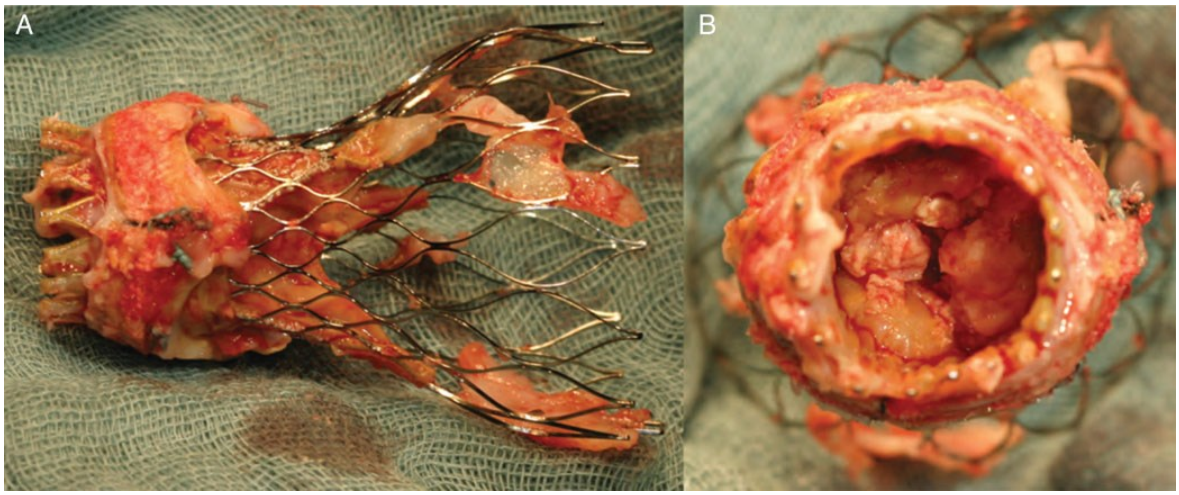

Figure 13. Medtronic CoreValve suffering from extreme restenosis (Mylotte et al. 2015).

There are also complications which are unique to TAVI and do not occur during or post SVR. The most common complication unique to TAVI is PAR. PAR occurs when the frame fails to make an effective seal inside the aortic root which allows blood to flow around the valve (John et al. 2010, Ewe et al. 2011). There are four grades of PAR, grade 1, which occurs in 74.8% of patients, grade 2, which occurs in 22.2% of patients, and grades 3-4, (being the most severe) occurring in 3% of patients (Hayashida et al. 2012). Severe PAR (grade 2-4) has been linked to early mortality within one year (Tamburino et al. 2011, Van Belle et al. 2012, Moat et al. 2011, Abdel-Wahab et al. 2011).

The deployment of TAVI devices is completely dependent on the valve frame being able to withstand the forces applied to it by the aortic tissue around it. Unfortunately, sometimes the valve is not stiff enough and the device can partially collapse or adopt a non-circular profile. It is a very difficult event

to recognise as the imaging techniques used to visualise the deployment often lack the resolution and clarity to detect this phenomenon. A series of examples of non-circular device frames are shown in Figure 14.

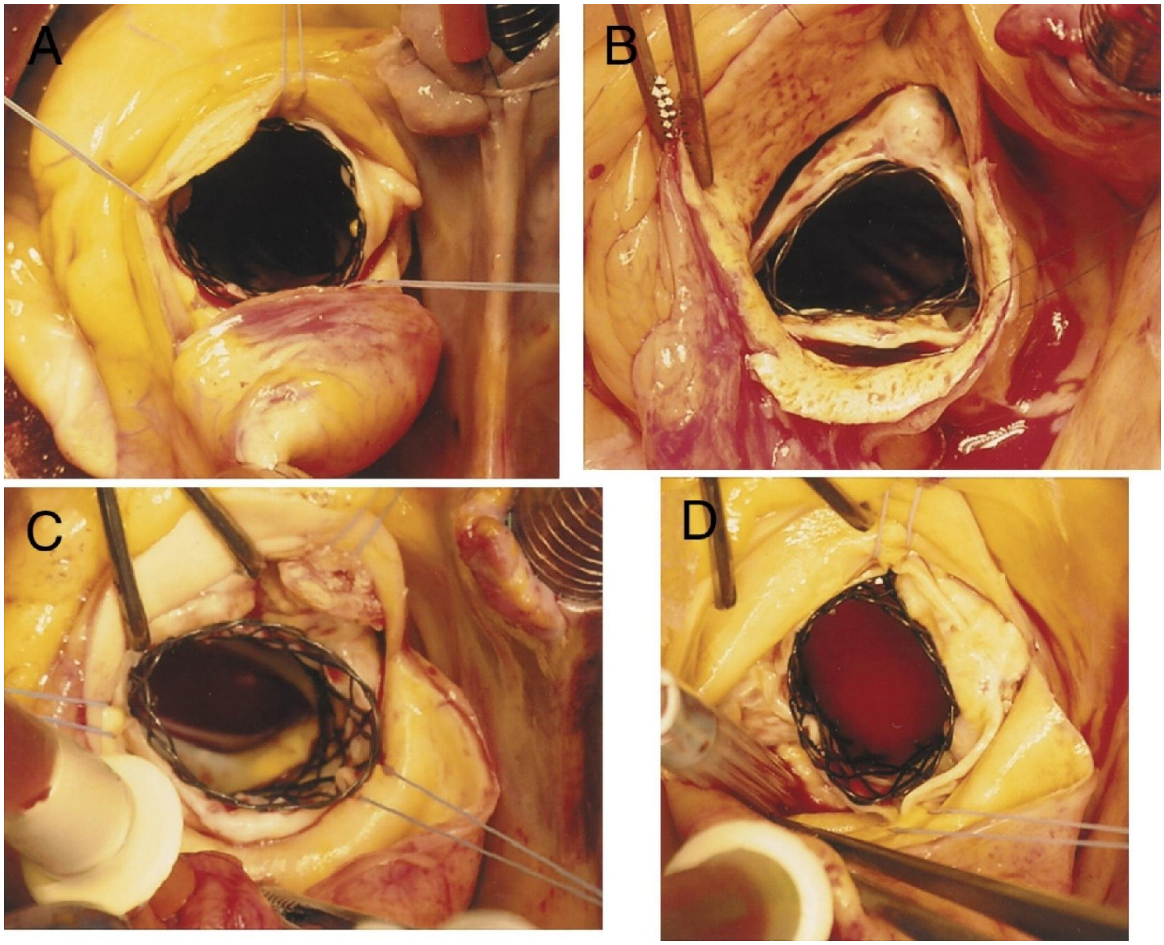

Figure 14. Variation in deployment shapes of TAVI devices including circular (A), triangular (B) and elliptical (C-D) (Zegdi et al. 2008).

Chapter 3: Complications Following Transcatheter Aortic Valve Implantation

3.1 Introduction

Although TAVI is safer than SVR, there are still major complications associated with the procedure that frequently occur. Two of the most common complications, which will be the focus of this work are:

1) PAR, occurs when the valve does not make an effective seal with the aortic root wall; PAR is common in patients and has been linked to early mortality.
2) Embolism, is present to some extent in all patients. Only a large cerebral embolism typically results in serious complications, however the result can be debilitating and is often fatal.

A further complication is hypothesised to occur: inefficient valve function associated with imperfect frame deployment. If the frame deviates from a cylinder due to calcified masses, it may increase the operation stress of the leaflets and therefore induce premature failure. Each of these complications will be reviewed in detail in this chapter.

3.2 Paravalvular Aortic Regurgitation

PAR is a common complication with TAVI that has been reported to occur in 74.8% of patients. Severe PAR has been linked to early mortality and requires further intervention to treat; it is present in 25.2% of patients (Tamburino et al. 2011, Van Belle et al. 2012, Moat et al. 2011, Abdel-Wahab et al. 2011, Hayashida et al. 2012). It is known that large irregular plaques are responsible for PAR, exactly how is still unknown (Azzalini et al. 2014, Scharfschwerdt et al. 2013). *Hooi Ewe et al. (2011)* used a multilayer CT scanner to locate large calcified plaques within the aortic root. The location of plaques were then correlated with the incidence of PAR. It was shown that plaques on the aortic root wall are most likely to induce PAR. There are two likely mechanisms that induce PAR, both of which are shown in Figure 15. The first case is where the plaque pulls the aortic root away from the frame of the TAVI device. This occurs as the plaques are relatively stiff in comparison to the soft aortic root. In the second case, the frame cannot fully expand or conform effectively to the plaque resulting in PAR. It is likely that both mechanisms play a partial role in PAR, and the degree to which each mechanism induces PAR is likely to be specific to each case.

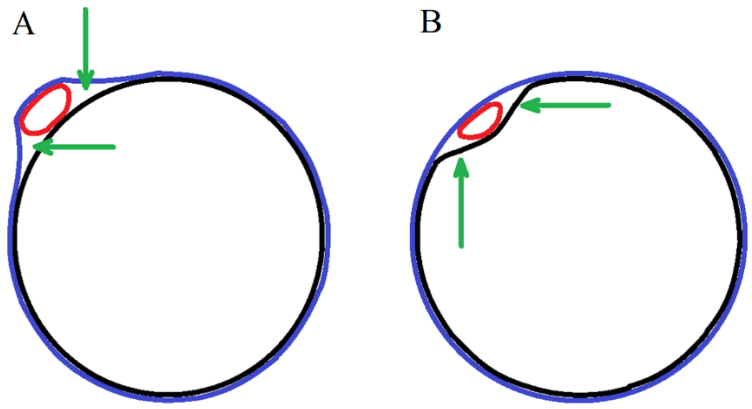

Figure 15. A TAVI frame (black) expanded in an aortic root (blue), however a stiff plaque (red) has induced two gaps to appear (labelled with green arrows). There are two hypothesised mechanisms for PAR, in the first, a stiff plaque pulls the aortic root away from the frame (A), in the second, the frame cannot fully expand because of the plaque (B).

Munoz-Garcia et al. (2011) successfully identified areas of a SE device that could not fully expand due to calcified plaques which frequently resulted in PAR. During TAVI of BE devices, the balloon pressure can be increased, therefore ensuring the device always reaches a full diameter. BE devices however, have been known to recoil post balloon expansion, as further discussed in section 3.4. This would make SE devices more susceptible to the second suggested mechanism behind PAR. This is supported by the incidence of PAR in both SE and BE devices which is 19.8% and 12.2% respectively (grades 2-4 - Van Belle et al. 2012).

The aortic root is frequently non-circular. Approximately 50% of patients have an aortic root with an ellipticity ratio (defined as the long axis divided by the short axis) greater than 1.2 (Hayashida et al. 2013). An ellipticity ratio greater than 1.25 has been shown to be associated with an increased incidence of PAR (Wong et al. 2010). The circular TAVI device cannot easily conform to the elliptical aortic root resulting in PAR. Elliptical aortic roots have also been associated with transvalvular aortic regurgitation (Sun, Li, and Sirois 2010, Kuetting et al. 2014).

The probability of PAR can be influenced by patient-prosthetic mismatch (PPM). PPM is where the device is too small, resulting in an insufficiently sized orifice. If PPM does occur, an increased incidence of PAR is observed, and furthermore, the device's axial traction can be compromised, potentially resulting in device migration (Détaint et al. 2009, Muñoz-García et al. 2011, Leber et al. 2013). PPM can be treated with post-deployment angioplasty, in an attempt to over-expand the device. Some SE devices fail to fully expand, in which case, post-deployment angioplasty can also be used to fully expand the device (Nombela-Franco et al. 2012).

Deploying a second TAVI device in a valve-in-valve (ViV) procedure can also alleviate PAR (Pasic, Unbehaun, et al. 2010, Pasic, Buz, et al. 2010). The second device over-expands the initial device resulting in improved contact between it and the native tissue. The seal between the two TAVI

devices is generally effective as the exterior device has a smooth interior surface, ideal for creating a seal. Despite the guidelines detailing which TAVI device size to use, it has been found that during a ViV procedure, oversizing the device reduces the rate of reoccurring PAR (Van Belle et al. 2011). It is important to note that ViV deployment is not unique to TAVI devices. In fact, it is more commonly used to treat a failing SVR prosthetic valve (Bapat et al. 2012, Piazza et al. 2011, Ihlberg et al. 2012). Performing ViV procedures, is not guaranteed to alleviate PAR. In 2013, an interesting case review was published, in which a valve-in-valve-in-valve procedure was performed because the initial ViV procedure did not alleviate PAR (Kempfert et al. 2013). Every additional valve implanted into an aortic root increases the risk of aortic rupture and reduces the devices orifice area. As a result, ViV procedures are not necessarily a suitable treatment for PAR.

SVR does not suffer from PAR as the prosthetic valve is sutured to the aortic root which creates a complete seal. In order for TAVI to supersede SVR, the incidence of PAR must be reduced. It is of no surprise that the latest prosthetic devices have added features to reduce the incidence of PAR. For example the SAPIEN 3 has a large cuff that creates a superior seal as described in section 2.5.2.

3.3 Embolism Associated with Transcatheter Aortic Valve Implantation

Stroke is a complication with TAVI that is both severe, and difficult to predict. The severity of stroke varies between patient cases and is categorised by the modified Rankin scale (MRS), which is shown in Table 4 (van Swieten et al. 1988, UK-TIA 1988).

Grade	Description
0	No symptoms at all
1	No significant disability despite symptoms: able to carry out all usual duties and activities
2	Slight disability: unable to carry out all previous activities but able to look after own affairs without assistance
3	Moderate disability: requiring some help, but able to walk without assistance
4	Moderately severe disability: unable to walk without assistance, and unable to attend to own bodily needs without assistance
5	Severe disability: bedridden, incontinent, and requiring constant nursing care and attention
6	Death

Table 4. Modified Rankin scale grades and definitions.

A comparison between the frequencies of stroke in inoperable patients between standard treatment (comprising a drug course and balloon angioplasty when appropriate) and TAVI was performed in the PARTNER trial; a multi-centre review of TAVI funded by Edwards Lifesciences. 358 patients with severe aortic stenosis who were not suitable for SVR, were randomly allocated either standard therapy (N=179) or TAVI (N=179). The results demonstrated that the incidence of both major (MRS 2-6) and minor (MRS 0-1) stroke was greater in the TAVI patients at both three months and one year after treatment. However, the all-cause mortality rate was lower in the TAVI group. This data is shown in Table 5 (Leon et al. 2010).

Complication	Thirty days		One year	
	TAVI	Standard treatment	TAVI	Standard treatment
Major stroke	9 (5%)	2 (1.1%)	14 (7.8%)	7 (3.9%)
Minor stroke	3 (1.7%)	1 (0.6%)	4 (2.2%)	1 (0.6%)
Mortality	9 (5%)	5 (2.8%)	55 (30.7%)	89 (49.7%)

Table 5. Comparison between the frequencies of stroke between patients treated with TAVI and standard therapy.

A second cohort of the PARTNER trial also compared SVR to TAVI. 699 patients were randomly assigned either TAVI (348) or SVR (351). Again, the incidence of both major and minor stroke (defined as MRS 2-6 and 0-1 respectively) in the TAVI group was significantly greater when compared to the SVR group. The results are tabulated in Table 6 (Smith et al. 2011).

Complication	Thirty days		One year	
	TAVI	SVR	TAVI	SVR
Major stroke	13 (3.8%)	7 (2.1%)	17 (5.1%)	8 (2.4%)
Minor stroke	3 (0.9%)	1 (0.3%)	3 (0.9%)	2 (0.7%)
Mortality	12 (3.4%)	22 (6.5%)	84 (24.2%)	89 (26.8%)

Table 6. Comparison between frequencies of stroke between patients treated with TAVI and SVR.

From these results it is clear that high risk TAVI patients are at a greater risk of stroke than high risk patients receiving alternative treatment at both 30 days and one year. All participants in the PARTNER trial were extremely high risk and as a result the incidence of stroke within the patient group is likely greater than the incidence over lower risk, *normal* patients. This correlates with a large study of 1416 TAVI patients that ranged from low-high risk. The incidence of in-hospital major and minor stroke were both 1% (Sabaté et al. 2013).

A further limitation of the PARTNER trial is that only strokes resulting in noticeable symptoms were detected. Often cerebral tissue is damaged due to embolism but, fortunately, the patient does not suffer any affects. *Rodés-Cabau et al. (2011)* used a diffusion weighted magnetic resonance imaging (DW-MRI) scanner to compare the brains of patients before and after TAVI. A cerebral DW-MRI was taken of patients within 24 hours before TAVI and within 144 hours after the procedure. Neurologic and cognitive function was assessed in the scans and cerebral lesions were identified (Figure 16). 41 patients (68%) presented new cerebral lesions, with an average of 6.1 new cerebral lesions per patient.

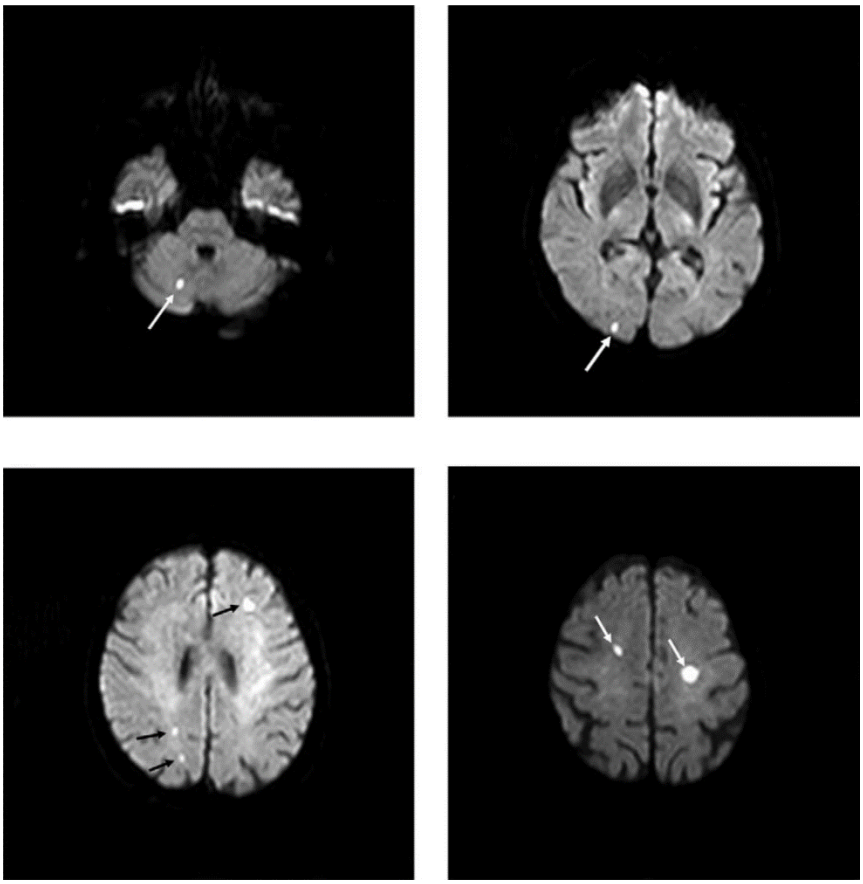

Figure 16. DW-MRI images of TAVI patient brains demonstrating cerebral lesions (Rodés-Cabau et al. 2011).

The incidence of debris release is much greater than the incidence of embolism as some debris will not cause embolism due to small size. Debris can be detected travelling through the cardiac system by Doppler ultrasound. A Doppler ultrasound system (DUS) measures the velocity of the blood travelling through the vessels of the cardiac system. The DUS can also detect debris within the blood appearing as a sharp peak in fluid acceleration (Figure 17), the magnitude of which is proportional to the size of the particle (Markus and Brown 1993). *Drews et al. (2011)* applied this technology to TAVI patients in an attempt to further understand what exactly was inducing debris release. Doppler echocardiograph probes were percutaneously positioned within both the middle cerebral arteries (MCA, left and right) before TAVI in fifty patients. All patients experienced some form of debris

release during the procedure. The procedural outline, with corresponding debris release count is shown in Table 7. This study demonstrated that most debris release is associated with the valvuloplasty balloon and the deployment balloon. Figure 17 precisely shows that debris is released after the valvuloplasty balloon has been deflated. It is likely that the balloon dislodges debris when inflated, but pins the debris in place with its body until deflation.

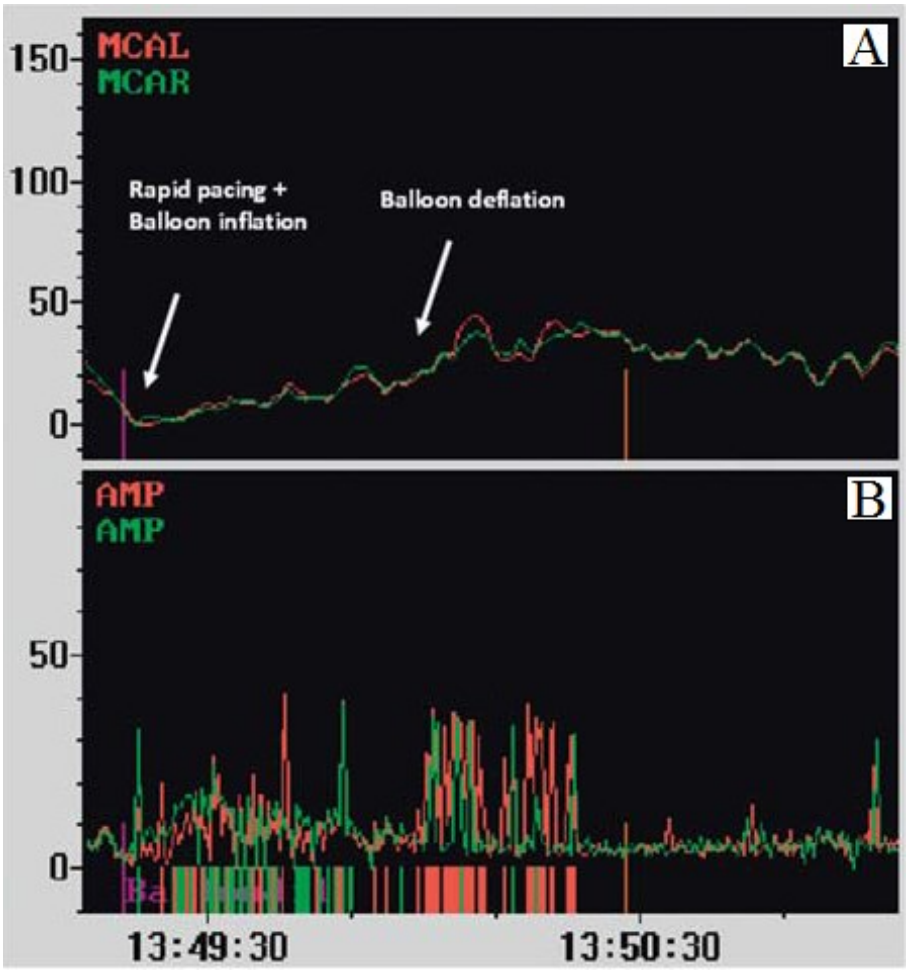

Figure 17. Doppler ultrasound examination of aortic balloon valvuloplasty. Flow velocities within the left and right middle carotid arteries (A) and flow acceleration within the left and right middle carotid arteries (B) that correspond to debris within the blood (Drews et al. 2011).

Process in question	Right middle cerebral artery	Left middle cerebral artery
Transfemoral pigtail catheter placement	6 ± 19 (0 – 167)	5 ± 7 (0 – 36)
Transapical soft sheath insertion	3 ± 9 (0 – 55)	4 ± 11 (0 – 68)
Placement of a transaortic guide wire (transapical access route)	9 ± 14 (0 – 66)	6 ± 12 (0 – 42)
Balloon valvuloplasty	21 ± 23 (0 – 99)	11 ± 18 (0 – 89)
Transapical valve delivery system positioning	8 ± 11 (0 – 51)	5 ± 12 (0 – 121)
Valve deployment	26 ± 28 (0 – 114)	12 ± 25 (0 – 121)
Removal of the transapical delivery system	5 ± 14 (0 – 52)	6 ± 10 (0 – 59)
Total	435 ± 922 (9 – 5765)	471 ± 996 (24 – 6432)
Period of recording (minutes)	122 ± 47 (49 – 258)	

Table 7. Transcranial Doppler ultrasound microembolic signals, mean ± standard deviation (range minimum-maximum).

The mechanism behind debris release is mechanical agitation. The valvuloplasty balloon and deployment balloon both exert large stresses upon the aortic root wall which can dislodge or rupture the plaques. It is also hypothesised that the delivery system and accompanying catheters may also dislodge debris during deployment as the catheters often rub on the vessel walls. If this is true, patients undergoing transapical deployment should experience fewer strokes as the delivery catheter does not follow the aortic arch. Currently, there is no conclusive evidence demonstrating which technique has a higher incidence of stroke (Sabaté et al. 2013). Furthermore, no study has randomly assigned transapical and transfemoral procedures to patients. Rather, transapical is a reserved technique only applied to patients with femoral arteries that are too frail to support a catheter and are therefore unsuitable for transfemoral TAVI.

The most frequent treatment for stroke is a drug course to treat the symptoms and to reduce the risk of further strokes. Occasionally, cardiovascular intervention is used to remove the blockage from the vessel. For TAVI, filters can be used as a preventative measure for cerebral emboli. A filter removes debris from the blood, or redirects the debris away from the brain. Preventative filters require additional catheters to be inserted into the patient which increases the procedural time and, therefore, the risk to the patient. A TriGuard cerebral protection device is shown in Figure 18. The objective of this device is not to capture debris, rather redirect the debris away from the brain (Heart 2015). To date, there is insufficient evidence to warrant use of embolism filters during TAVI (Praz and Nietlispach 2013).

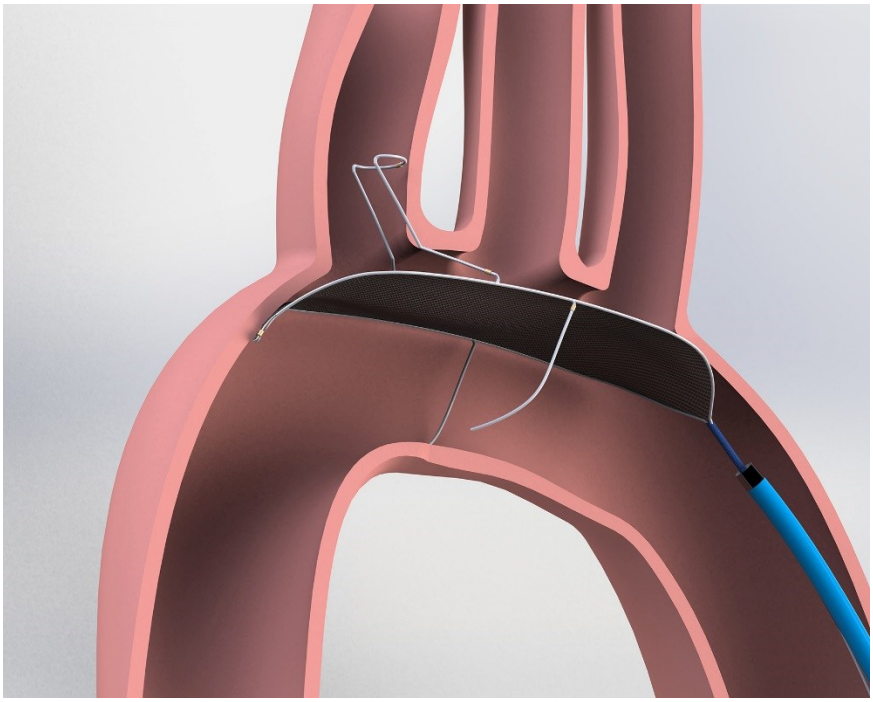

Figure 18. TriGuard cerebral protection device by Keystone Heart. The device deflects debris away from the carotid arteries which lead to the brain (Heart 2015).

3.4 Reduced Device Lifespan

The device lifespan is universally understood to decrease as the operating stress within the leaflets increases (Thubrikar et al. 1981). The operating stress of the TAVI device leaflets can increase for two reasons:

1) The TAVI device leaflets were designed to operate within a cylindrical device, if the frame deviates from cylindrical (an imperfect frame), the operating stress will increase.
2) If the TAVI device leaflets are damaged, local stress concentrations may occur.

Sun et al. (2010) computationally explored the concept of non-circular frames affecting leaflet operation by developing a FEA model of a TAVI device in Abaqus CAE, before distorting the frame and monitoring the stresses. The model comprised three leaflets and a cylindrical tube that represented the frame. The leaflets were attached to the tube by means of tie constraints, such that the lower edges of the leaflets could not move in any dimension relative to the frame. This is not necessarily representative of a TAVI device as the leaflets are actually attached to a thin film of fabric which is then itself attached to the frame, allowing for the lower edge of the leaflet to be slightly flexible (this is true for the majority of devices, although some exceptions do exist such as the Straight Access Technologies Synthetic Heart Valve). The model device was then deformed to a specific eccentricity factor, defined by

$$e = \sqrt{1 - \left(\frac{b}{a}\right)^2} \qquad [1]$$

where a and b are the major and minor diameters, respectively. The eccentricity factors analysed were 0.3, 0.5 and 0.68 in two scenarios (1 and 2) as shown in Figure 19. The cylinder representing the frame of the device was constrained in all degrees of freedom, and a uniform pressure load of 120 mmHg was applied to the leaflets. The maximum stresses and leakage area is documented in Table 8. Eccentric valves experienced greater maximum stresses in all the leaflets, with exception of a single case, scenario 2, $e = 0.5$, leaflet 1, in which the maximum stresses were 904 kPa and 848 kPa.

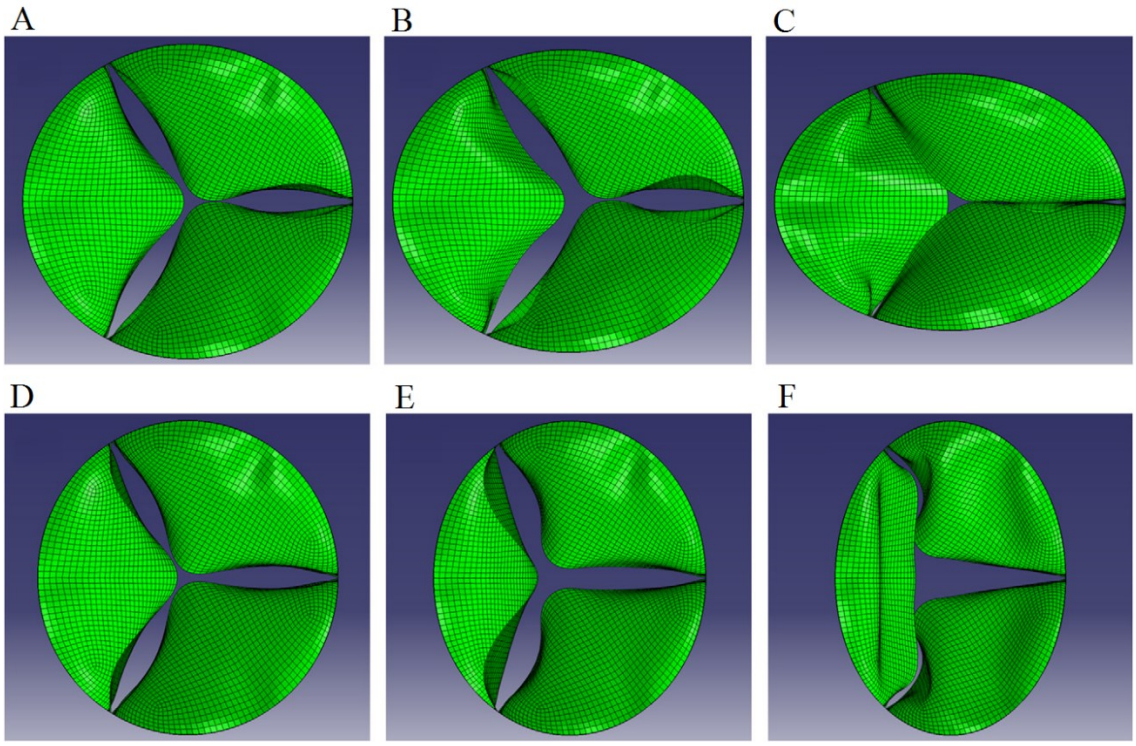

Figure 19. Computational models of prosthetic leaflets under varying eccentricity ratios: e = 0.3 (A, D), e = 0.5 (B, E) and e = 0.68 (C, F). Two device orientations relative to eccentricity are presented, scenario 1 (A – C) and scenario 2 (D – F) (Sun, Li, and Sirois 2010).

Model	Maximum stress, leaflet 1	Maximum stress, leaflet 2	Maximum stress, leaflet 3	Leakage area
Scenario 1, e=0.3	1221 kPa	1130 kPa	1075 kPa	0
Scenario 1, e=0.5	1413 kPa	1071 kPa	962 kPa	0.84 mm^2
Scenario 1, e=0.68	1189 kPa	1452 kPa	971 kPa	0.56 mm^2
Scenario 2, e=0.3	1020 kPa	1056 kPa	1047 kPa	0
Scenario 2, e=0.5	848 kPa	1319 kPa	1037 kPa	0
Scenario 2, e=0.68	2227 kPa	1586 kPa	1488 kPa	0.56 mm^2
Circular valve	904 kPa	915 kPa	916 kPa	0

Table 8. Maximum principal stresses and leakage area in eccentric valves.

Experimental analysis has also been applied to this area of research. *R. Zegdi et al. (2008)* observed that in many patients undergoing TAVI, the devices post deployment orientation was far from the intended cylindrical shape. In order to investigate any problem this may cause with the device valve, a simple experiment was performed. A *homemade* TAVI device was deployed into a circular orifice, as well as orifices of varying deformity, after which the leaflet orientation was observed. The leaflets adopted the stereotypical *Mercedes* orientation after deployment into an ideal, cylindrical aortic root. If the device was deployed into any aortic root model that was not ideal (undersized, elliptical, triangular, asymmetric), the leaflet orientation deviated from the ideal orientation (Figure 20). The resultant elevation of stress within the leaflets in the distorted orientation is not known. The scenario to which the leaflets must operate will likely affect the stress within the valve. The stress in non-circular frames are likely to be greater than the intended *Mercedes* orientation, however some scenarios may even decrease the stress within the valve.

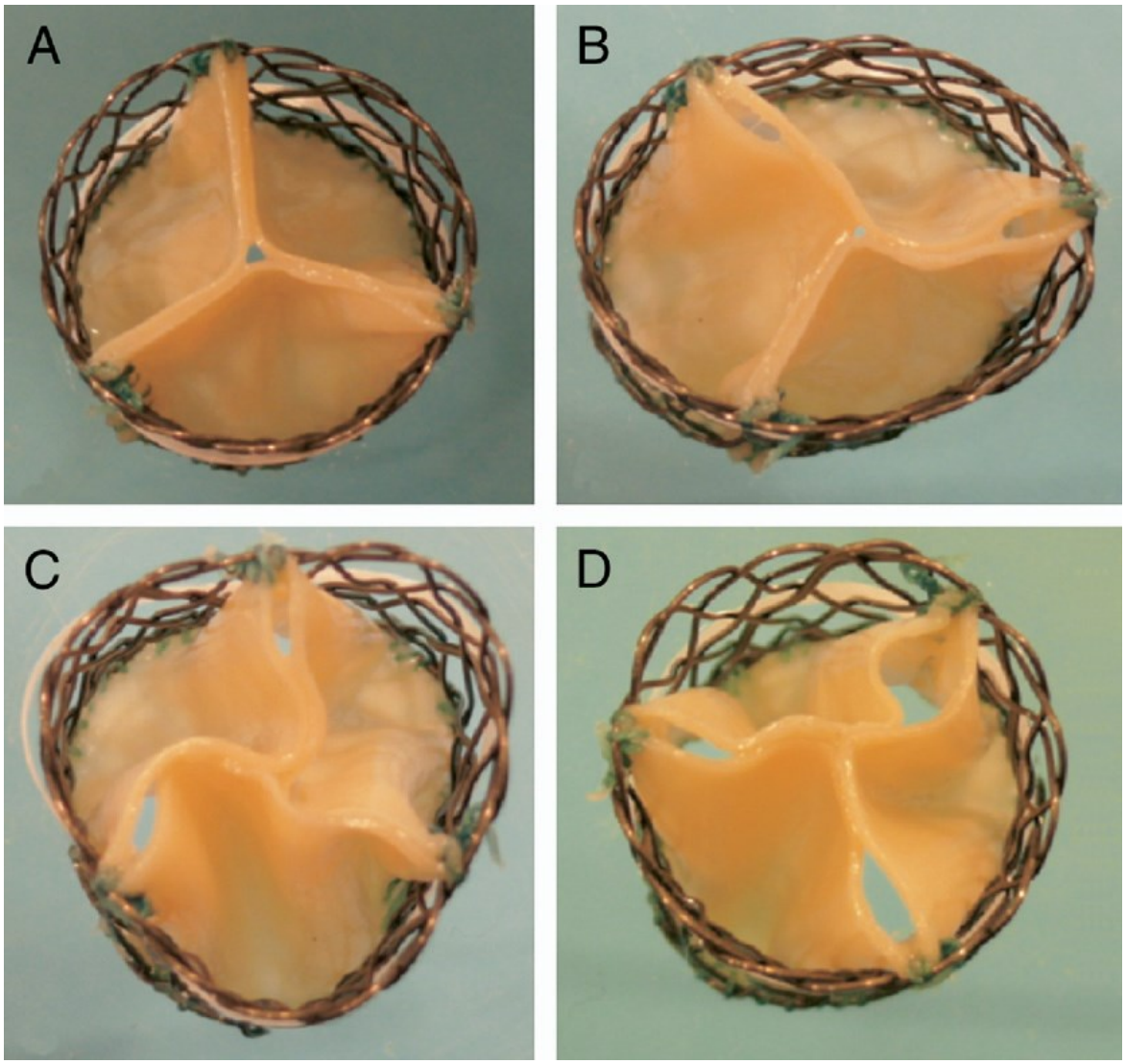

Figure 20. Resultant leaflet orientations for the frame shape: circular (A), eccentric (B, eccentricity factor of 0.73), triangular (C) and reduced diameter (D) (Zegdi et al. 2008).

Deployed TAVI devices can suffer from further imperfections other than eccentricity. The frames can be dented or skewed (Figure 21). The reason the frames suffer from these abnormalities is due to the stress exerted on the frames by the surrounding native tissue. The manner of imperfection in the frame is likely to be dependent on the size and location of the plaques within the aortic root.

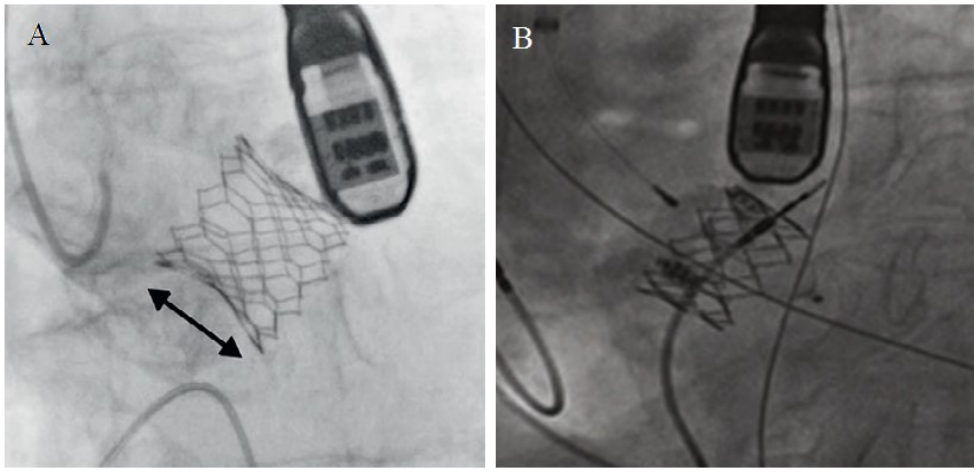

Figure 21. SAPIEN 3 device with an inconsistent radius (A) and a skewed SAPIEN XT device (B) (Rossi et al. , Garcia et al. 2014).

Identifying an imperfect frame can be difficult, the only imaging techniques used during TAVI is angioplastic fluoroscopy (which can function as an X-ray) and TOE. TOE can be capable of visualising a TAVI device post deployment, although it is difficult to identify any areas of imperfection as the images are often noisy, low resolution and suffering poor contrast. The X-Ray machine used for angioplastic fluoroscopy could potentially identify an imperfect frame. However, due to limited resolution, and the nature of the device, it may not be possible to see non-circular devices. Figure 22 shows two X-Ray images of the same deployed 26 mm SAPIEN XT TAVI device. In Figure 22(A), the device appears to be appropriately deployed with a circular cross section. Figure 22(B) shows the device to be skewed, the axial struts are not parallel to each other.

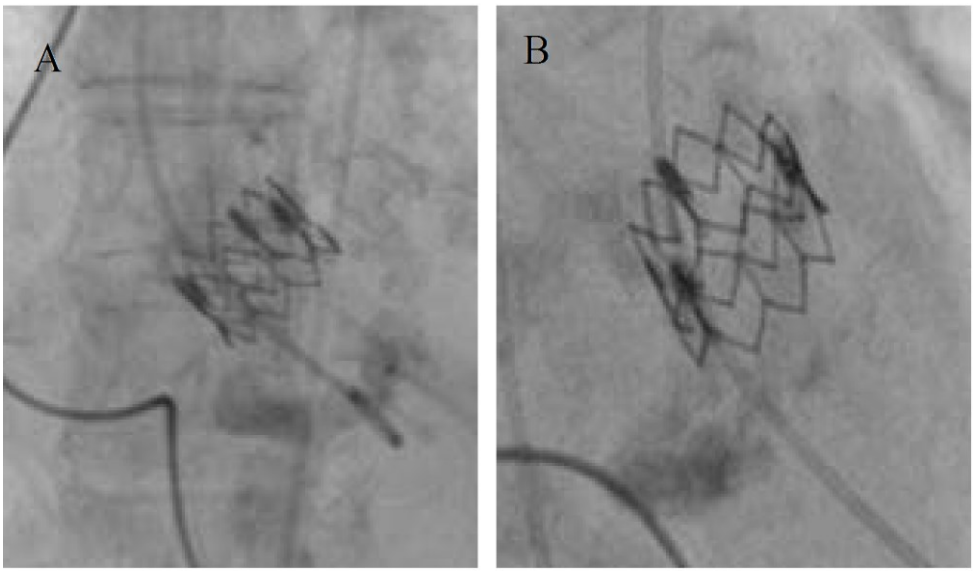

Figure 22. A SAPIEN XT device imaged from two angles, in the first the device appears to be a cylinder (A), however in the second it is apparent that the device is skewed (B) (Ulrich Gerckens 2013).

Even if imperfections within the device frame are visible on the medical image scans, it is not often recognised as a complication. Figure 22 and Figure 21 both show X-Ray images of implanted devices suffering from an imperfect frame, however the procedure was assumed to be a success and no further action was taken in either case (Garcia et al. 2014, Rossi et al.).

There was only a single study found that focused on the incidence of imperfect frame deployment. Thirty patients had a Medtronic CoreValve implanted, after which a multi slice CT scanner (MSCT) was used to scan the patient's heart. Because the plane of observation can be changed in a MSCT scan, it can easily identify imperfect frames (Figure 23).

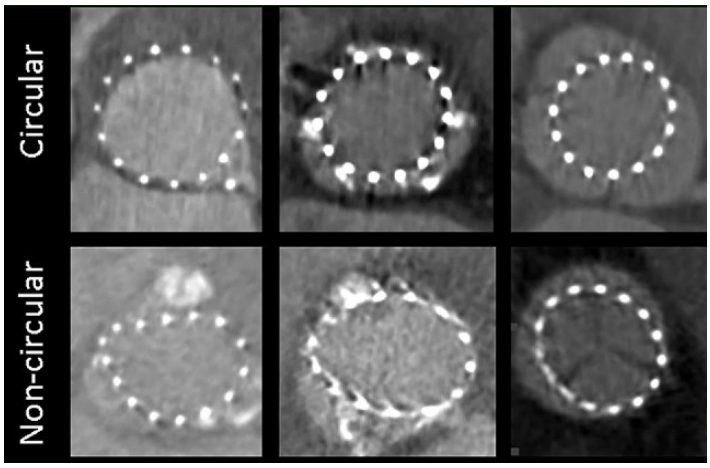

Figure 23. MSCT images of a CoreValve prosthesis. Examples of circular and non-circular cross sections (Schultz et al. 2009).

Of the thirty patients, seven had circular frames at the devices commissures (circular is defined by equation 2). This suggests that in self-expanding devices, a large proportion of the TAVI device recipients have elliptical valves (Schultz et al. 2009).

$$\frac{Diameter_{major}}{Diameter_{minor}} < 1.1 \qquad [2]$$

The leaflets can also be damaged and weakened when subjected to elevated stresses that disrupt the collagen fibres. *W. de Buhr et al. (2012)* manufactured a TAVI device with a laser cut stainless steel tube and bovine pericardium leaflets. The device was crimped on to a balloon before undergoing deployment through balloon inflation (at a pressure of 2 bar, applied for 3 seconds). Microscope inspection revealed damaged collagen fibres which if exposed can increase the risk of valve thrombosis and therefore reduce the lifespan of the device (as seen in Figure 24).

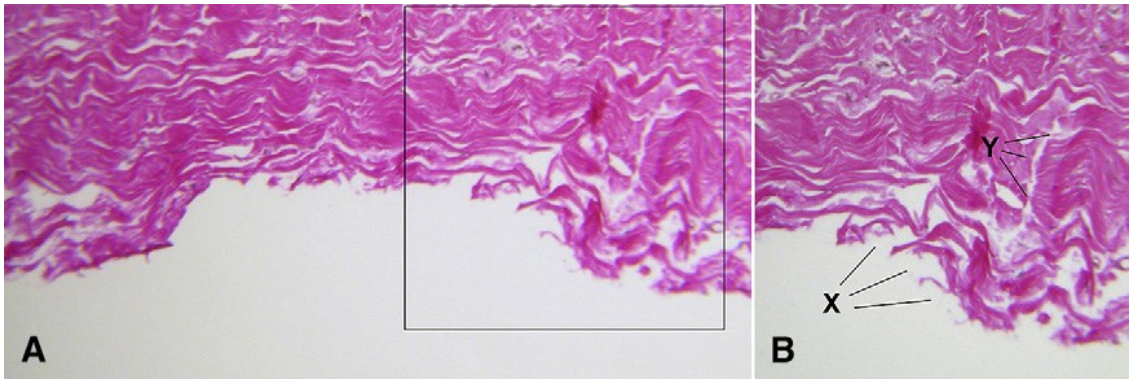

Figure 24. Histology of the pericardium indented by the TAVI devices frame (A). The histology of the boxed area from (A) contains disrupted and broken surface collagen fibres labelled X, and broken collagen fibres in the deeper layers of the pericardium labelled Y (B) (de Buhr et al. 2012).

Device expansion is not the only part of the deployment procedure that can damage the leaflets of a TAVI device as the crimping procedure can also exert excessive force on the leaflets resulting in damage. *Hamed Alavi et al. (2014)* used both scanning electron microscopy (SEM) and second-harmonic generation microscopy (SHGM) to image TAVI leaflets before and after crimping. The device analysed was a self-expanding TAVI device purposefully manufactured for the analysis. Since it was not balloon expandable, damage was not due to balloon expansion. Three devices were manufactured at a diameter of 25 mm, and then crimped to different diameters of 6 mm (18 Fr), 5.33 mm (16 Fr) and 4.66 mm (14 Fr). The devices were maintained in the crimped position for 20 minutes (the average time in TAVI practice) before being released, at which point the self-expanding devices returned to their original state. SEM was used to image the surface of the leaflets before and after the crimping procedure and the results are shown in Figure 25. The surface texture was dramatically altered due to the crimping procedure, the extent of which increased as the diameter to which the devices were crimped decreased.

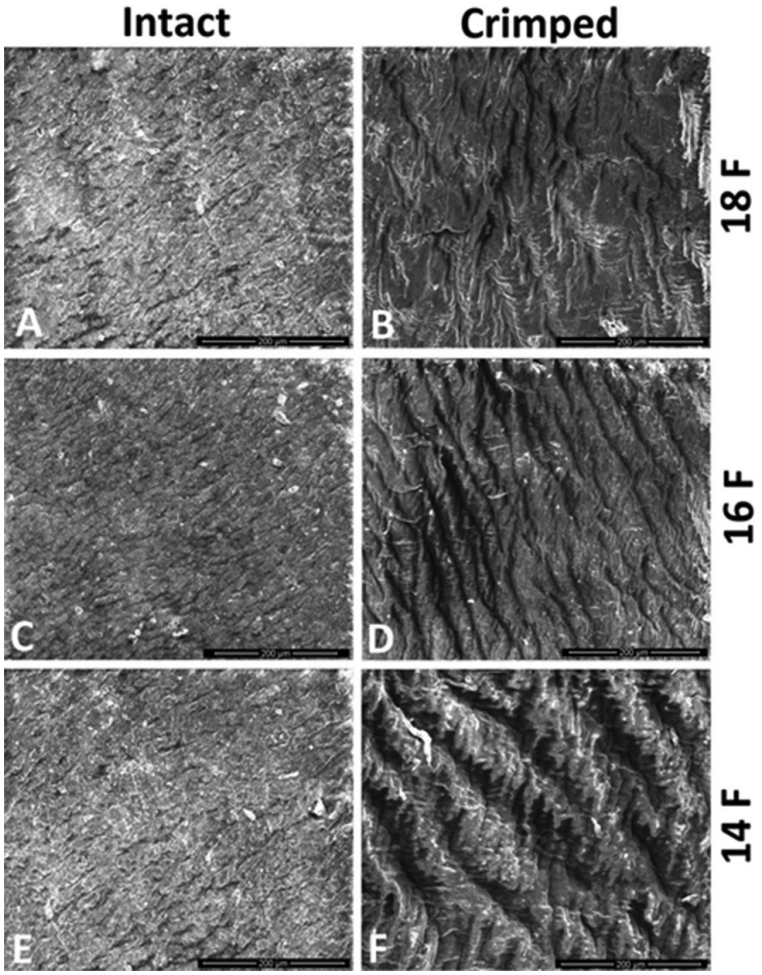

Figure 25. Scanning electron microscopy images of TAVI leaflets before and after crimping (Alavi, Groves, and Kheradvar 2014).

The damage could potentially be superficial. In order to verify if collagen disruption had occurred, which would reduce the mechanical properties of the device, SHGM was performed; to map the collagen fibre orientation within the leaflets at three depths (10 μm, 40 μm and 60 μm), before the crimping procedure and at three time points after the crimping procedure (0 minutes, 20 minutes and 60 minutes). The collagen fibres were shown to be disrupted as shown in Figure 26. Statistical analysis was performed on the images to determine a damage index based on the width of gaps between collagen fibres. It was found that as the device diameter is decreased, the extent of damage is increased in both severity and depth.

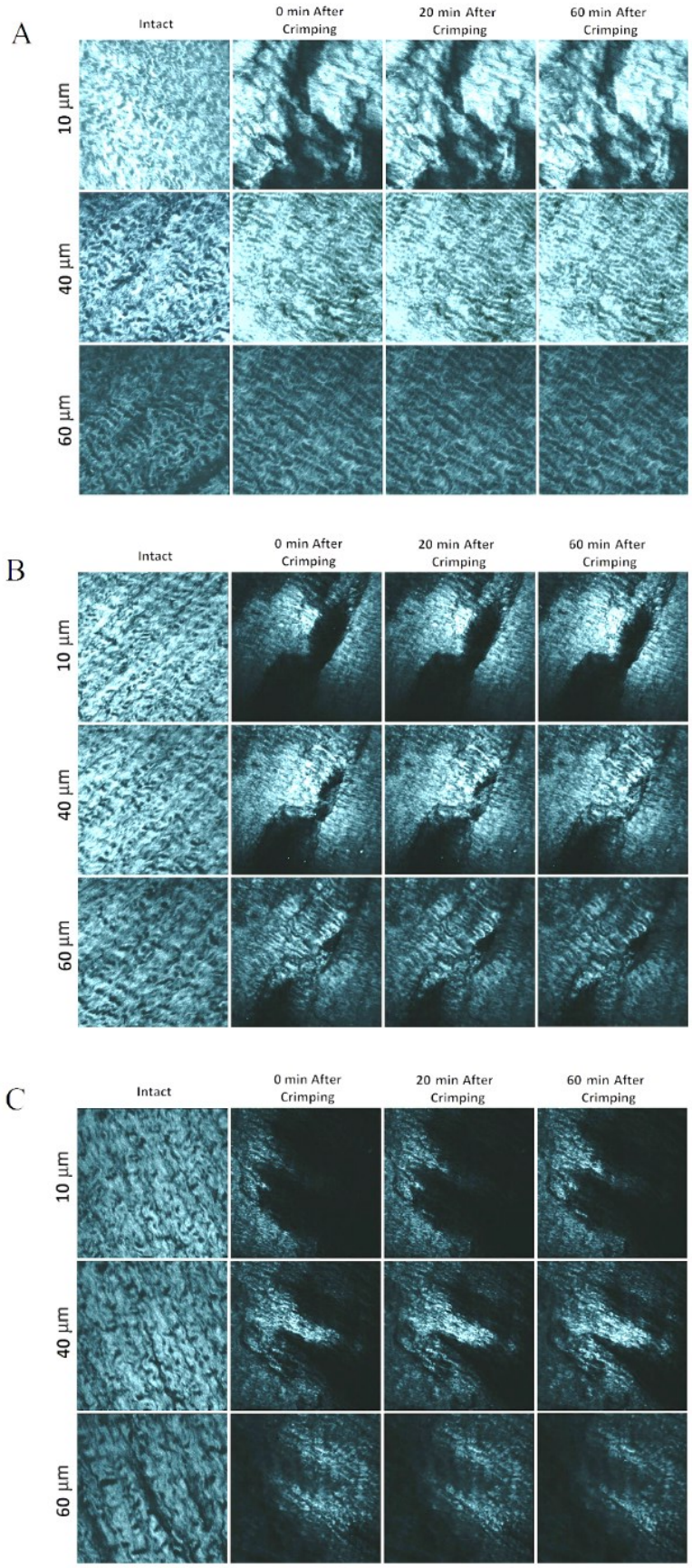

Figure 26. Second-harmonic generation microscopy images comparing the structural changes of bioprosthetic leaflets before and after being crimped to a diameter of A: 18 Fr, B: 16 Fr and C: 14 Fr (Alavi, Groves, and Kheradvar 2014)

Chapter 4: Computational Modelling of Transcatheter Aortic Valve Implantation

In this chapter, computational TAVI simulation has been partitioned into two categories. The first is modelling the deployment and analysing the results. The second is analysing the valve function which can be achieved through either structural FEA, CFD or experimental analysis.

4.1 Deployment Simulation

Computational analysis of TAVI was uncommon until four years ago as the procedure was still immature. In January 2012, *C. Capelli et al. (2012)* published the first paper depicting a simulation of a simplified TAVI deployment. Abaqus Explicit 6.9 was used to simulate a SAPIEN 2 TAVI device frame being deployed (by means of a balloon) into an aortic root model. Five aortic root models were extracted from patient CT data, and a TAVI device was simulated undergoing deployment into each. The aortic roots were treated as shell structures and without native leaflets. Bioprosthetic valves were separately modelled and then placed within the aortic roots. During simulated deployment, data was collected on the stresses within the device frame and the aortic root. Since this initial publication, only seven further papers have been found in the area of TAVI deployment simulation.

Q. Wang et al. (2012) simulated a BE deployment of a SAPIEN XT style frame into an aortic root model which was used to assess PAR. However, in this study, an idealised aortic root model was developed in a CAD package. Although the aortic root model was not based on a specific patient, it did feature native leaflets. The leaflets had two material sections assigned to them. The upper regions and free edge were representative of healthy leaflets while the base of the leaflets were stiffer in order to represent areas of the leaflets that were ridden with plaque. A limitation of this method is that the diseased leaflets retained idealised geometry, as opposed to being thickened. When the frame was deployed into the model, the frame did not achieve a seal with the aortic root. Gaps between the aortic root and frame which would succumb to PAR were visible.

In 2013, *C. Russ e. al. (2013)* described the simulation of device deployment into a patient-specific aortic root model with native leaflets, which were treated as shell structures during the simulation. The frame was a SE device which was based on μCT data of the Medtronic CoreValve. The simulation was run twice, once with and once without plaques that were modelled as solid masses. It was shown (Figure 27) that the final position of the frame was heavily dependent on the presence of plaques**.**

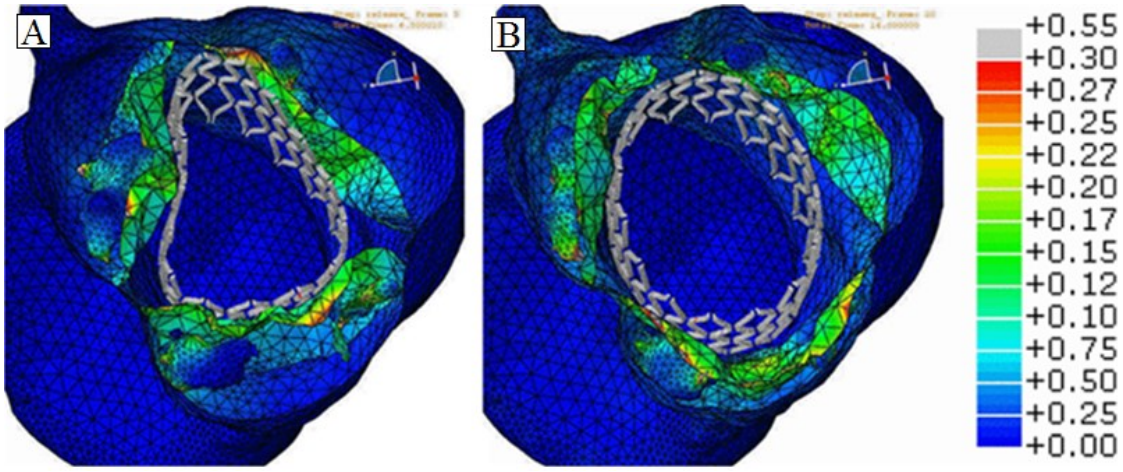

Figure 27. Simulated dynamic TAVI device expansion showing large frame deformation dependent on initial plaque location (A) and the fully expanded frame at the end of the simulation (B, colour scale shows stress in MPa - Russ et al. 2013)

In 2014, three papers appeared, which simulated frame deployment, and then utilized a mapping technique of the leaflets to the frame. *F. Auricchio et al. (2014)* used this technique to evaluate the effect of the deployment zone of the device on the prosthetic leaflets. Deployment of a valve representing the SAPIEN 2 TAVI device was modelled using balloon inflation. It was shown that a variance of 7 mm along the aortic root could result in a 24% discrepancy in coaptation area, and a 22.4% variance in stress induced in the aortic root wall. It was concluded that a slightly more proximal deployment location was preferable.

The second paper, by *P. S. Gunning et al. (2014),* is one of few papers to explore self-expanding devices. A generalised TAVI device was crimped and deployed into a realistic aortic root with the leaflets aligned with the native leaflets and into a realistic aortic root with the TAVI leaflets rotated 60 degrees from the native leaflets. The geometry of the aortic root was generated from a CT scan. It was shown that the stress on the leaflets in the coaptation area was increased in the realistic aortic root model (2.97 MPa vs. 1.52 MPa), provided the leaflets were out of alignment. The out of alignment leaflet simulation also had an increased stress in the leaflets during a simulated cardiac cycle when compared with the aligned leaflet simulation (2.97 MPa vs. 2.35 MPa). This demonstrated for the first time that the rotational orientation of the TAVI device impacts the function of the valve. It also casts doubt on whether an idealised frame geometry is sufficiently representative of *in vivo* functioning of the device.

S. Morganti et al. (2014) developed two patient-specific aortic root models. What separates this work from any other previously seen, is the presence of native leaflets in the model. Idealised native leaflets were developed and integrated into the patient-specific aortic root models, after which the plaques were mapped to the idealised leaflets. A SAPIEN XT frame was used to represent a TAVI device and was deployed into both patients. The resultant shape of the device was shown to be patient

dependent, and neither frame was circular in cross section post deployment in both patients. The leaflets were then mapped to the frame, both of which demonstrated a prolapsed leaflet during a simulated cardiac cycle.

Modelling TAVI device deployment is particularly difficult since the leaflets comprise a complex geometry which is difficult to both replicate in CAD software, and suitably mesh with sufficient rigidity to undergo a deployment simulation. The deployment procedure of BE devices involves a balloon inflating within the leaflets, which expands the metallic frame on the exterior of the leaflets. This means a great deal of force is transferred through the leaflets from the balloon to the frame. Since the leaflets have a low elastic modulus relative to the frame or balloon (E = 7 MPa, E = 232 GPa and E = 900 MPa respectively) the elements within the leaflets undergo extreme deformation. To date, only a single research paper has described a deployment simulation of a complete TAVI device. *Bailey et. al. (2015)* developed techniques to derive the geometry, and effectively mesh TAVI device prosthetic leaflets. These advances allowed for complete device deployment simulations and are discussed in chapter 7 and 8.

4.2 Valvular Simulation

Due to SVR being a viable treatment to AS for several decades, there are numerous publications focused on bioprosthetic leaflets. The experimental study by *W. B. Gao et al. (2000)* depicted a method for monitoring the movement of prosthetic valve leaflets during the cardiac cycle using stereo photogrammetry. The technique was shown to work, but no consideration was given to stresses in the leaflets during the cardiac cycle, the primary application of the technology.

Despite advances in computational power and FEA software, experimental analysis on prosthetic leaflets is still common. In 2012, *N. Saikrishnan et al. (2012a)* used particle image velocimetry to assess and compare haemodynamic performance of porcine bicuspid and tricuspid aortic valves. Variation in flow velocity was detected and increased turbulence was shown to occur in bicuspid valves.

There are also many papers concerning computational analysis of the leaflets. The analysis is normally solid mechanics, as opposed to fluid dynamic analysis. Dynamic fluid structure interaction (FSI) more closely represents real leaflet behaviour relative to computational fluid dynamic (CFD) analysis, but FSI is extremely computationally demanding. This is because solid-fluid co-simulation, which is frequently used to analyse FSI, does not consider fluid voids and therefore cannot model non-static solid objects. As a result, coupled Eulerian Lagrangian (CEL) analysis is required which is computationally expensive. Despite the computational expense, FSI has been used to analyse the

aortic valve for some time. *De Hart et al. (2003)* documented a functional FSI analysis of the aortic valve that was modelled as an impressive fibre reinforced structure.

More recently, *Sturla et al. (2013),* created a patient-specific aortic root model from magnetic resonance imaging (MRI) data, which was enveloped in a fluid domain comprising 212,425 hexahedral elements. FSI was performed in LS-DYNA 971, in which a pressure gradient representative of a cardiac cycle was applied to the fluid domain (LSTC 2013). A second structural simulation was developed as a control, in which a uniform pressure load representative of a cardiac cycle was applied across the leaflets. The FSI and structural simulations had very similar stresses within the aortic root as shown in Figure 28. The FSI simulation also produced fluid dynamic results which showed recirculation of fluid within the aortic sinuses (Figure 29). Although the stress results correlated between the FSI simulation and the structural analysis, the fluid results are likely to be inaccurate as the mesh density was extremely low, a product no doubt of computational limitation.

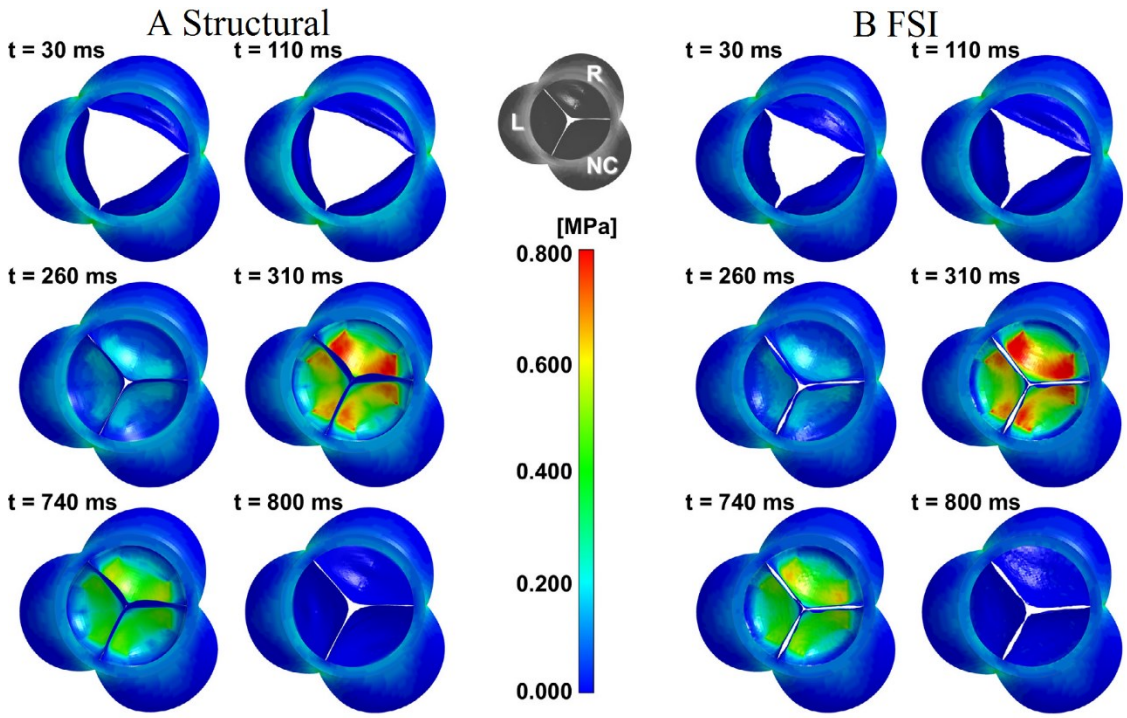

Figure 28. Aortic root in plane maximum and principal stress distributions throughout the cardiac cycle determined through both structural analysis (A) and FSI (B) (Sturla et al. 2013).

Since FSI is extremely computationally demanding, computational solid analysis on its own is a significantly more common area of research (Sun, Abad, and Sacks 2005, Mohammadi, Bahramian, and Wan 2009, Kim et al. 2008, Saleeb, Kumar, and Thomas 2013, Arcidiacono, Corvi, and Severi 2005, Li and Sun 2010).

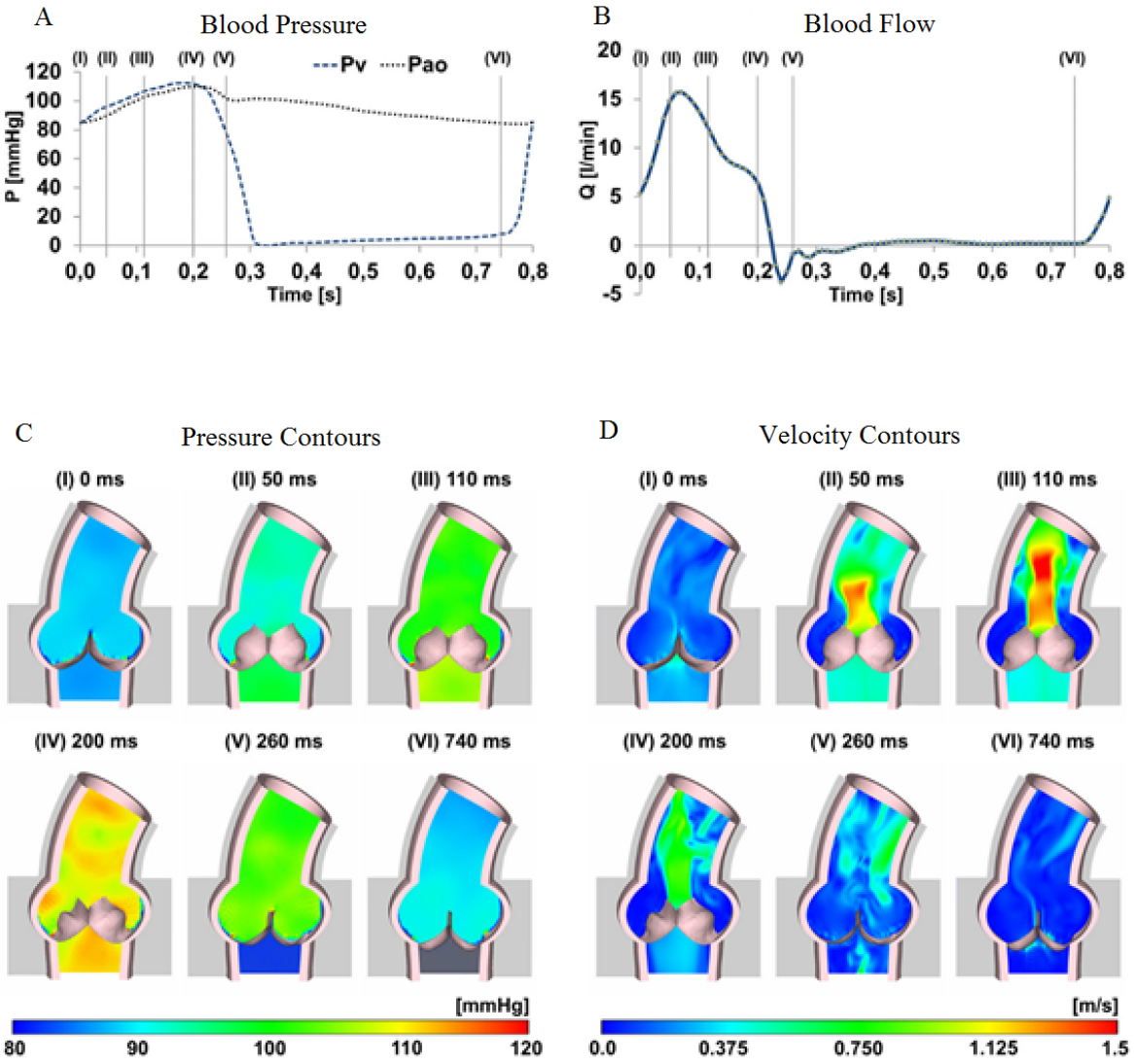

Figure 29. FSI model of the aortic root. Time-dependent blood pressure boundary conditions (A). Computed transvalvular blood flow (B). Blood pressure (C) and velocity contours (D) depicted on a long-axis section passing by the left and right coronary sinuses at six time frames indicated in A and B (Sturla et al. 2013).

Due to computational constraints, structural analysis is more common. It was shown that computational modelling of prosthetic heart valves could reproduce results that have been seen in experimental analysis; the results are shown in Figure 30. The analysis also demonstrated the importance of material models by showing that isotropic and orthotropic material models yielded different dynamic behaviour (Arcidiacono, Corvi, and Severi 2005).

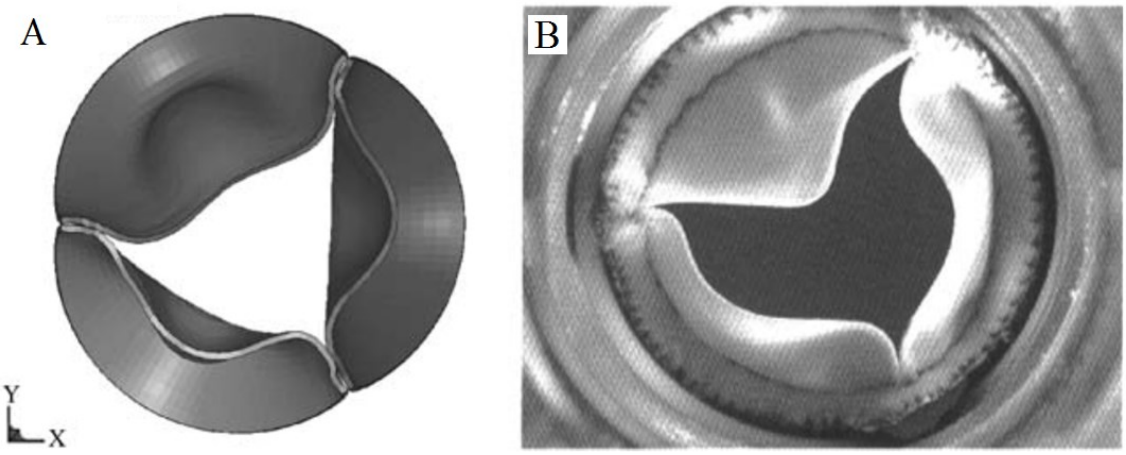

Figure 30. Comparison between computational (A) and experimental (B) analysis of prosthetic heart valve leaflets (Arcidiacono, Corvi, and Severi 2005).

In 2010, the first publication that specifically focused on TAVI leaflets was published by *K. Li et al. (2010).* By mechanically testing bovine pericardium, coefficients for the *Fung* material model were computed. The *Fung* model is a non-linear, hyperelastic, anisotropic and inhomogeneous material model. It was shown that the maximum principal stress can be reduced by 36% if the leaflet thickness was increased from the mean value measured (0.24 mm) to 0.35 mm. This poses a problem for TAVI leaflet design as the leaflets are manufactured from either bovine or porcine pericardium, which has an inconsistent thickness.

It is known that the tissue that the leaflets comprise is fibrous which results in both anisotropic and inhomogeneous material properties. In 2013, *A. F. Saleeb et al. (2013)* reiterated the importance of material models by showing a discrepancy between isotropic and anisotropic material models in leaflets, which was validated with experimental analysis. The leaflet geometric model resembled the leaflets that are common in TAVI devices. Figure 31 shows the comparison between the isotropic and anisotropic material models. The dynamic behaviour of the leaflets changed, however the open and closed position was identical. This is an important result for this research as isotropic material properties are used, however the results are extracted from the closed position of the leaflets only.

Although the valve is not modelled functionally working, CFD analysis is still used in the area of prosthetic device analysis. *F. P. P. Tan et al. (2012)* produced geometric models of the aortic root and aorta from MRI scans. A patient was scanned twice, once before, and once after the implantation of a TAVI valve. The two associated geometries were then used as fluid domains and CFD haemodynamic analysis was performed for the two cases. However, the valve was not present in either simulation so the flow lacked realism.

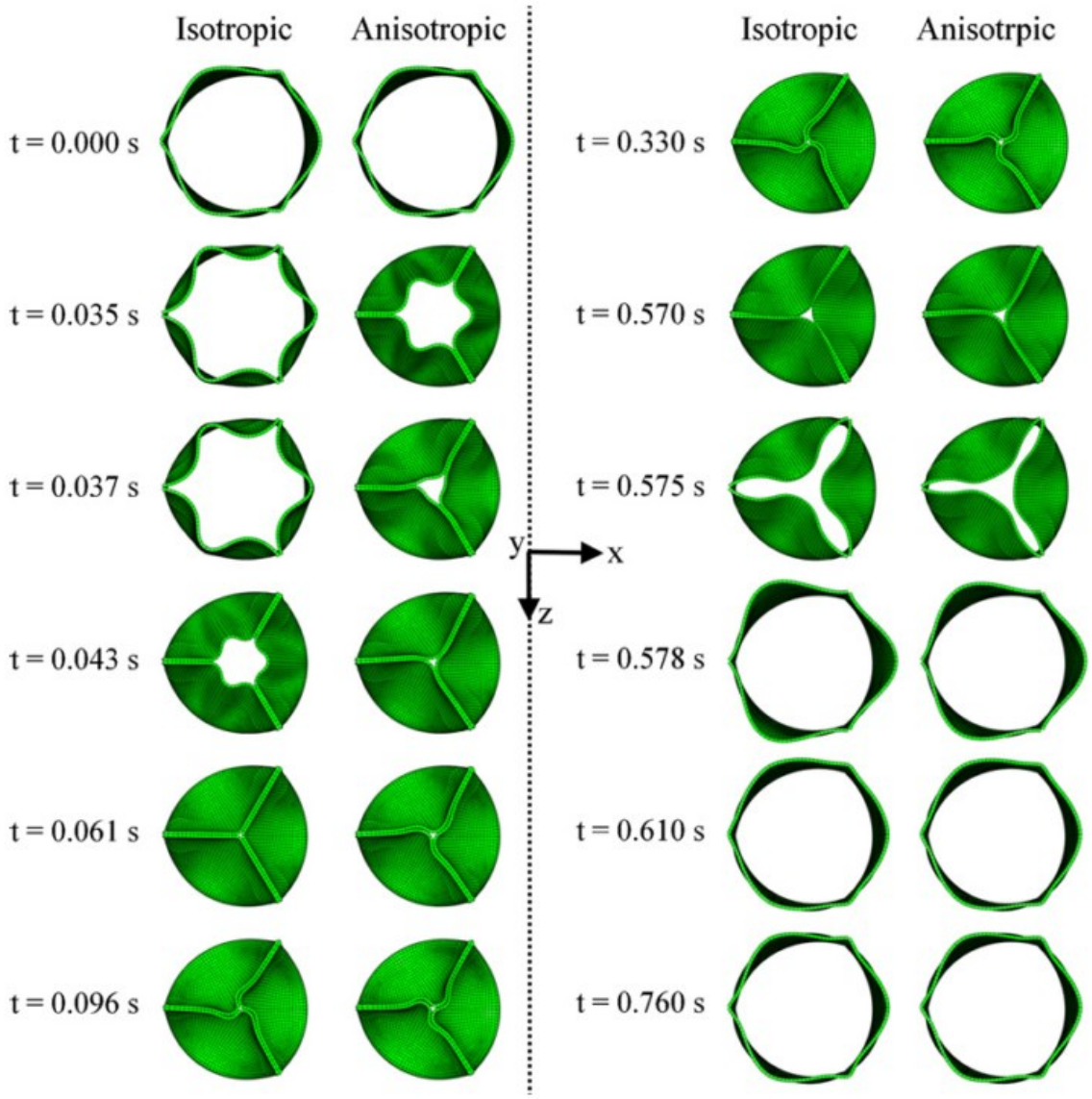

Figure 31. Computational analysis of prosthetic heart valve leaflets undergoing a cardiac cycle; a comparison between isotropic and anisotropic material models (Saleeb, Kumar, and Thomas 2013).

In contrast, *W. Sun et al. (2010)* simulated the haemodynamics of TAVI leaflets post-deployment using solid mechanics FEA. As shown in section 3.4, although the leaflets are designed to operate within a circular frame the presence of large plaques may lead to the deployed frame not having a circular cross section. Furthermore, the human aortic root is not necessarily circular and in fact, it is frequently elliptical. *W. Sun et al. (2010)*, generated a simple triplet of leaflets which can be distorted in order to create an elliptical cross section. A pressure load was then applied to the upper surface of the leaflets in order to close them. This geometry was imported into Star-CCM+ (CD-adapco 2014) in which CFD analysis of flow about the leaflets was performed to determine the extent of any transvalvular aortic regurgitation. It was shown that if the aortic root had an elliptical factor of 1.47, the maximum stress in the leaflets increased by 143%.

4.3 Summary

The first TAVI device implanted in to a human was in 2002, a decade had passed before the first research paper was published on computational simulation of TAVI (Capelli et al. 2012). Since then, to the Authors knowledge, a further six papers have been published in the area. The papers focused on PAR, aortic root rupture and leaflet operating stress analysis (Russ et al. 2013, Wang, Sirois, and Sun 2012, Auricchio et al. 2014, Gunning, Vaughan, and McNamara 2014, Morganti et al. 2013, Bailey, Curzen, and Bressloff 2015).

It was shown that computational simulation can replicate an ineffective seal between the TAVI device and native tissue (Wang, Sirois, and Sun 2012). Furthermore, computational simulation has been used to compare post-procedural outcome between two cases, one including the calcified plaques, and one excluding the plaques. PAR was found to be dependent on the presence of plaques (Russ et al. 2013).

Unfortunately, with the exception to our paper, no other paper included the leaflets throughout the deployment simulation. Alternatively a mapping technique was used to position the leaflets about the distorted frame. This technique offers no insight into the stresses of the leaflets during deployment and results in a leaflet model that does not properly capture the shape of the leaflets. Despite the limitations, valvular operating stress was analysed (Morganti et al. 2013, Gunning, Vaughan, and McNamara 2014, Bailey, Curzen, and Bressloff 2015, Auricchio et al. 2014).

Chapter 5: Transcatheter Aortic Valve Implantation Device Model Development

A CAD model of a TAVI device had to be developed in order to fulfil the objective of this project; assessing leaflet stresses within TAVI devices and assessing the application of patient-specific deployment simulations.

It was decided that the device used in the base simulations should be representative of an existing TAVI device. When the project was started, there were only two devices in the UK that were approved for use, the Edwards Lifesciences SAPIEN XT and the Medtronic CoreValve. Of the two devices, the Edwards Lifesciences SAPIEN XT was chosen to be modelled for the following reasons:

1) The University Hospital Southampton Trust (UHST - NHS 2014) is licensed to use the SAPIEN XT. Opportunity to observe the deployment procedure has occurred and it allowed close inspection of the device.
2) The SAPIEN XT frame is easier to model than the Medtronic CoreValve as it comprises a simple network of straight struts, as opposed to a complicated network of curved struts.
3) The material properties of the frame are easier to model. The SAPIEN XT frame is laser cut from a cobalt chromium alloy tube. The specific alloy is MP35N which is a plasto-elastic alloy. The CoreValve however is manufactured from a Ni-Ti super-elastic alloy which is difficult to simulate computationally (Tzamtzis et al. 2013).

During device selection, the SAPIEN XT was available in three sizes: 23 mm, 26 mm and 29 mm diameter. The 26 mm device was used throughout the simulation as it is the most commonly deployed size, the mean and the median of the range. The SAPIEN XT range has now been increased to include a 20 mm device.

Each component of the device has been modelled, the method behind which is described in the following sections.

In order to produce some of the component geometries, FEA is used. As a result, a brief introduction into the FEA software and analysis type is presented before the component model descriptions within this chapter.

5.1 Computational Simulation Development

The FEA model used to simulate TAVI has multiple options and parameters that must be predetermined in order to ensure the simulations are both accurate and efficient.

The software package used to simulate TAVI throughout this project was Abaqus v6.12, which has two main variants for simulating dynamic structural problems: Explicit and Implicit (SIMULIA 2013c). In this thesis, Explicit was used for two reasons: firstly TAVI includes incredibly difficult contact instances that are extremely difficult to model such as the balloon inflating and unfurling. Explicit analysis has superior contact solving algorithms in comparison to Implicit.

Secondly, there is a dynamic event known as *snapping*, which occurs in both the balloon and the leaflets featured in the simulations. Snapping is when a thin piece of material within a confined space featuring a kink (Figure 32(A)) is pulled taut until it becomes straight (Figure 32(B)). The process in which the material distorts sufficiently and the kink is pulled out is called *snapping,* and occurs over an extremely short time period. Explicit analysis is capable of modelling extremely fast events such as impact and *snapping*.

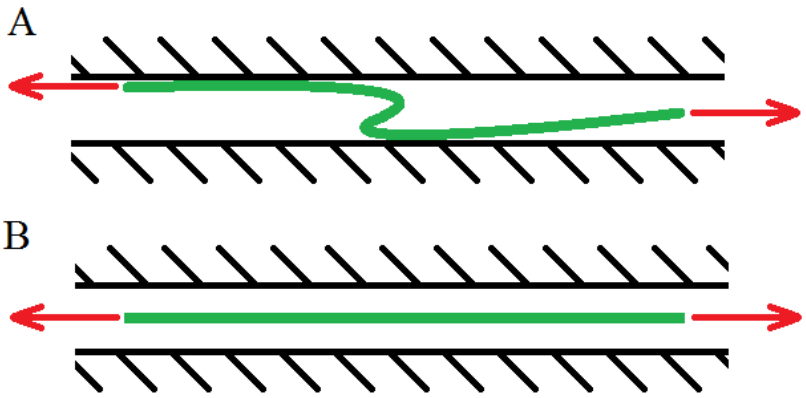

Figure 32. If a thin piece of material (green) within a confined space is pulled taught by forces at either end (red).

There is however a drawback of Explicit analysis: small time increments. During dynamic analysis, a period of time (time step) is split into increments (time increments). The system must be solved at each increment, therefore decreasing the time increment increases the number of time instances for which the system must be solved, which in turn increases the computational time. In Implicit analysis, at the end of each time increment an iterative process is applied to induce equilibrium within the internal forces of the system, ensuring the simulation retains accuracy. In Explicit however, this process does not occur and in order to retain accuracy the time increment must be extremely small (SIMULIA 2013a).

Although a limitation of Explicit is the small time increment, measures can be taken to increase the time increment while retaining simulation stability and accuracy. Each time increment must be less than the time required for a shockwave to travel across any of the elements in the system. Therefore the stable time increment is given by the following equation:

$$\Delta t \ll \frac{L^e}{c} \qquad [3]$$

where L^e is the length of the smallest elements length, Δt is the discrete time increment and c is the wave propagation speed given by:

$$c = \sqrt{\frac{\lambda + 2\mu}{\rho}} \qquad [4]$$

λ and μ are Lame's constants and ρ is density. In order to increase the time increment, the wave propagation speed must be decreased, which can be achieved through increasing the density, this practice is known as mass scaling (Cocchetti, Pagani, and Perego). Within Abaqus, a target time increment can be set, according to which the mass is automatically scaled. In order to ensure that the simulations used in this research are both efficient and accurate, a mass scaling study was used to compare different mass scaling target increments (shown in the appendix). It was concluded that a mass scaling target time increment of 10^{-7} seconds was most appropriate.

Further consideration must be given to the step time. If the event is too fast, erroneous momentum will start to take effect. In order to ensure that momentum was negligible, the step time was increased until the kinetic energy was below 5% of the total internal energy. For every simulation within this thesis, each step time was individually considered and the energies monitored.

Many components within the simulations demonstrated an oscillatory response. In order to supress the oscillation, the Rayleigh damping model was used to account for the energy dissipation that will occur within the real components. The Rayleigh damping factor is of the form:

$$\zeta_i = \frac{\alpha}{2\omega_i} + \frac{\beta\omega_i}{2} \qquad [5]$$

where ζ is the damping ratio, i is the mode number, α is the mass scaling factor, β is the stiffness scaling factor and ω_i is the natural frequency of the *i-th* mode of vibration (SIMULIA 2013b).

In this thesis, the α parameter was used as it removes low frequency oscillations that were typically observed in the components. The method for calculating α varied between each component and is discussed both in the remainder of this chapter and the appendix.

5.2 The Frames

Although this thesis focuses on the SAPIEN XT, the SAPIEN 3 was also modelled for comparative purposes. The device frames were designed in Rhinoceros3D (McNeel 2013), and are shown in Figure 33 and Figure 39.

For the case of the SAPIEN XT frame, a python script was developed that had parameterised features. These parameters were edited until the device visually appeared identical to the actual device (Figure 33).

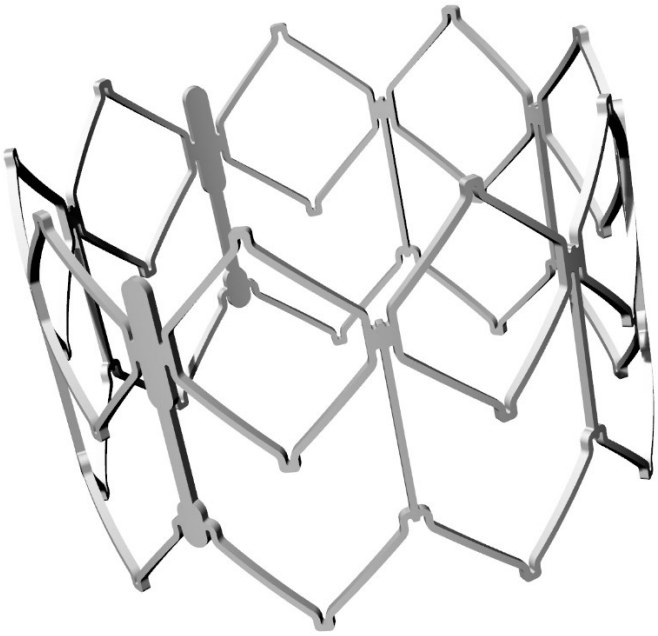

Figure 33. CAD frame model for the Edwards Lifesciences SAPIEN XT (26 mm).

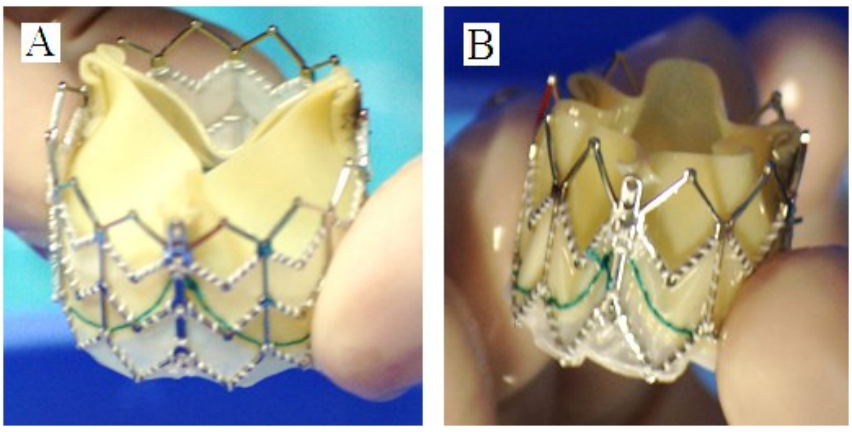

Figure 34. The 29 mm (A) and 23 mm (B) SAPIEN XT.

The SAPIEN XT 23 mm and 29 mm TAVI devices were photographed at UHST before the crimping procedure and are shown in Figure 34 (NHS 2014). It is evident that the 29 mm device was manufactured at the full diameter, the 23 mm device however appears to be manufactured with a reduced diameter. This is visually apparent as the cells are not square, rather diamond shape. The parameterised model was written in such a way that the manufactured diameter and deployed diameter do not have to be equal, as it would allow the code to be capable of generating both the 26 mm and 23 mm devices. The frame geometry is defined in Figure 35-37 the parameters for which are tabulated in Table 9.

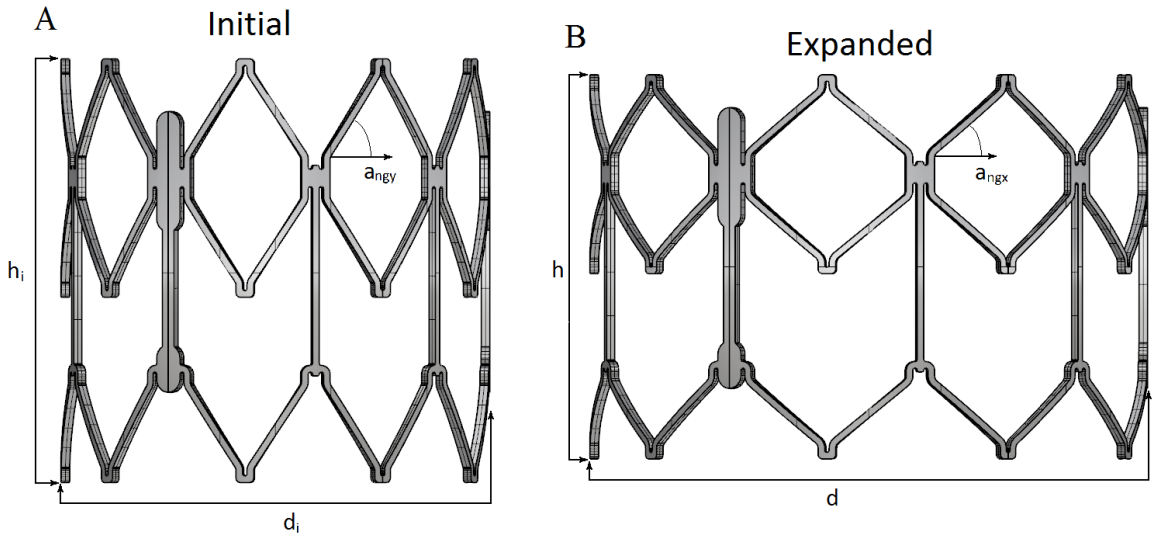

Figure 35. The 26 mm SAPIEN XT with both a reduced diameter (A) and full diameter (B).

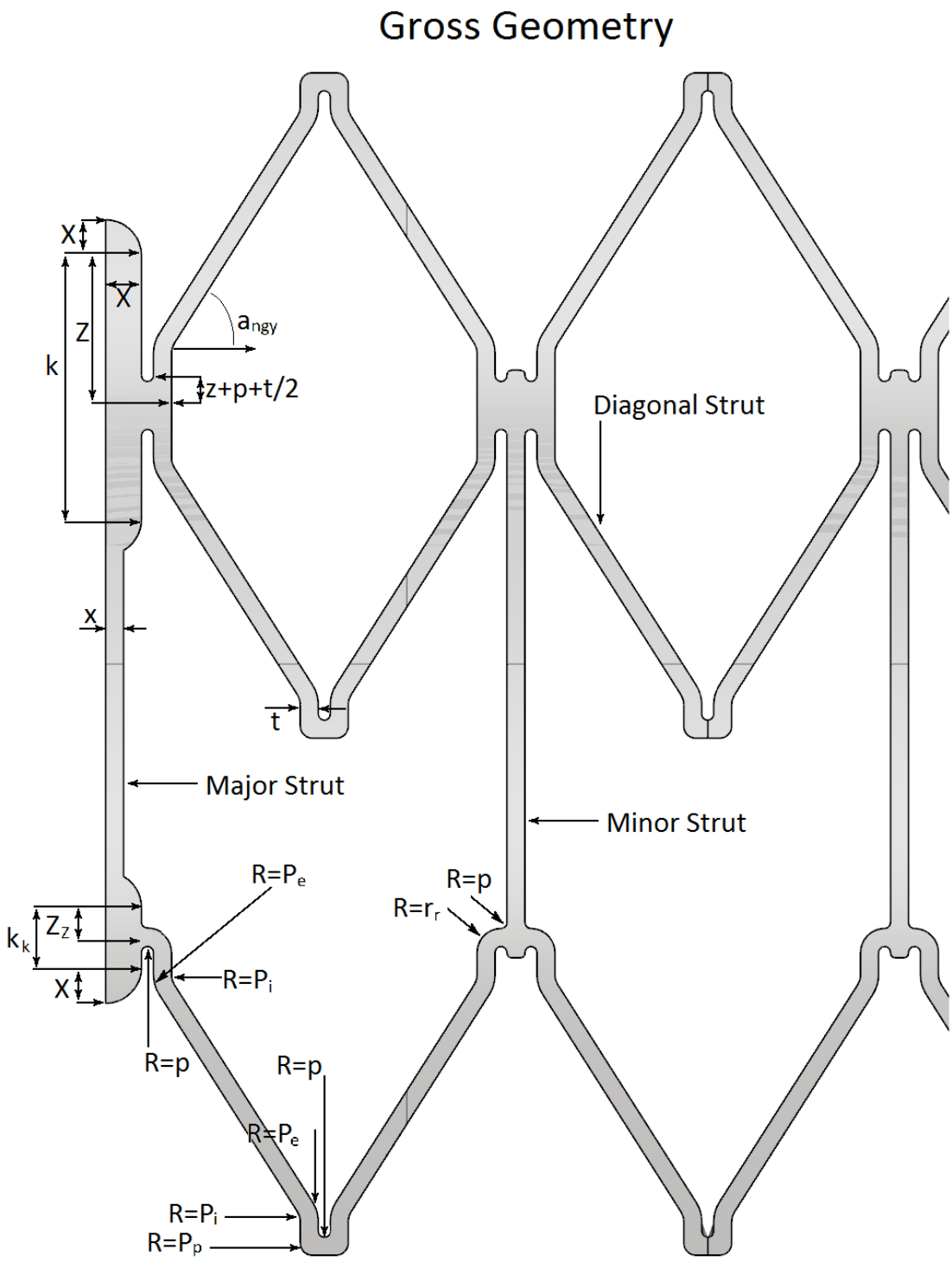

Figure 36. SAPIEN XT parameterised geometry.

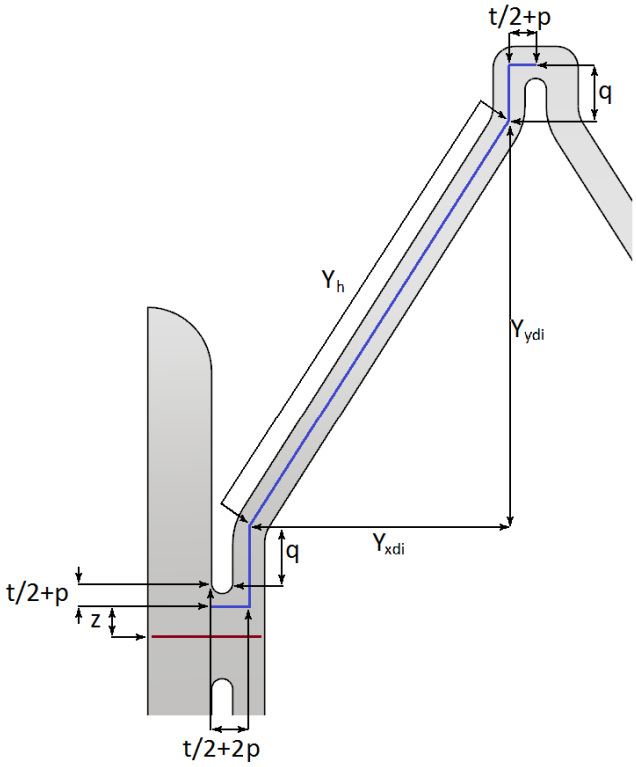

Figure 37. SAPIEN XT model subunit, with additional labelled parameters.

Parameter	Description	Value
d	Diameter	26 mm
d_i	Initial or tube diameter	26 mm
t	Strut thickness - circumferentially	0.3 mm
T	Strut thickness - radially	0.4 mm
a_{ngx}	Pitch of the diagonal struts	42.5 degrees
h	Height of the frame (expanded)	17.2 mm
X	Half the width of the major struts at the widest point	0.6 mm
x	Half the width of the major struts at the thinnest point	0.3 mm
Z	Vertical offset of the upper rings of diagonal struts	2.5 mm
z	Vertical offset of the upper rings from Z	0.25 mm
Z_Z	Vertical offset of the lower rings of the diagonal struts	0.5 mm
p	Internal radius of the arcs associated with the diagonal struts at the crowns	0.1 mm
P_p	External radius of the arcs associated with the diagonal struts at the crowns	0.2 mm
P_e	External radius of the arcs associated with the diagonal struts	0.6 mm
P_i	Internal radius of the arcs associated with the diagonal struts	0.3 mm
q	Vertical offset associated with the crowns	0.065 mm
k	Upper hoop length excluding the arcs	5 mm
k_k	Lower hoop length excluding the arcs	1 mm

Table 9. Parameters and assumed values to describe a 26 mm SAPIEN XT TAVI frame.

With the given parameters, the remaining unknown values can be calculated. Since the diameter is known it is possible to find the *x* component of Y_h (Y_x), when the stent is in its expanded form:

$$Y_x = \frac{d\pi - 6X - 54p - 24t}{18} \quad [6]$$

The *y* component of Y_h (Y_y) and Y_h can then be calculated through equation 7 and 8.

$$Y_h = \frac{Y_x}{\cos(a_{ngx})} \quad [7]$$

$$Y_y = ({Y_h}^2 - {Y_x}^2)^{0.5} \quad [8]$$

The model is described in terms of the tube diameter which has equivalent values of Y_x and Y_y; Y_{xdi} and Y_{ydi}, which are given by:

$$Y_{xdi} = \frac{d_i\pi - 6X - 54p - 24t}{18} \quad [9]$$

$$Y_{ydi} = ({Y_h}^2 - {Y_{xdi}}^2)^{0.5} \quad [10]$$

These two values can be used to find the angle a_{ngy}:

$$a_{ngy} = \left(cos\frac{Y_{xdi}}{Y_h}\right) \quad [11]$$

The height of the frame when it is at its tube diameter is

$$h_i = h + 2\left(Y_{ydi} - Y_y\right) \quad [12]$$

The only remaining value that has not been found is r_r, which is given by:

$$r_r = t + p \quad [13]$$

During the course of this research, another TAVI device was made available in the UK: the Edwards Lifesciences SAPIEN 3. Although the majority of this research focused on the SAPIEN XT model, for the purpose of frame comparison, a SAPIEN 3 model was also developed. The SAPIEN 3 is available in three sizes: 23 mm, 26 mm and 29 mm. The SAPIEN 3 could not be modelled with the same parameterised code as the SAPIEN XT, and so an alternative code was developed.

The geometry of the SAPIEN 3 frame was extracted from an image on the Edwards Lifesciences website, shown in Figure 38(A). The image was assumed to accurately depict the frame.

The cellular geometry was found through pixel counting. The height of the frame in the image was 218 pixels. In reality it is known to be 20 mm, so each pixel is 0.092 mm in length. The size of each cell was then derived through pixel counting which gave the gross geometry of the frame. The strut cross section was assumed to be square, with an edge length of 0.3 mm. The SAPIEN 3 CAD model in its planar form is shown in Figure 38B next to the image taken from the Edwards Lifesciences website (Figure 38(A)) for comparison. The complete frame model is shown in Figure 39.

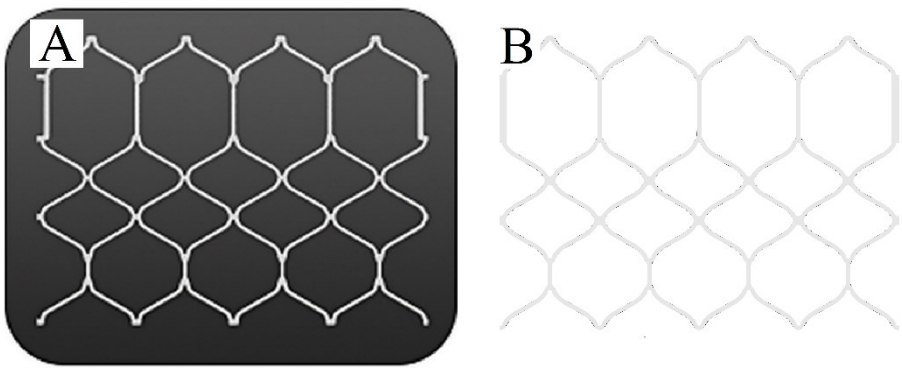

Figure 38. SAPIEN 3 geometry in the unwrapped form, taken from the Edwards Lifesciences website (A) and computationally modelled (B) (Lifesciences 2014).

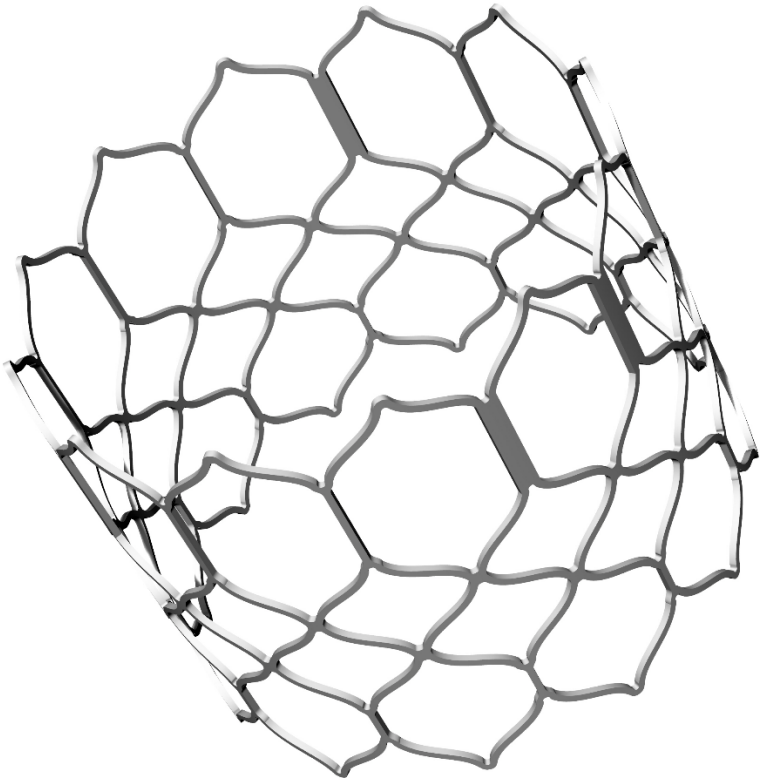

Figure 39. SAPIEN 3 frame CAD model.

The frame of the SAPIEN XT and the SAPIEN 3 are manufactured from cobalt-chromium MP35N alloy which was modelled as having the following properties; an elastic modulus of 232 GPa, a yield stress of 379 MPa, Poisson's ratio of 0.3, and a density of 8.4 g/cm^3, (Latrobe 2013, Stockholders 2013, Edwards Lifesciences 2013d). Additionally, Rayleigh damping was employed to remove observed oscillation from the model, defined by an alpha coefficient equal to 2450 (experimentally calculated as shown in the appendix).

Both the SAPIEN XT and the SAPIEN 3 were meshed using linear hexahedral elements with a target element size of 0.08 mm (calculated through a mesh refinement study presented in the appendix) resulting in 168,735 and 137,040 elements respectively. The target element length was determined through a mesh refinement study.

5.3 The Cuffs

In many previous simulations of TAVI devices, a frequently overlooked component is the cuff (visible in Figure 34). It is a thin film of fabric that spans the lower cells of the frame. The primary function of the cuff is to attach the leaflets to the frame. The secondary function is to inhibit blood flowing through the lower cells of the frame, therefore reducing the chance of PAR. The geometry of the cuff is dictated by the geometry of the frame, as it must mimic the shape of the lower cells. As a result, the cuff geometry was generated through a modification of the code used to create the frame geometry. A comparison between the cuff produced for this model, and the cuff of the SAPIEN XT (both in planar form) are shown in Figure 40.

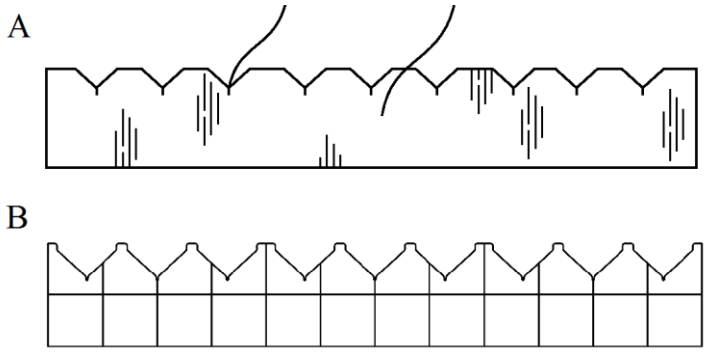

Figure 40. A comparison between the cuff in its planar form between an image presented in a patent (A) and the computational model (B) (Edwards-Lifesciences 2009).

The fabric of the cuff can be considered as an orthotropic material as it can only resist stress in plane with itself. This behaviour can be captured in Abaqus by using membrane elements. Unfortunately through computational experimentation it was found that membrane elements decreased the stability of the simulation, as a result shell elements were used. The fabric is thought to be approximately 0.3 mm thick, however, since it is modelled with a stiffer shell element, the thickness was reduced to 0.01 mm.

Linear triangular shell elements (totalling 413,207) were used to mesh the cuff as they are resistant to being severely distorted due to twisting, which occurs during the crimping procedure. The mesh comprised 413,207 elements which was determined through computational stability analysis; this is the coarsest mesh that can still undergo crimping and expansion without destabilising the simulation.

A cuff model was also developed for the SAPIEN 3. In reality the SAPIEN 3 cuff internally spans the lower cells of the frame before wrapping around the lower edge of the frame, where it forms an external cushion, the purpose for which is enhancing the seal between the device and aortic root. In reality, the prosthetic leaflets are stitched to the internal section of the cuff, and so, the internal section was the only part of the cuff that was modelled. The geometry for the cuff was produced in the same

fashion as the SAPIEN XT: the parameterised code used to produce the frame geometry was modified to generate the upper edge of the cuff, from which the rest of the cuff was constructed. The cuff of the SAPIEN 3 was again assumed to be a 0.01 mm thick shell, and was meshed with 331,994 linear triangular elements.

The material properties for both the SAPIEN 3 and SAPIEN XT cuffs were based on those for polyethylene terephthalate: the elastic modulus E = 500 MPa, the density $\rho = 1.28$ g/cm^3, a Poisson's ratio $\nu = 0.3$ and a Rayleigh damping alpha coefficient of 20500. The Rayleigh damping coefficient applied to the cuff is relatively high as a large oscillatory response was demonstrated. Furthermore, the elements within the cuff were prone to excessively distort due to excessive energy within the mesh. Both of these propeties were considered while allocating a Rayleigh damping factor to the cuff. The final SAPIEN XT and SAPIEN 3 cuff models, with the frame are shown in Figure 41.

Although there are multiple assumptions surrounding the material properties, and element types of the cuff, these limitations are assumed to be negligible as the cuff has a non-structural role.

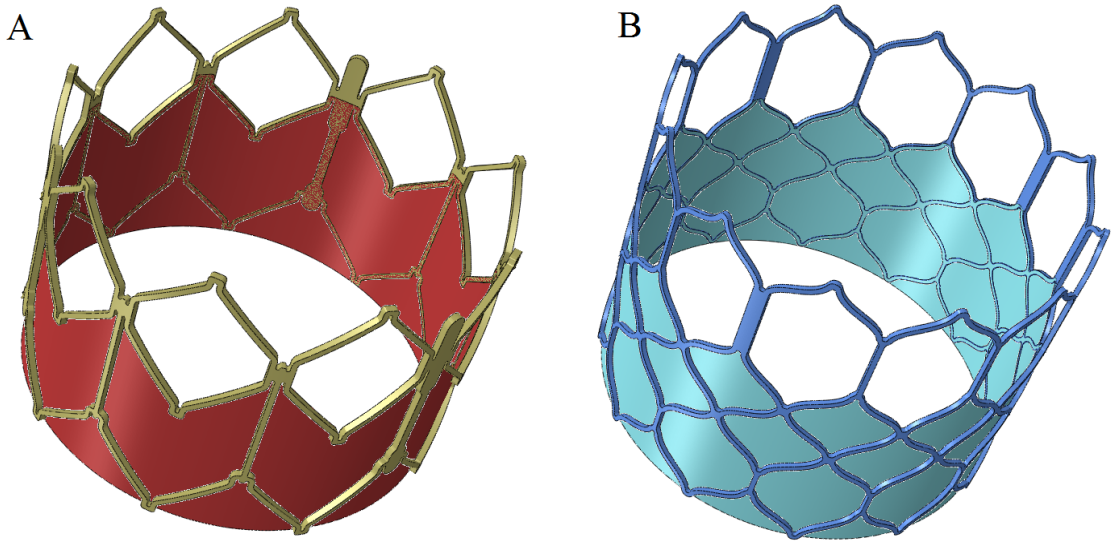

Figure 41. SAPIEN XT frame and cuff model (A) and the SAPIEN 3 frame and cuff model (B).

5.4 The Clips

Figure 42 shows a small object to be present in the uppermost corner of the leaflets that appears to pin the two leaflets together. Unfortunately, the leaflets obscure most of this feature, with exception to the upper most part. For the purpose of this research, they were assumed to be metallic clips, which are stitched together through the leaflets, therefore pinning the leaflets in place. Each clip had a circular cross section of 0.28 mm diameter and was wrapped into the shape of a caribena 4.5 mm

long and 1.12 mm in width at the widest point (see Figure 43(A)). It was later found that this was an incorrect geometry as the clips are in fact solid with multiple holes (Figure 43(B)). However, the inaccuracy of the clip geometry would not change the manner to which the clips function and as a result, the geometry was not altered.

Figure 42. 26 mm SAPIEN XT (Edwards LifeSciences 2013c)

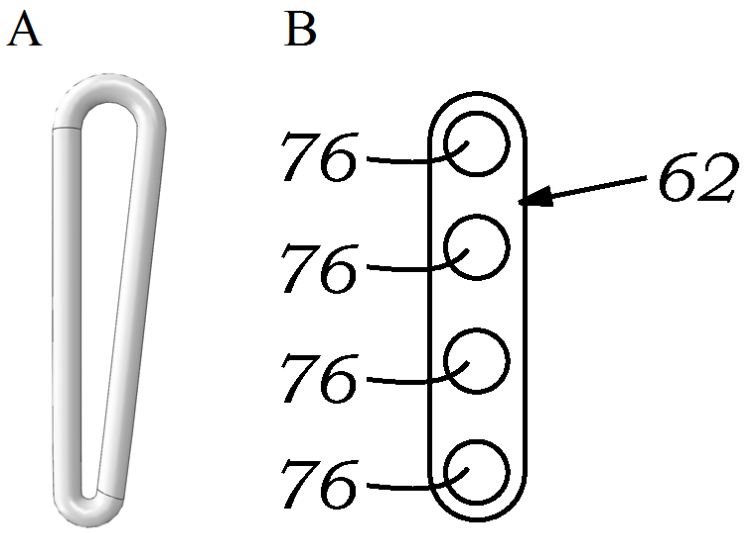

Figure 43. Comparison between the clip geometry from the CAD model (A) and the geometry presented in a patent of the SAPIEN XT (B) (Edwards-Lifesciences 2009).

The clips were assumed to be manufactured from Co-Cr MP35N which is the same material as the frame, the material properties for which are described in section 5.2. The clips couldn't be meshed with hexahedral elements without reducing the element size to the extent that it would both slow and

decrease the stability of the simulation. As a result, tetrahedral elements were used. A pair of clips were meshed such that as few elements were used as possible, while still retaining a visually evident circular cross section. The meshing software used was Abaqus CAE, despite the geometry being identical, the number of elements in each clip varied: 10,084 and 10,141 quadratic tetrahedral elements. Although there are limitations surrounding the mesh and material properties of the clips, due to the constraints used to hold the clips in place, the clips are non-deformable. As a result the element type and material properties are independent of performance.

5.5 The Leaflets

The leaflets are very challenging to model for two reasons:

1) Leaflet geometry, in the functional position, is very difficult to replicate in CAD because the leaflets adopt a complicated shape.
2) When crimped, the leaflets are crushed between the frame of the TAVI device and the balloon. This means that the computational mesh must be robust enough to withstand extreme deformation.

A few studies have simulated the frame being deployed with the leaflets excluded and then map the leaflets to the deformed frame (Gunning, Vaughan, and McNamara 2014, Auricchio et al. 2014, Morganti et al. 2013). However, this technique does not allow analysis of the leaflets during deployment, something that is particularly important since high stresses can result in leaflet damage, leading to reduced life span of the valve.

Since the SAPIEN XT leaflets are manufactured from bovine pericardium, the actual leaflet is likely to be cut from planar, or near planar sheets of material (Mack et al. 2013). The leaflets in the planar orientation are significantly easier to model in CAD (Figure 45(B)), and are also easier to mesh with regular elements which are resistant to distortion. Furthermore, the leaflet geometry, in the planar position is significantly easier to model in CAD.

Using FEA, the planar leaflets were manipulated into the functional position in a preliminary simulation. Due to the high quality of the mesh, the leaflets in this functional position were capable of undergoing the large distortions experienced during crimping and deployment simulations.

The planar definition of the leaflet geometry enabled additional detail to be included. For instance, each leaflet has a set of wings that protrude from either side of the leaflet (for the case of the Edwards Lifesciences SAPIEN range of devices). These wings are folded around the clips, and have not featured in any other known publications on device simulation.

As the leaflets in the planar position are easily meshed, a purely hexahedral mesh was generated comprising 135,536 elements. This mesh is the equivalent of four integration points (three linear elements) across the thickness of the leaflets. If the number of integration points was increased to five, the simulation suffers from decreased stability associated with the leaflets being crushed against the frame.

The leaflets are known to have orthotropic material properties. In this research, the material properties were assumed to be isotropic, and adopted the stiffer, in-plane setup. The material properties were assumed to be hyperelastic and employed the Ogden model wherein the strain energy function is

$$U = \sum_{i=1}^{N} \frac{2\mu_i}{\alpha_i^2}\left(\bar{\lambda}_1^{\alpha i} + \bar{\lambda}_2^{\alpha i} + \bar{\lambda}_3^{\alpha i} - 3\right) + \sum_{i=1}^{N} \frac{1}{D_i}\left(J^{el} - 1\right)^{2i} \qquad [14]$$

$\lambda_n^{\alpha i}$ are the deviatoric principal stretches (n = 1, 2 and 3), $\bar{\lambda_i} = J^{-\frac{1}{3}}\lambda_i$, λ_i are the principal stretches, N is the strain energy potential order, in this case 1, and μ_i, α_i, and D_i are temperature-dependent material properties. In this study, $\mu_i = 0.1591$, $\alpha_i = 10.89$, $D_1 = 0$ (an equivalent Poisson's ratio of 0.475) and the density, $\rho = 1.1\ \mathrm{g/cm^3}$. The Rayleigh damping factor applied to the leaflets was defined by $\alpha = 1500$ (derived through experimental analysis shown in the appendix). The stress-strain curve for the hyperelastic model, experimental results and a simplified linear elastic model are shown in Figure 44 (Lin, Akula, and Gu 2013). The leaflet thickness was 0.3 mm and further geometry parameters are defined in Figure 45. Only one of the leaflets was modelled and the final shape was duplicated in the final assembly.

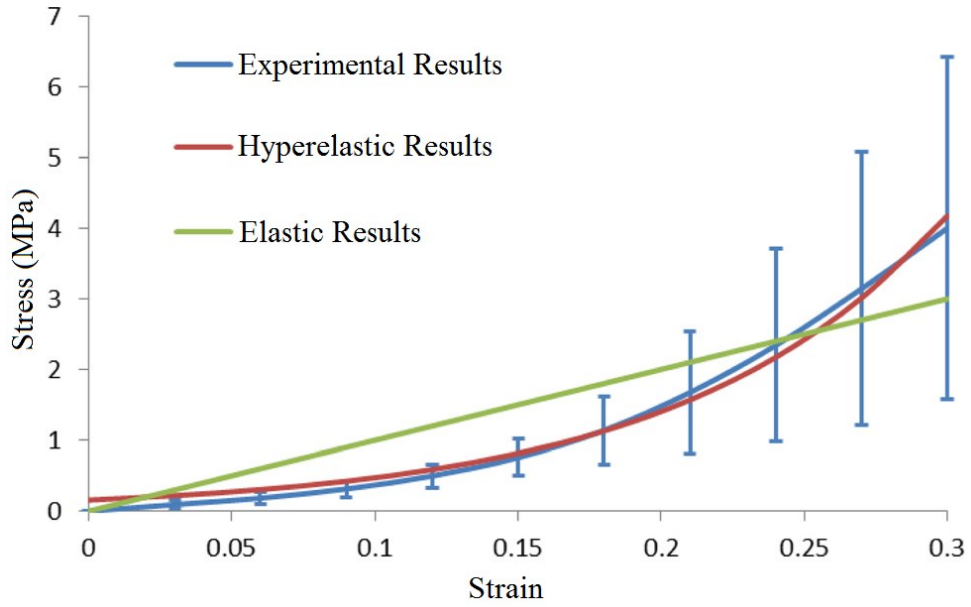

Figure 44. Stress-strain relationship in uniaxial tension test of bovine pericardium with different material models fitted.

The model used to manipulate the leaflets into the functional position comprised 12 surfaces (Figure 45), constrained in six degrees of freedom, as well as the planar leaflet and a pair of clips described in section 5.4. The surfaces, clips and node groups on the leaflet were translated in order to manipulate the leaflet into an appropriate final position. The tangential contact definition was frictionless; this is to remove any element distortion associated with friction. The normal contact definition was *hard*. The leaflet had a plane of symmetry which is shown in Figure 45(B). If the leaflet was to be bisected along the symmetry plane, a group of nodes would be revealed; these nodes were constrained to remain within the symmetry plane, in order to ensure symmetry.

The simulation involved a five step process as described below.

Step 1: Each leaflet must span a 120 degree segment of the valve orifice. The interface between the leaflet being manipulated and its theoretical neighbouring leaflets was represented by surfaces S3 and S4. In this step the leaflet was manipulated to lie within its orifice segment, over a time period of 0.04 seconds. This was achieved by translating node sets X and Y (highlighted red in Figure 45(B)). The translation resulted in the leaflet wings being flush with S3 and S4 (Figure 45(F)).

Step 2: During the first step there were no contact definitions defined between the leaflet and the clips (labelled in Figure 45(E)), so as to avoid volumetric intersections occurring. During Step 2, the contact definitions were instated. The clips were then translated in a normal direction to the surfaces S3 and S4, until contact was made with the leaflet, over a time period of 0.02 seconds. Figure 45(E-F) depicts the model with the clips in the original position and final position.

Step 3: The leaflet wings were then wrapped about the clips. This was achieved by systematically translating planar surfaces towards the clips. This is shown in Figure 45(F-G), although only half the system is shown for clarity and it was a symmetrical process. The order in which the surfaces translated was Sa, Sb, Sc and finally Sd (the surfaces are labelled in Figure 45(E)). Each translation lasted 0.015 seconds, resulting in a complete step time of 0.06 seconds.

Step 4: S1 is a cylindrical surface that represents the internal surface of the TAVI frame. The radius of S1 was reduced from 16.6 mm to 12.6 mm by means of a boundary condition using a cylindrical datum system. S1 was used to ensure that a volumetric intersection between the leaflet and the frame could not occur. The positions of the surfaces after this step are shown in Figure 45(H).

Step 5: The final step involved pulling the lower edge of the leaflet to the frame; in reality this edge is stitched to a cuff attached to the frame. This was achieved by displacing S2 radially to a radius of 12.6 mm, again by means of a boundary condition using a cylindrical datum system. The contact definition between S2 and the leaflet was only implemented on a surface along the lower edge (the surface is highlighted in Figure 46). This step was modelled as a 0.03 second process with the final position shown in Figure 45(I).

The final geometry is shown in Figure 45(J-L).

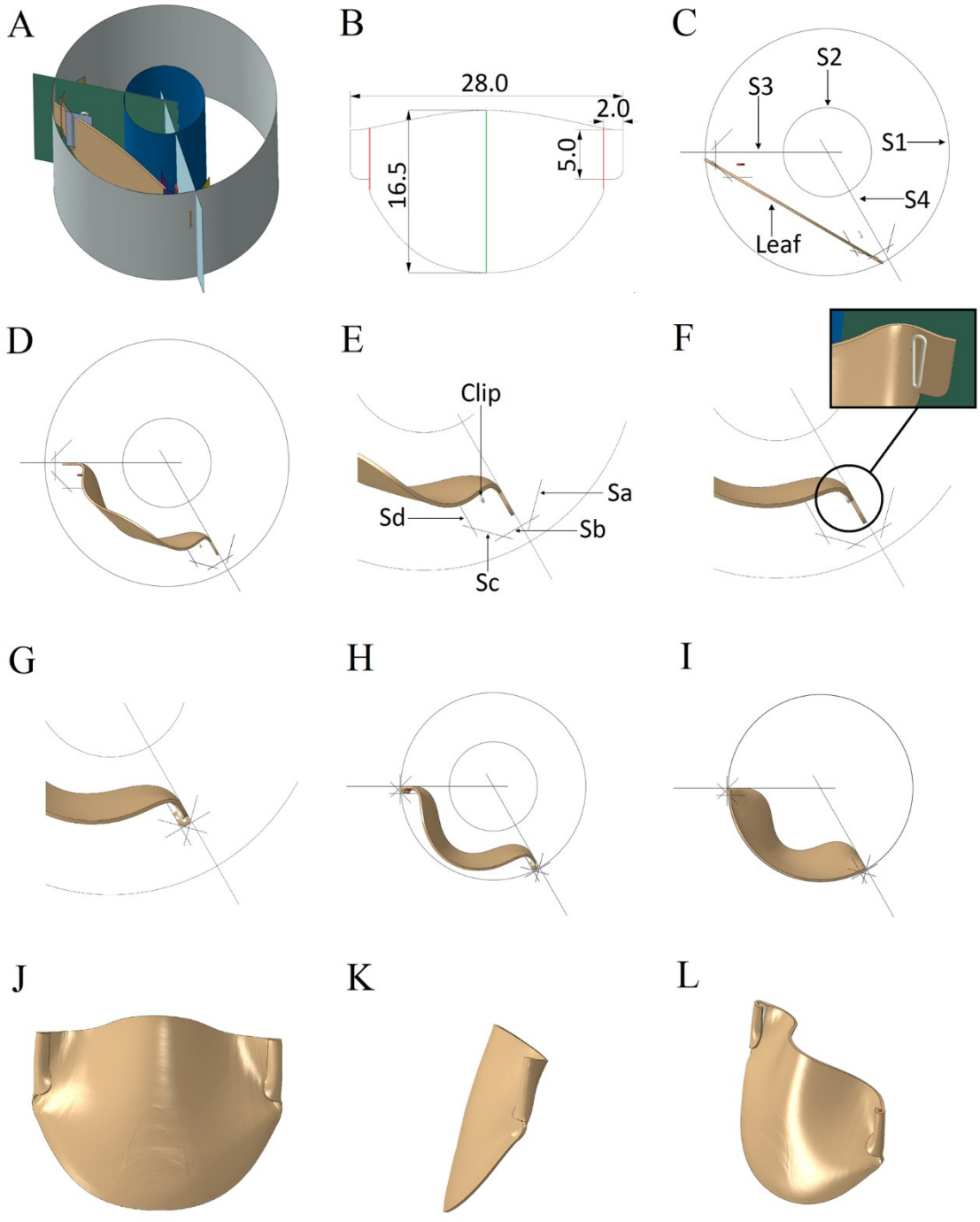

Figure 45. An isometric view of the leaflet manipulation system (A). The leaflet geometry the units of which are millimetres; nodes sets *X* and *Y* are highlighted in red (B). The manipulation of the leaflets through the folding simulation (C-I). The final geometry of the leaflet presented in the rear view (J), side view (K) and isometric view (L).

5.5.1 Structural Analysis of the Leaflets

In order to check that the leaflet geometry was suitable for a full model of the device, an analysis was set up that tested the ability of the leaflets to close together in a realistic manner. An orphan mesh of the leaflet and its clips was created from the leaflet geometry manipulation simulation. The orphan mesh was duplicated before being repositioned to create a triplet of leaflets. The lower edges of the leaflets (Figure 46) which are stitched to the frame and the cuff, were constrained in all degrees of freedom, as were all six of the clips. A load was applied to the top surface of the leaflets which was used to represent the pressure during the cardiac cycle. A typical loading profile experienced by the aortic valve during the cardiac cycle is shown in Figure 47 (Kim, Lu et al. 2008). In the interest of reducing computational time, the loading profile was accelerated with respect to time in the simulation. That is, the loading cycle of 0.78 seconds was reduced to 0.039 seconds (shown in Figure 47). Since none of the material properties of the components were time dependent, accelerating the process did not affect the simulation, provided the kinetic energy did not exceed 5% of the total internal energy. The contact definitions in this simulation were *hard* normal behaviour while the tangential behaviour was modelled with a penalty friction model (frictional coefficient of 0.2). Contact definitions were applied between all the components and self-contact was applied to the leaflets. The results are shown in Figure 48.

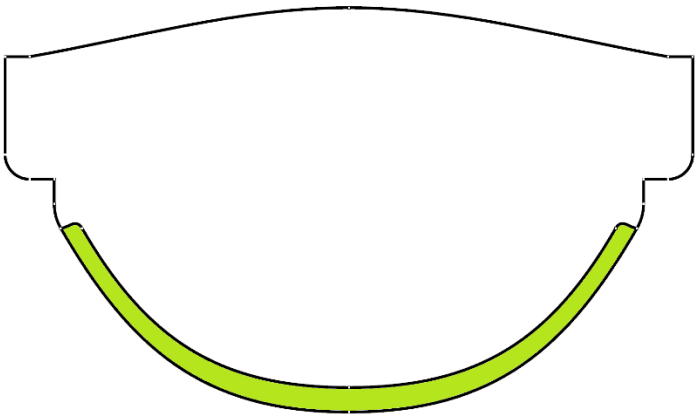

Figure 46. The planar leaflet geometry. The green section is used to represent the section of the leaflet that is stitched to the cuff.

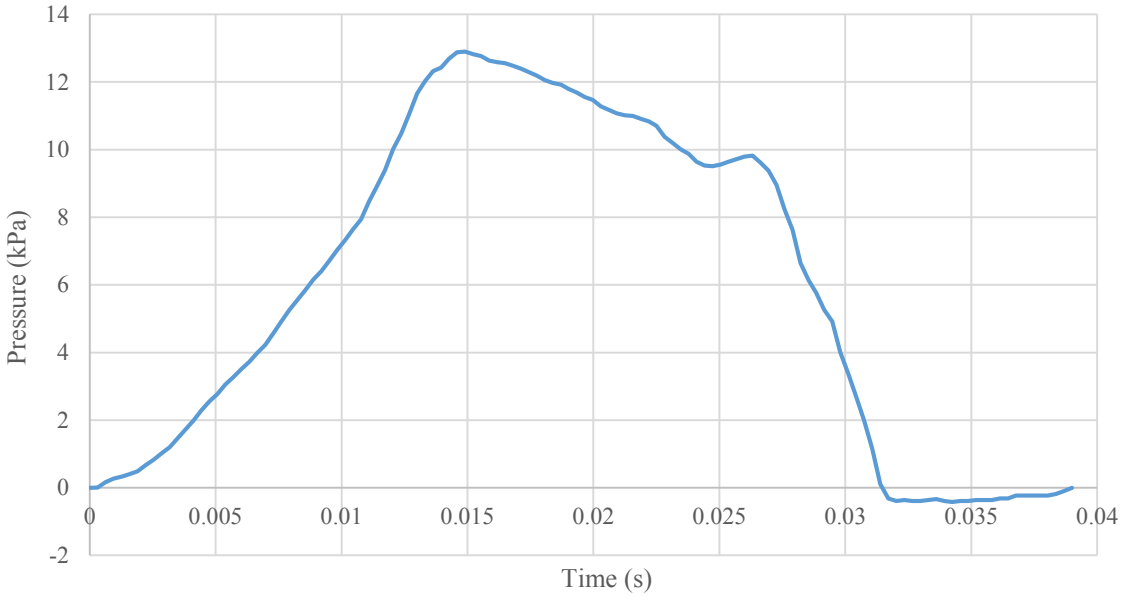

Figure 47. The loading profile used to represent the pressure experienced by the aortic valve during a single cardiac cycle (Kim, Lu et al. 2008).

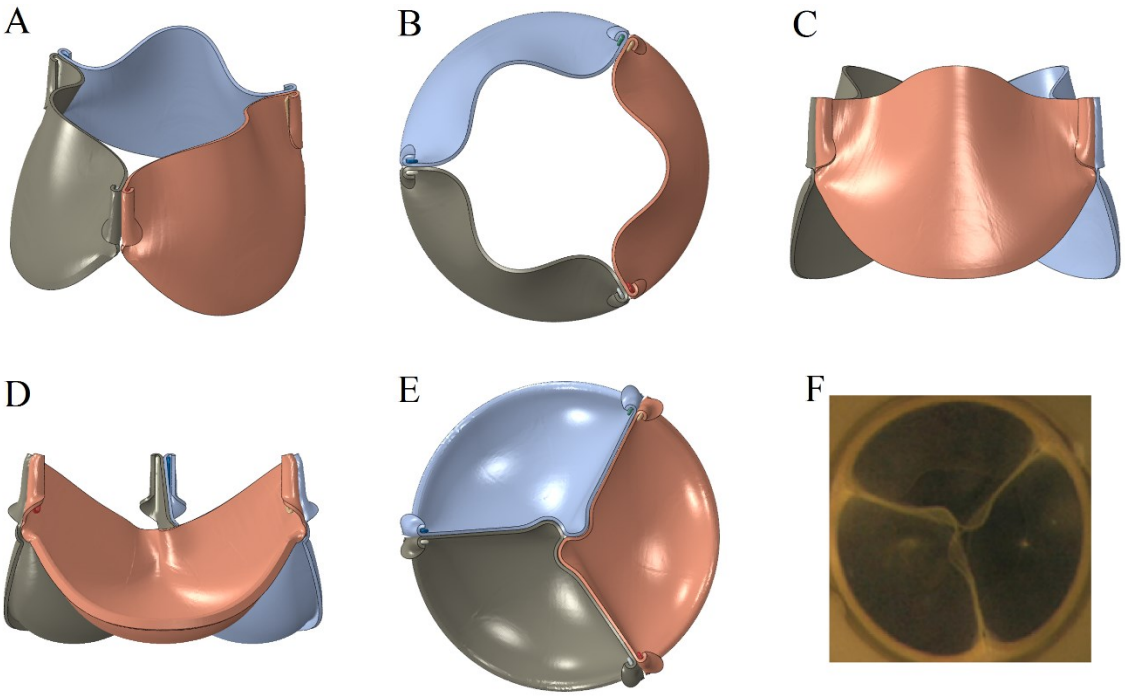

Figure 48. The triple leaflet model presented in the open isometric view (A), open top view (B), open side view (C), closed side view (D) and closed top view (E). For the purpose of comparison, a prosthetic valve in the closed top view is also shown (F) (Saleeb, Kumar, and Thomas 2013).

The simulations showed that the leaflets successfully closed (Figure 48(D-E)). A twisting motion was present in the centre of the closed leaflets, something can also be observed in experimental analysis of prosthetic leaflets (Figure 48(E-F)) (Watton et al. 2007).

5.5.2 Fluid Structure Interaction Analysis of the Leaflets

FSI was thought to be a potentially valuable area of research that could enhance our understanding of leaflet behaviour and stress variation during the cardiac cycle. Furthermore, haemodynamic performance of the prosthetic valves could be quantified.

There are two main types of FSI that can be performed in Abaqus CAE: co-simulation and coupled Eulerian Lagrangian (CEL) simulation. Co-simulation comprises two simulations running in parallel, one fluid and one solid. The fluid domain has static elements through which the fluid flows. Any surfaces of the fluid domain that are in contact with the solid body can have a boundary condition applied to them inhibiting flow through the surface. The nodes of the fluid domain are then mapped to the nodes on the solid domain. This allows a transfer of stress from the fluid domain to the solid domain. If the solid moves, the fluid domain must be re-mapped in order to account for the change in the physical fluid domain, which is computationally inefficient. As a result, it is not a viable analysis for this research (SIMULIA 2014a).

The second common form of FSI analysis is CEL. CEL has an Eulerian fluid domain with a static mesh through which fluid can flow. Unlike other CFD and FSI approaches, the elements within the Eulerian mesh do not have to contain any fluid, rather, the elements can be void, partially void, or full. The fluid also interacts with the Lagrangian solid mesh. This allows for solid objects to pass through the fluid domain and push fluid out of the Eulerian elements. Alternatively, the fluid can be forced through the domain pushing the solid along with it (SIMULIA 2014c). Although CEL is a quasistatic analysis, it has one major drawback in that mass scaling cannot be performed on the Eulerian elements. This means that the computational time for simulation is prohibitively high and increases further as the mesh resolution increases. Despite the limitations of mass scaling, CEL was considered the most computationally efficient approach to be used for modelling the flow of blood through the deformable leaflets.

Due to concerns surrounding excessive computational times, a preliminary study with a low mesh resolution was constructed. A fluid domain was defined as a cylinder with a diameter of 25.2 mm and a height of 24 mm. A triplet of leaflets was positioned within the domains shown in Figure 49. The fluid domain was meshed with a target element size of 0.7 mm resulting in 44,616 Eulerian elements.

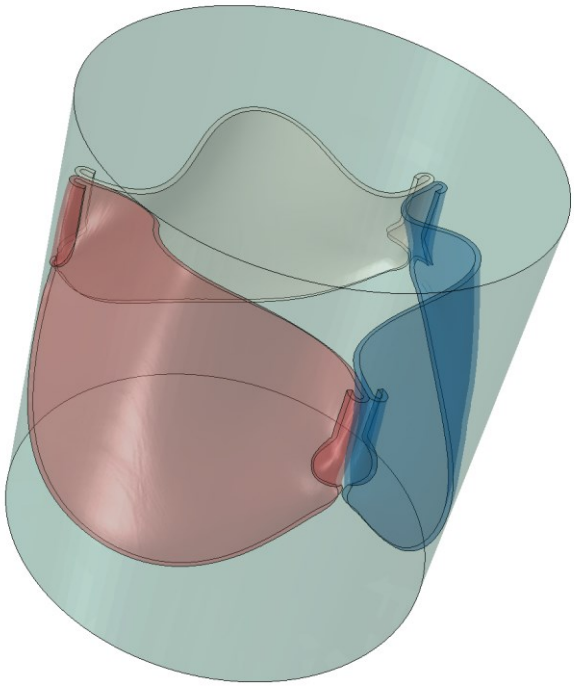

Figure 49. Computational model assembly used in FSI analysis, the cylindrical fluid domain envelopes a triplet of leaflets.

The equation of state (EOS), of a CFD system, defines all possible equilibrium states that can exist in a material. The EOS is a function of both current density (ρ) and the internal energy per unit mass (E_m) for the pressure in the system:

$$p = f(\rho, E_m) \qquad [15]$$

If the E_m term is removed from the EOS, a p against ρ^{-1} relationship unique to the material in question is generated. If the relationship is plotted, the obtained curve is known as a *Hugoniot* curve (Figure 50).

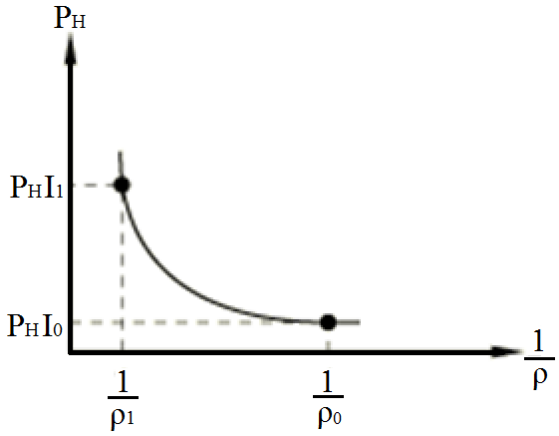

Figure 50. An example Hugoniot curve. The P_H term is Hugoniot pressure, which is derived entirely from fluid density (SIMULIA 2014b).

In this study, the EOS used to model the material properties of blood was in the U_s-U_p Hugoniot form in which the following equation is fitted to the Hugoniot curve:

$$p_H = \frac{\rho_0 c_0^2 \eta}{(1 - s\eta)^2} \quad [16]$$

where p_H is the Hugoniot pressure, ρ_0 is the reference density, η is the dynamic viscosity and c_o is the reference sound speed. s defines the change in linear shock wave velocity (U_s) associated with particles within the fluid by:

$$U_s = c_0 + sU_p \quad [17]$$

Where U_P is the particle wave velocity. With the U_s-U_p relationship stated above, the U_s-U_p Hugoniot EOS is given by:

$$p = \frac{p_0 c_0^2 \eta}{(1 - s\eta)^2}\left(1 - \frac{\Gamma_0}{2}\right) \quad [18]$$

The coefficients used to model blood are as follows: dynamic viscosity η = 0.0001 Ns/m^2, reference sound speed c_0 = 1483 m/s, s = 0 and density ρ = 1.06 g/cm^3 (Shahmirzadi and Konofagou 2012, Lide 1990, Kaatze 1995, SIMULIA 2014b).

An initial state must be used to specify the ratio of void to filled elements within the Eulerian mesh. In preliminary analysis, the ratio of fluid to void was 1:0.0229, which is the ratio of the volume of the fluid in the domain to the volume of solid objects in the domain (leaflets). This was found to result in an unstable simulation due to the wave propagation speed increasing in the Eulerian mesh. This was possibly due to the target element size being greater than the leaflet thickness (0.7 mm and 0.3 mm respectively), making it difficult to accurately predict the volume of void in each element. In order to continue the analysis with a coarse mesh, the elements were modelled as being completely full of fluid.

Three boundary conditions were applied; one to the cylindrical side of the domain which inhibits fluid flowing in or out during the analysis. The remaining two boundary conditions were applied to the top and bottom of the domain, allowing fluid to flow in and out of the domain without resistance. Two pressure loads were also applied, one to the top and one to the bottom of the domain. The loads were to represent the pressure within the aorta (top surface) and left ventricle (bottom surface) during a complete cardiac cycle. The resting pressure within the aorta is approximately 80 mmHg. However, in the simulation, the resting pressure is zero. Therefore, for the first 0.008 seconds, the pressure is linearly increased to 80 mmHg. The loading profiles for the pressure loads are shown in Figure 51 (Labrosse, Lobo, and Beller 2010).

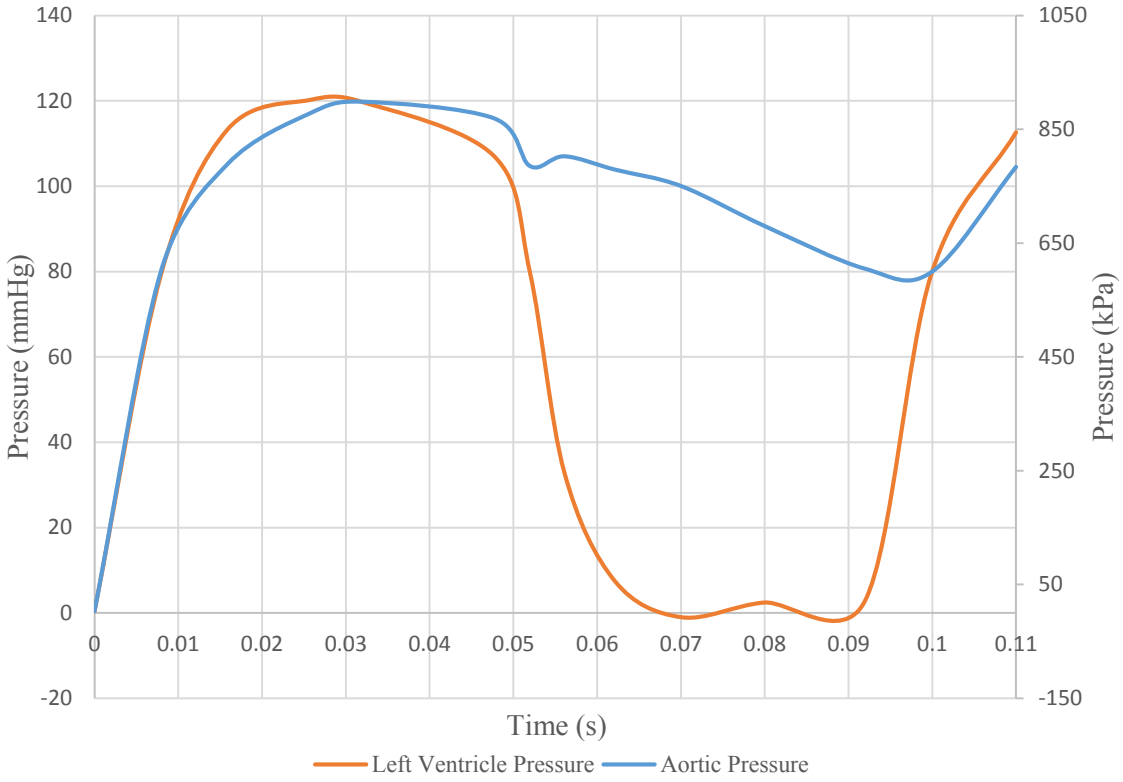

Figure 51. Pressure experienced in the aorta and left ventricle over a cardiac cycle (Kim, Lu et al. 2008).

During the simulation, the leaflets did not make contact with each other (although blood flow does stop), as shown in Figure 52. There is always a small fluid gap between the leaflets. The exact reason behind this is unknown. It's possible that the inability of the leaflets to close is induced by the coarse Eulerian mesh. The coarse mesh inhibits the pressure on each node of the leaflet to be calculated correctly.

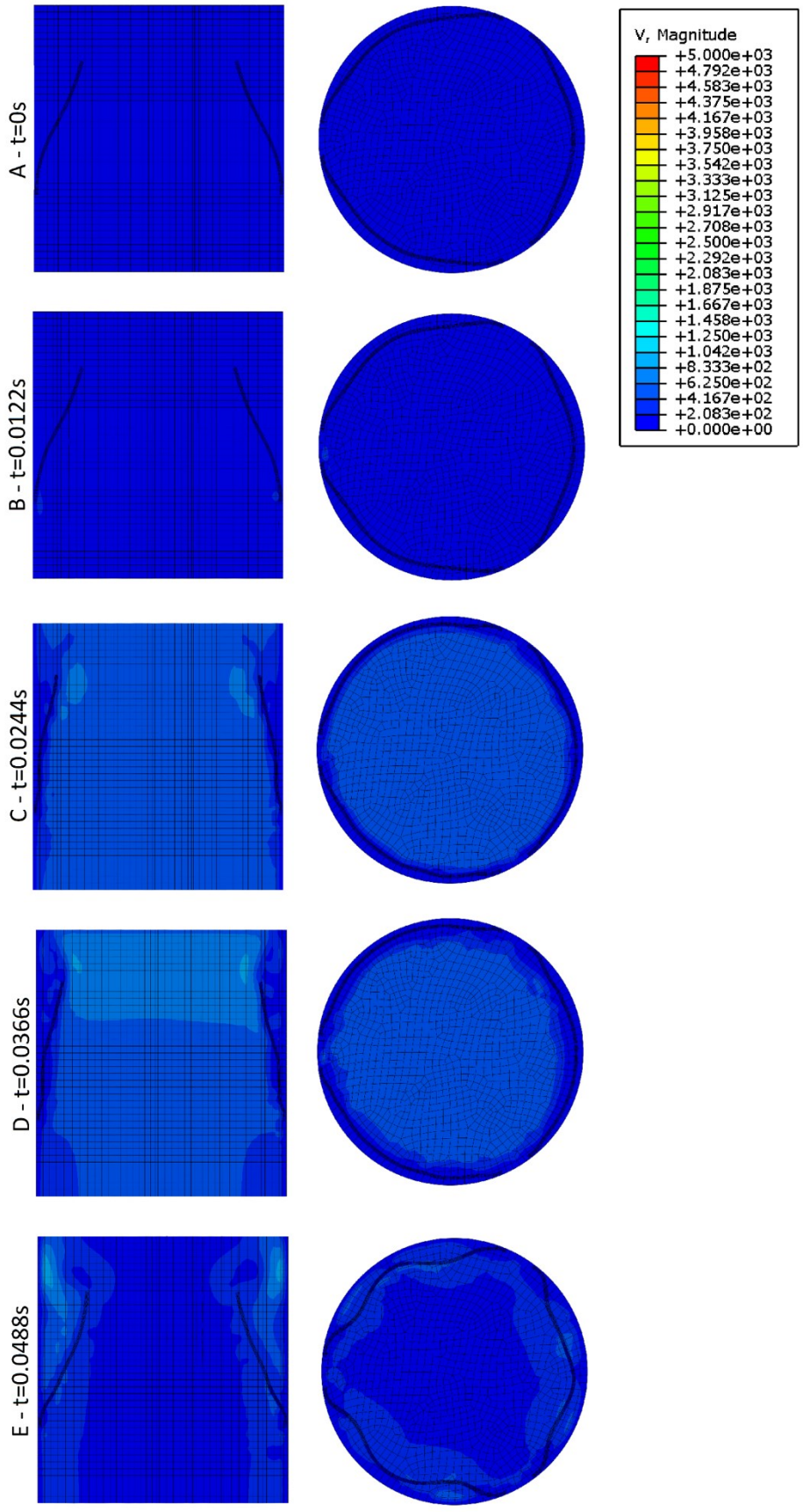

Figure 52. Two sections are used to show the fluid velocity magnitude (mm/s) about a prosthetic heart valve (part 1). The first is a section across the diameter of the cylinder, the second is a circular cross section. Each set of images is taken at a different time throughout the cardiac cycle.

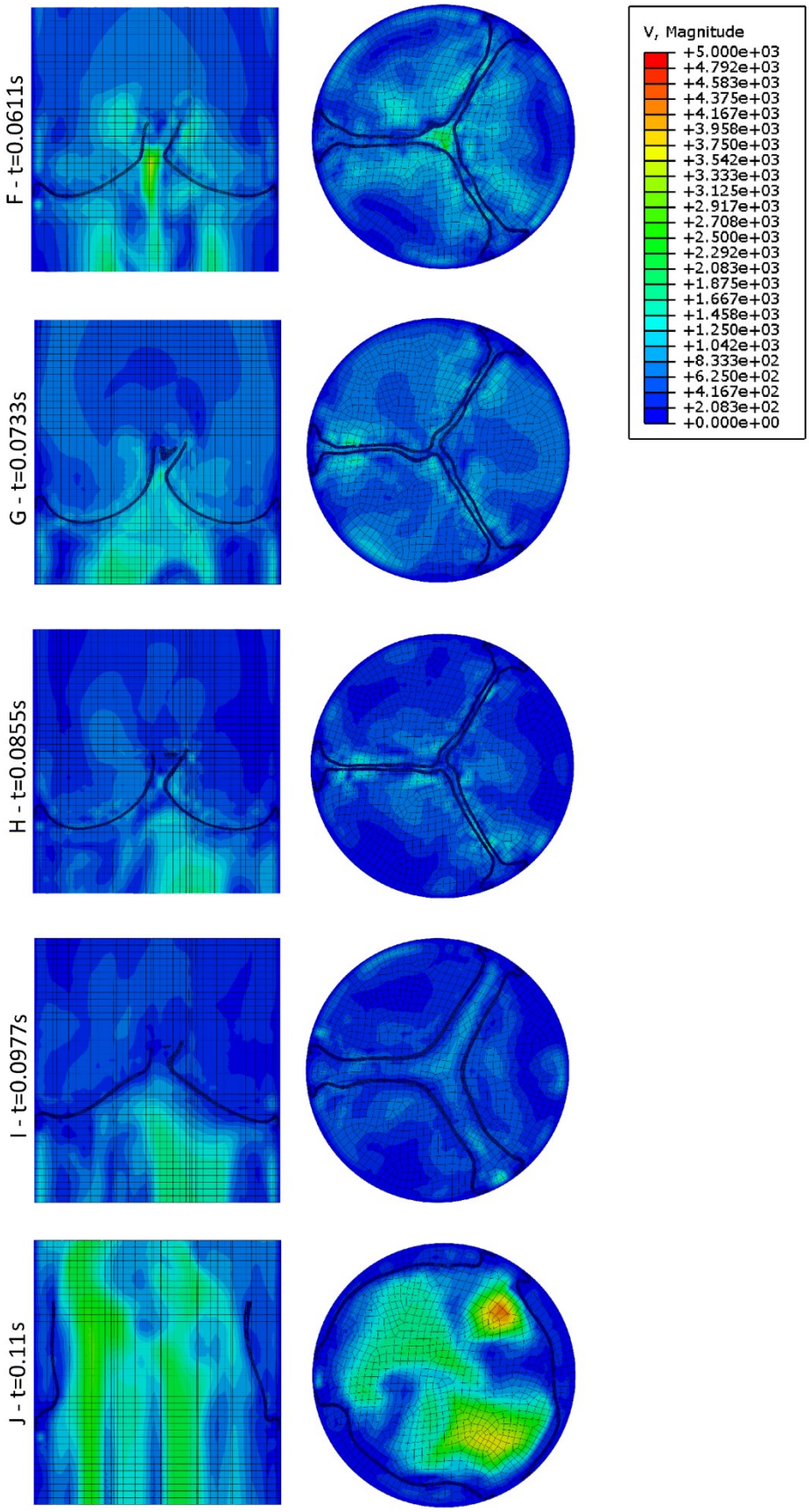

Figure 53. Two sections are used to show the fluid velocity magnitude (mm/s) about a prosthetic heart valve (part 2). The first is a section across the diameter of the cylinder, the second is a circular cross section. Each set of images is taken at a different time throughout the cardiac cycle.

The simulation was run over a single node with dual Xeon E5-4640 processors totalling 16 cores running at 2.4 GHz. The computational time was 42 hours. There is asymmetry within the leaflet response. This is likely due to the course fluid mesh creating numerical artefacts. If any detail about the flow around the leaflets is to be observed, the mesh resolution would have to be increased such that the elements are small enough to capture flow around the leaflets free edge. This would further increase the computational time.

It was concluded that the leaflets have the correct shape as indicated by the initial leaflet closing simulation. Due to computational time constraints, FSI will not be further pursued and applying an even pressure across the leaflets was recognised as the most appropriate approach to assessing leaflet efficacy.

5.6 Complete Model Construction

The components which comprise the TAVI device were assembled in Abaqus CAE. The cuff was attached to the frame by means of a tie constraint applied to the surfaces of both the frame and the cuff. Tie constraints were again used to attach the leaflets to the cuff, the constraints were applied to a strip of each leaflet, which are highlighted green in Figure 46. A second constraint was applied to node sets *X* and *Y* on the leaflet, highlighted in red in Figure 45(B). These nodes were coupled to control points on the frame which are shown in Figure 54. This constraint resulted in the selected nodes on each leaflet mimicking the motion of the control points on the frame. The clips were also attached to the frame, by means of a couple constraint between all the nodes in the clip, and the control points on the frame.

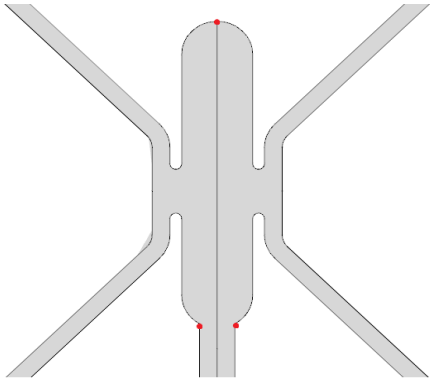

Figure 54. Control point positions on the frame. Each dot represents two points, one on either side of the frame.

The assembled device is visually very similar to its real life counterpart (shown in Figure 55). However, the constraints used to attach the clips to the frame are not realistic. In the actual device, the clips are likely to be stitched to the frame, such that the clips can move independently to the

frame. As opposed to the computational model, the couple constraints result in the clips being rigid to the frame.

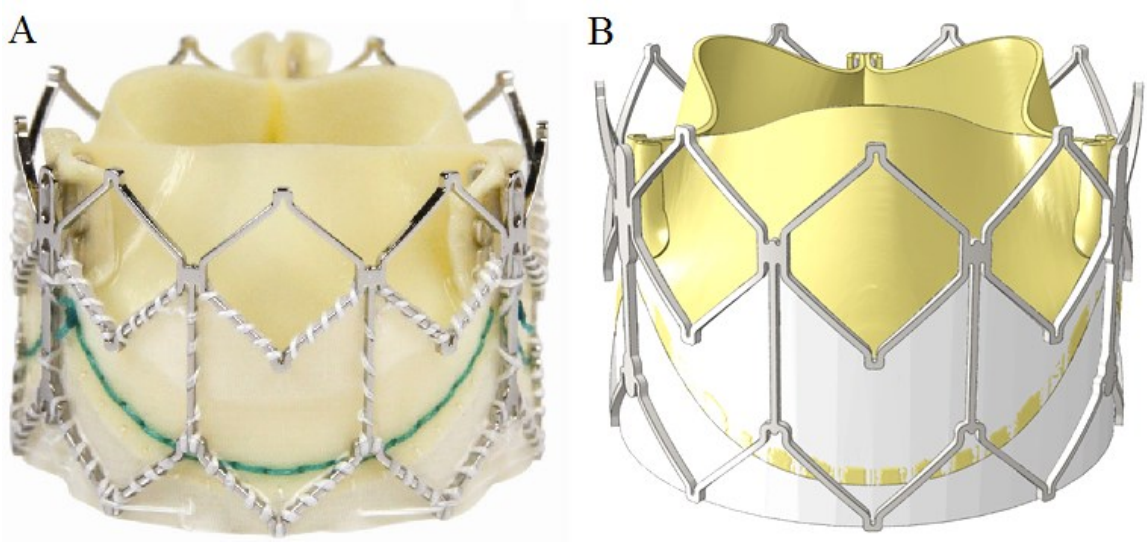

Figure 55. Comparison between the actual SAPIEN XT (A) and computational model (B) (Edwards LifeSciences 2013c).

5.7 Delivery System Model Development

In order to simulate the deployment of a BE TAVI device, a delivery system must also be modelled. In early models, a cylindrical surface was positioned within the crimped TAVI device, which would then radially expand. Using a displacement boundary condition applied to the surface of the cylinder to radially expand the cylinder and deploy the device, would result in the surface having an infinite stiffness. However, this approach was found to excessively distort the elements within the leaflets. As a result, a computational model of a 26 mm balloon was developed.

The deployment device used for the SAPIEN XT is the NovaFlex+ delivery system, pictured in Figure 56 (Edwards Lifesciences 2014a). Each TAVI device size has a corresponding balloon of the same diameter, as to ensure the device is deployed correctly.

Two balloons were acquired, one used to deliver a 26 mm SAPIEN XT, the second for a 23 mm SAPIEN XT. Measurements of a 26 mm balloon from a discarded system were made. The length was 76.5 mm and the measured thickness was 0.07 mm. Due to damage to the 26 mm balloon, it could not be inflated, the 23 mm balloon was therefore inflated in order to easily capture its shape.

Figure 56. Edwards Lifesciences NovaFlex+ delivery system with a SAPIEN XT valve mounted (Edwards Lifesciences 2014a).

Once inflated, the 23 mm balloon was photographed. Then, a parameterised model was produced and calibrated to the balloon photograph, as shown in Figure 57. The values of the calibrated parameters are listed in Table 10.

The intention of the geometric model was to scale the parameters from 23 mm up to 26 mm. However, when the parameters were scaled by a factor of 26/23, the resulting geometry had an incorrect length. As a result, the parameters were modified in order to create a geometry which was still based on the calibrated parameters but also agrees with the known length of the 26 mm balloon. The measured and adapted parameters are also listed in Table 10. The profile of the balloon was then revolved about the axis of the balloon to create a surface.

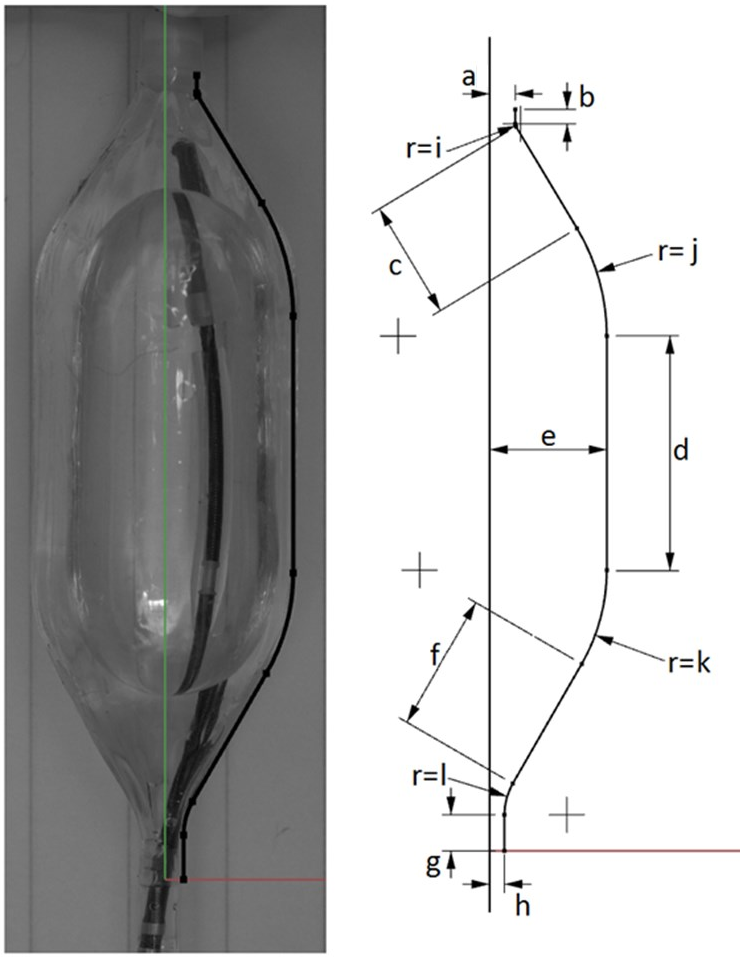

Figure 57. NovaFlex+ delivery system with the outline of the geometric model overlay (A). The geometric model with parameter definition (B).

Parameter	23 mm Measured	26 mm Derived
a	2.85 mm	2.85 mm
b	1.60 mm	1.60 mm
c	11.18 mm	13.13 mm
d	23.00 mm	25.90 mm
e	11.50 mm	13.00 mm
f	13.26 mm	15.29 mm
g	4.00 mm	4.00 mm
h	1.65 mm	1.65 mm
i	0.50 mm	0.59 mm
j	19.17 mm	23.13 mm
k	18.03 mm	20.75 mm
l	6.00 mm	6.91 mm

Table 10. Balloon model parameters.

The deployment device comprises several other components. There is a cone, a tube through the centre, a plastic tube within the balloon into which the TAVI device is actually crimped, and a second component within the balloon that limits the distance the device can be pushed along the balloon. The relevant components are described in the Appendix.

For the purpose of TAVI deployment, the balloon must be in the deflated state. In order to capture the deflated balloon geometry, a preliminary FEA simulation was performed.

The material used to model the balloon was based on polyethylene terephthalate: elastic modulus E = 900 MPa, Poisson's ratio $\nu = 0.3$, Rayleigh damping factor coefficient $\alpha = 1100$ and density $\rho = 1$ g/cm^3. The cylindrical body of the balloon was meshed with 368,114 quadrilateral shell elements, while the ends of the balloon were meshed with 428,262 triangular elements.

Preliminary boundary conditions were applied to the lower edge of the balloon which was constrained to a plane normal to the axis of the balloon. This is to account for elongation of the balloon as it inflates, in reality the wire running through the centre bends. Further tie constraints were used to attach the upper edge of the balloon and the wire to the cone. These preliminary constraints were used throughout this research, in all simulations that included the balloon.

Two node sets were used to apply loads to the balloon: *A* and *B*, which are depicted in Figure 58(A). The entirety of the balloon had self-contact applied to it with *hard* normal contact and frictionless tangential behaviour.

The simulation had two distinct steps. In the first step, two loads were applied. The first to set *A* of magnitude 0.04 N radially inwards. The second was applied to set *B* with a magnitude of 0.02 N radially outwards. These values were determined through computational experiments such that the balloon folded into the required shape, without stretching. This resulted in the cross section of the balloon folding from a circle, to an eight armed star shape, as depicted in Figure 58(B-E).

In the second step, the node set *A* was constrained in all degrees of freedom, Node set *B* had a load of 0.05 N (again experimentally determined) applied tangentially about the axis of the balloon. The coordinate system recalculated the direction of the load every increment to retain its tangential orientation to the balloon axis. In order of change, the balloon preparations are shown in Figure 58(E-H).

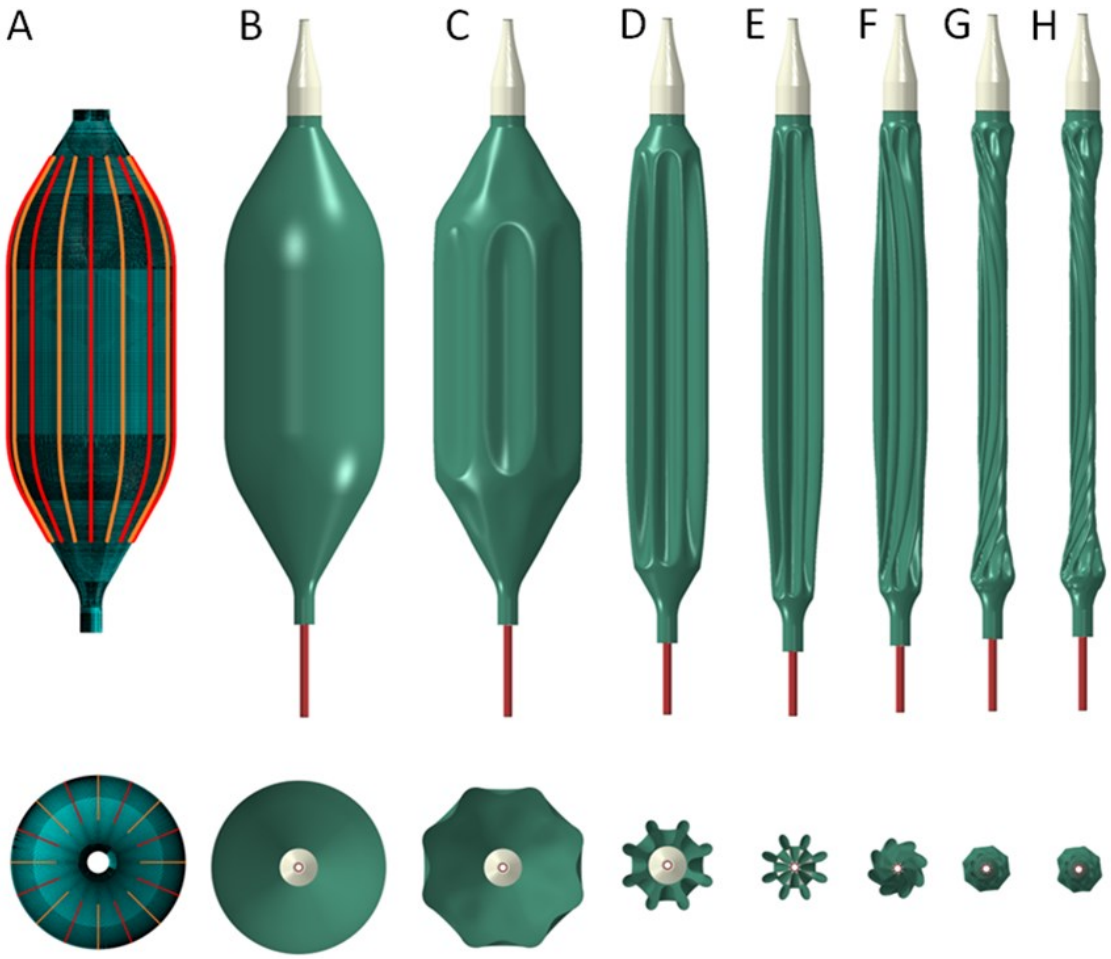

Figure 58. Balloon folding simulation. Loads were applied to node sets *A* and *B* which are highlighted in red and orange (A), resulting in the balloon folding (B-H).

The components described in this chapter are representative of the components present in a complete SAPIEN XT device, delivery system and a SAPIEN 3 frame. These components were used to analyse the behaviour of the prosthetic leaflets during and after a range of deployment simulations in a detailed model of a heavily calcified patient-specific aortic root model discussed in chapter 6.

5.8 Summary

A 26 mm SAPIEN XT, 26 mm SAPIEN 3 and NovaFlex+ delivery apparatus models were developed and detailed in this chapter.

The SAPIEN XT model includes all of the components of the actual device: six clips, three leaflets, a cuff and a frame. The frame was generated through a parameterised CAD model, from which the geometry of the cuff was extracted. This is the only TAVI device model that includes the leaflets, and is capable of undergoing deployment. Some leaflet models have been presented in the literature, however the geometry of the leaflets is unrealistic as it was produced through a leaflet mapping technique. In order to improve the leaflet geometry in this thesis, the leaflets were modelled as a planar piece of material and then manipulated into a functional position, resulting in a superior geometry. The material properties applied to the leaflets was hyperelastic. Computational analysis of the leaflets was performed to confirm the leaflets are functional.

The SAPIEN 3 model comprises a frame and cuff. In reality, the cuff of the SAPIEN 3 partially spans the inner surface of the frame, before wrapping around the underside of the device and partially covering the outer surface also. This detail is not included in the model as the cuff only spans the inner surface and ends at the lower edge of the device. This simplification is assumed to be acceptable as the cuff on the exterior of the device does not offer any additional structural properties to the device. Finally, the leaflets and clips are neglected from this model as it was used for PAR analysis which was found to be effective without the inclusion of leaflets.

Both the SAPIEN XT and SAPIEN 3 are BE devices, as a result a BE delivery apparatus model was also developed. The model was based on measurements taken from an actual NovaFlex+ delivery system. The model comprises a balloon, internal wire and cone.

Chapter 6: Patient-specific Aortic Root Model Development

In order to achieve insight into the performance factors of the SAPIEN XT when deployed in practice, a computational model of an aortic root is needed. An aortic root model can be produced in one of two ways:

1) It can be developed from a parameterised CAD model of an aortic root.
2) It can be extracted from either CT of MRI scans of a human heart.

Each method has advantages and disadvantages. The first allows for acute, and specific changes to the aortic root geometry. Systematically changing the geometry of an aortic root is an attractive option as it would allow for in depth analysis. However, the aortic root is a challenging geometry to model in CAD making this process very time consuming. Furthermore, as the geometry would not be patient-specific it wold not fulfil the objectives of this study. The second method results in an aortic root geometry that is representative of a specific patient, therefore guaranteeing the model is realistic. Additionally, patient-specific computational models could potentially lead to computational procedural planning, resulting in superior patient selection and safer procedures.

We briefly attempted to produce a parameterised model, but due to difficulty in generating a geometry that conformed to measurements taken of patients, and the possibility of patient-specific procedural prediction, it was decided that pursuing a CT or MRI derived aortic root model was the most beneficial option for this research.

6.1 Initial CT Derived Model

CT scans of a series of patients suffering AS were supplied by UHST. The set with the smallest voxel dimensions was selected as it demonstrated superior detail to the other scans, a single frame of which is pictured in Figure 59.

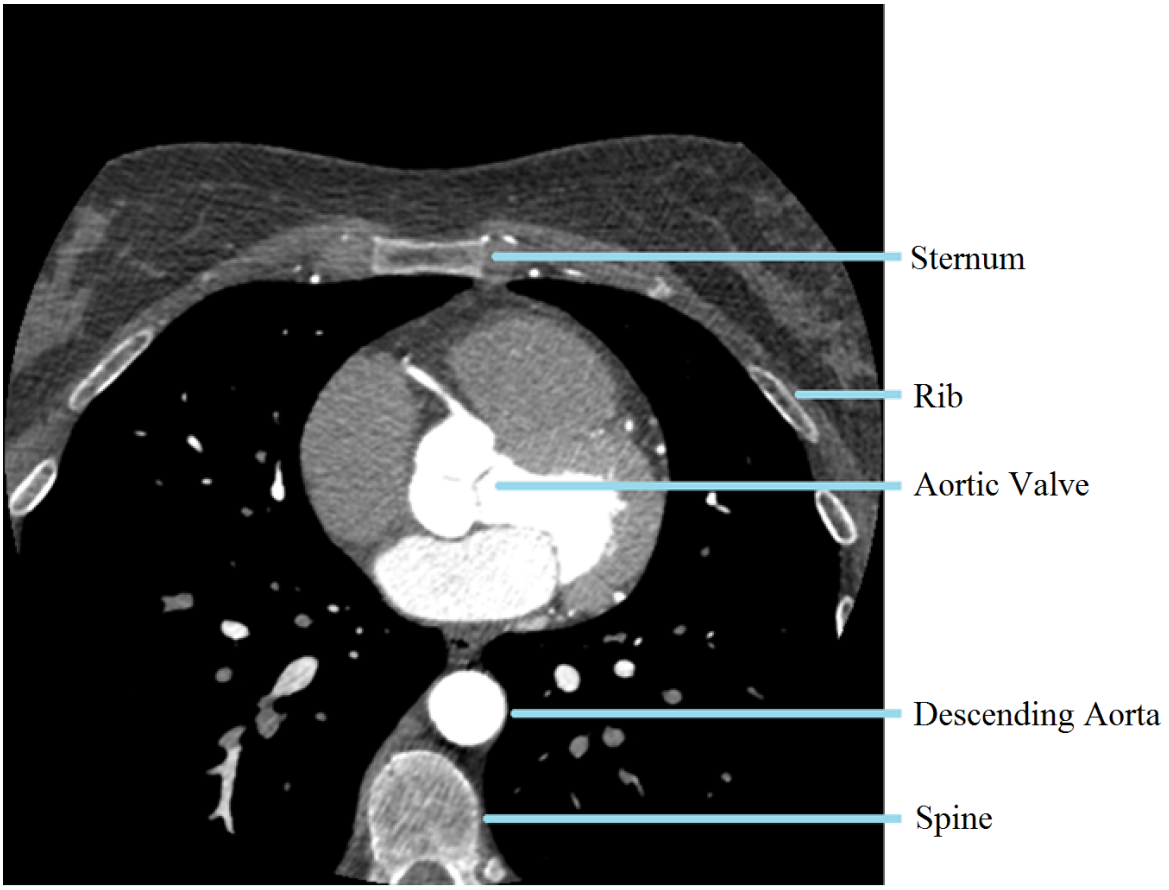

Figure 59. CT scan image revealing a cross section of the heart. The ribs, sternum, aortic valve, descending aorta and spine are all visible in the image. The dark areas with white islands on either side of the heart are the lungs.

A CT scanner is effectively an X-ray machine that can rotate about an axis. For this example, consider a 3-dimensional datum system *x, y, z*, where the CT scanner rotates about the *z-axis*. The X-ray machine consists of a radioactive source, and an array of detectors. The X-rays from the source travel through the specimen and into the detector creating a map of intensities. The maps are an integration of the radio-opacity through the specimen. However, this is where similarities with an X-ray machine end. The CT scanner rotates about the *z-axis* capturing maps at regular rotational increments. These maps then undergo a tomographic algorithm generating a set of images, all of which are parallel to the *x-y* plane, and are offset from each other by a specific increment. These images are not the integration of radio-opacity, rather the radio-opacity of local areas (voxels) (Bertolini and Prokop 2011).

The resolution of the resultant images is proportional to both the resolution of the sensor, and the number of intensity maps taken. As a result, medical CT scanners are normally low resolution, as increasing the resolution requires more intensity maps, increasing the radiation dose to the patient. However, the voxel size can be reduced by focusing the CT scanner on to the object of interest. The voxel size is equal to the CT scanner field of view divided by the number of voxels across a scan (medical CT scanners produce images that are 512 voxels in width and height). Therefore, if the

scanner is focused on the heart, the voxel size would be equal to the width of the heart divided by 512. Unfortunately, if a CT scanner is to be used to assess AS, it is common practice to capture the entire abdomen and this increases the voxel size and decreases the quality of the data.

The output of a CT scanner is an image with a grey scale which is measured in Hounsfield units (HU) as defined by:

$$HU = 1000\frac{\mu_{\mathrm{x}} - \mu_{\mathrm{water}}}{\mu_{\mathrm{water}} - \mu_{\mathrm{air}}} \qquad [19]$$

where μ_{x} is the linear attenuation of the object of interest, μ_{water} is the linear attenuation of water and μ_{air} is the linear attenuation of air. The linear attenuation is a measurement of how easily a substance can be penetrated by a beam, in this case, radiation (Hounsfield 1979). While all tissue has a specific radio opacity, it is not unique to any specific tissue. It is potentially possible to extract different tissues from the scan (a process called segmentation) by extracting areas of a specific radio-opacity (thresholding), provided the neighbouring tissues do not have the same radio-opacity. Unfortunately, the tissues in the heart all have a very similar radio-opacity. As a result the tissue that constitutes the aortic root wall cannot be distinguished from the surrounding tissue.

In order to highlight the features of interest, radio-opaque dyes can be used. For the case of medical scans assessing the cardiac system, radio-opaque dyes are injected into the patient resulting in the circulatory system appearing bright white on CT scans (visible in Figure 59). Although the orifice of the circulatory system is highlighted by the opaque dye, the plaques which have a similar radio-opacity are often masked by the dyes.

Despite the limitations of the CT scan data set, it was still used to derive an aortic root model. The procedure is described in Table 11.

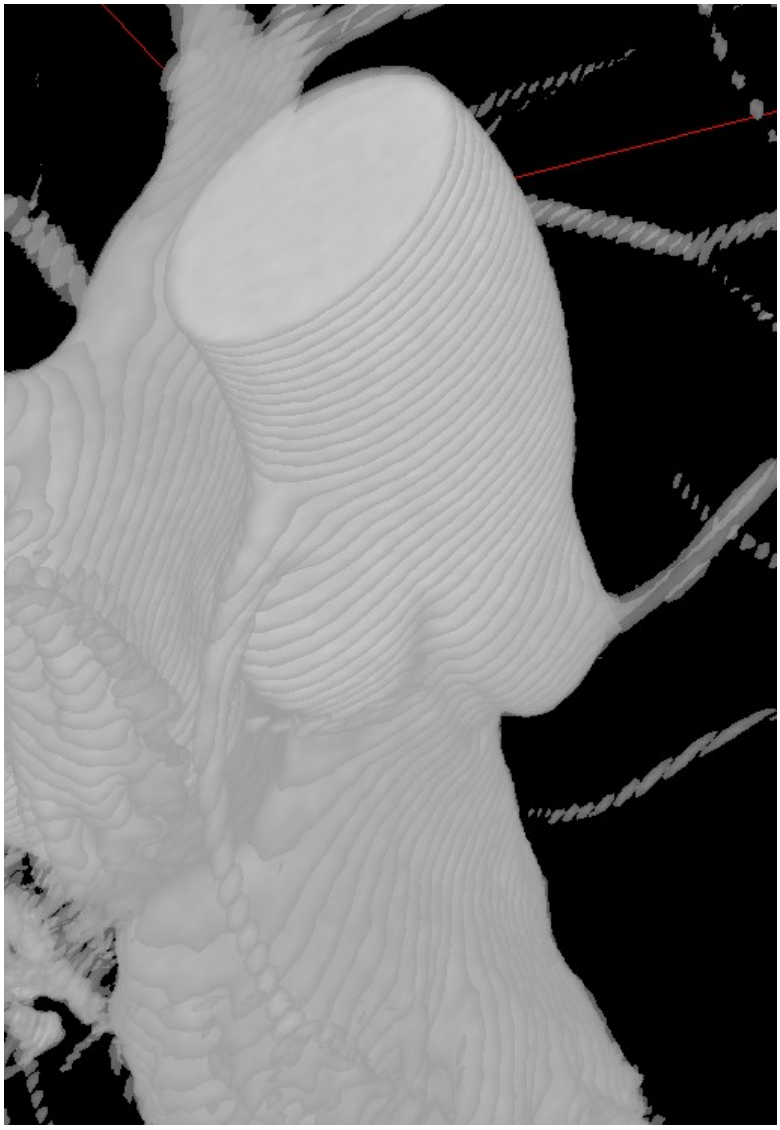

Figure 60. An aortic root constructed from patient data. The striations represent the individual images of the CT scan.

Step	Mask	Description
1	-	In order to extract the aortic root, the data must first be cropped to have the minimum volume while still containing the aortic root that is of interest, as this reduces computational time for any image processing operations. ScanIP (Simpleware 2014) was used for this task.
2	-	Due to the CT scanners low resolution, relative to the intricacy of human tissue, the data appears noisy. A median filter was used in an attempt to remove some of the noise. The neighbourhood radius of the median filter was three voxels in all dimensions.
3	R1	The images were then segmented by means of thresholding. That is, any voxels which had a Hounsfield value above 150, were selected in the resultant mask (A 3D representation of this mask is shown in Figure 60).
4	R2	*R1* did not have a smooth exterior surface. As a result the mask underwent an eroding procedure, in which the mask had the outermost layer of voxels removed. This process was repeated three times. The mask was then dilated, in which a layer of voxels were added to the exterior surface. This process again, was repeated three times.
5	-	The exterior surface of the segment was then meshed in ScanIP. It was found that the mesh could sufficiently represent the geometry with as few as 1913 triangular elements.
6	-	The surface mesh completely encapsulates the segment. However, the upper and lower ends should be open as the lumen continues beyond the boundary of the scan. The mesh was imported into Rhino3D where the elements that comprise the top and bottom were removed.
7	-	Some of the elements in the mesh were poor quality due to the aspect ratio. In these case, the elements are manually deleted and re-meshed in Rhino3D.

Table 11. Procedure for extracting an aortic root model from medical CT data.

The resultant computational model is shown in Figure 61. The model was used for preliminary computational analysis. However, due to the lack of leaflets, and plaques, further models were sought subsequently.

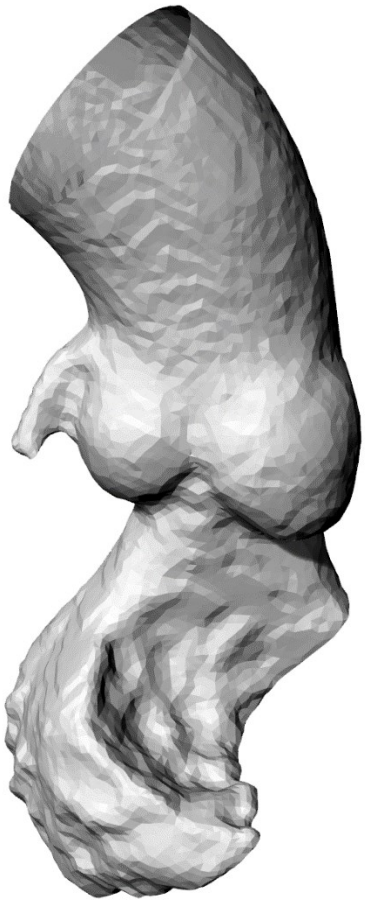

Figure 61. Computational model of a human aortic root and left ventricle, the geometry was derived from medical data of a patient of UHST.

6.2 µCT Derived Model

Due to the lack of detail in the initial model, alternative sources of geometry were explored. The main reason the model lacks detail is the low resolution of the medical CT scanner, as well as the radio-opaque dye which masks the plaques. An alternative to a medical CT scanner, is a research µCT scanner, which is capable of capturing volumes at a resolution of 8000x8000x8000 voxels, where each voxel could be less than a micron in length. A µCT scanner would be capable of imaging a heart, accurately capturing the leaflets and the plaques. The radiation dose associated with a µCT scanner would be extremely damaging to a patient's health. Furthermore, a µCT scan can take several days to complete; it is unrealistic to expect a patient to remain in a similar position for so long. As a result, any model produced from µCT data cannot be of a living heart, or used for patient-specific computational procedure prediction and planning.

Although the μCT scanner cannot be used to image a living patient's heart, it could be used to image a cadaver's heart. However, there are still further complications: although the scan will be accurate to the tissue, the tissue itself will not be representative of living tissue because it will have deteriorated and distorted during the embalming process.

It was decided that using a μCT scanner was a good option. Although the tissue would be distorted, it was theorised that it would be possible to pull the computational model of the tissue back into its original position through FEA. Although this process would be difficult, a model with such a high level of detail would be valuable to this project.

The University of Southampton Anatomical Learning Science centre (ALS 2014) offers a selection of hearts which can be loaned out. Preliminary studies were performed on the hearts to ensure useful data could be collected. The hearts were visually inspected to see if the aortic valve and leaflets were intact. The size of the heart was also important, the heart should be *medium* in size to accommodate the 26 mm TAVI device that had been modelled in CAD. A single heart (labelled No. 445) met all the criteria, despite being preserved for nearly a decade at the time of the scan, it had an intact aortic root and valve.

The μCT scan was undertaken at the University of Southampton μ-VIS centre (μ-VIS 2013). A XT H 225L μCT scanner was used to scan the heart yielding a resolution of 2000x2000x2800 voxels (Nikon 2013). The heart was first loaded into an airtight container to ensure it didn't dry out which would cause it to distort during the scan creating a blurred image. It was then mounted in the scanner where it was scanned by the technical staff. The scanner was calibrated to 59 KV, 125 μA, with an exposure time of 708 ms and 3142 projections with an average of four frames taken per projection. Two scans were performed, one of the upper half, one of the lower, the duration of each scan was six hours.

The μCT scanner does not export a CT image, rather a series of X-ray images that are then aggregated into a CT image. One of the images is shown in Figure 62. The plastic bag holding the heart is clearly visible, as is the elastic band that holds the heart together.

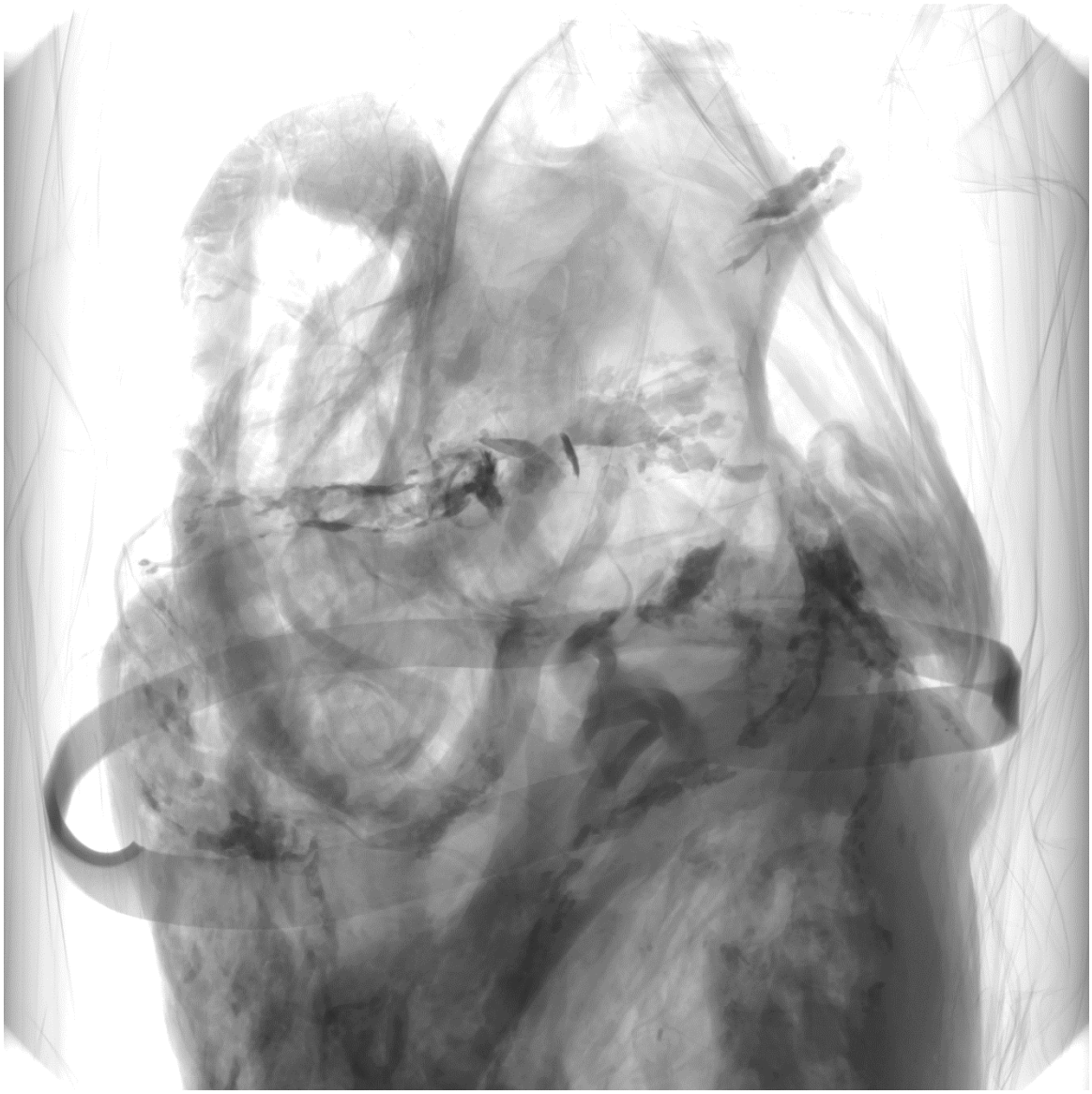

Figure 62. X-ray of a human heart taken using a μCT scanner.

Both the scans were individually compiled into a series of CT images. A common image was found in both sets, and the two were merged together with the common image as a reference. VG Studio MAX V2.1 was used to compile the images, while ImageJ was used to merge the two sets (Open-Source 2014, VolumeGraphics 2014). A section of a single slice is shown in Figure 63. Using thresholding in 3D Studio MAX, a render of the tissue of the heart was produced and is shown in Figure 64.

The heart must then be segmented and a mesh extracted, the procedure is shown in Table 12.

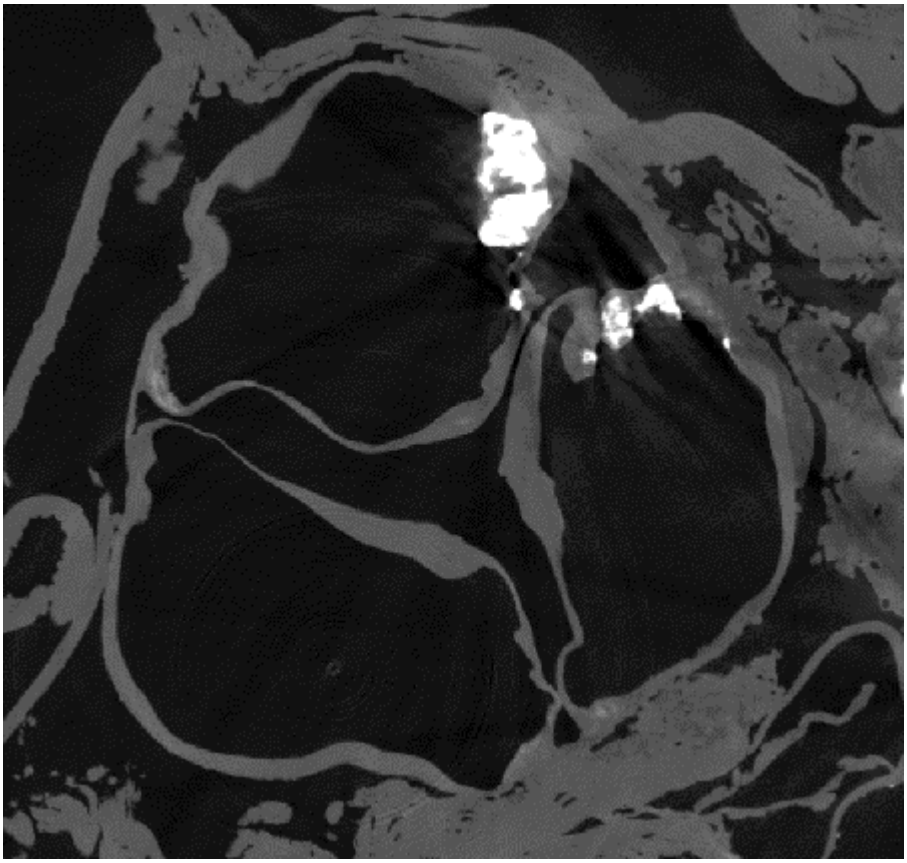

Figure 63. µCT slice of a human heart. The aortic valve and the three leaflets can be clearly seen approaching each other in the centre of the image. Calcified plaques are present in the image, highlighted in bright white.

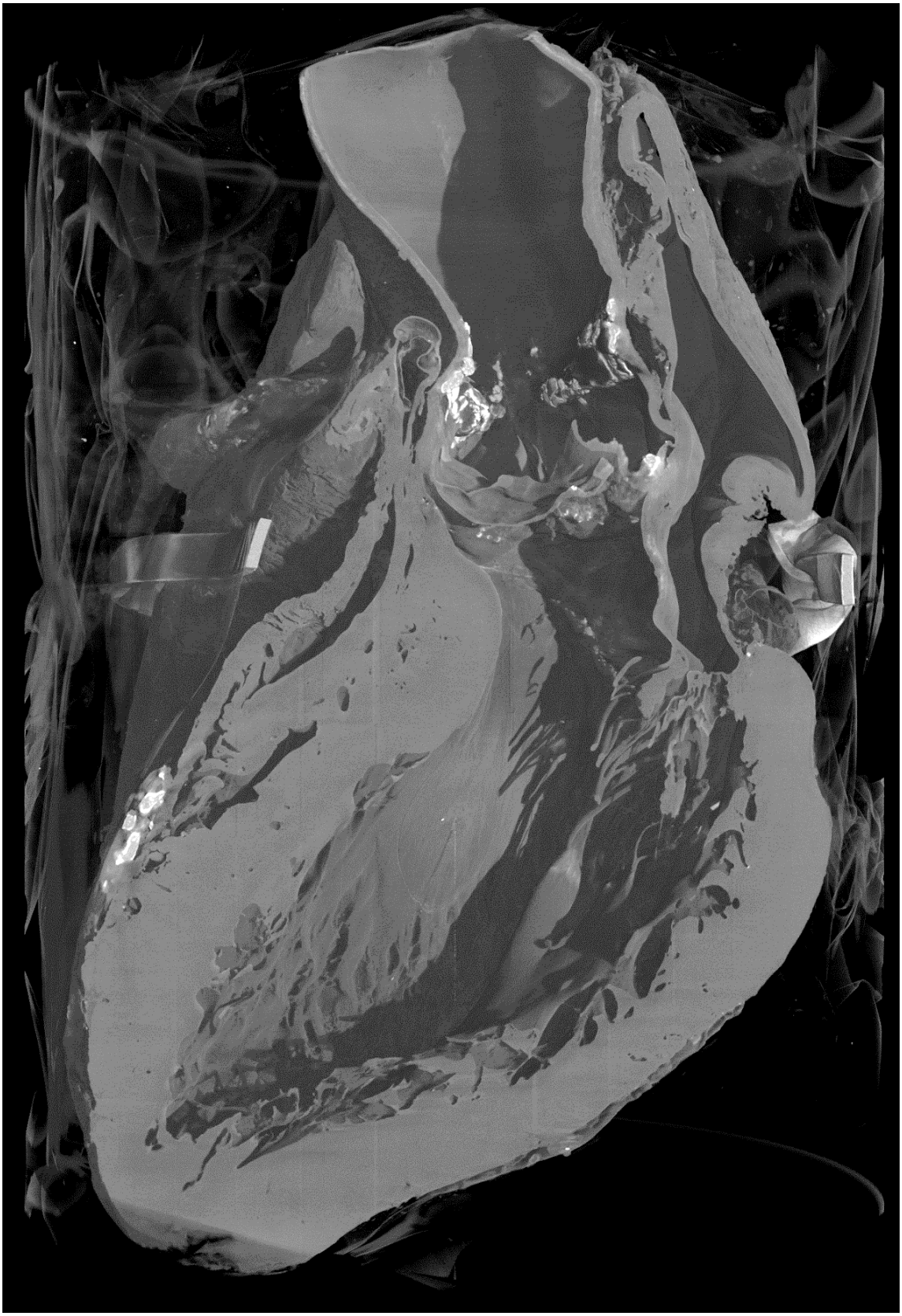

Figure 64. 3D render of a human heart (with a section removed) based on μCT data. The grey wisps about the heart are due to a plastic bag that could not be completely removed from the image. Furthermore an elastic band is visible encircling the heart. Bright white plaques are visible in various locations about the heart.

Step	Mask	Description
1	-	With an image resolution of 2000x2000x2800, and 32 bit greyscale voxels, the entire data set was approximately 50 Gb. In order to reduce the file size, the data was reduced from 32 it to 8 bit using ImageJ. The resultant data set was 11 Gb.
2	-	Manipulating such a large image at once is difficult because it requires a large amount of RAM. In fact, some simple operations, like island removal, used in excess of 192 Gb of RAM. As a result the image was cropped so that only the aortic root was included (resultant resolution was 727x753x570 voxels) using ScanIP.
3	T1	The plaques were then segmented from the data. Thresholding was used, any voxel exceeding 90 HU was assumed to be a plaque.
4	T2	The tissue was then segmented from the data. Thresholding was used, any voxel between 25-89 HU was assumed to be tissue.
5	T3	Unfortunately, some of the very thin leaflet portions were excluded from *T2* as the HU value was too low. As a result, these segments were manually selected using localised thresholding technique (with a lowered threshold of 19 HU), which was focused on the leaflets.
6	T4	Further smoothing of the segments was applied with a recursive Gaussian smoothing function across a five voxel radius.
7	-	The aortic root segment was then meshed in ScanIP. The elements used to mesh the aortic root were linear tetrahedral elements with a target minimum edge length of 0.2 mm, a maximum edge length of 2 mm and a target maximum error of 0.05 mm. The resulting mesh had 1,834,471 elements.
8	-	The plaque segment was then also meshed with the same parameters as the aortic root, resulting in a mesh with 334,703 tetrahedral elements

Table 12. Procedure for extracting an aortic root model from μCT data.

The resultant model is shown in Figure 65. The heart has clearly been distorted during the embalming process and through ageing outside the body. The aorta is no longer circular, rather an irregular cross section is present. The surrounding tissue is also attached to the model as it would require each slice to be manually segmented. However, the aortic leaflets are present, although a little crumpled.

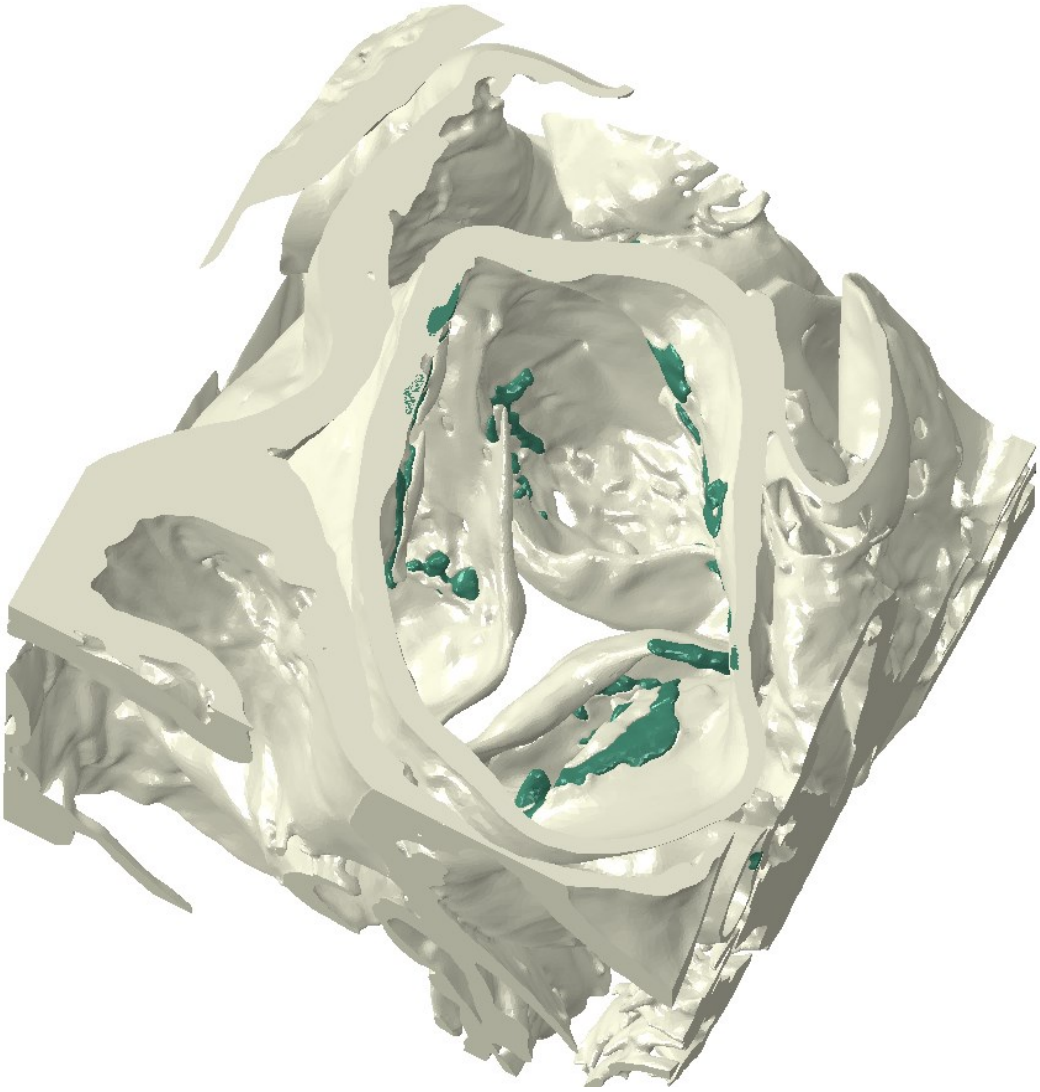

Figure 65. High resolution model of an aortic root derived from μCT data. The aortic root is orientated such that the aortic valve leaflets are visible through the aorta. The green regions are calcified plaques.

Because of the large number of elements present in this model (1,834,471 elements, as opposed to the 1913 elements in the previous model) and the small element size. Preliminary simulations were performed on the aortic root model. In one simulation the leaflets were partially opened, the computational time was 10 hours. This aortic root model was therefore concluded to be too computationally expensive for practical use.

6.3 Improving the Initial Patient-specific Model

In the absence of appropriate computational models, and patient data to base the models upon, attention was turned back to the initial data set (Figure 59). The segmentation procedure was modified to create an aortic root volume with a uniform wall thickness of 2.5 mm, as well as native aortic leaflets. The first four steps of the segmentation process were identical to the original procedure, after which an alternative process was developed, as shown in Table 13.

Step	Mask	Description
1	-	In order to extract the aortic root, the data must first be cropped to have the minimum volume while still containing the aortic root that is of interest, as this reduces computational time for any image processing operations. ScanIP was used for this task.
2	-	Due to the CT scanners low resolution, relative to the intricacy of human tissue, the data appears noisy. A median filter was used in an attempt to remove some of the noise. The neighbourhood radius of the median filter was three voxels in all dimensions.
3	R1	The images were then segmented by means of thresholding. That is, any voxels which had a Hounsfield value above 150, were selected in the resultant mask (A 3D representation of this mask is shown in Figure 60(A)).
4	R2	*R1* did not have a smooth exterior surface. As a result, the mask underwent an eroding procedure, in which the mask had the outermost layer of voxels removed. This process is repeated three times. The mask was then dilated, in which a layer of voxels was added to the exterior surface. This process again, was repeated three times.
5	R3	*R2* was then dilated by three voxels (2.5 mm).
6	R4	A hollow shell, with a wall thickness of 2.5 mm, was created by subtracting *R2* from *R3*.
7	R5	Because the dilation procedure in *step 5* adds voxels to the model in all three dimensions, caps were added to the top and bottom of the aortic root, which should be open. These caps were manually removed in this step.
8	-	The aortic root was then meshed in ScanIP with 336,562 linear tetrahedral elements.

Table 13. Procedure for extracting a volumised aortic root model from medical CT data.

The leaflets were partially visible in the CT scans and can be seen in Figure 59, appearing as a three armed star in the centre of the aortic root. The leaflets were manually segmented from the CT data, that is, the voxels that were included in the masks were manually chosen. The leaflets were meshed within ScanIP, producing a total of 95,024 linear tetrahedral elements. The leaflets were attached to the aortic root within Abaqus CAE by means of tie constraints, as shown in Figure 66.

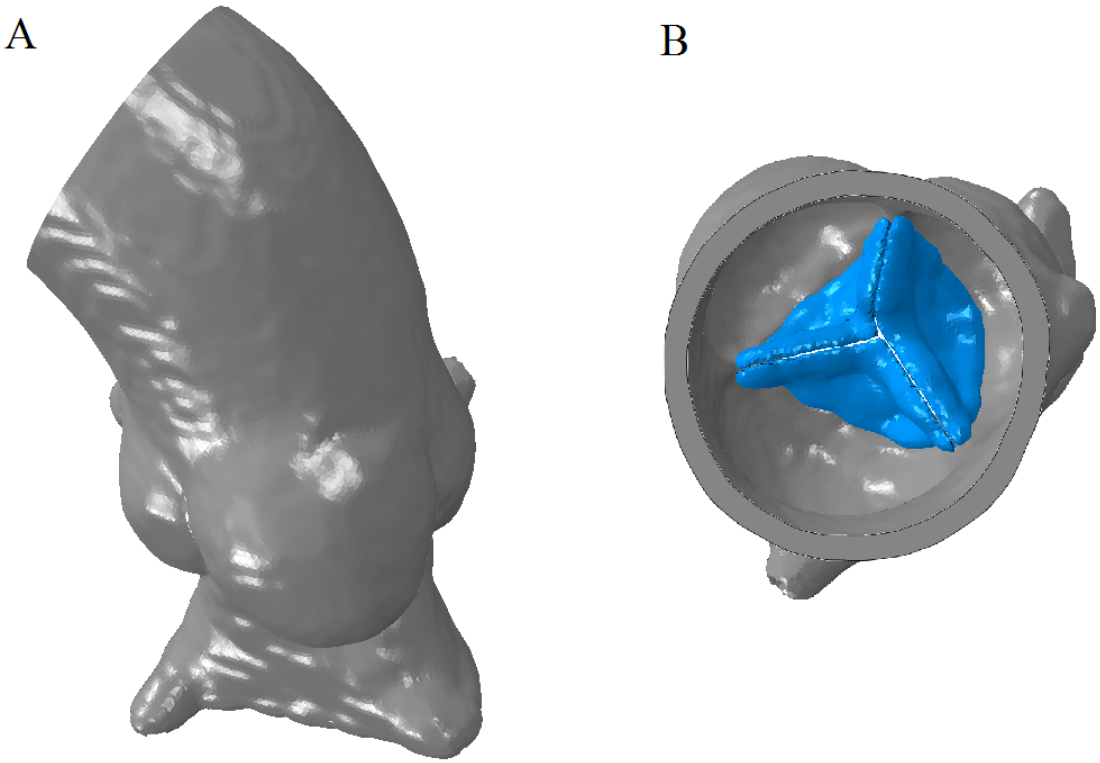

Figure 66. The aortic root model.

Because the leaflets in this model were manually segmented, the geometric accuracy of the leaflets is questionable. In addition to human error the leaflets were not fully visible and had to have holes within them patched. The aortic root and aorta also have a uniform thickness, which is not representative of the natural tissue. Furthermore, the plaques were missing from the model. Due to inaccuracies in the model, its application is limited. However, the model was still used for preliminary simulations described in section 7.1, in which the material properties implemented to the aortic root and its leaflets are summarised in Table 14 (Azadani et al. 2012, Mohammadi, Bahramian, and Wan 2009).

	Aortic root wall	Native aortic leaflets
Elastic Modulus	2 MPa	3.3 MPa
Poisson's Ratio	0.45	0.3
Mass Density	1.1 g/cm^3	1.1 g/cm^3
Rayleigh Damping Factor α Coefficient	2000	2000

Table 14. Material properties applied to the aortic root model.

6.4 Second Patient-specific CT Derived Model

A second CT data set of an 83 year old male was acquired from UHST (pictured in Figure 67). The radio-opaque dye dosage was sufficiently low to allow identification of the stenotic plaques and leaflets, while still being high enough to allow easy identification of the aortic root lumen.

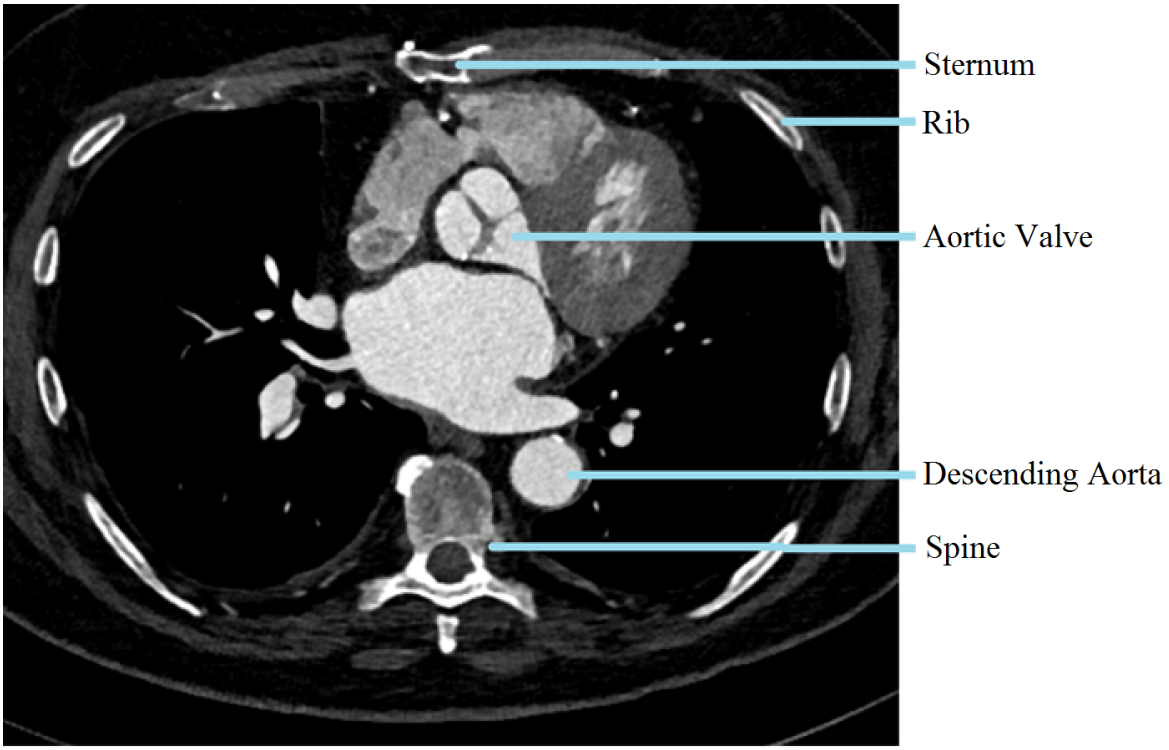

Figure 67. Medical CT image of a human torso. The aortic valve with its leaflet is visible in the centre. Plaques can be seen attached to the leaflets and appear as bright white dots.

The data was segmented such that the aortic root wall, plaques and leaflets were individually segmented in ScanIP before being meshed and exported to Abaqus CAE. The data was cropped to the smaller region that included the aortic root, in order to decrease computational time. A 3D render

of the cropped data is shown in Figure 68. Each voxel in this case is not a cube, rather the voxel dimensions are 0.65 × 0.65 × 0.75 mm with the longest axis being parallel to the patient's spine.

The plaques were segmented from the data using the method shown in Table 15.

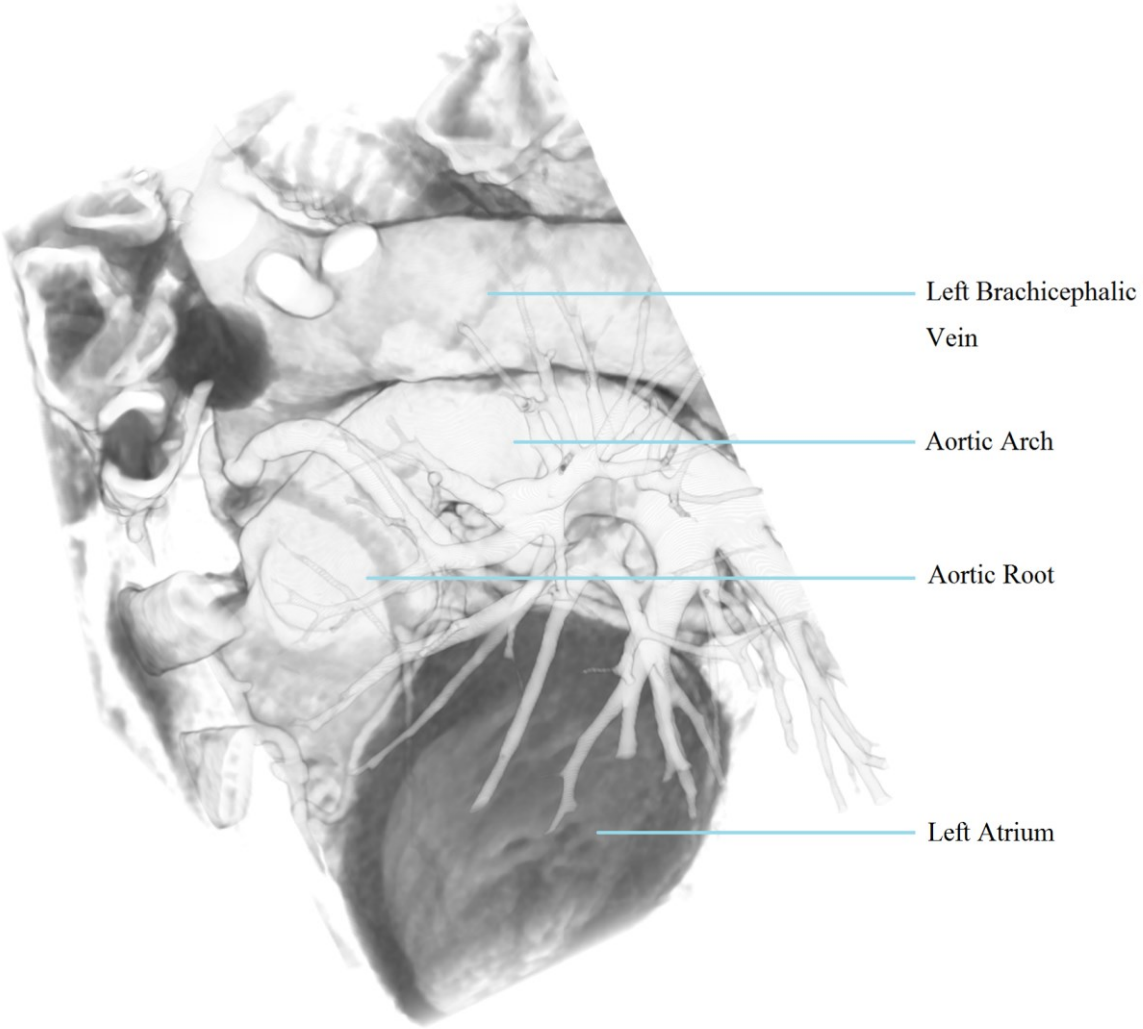

Figure 68. 3D render of a medical CT scan of a human heart. The left brachiocephalic vein, aortic arch, aortic root and left atrial are labelled. Furthermore, the branch like structure in the centre of the image is the cardiovascular system of the left lung.

Step	Mask	Description	Figure
1	P1	All voxels inside the aortic root and aorta, with a HU value greater than 450 were segmented.	69(B)
2	P2	An island removal algorithm was used to remove all plaques smaller than 20 voxels from *P1*.	69(C)
3	P3	The remaining islands that were not in contact with the aortic root wall and leaflets were removed.	69(D)
4	P4	A recursive Gaussian algorithm was used to smooth the geometry (Gaussian sigma value of 0.8 voxels was used).	69(E)

Table 15. Procedure for extracting a calcified plaque model from medical CT data.

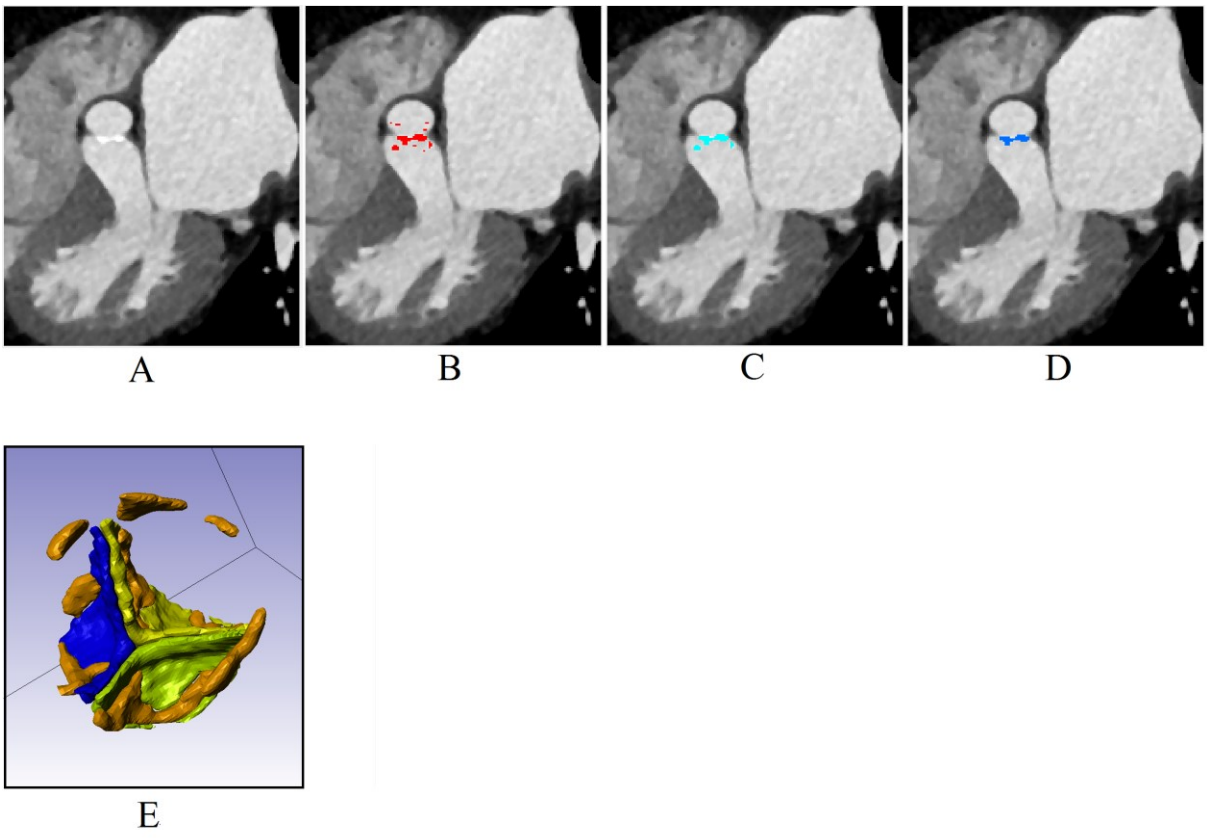

Figure 69. Medical CT images that have masks highlighted: No mask highlighted (A), Mask P1 (B), Mask P2 (C), Mask P3 (D) and Mask P4 with the leaflets (Mask L12) for context (E).

Unlike the plaques, the actual tissue that comprises the aortic root wall is not visible in the scan, rather the lumen of the vessel. As a result, the wall thickness was digitally added by dilating the masks using ScanIP. However, masks can only be dilated by whole voxels and, as a result, the wall

thickness must be divisible by the voxel size in the respective dimensions (0.65 × 0.65 × 0.75 mm). The aortic annulus of the patient is non-circular: the largest width was 22 mm, while the shortest width was 19 mm. As this is too small for a 26 mm TAVI device, the aortic root was scaled in size by a factor of 1.15, increasing the longest and shortest lengths to 25.3 mm and 22 mm respectively. This increase in size must be taken into account when the data is segmented, and the aortic root wall generated. Measured wall thicknesses of the sinuses and aorta are shown in Table 16 (Grande et al. 1998, Li et al. 2004), along with the number of voxels used to represent these thicknesses and the computational wall thickness before and after scaling.

Wall thickness location	Measured	Number of voxels	Initial model thickness	Scaled model thickness
Aortic sinuses	0.6-1.977 mm	2	1.3 mm	1.495 mm
Aorta	2.32 mm avg, 3.85 mm max	5	3.25 mm	3.73 mm

Table 16. Aortic root wall thicknesses.

Aortic wall thickness can vary considerably between individuals and tends to increase with age (Li et al. 2004). The scaled aortic wall thickness of 3.73 mm is towards the high end of measured data. In order to avoid a large step in wall thickness between the aortic wall and sinuses, the aortic wall was increased in thickness in two steps. The sinus thickness was 1.495 mm, which is also close to the upper end of the measured values.

The aortic root wall segmentation and modelling process had two distinct steps:

1) Segmentation of the interior of the aortic root.
2) Boolean operations upon the masks from *step 1*.

Step 1 is described in Table 17, and graphically shown in Figure 70 and *Step 2* is tabulated in Table 18 and visualised in Figure 71.

Finally, the leaflets were segmented through the steps shown in both Table 19 and Figure 72.

Mask	Description	Figure
R1	A thresholded floodfill function was used to select the interior of the aortic root. All voxels greater than 300 HU were selected that were connected to the initial point by voxels with a HU value above 300. The initial points were in the centre of the aorta, and in the centre of the left ventricle.	70(B)
R2	The left atrium and ventricle were included in *R1*. The mask volume that represents the left atrial was manually disconnected from the aortic root *R1*.	70(C)
R3	The aortic root mask was selected, and then separated from *R2* by using a floodfill algorithm with an initial point inside the aortic root.	70(D-F)
R4	The leaflets were not selected in the segment as the leaflets had a HU value below 300. The leaflets were manually selected and combined with *R3*	70(G-I)
R5	The Mask volume representing the left ventricle was then manually removed from the aortic root volume in *R4*.	70(J)
R6	The coronary and subclavian arteries were only partially included in *R5*. An area specific thesholding (using a limit of 250-1000 HU) technique was used to incorporate the lumen of these arteries with *R5*.	70(L)

Table 17. Initial step of the procedure used to extract an aortic root model from medical CT data.

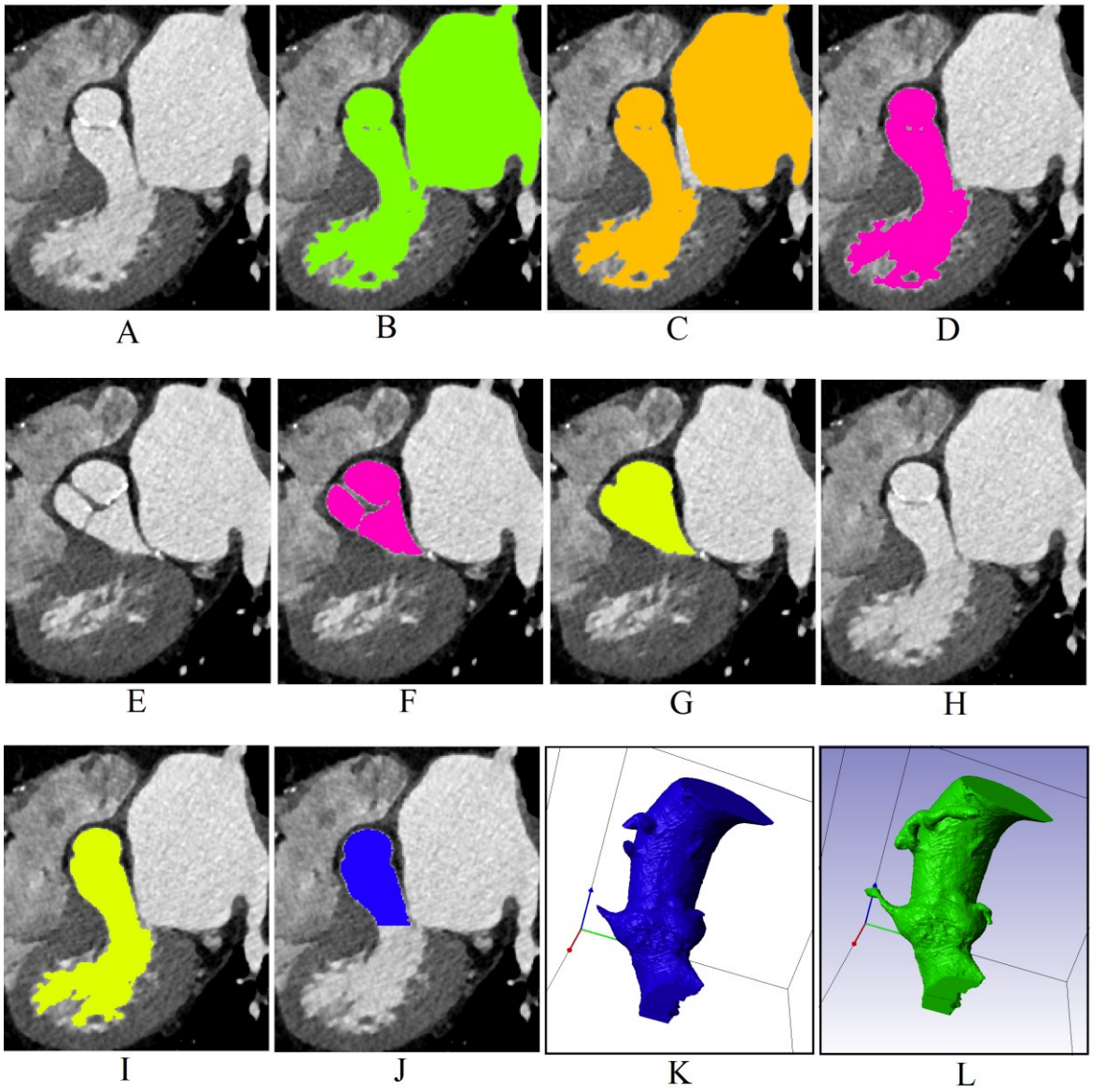

Figure 70. Medical CT images with the following masks highlighted: No mask (A), Mask R1 (B), Mask R2 (C), Mask R3 (D), No mask (E), Mask R4 (F), Mask R4 (G), No mask (H), Mask R4 (I), Mask R5 (J), 3D render of Mask R5 (K) and Mask R6 (L).

Mask	Description	Figure
R7	The aorta was completely removed from *R6* leaving the aortic root, upper left ventricle and coronary arteries.	71(A)
R8	The coronary and subclavian arteries were partially visible in *R5*, appearing as stumps protruding from the sinuses and aortic arch. These stumps were manually removed.	71(B)
R9	*R8* was dilated by three voxels (1.95 mm) to create *R9*.	71(C)
R10	*R6* was dilated by two voxels (1.3 mm) to create *R10*.	71(D)
R11	The aorta was completely removed from *R10* leaving just the aortic root, upper left ventricle and coronary arteries.	71(E)
R12	*R12* was created by combining *R11* and *R9*. The resultant was an aortic root, coronary arteries and upper left ventricle which have been dilated by two voxels (1.3 mm), while the aorta had been dilated by three voxels (1.95 mm).	71(F)
R13	This Mask was generated by subtracting *R7* and *R8* from *R12*. *R13* is therefore a hollow volume, with a wall thickness of 1.3 mm at the sinuses and 1.95 mm at the aortic root. The interior profile was that of *R8*: the profile of the aortic root lumen.	71(G)
R14	*R13* was a closed volume, the top and bottom had to be removed manually, before it resembles a tube.	71(H)
R15	*R8* was eroded by two voxels to create *R15*.	71(I)
R16	*R16* was based on *R8* after having *R15* removed from it, as well as the sinuses, all the tissue below the sinuses, and part of the ascending aorta. The resultant was part of the aorta with a wall thickness of 2 voxels (1.3 mm).	71(J)
R17	*R17* was created by adding *R16* to *R14*. The resultant was an aortic root model, in which the aortic sinuses (and lower aortic root) had a wall thickness of two voxels (1.3 mm), and an aorta that increases in wall thickness from four voxels to six voxels (2.6 mm and 3.25 mm respectively).	71(K)
R18	A recursive Gaussian algorithm was used to smooth the geometry of *R17* (Gaussian sigma value of 1 voxels was used) resulting in the final geometry, *R18*.	71(L)

Table 18. Second step, the procedure used to extract an aortic root model from medical CT data.

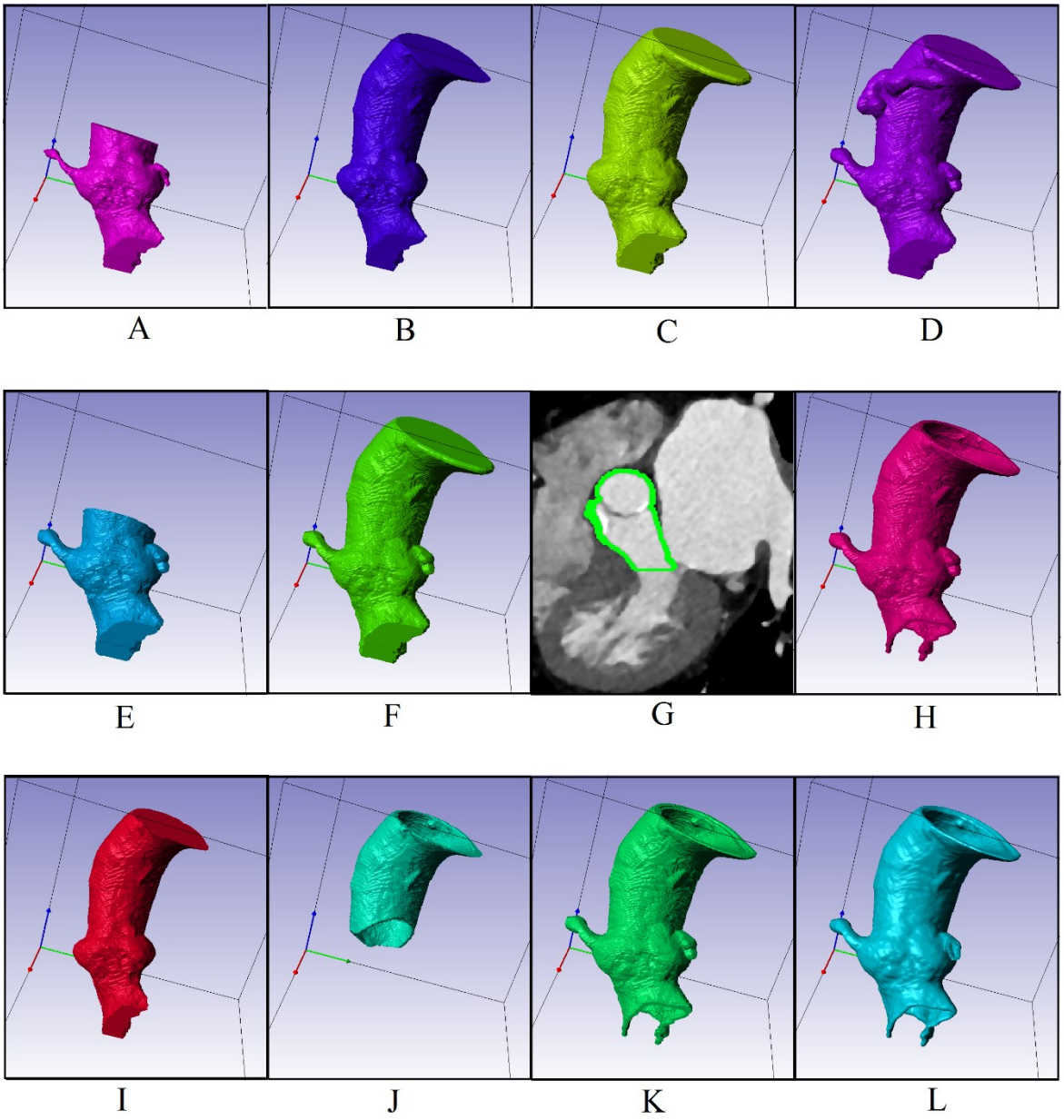

Figure 71. 3D renders of the following masks: Mask R7 (A), Mask R8 (B), Mask R9 (C), Mask R10 (D), Mask R11 (E), Mask R12 (F), Mask R13 (G, 2D image), Mask R14 (H), Mask R15 (I), Mask R16 (J), Mask R17 (K) and Mask R18 (L).

Mask	Description	Figure
L1	The initial segmentation was performed with a thresholding technique (between 0 HU and 330 HU) that was applied specifically to the aortic root.	72(B)
L2	An island removal algorithm removed all the islands that were less than 10 voxels in diameter from *L1*.	72(C)
L3	The plaques had left large holes in the leaflet soft tissue, this was reflected in *L2* which also had large holes, making it difficult to visualise. As a result the plaques from *P3* were combined with *L2*.	72(D)
L4	*L3* was dilated by one voxel (0.65 mm).	72(E)
L5	*L4* was then eroded by one voxel (0.65 mm). This process of dilation and erosion fills small cavities and smooths the geometry.	72(F)
L6	Larger cavities in *L5* had to be manually filled using a paint tool. The cavities often fell between the leaflets and *R18*.	72(G)
L7	There is some overlap between the leaflets and the aortic root due to the segmentation process. As a result, *L6* was created by subtracting *R18* from *L5*.	72(H)
L8	Some islands were created in *L7*, these were manually removed, creating *L8*.	72(I)
L9	The leaflet-root interface in *L8* had discontinuous surfaces between the components. This was manually repaired. There were also protrusions into the sinuses which were also manually removed.	72(J)
L10	*L10* was created by subtracting the plaques (*P3*), from the leaflets of *L9*.	72(K)
L11	The leaflets were still a single component at this point of the process, the three leaflets were manually separated to create *L12*.	72(M)
L12	Finally, the Leaflet geometry was smoothed using recursive Gaussian function (the Gaussian sigma value was set to 0.8 voxels).	72(N-O)

Table 19. Procedure for extracting a leaflet model from medical CT data.

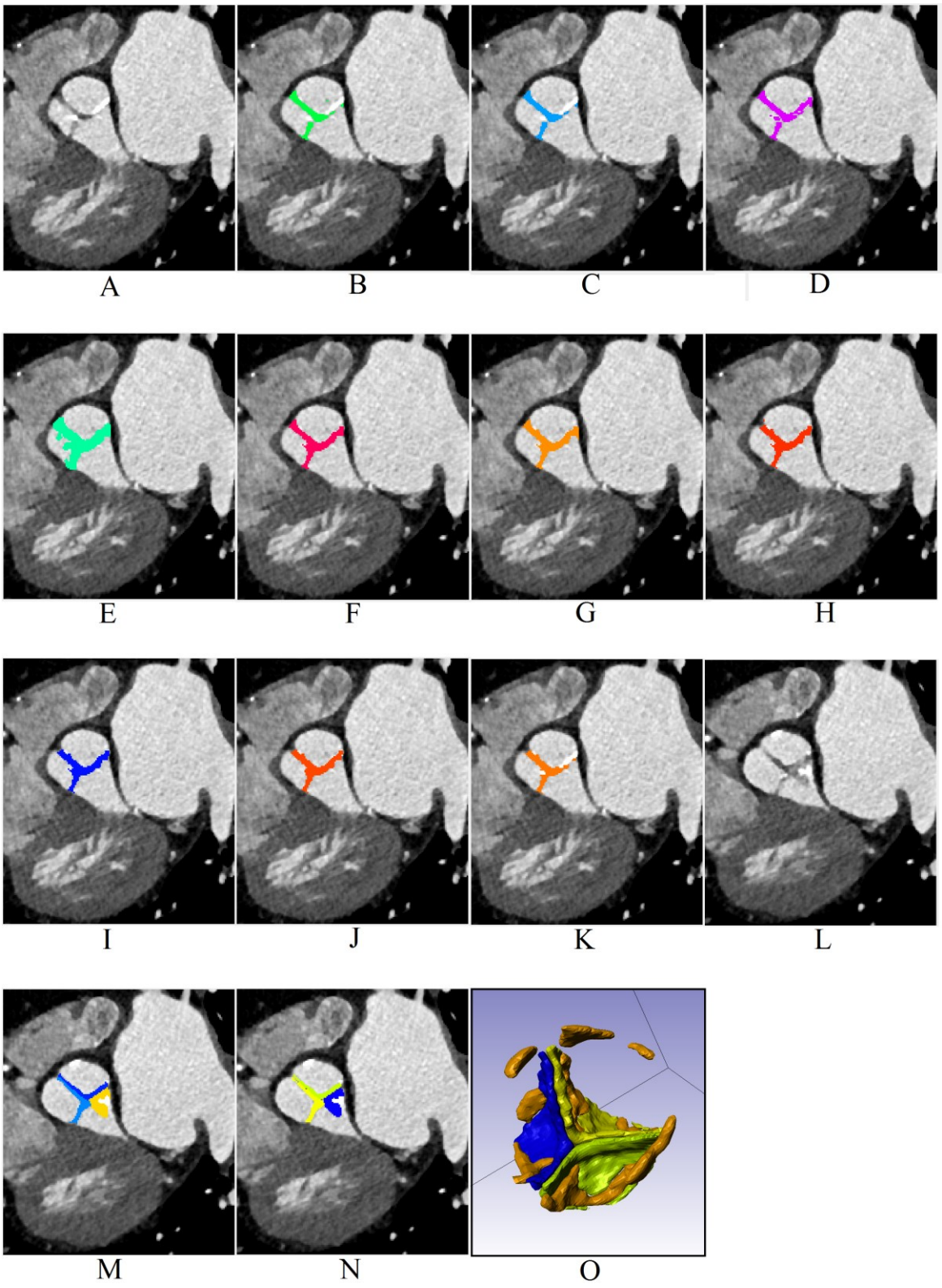

Figure 72. Medical CT images that have the following masks highlighted: No Mask (A), Mask L1 (B), Mask L2 (C), Mask L3 (D), Mask L4 (E), Mask L5 (F), Mask L6 (G), Mask L7 (H), Mask L8 (I), Mask L9 (J), Mask L10 (K), No Mask (L), Mask L11 (M), Mask L12 (N) and a 3D render of the leaflets (O, Mask L12, P4).

All the components were meshed within ScanIP before being exported to Abaqus CAE. The meshing parameters for the components are tabulated in Table 20. A total of eight plaques were extracted from the aortic root CT scan, the number of elements in each plaque were 1484, 2494, 1785, 871, 1253, 783, 1022 and 314, totalling 9692 linear tetrahedral elements. The aortic root wall was meshed with a total of 19426 linear tetrahedral elements. The three leaflets were each meshed with 6660, 6735 and 8743 elements, resulting in a total of 22,138 linear tetrahedral elements. The total model comprised 51,256 elements. The mesh resolution for each component was chosen such that the mesh had a good representation of the geometry, while also including steep mesh gradients in order to reduce the element count. Due to the difficulty of meshing the aortic root, and the complexity of the meshing parameters, there was no mesh refinement analysis performed.

Component	Aortic Root wall	Plaques and Leaflets
Minimum edge length (mm)	3	0.8
Maximum edge length (mm)	6	1
Maximum error (mm)	0.5	0.05
Surface change rate (1 = slow, 100 = fast)	50	65
Internal change rate (1 = slow, 100 = fast)	30	40
Maximum off surface distance (fraction of local edge length)	0.2	0.3
Element type	Linear tetrahedral	Linear tetrahedral

Table 20. Aortic root model meshing parameters.

The meshes were exported from ScanIP into Abaqus CAE, where each mesh was scaled by a factor of 1.15. The plaques were attached to the aortic root, or a specific leaflet, depending on location, by means of tie constraints. The leaflets were also attached to the aortic root, again through tie constrains. The complete assembly has superior detail to any other model seen in the literature and is shown in Figure 73.

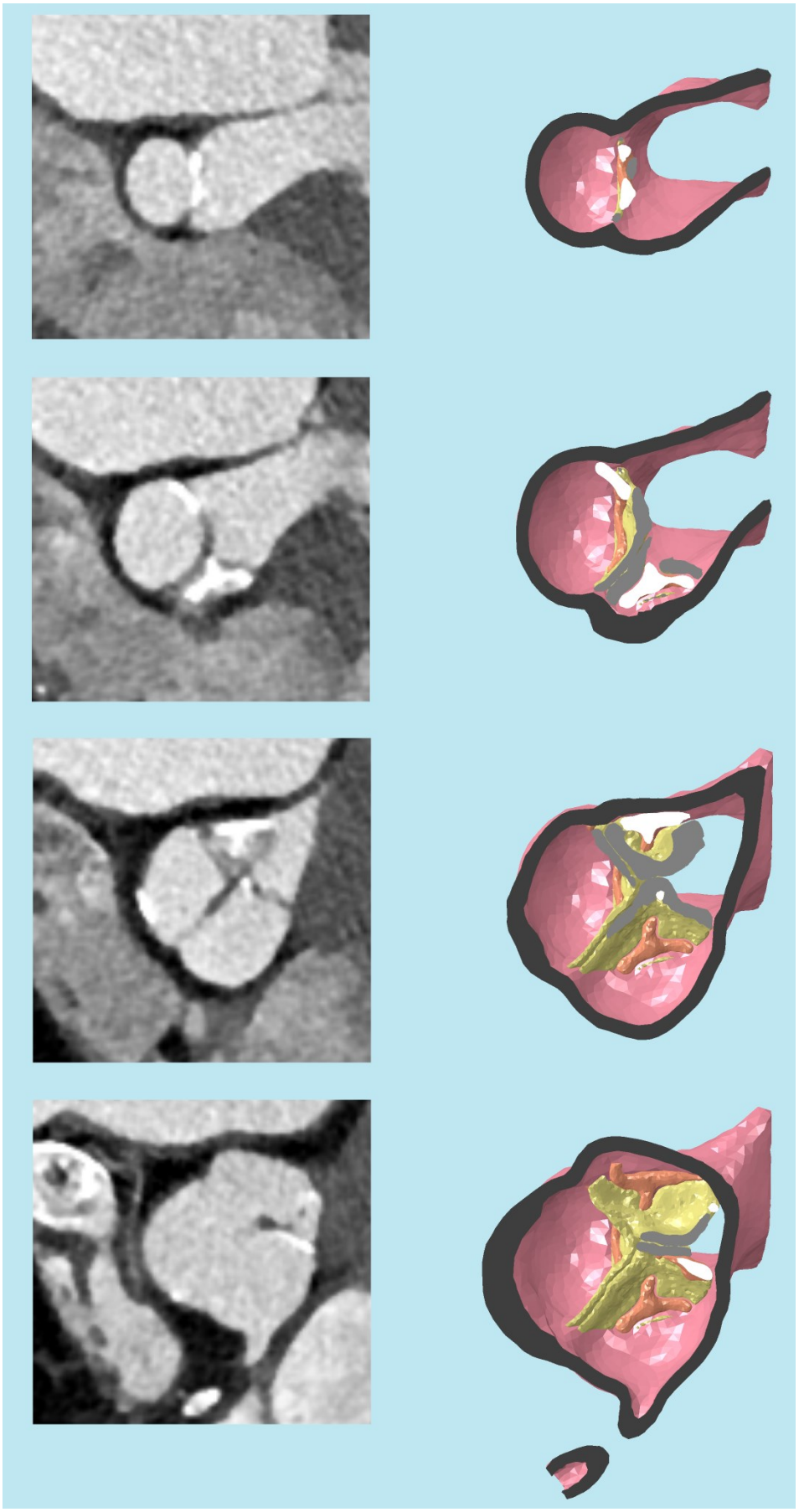

Figure 73. A comparison between medical CT scan images and the respective section of the aortic root model. The aortic root wall is seen in dark grey, the leaflets are light grey and the plaques are white.

As the geometric model advanced, so did the associated material model. The aorta, left ventricular outflow tract (LVOT), plaques, each sinus and each leaflet were all assigned individual material properties. The sinuses and leaflets are hyperelastic, anisotropic and inhomogeneous. In this study, however, the material properties were assumed to be isotropic, homogeneous and hyperelastic. The actual material properties are almost orthotropic and since the in-plane material behaviour is the most influential for this study, an isotropic assumption is not considered to be an extreme simplification (Gundiah et al. 2008).

The material model used in this thesis is nearly incompressible and hyperelastic. It was based on the experimental data determined through biaxial testing (for the case of the sinuses, the data is shown in Figure 74 (Martin, Pham, and Sun 2011).

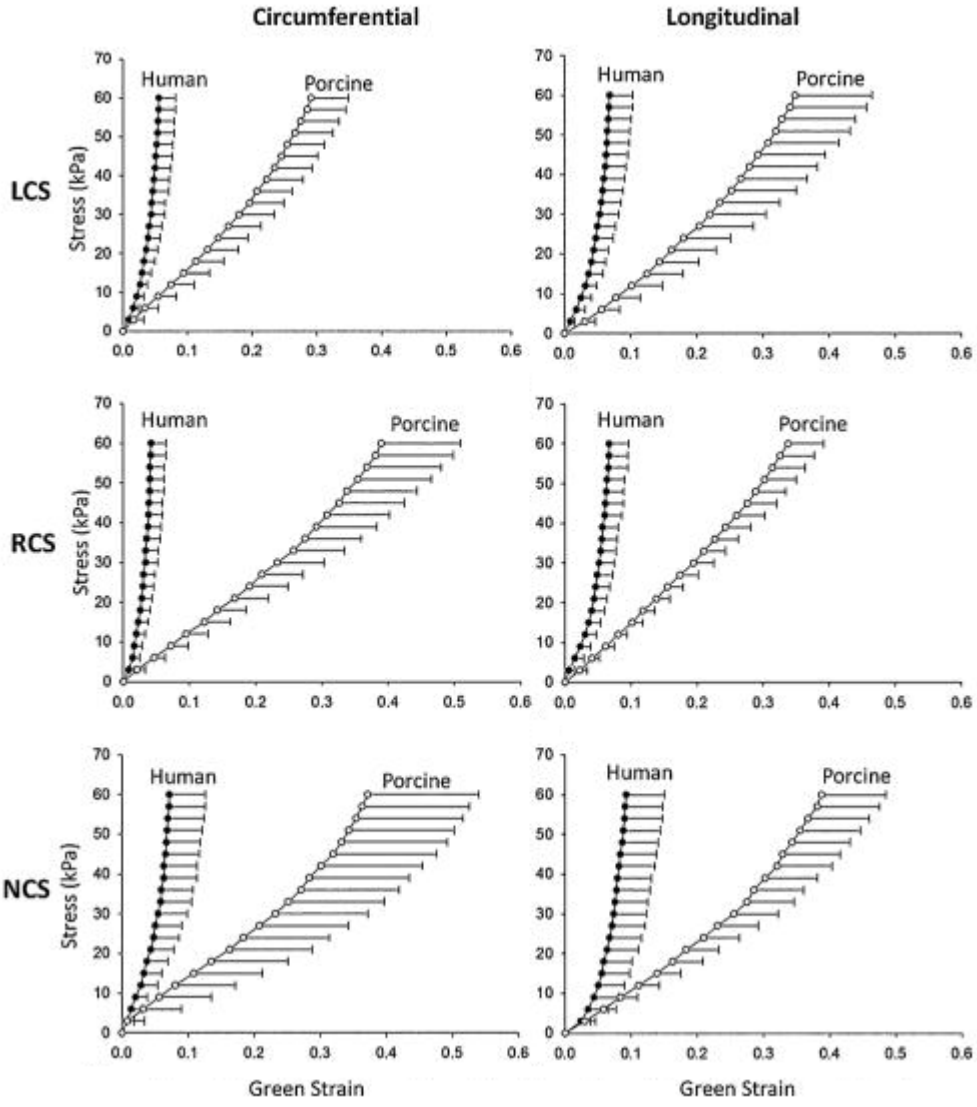

Figure 74. Biaxial experimental test data of human (closed dots) and porcine (open dots) left coronary sinus (LCS), right coronary sinus (RCS) and non-coronary sinus (NCS).

A nearly incompressible, reduced polynomial hyperelastic material model was then fitted to the biaxial data (Morganti et al. 2014, Auricchio, Ferrara, and Morganti 2012). The strain energy potential per unit volume for the reduced polynomial model is defined as:

$$U = \sum_{i=1}^{N} C_{i0}(\bar{I}_1 - 3)^i + \sum_{i=1}^{N} \frac{1}{D_i}(J^{el} - 1)^{2i} \quad [20]$$

where N is the polynomial order, C_{ij} and D_i are material parameters and $\bar{I}_1$ is the first deviatoric strain invariant defined as:

$$\bar{I}_1 = \bar{\lambda}_1^2 + \bar{\lambda}_2^2 + \bar{\lambda}_3^2 \quad [21]$$

$\bar{\lambda}_i$ are the diviatoric stretches given by:

$$\bar{\lambda}_i = J^{-\frac{1}{3}} \quad [22]$$

J is the total volume ratio, J^{el} is the elastic volume ratio and λ_i are the principal stretches. The initial shear modulus (μ_0) and bulk modulus (K_0) are defined as:

$$\mu_0 = 2C_{10} \quad [23]$$

$$K_0 = \frac{2}{D_1} \quad [24]$$

The tissue is assumed to be nearly incompressible, with a Poisson's ratio of 0.475, as defined by:

$$\nu = \frac{3K_0 - 2\mu_0}{6K_0 + 2\mu_0} \quad [25]$$

In this case N = 6, and the values of C_{i0} are shown in Table 21. The density of the sinuses and leaflets were assumed to be constant and equal to 1.1 g/cm^3, the Rayleigh alpha damping factor was equal to 800 (Morganti et al. 2014, Simulia 2014d).

Region	C_{10}	C_{20}	C_{30}	C_{40}	C_{50}	C_{60}
Sinus						
Left-coronary	23.29	624.4	1980	201.5	22.15	29.11
Non-coronary	18.35	190.9	1220	1040	629.7	1580
Right-coronary	22.44	959.9	2580	1190	1360	205.3
Leaflet						
Left-coronary	23.46	1010	2110	607.8	674.3	679.9
Non-coronary	18.01	1690	1950	994.1	1490	301.5
Right-coronary	0.11	758.2	941	895.7	1040	752.8

Table 21 Yeoh parameters (kPa) for various tissue sections within the aortic root (Morganti et al. 2014).

Aortic plaques are difficult to model as the composition is an irregular matrix of fibrous soft tissue and calcified masses. The plaques are thought to be highly nonlinear, anisotropic and inhomogeneous. The composition and matrix structure within each plaque determines the material properties, but is very much unique to each plaque. Accurately modelling the plaques would require mechanical testing, which is not possible within this study. Despite the complex material properties of the plaques, during device deployment, the plaque behaviour is relatively simple in that it tends to behave as a large, rigid and near unmovable mass. Capturing this behaviour is achievable with a linear elastic model as defined in Table 22 (Morganti et al. 2014, Wang et al. 2014).

It was assumed that the material properties associated with the aorta LVOT have a negligible effect on the simulation, as the TAVI device predominantly interacts with the sinuses and leaflets of the aortic valve. It was therefore decided that a simple linear elastic model was sufficient for modelling the aorta and LVOT, the parameters for which are shown in Table 22 (Xiong et al. 2010).

In many of the simulations friction is neglected, as a result low damping was applied to the aortic root in order to dissipate some of the energy within the tissue.

Material property	Plaques	Aorta and LVOT
Elastic modulus	12.6 MPa	2 MPa
Poisson's ratio	0.35	0.45
Density	2 g/cm^3	1.1 g/cm^3
Rayleigh damping α coefficient	-	800

Table 22. Material properties applied to the plaques, aorta and LVOT.

This model is superior to the earlier attempts to generate patient-specific models (see sections 6.1, 6.2, 6.3) as it features a realistic aortic wall thickness, plaques and leaflets. Although the level of detail is inferior to the μCT scan, the number of elements in the model is dramatically lower (1,834,471 elements in the μCT model versus 51,256 elements in this patient-specific model), allowing for deployment simulations to be completed in a practical length of time. Furthermore, the hyperelastic material models featured in this aortic root model offer superior representation of the native tissue to which they are based. The aortic root tissue material properties are inconsistent throughout the geometry, this is captured in this aortic root model by applying different material properties to each group of tissue. Due to the advantages of this model, it was used for the majority of simulations described in this thesis.

6.5 Summary

Four aortic root computational models were produced and described in this chapter.

The first aortic root model was based on medical CT data, it comprised of an aortic root wall which was assumed to be a shell. As this model lacked native leaflets and plaques a second model was pursued. In order to ensure the second model had superior detail, it was based on a μCT scan of a cadaver heart. The μCT model included a high level of detail, however it was not patient specific and was extremely computationally demanding to simulate. As a result, a third model was produced that was based on the same medical data as the first model. Much of the model generation procedure was the same. However this improved model featured a volumised aortic root wall and native leaflets. The third model was used for preliminary work in section 7.1.

The Final model presented in this chapter was based on a second set of patient medical CT data. It includes an aortic root wall with inconsistent thickness, native leaflets and plaques. As of yet no other aortic root model seen in the literature has such a high level of detail. Each sinus and leaflet was assigned an individual hyperelastic material property found through experimental analysis (Morganti et al. 2014).

Chapter 7: Application of Patient-Specific Deployment Simulations

The first computational simulation of TAVI was published in early 2012 (Capelli et al. 2012); a TAVI device frame was deployed by means of balloon inflation into a series of patient-specific aortic root models that featured SVR prosthetic valves. The objective of the research was to identify areas of the aortic root which may rupture. Since these early simulations, aortic root models have improved by including a volumised wall, native leaflets and plaques. Also, the material properties have advanced from linear elastic to hyperelastic. With these additional features, it has become increasingly possible to accurately predict the likelihood of paravalvular aortic regurgitation and embolisation. This chapter focuses on the application of computational patient-specific procedural prediction.

7.1 Requirements of a Full Device Model for Paravalvular Aortic Regurgitation Analysis

To the Authors knowledge, as of yet all TAVI deployment simulations presented in the literature have neglected the leaflets. Since PAR is entirely dependent on the frame's position relative to the native tissue about it, the leaflets do not have to be included, provided that the leaflets have a negligible effect on the frame's final position during deployment. In order to test this hypothesis and potentially reduce the number of components required for individual simulations which, in turn, decreases computational time, the impact of including leaflets and other components of the TAVI device in deployment simulations was explored.

7.1.1 Methods

A deployment simulation of the SAPIEN XT computational model (section 5.6) undergoing deployment by means of the NovaFlex+ delivery system (section 5.7) into a native aortic root (section 6.3) was constructed. The delivery balloon was positioned in a transapical deployment orientation within the native aortic root model, such that the centre of the balloon passed through the centre of the valve, and no part of the delivery system was in contact with the aortic root model. The SAPIEN XT was positioned such that it was concentric with the balloon. The device was aligned with the native aortic root and the centre of the balloon (see Figure 75(B)).

Multiple simulations were performed each with different components present in the SAPIEN XT model. The simulations and components present in each case are summarised in Table 23.

Simulation\Component	Frame	Cuff	Clips	Leaflets
Simulation_1	Included	Included	Included	Included
Simulation_2	Included	Included	Included	-
Simulation_3	Included	Included	-	-
Simulation_4	Included	-	-	-

Table 23. Components included in each simulation.

The contact definitions within the simulations were defined as *hard* (normal behaviour) and frictionless (tangential behaviour). Contact definitions were defined between specific parts within the model. The contact definition pairings for Simulation_1 are presented in Table 24.

Contact pair\step	Step 1	Step 2	Step3	Step 4
Balloon – Balloon	Active	Active	Active	Active
Balloon – Wire	Active	Active	Active	Active
Balloon – Frame	Active	Active	Active	Active
Balloon – Native Leaflets	-	Active	Active	Active
Balloon – Aortic Root	Active	Active	Active	Active
Device Leaflets – Device Leaflets	Active	Active	Active	Active
Frame – Frame	Active	Active	Active	Active
Frame – Device Leaflets	Active	Active	Active	Active
Native Leaflet – Device Leaflet	Active	Active	Active	Active
Aortic Root – Frame	-	Active	Active	Active
Aortic Root – Device Leaflet	Active	Active	Active	Active
Crimping Surface - Frame	Active	-	-	-
Frame – Device Leaflets	-	Active	Active	Active

Table 24. Contact pairs throughout the deployment simulation.

The SAPIEN XT model must first be crimped before deployment. This was achieved using an additional cylindrical surface (visible in Figure 75(A)) that is concentric with the frame. A displacement boundary condition was used to radially contract this surface and crimp the device.

During TAVI the diameter of the balloon is controlled by inflating the balloon by a specific volume. In the simulation, the volume of the balloon is unknown, as a result a specific pressure must be used to inflate the balloon. It was found that 300 kPa was a sufficient pressure to inflate the balloon and deploy the device. Since the balloon reaches full diameter with the TAVI device around it, increasing the pressure would only over expand the device. Increasing the pressure would however increase the amount of energy within the simulation, which would require additional iterations to solve.

The deployment simulation involved a four step procedure:

Step 1: The TAVI device was crimped by means of the cylindrical surface. Displacement boundary conditions reduced the diameter of the cylinder to 10 mm, thus reducing the diameter of the frame to 10 mm at its widest point (Figure 75(A-C)). Simultaneously, a 30 kPa pressure load was applied to the underside of the native aortic leaflets in order to open the native valve. As the valve was constructed in the closed position, it must be opened in order to avoid volumetric intersection with the TAVI and deployment devices (Figure 75(D-E)). This step was modelled over a 0.03 second time step.

Step 2: The contact definition between the crimping surface and the frame was removed, and the frame elastically recoiled. The contact definitions between the native leaflets and medical device were implemented, as well as the pressure load applied to the leaflets deactivated. The native aortic leaflets also recoiled during this step (0.01 seconds) and is shown in Figure 75(F-G).

Step 3: An internal pressure was applied to the balloon of magnitude 300 kPa over a time period of 0.1 seconds, which fully inflated the balloon. The loading profile was not linear, rather a smooth step. This is shown in Figure 75(G-I).

Step 4: The internal pressure of the balloon was decreased with a smooth step over a time period of 0.02 seconds. The balloon returned to its original position through elastic recoil and, furthermore, the TAVI frame recoiled slightly and the leaflets adopted a natural open position. This is shown in Figure 75(I-J).

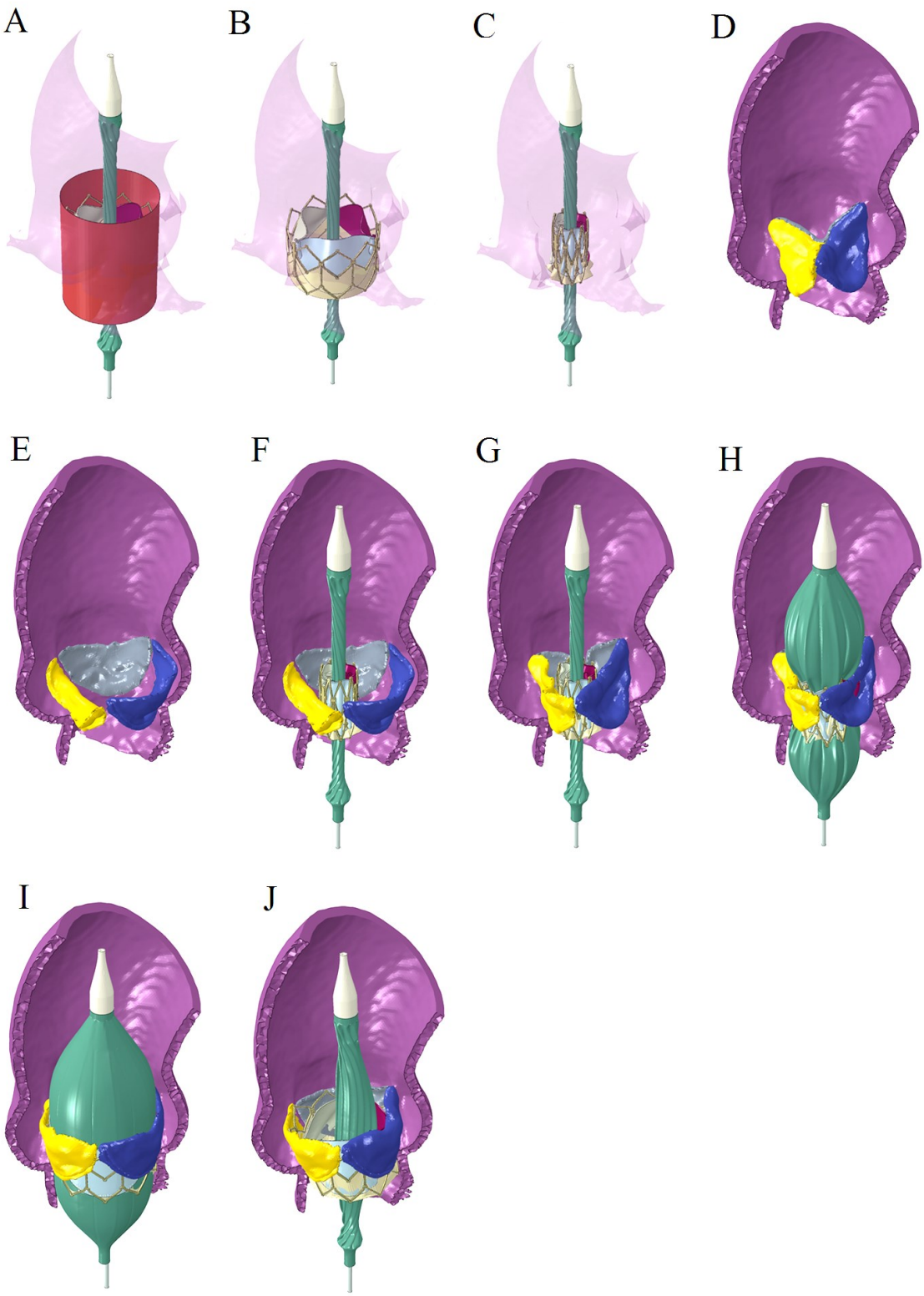

Figure 75. Full device simulation. The full TAVI device being crimped about the balloon with the aortic root wall (ghosted) and the crimping surface (A, only) present (A-C). The native aortic root leaflets opening under a pressure load with the aortic root wall (D-E, section removed). The native leaflets and TAVI devices relaxing during step 2, with the aortic root wall (F-G section removed). The delivery system deploying the full TAVI device into the aortic root model (section removed from the aortic root wall), before relaxing (G-J).

7.1.2 Results

Simulation_1 contained 2,192,247 elements and was run across sixteen domains on dual 2.4 GHz Intel Xeon E5-4640 CPUs in 131 hours. Small discrepancies between frame positions were evident when the post-deployment frames from each simulation were superimposed (Figure 76).

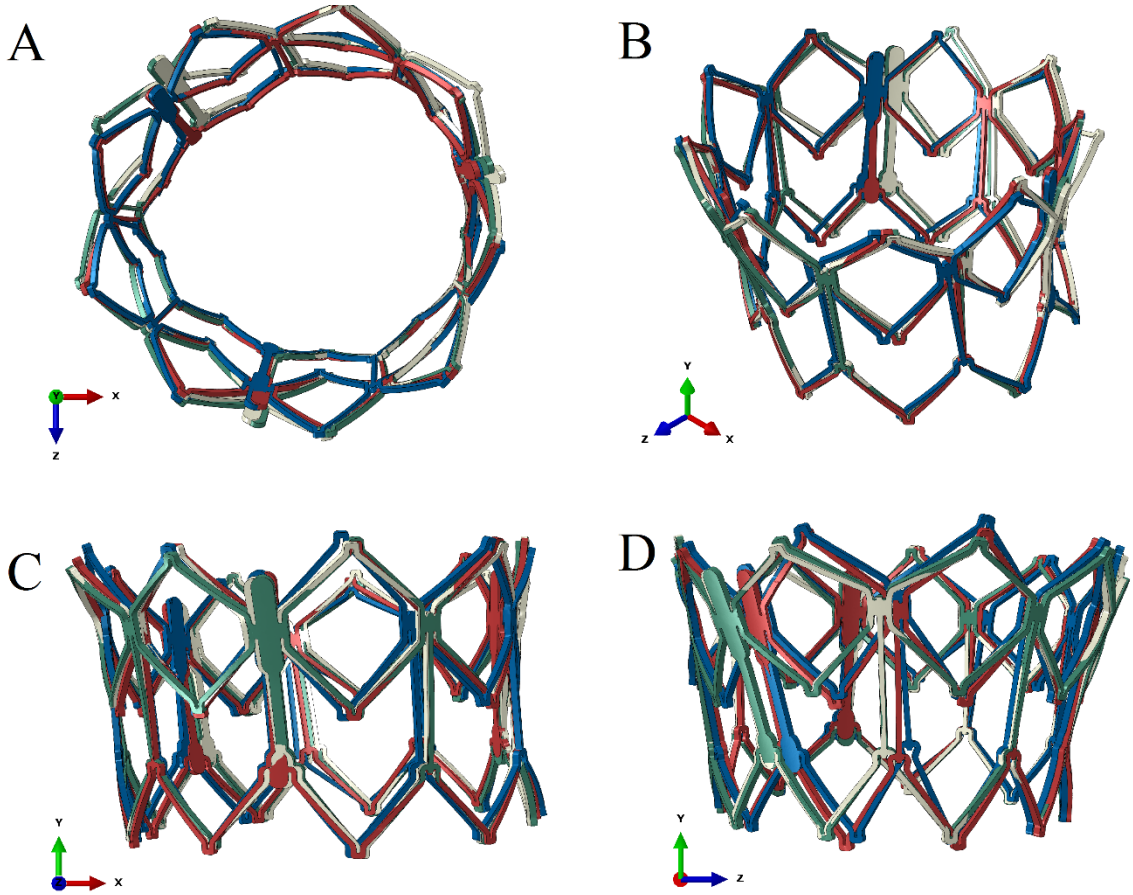

Figure 76. Post-deployment frame position for simulation_1 (green), simulation_2 (white), simulation_3 (red) and simulation_4 (blue).

To quantify the discrepancy in frame position, the average nodal position of each frame was calculated and then compared. The average nodal position discrepancies (ANPD) are shown in Table 24.

	Simulation_1	Simulation_2	Simulation_3	Simulation_4
Simulation_1	-	0.0613 mm	0.0343 mm	0.228 mm
Simulation_2	0.0613 mm	-	0.0956 mm	0.167 mm
Simulation_3	0.0343 mm	0.0956 mm	-	0.263 mm
Simulation_4	0.228 mm	0.167 mm	0.263 mm	-

Table 25. Average nodal position discrepancies between the four simulations.

7.1.3 Discussion

Figure 76 shows the four frames from each simulation superimposed. The frames from Simulation_1 and Simulation_2 are visually very similar. The similarity between the two frames is further demonstrated by the ANPD being 0.0613 mm. This demonstrates that the inclusion of the leaflets for the deployment simulation has a minimal effect on the post-deployment position of the frame.

Although each frame is in a slightly different position, there is a noticeable discrepancy related to the constraint applied to the clips to construct the model. Coupling constraints were applied to the clips, which are completely rigid, where as in reality, the clips are stitched to the frame, resulting in a flexible structure. Inclusion of the clips resulted in an ANPD of 0.0956 mm.

Similar to Simulation_1 and Simulation_2, Simulation_3 and Simulation_4 are visually similar in Figure 76. Counterintuitively, the ANPD between Simulation_3 and Simulation_4 was found to be 0.263 mm. This suggests that the cuff has a larger impact on the frame's final position than the leaflets.

It was found that the leaflets and cuff can become unstable if severely distorted. As a result, the device was crimped down to 10 mm in diameter, as opposed to the reality in which the device is crimped down to 8 mm. A TAVI device represented by the frame alone however, can be crimped to 8 mm. If the application of a simulated TAVI device requires it to be crimped to a more realistic deployment diameter, it may not be possible to feature the leaflets.

The primary limitation of this study is the aortic root model used for the analysis. The aortic root does not feature plaques, neither are the leaflets a reliable representation of the patient-specific case. As a result, it would be unsuitable in predicting PAR. However, for the purpose of comparing the frame positions it provides useful insight into this report of device detail.

A further limitation concerns leaflet material properties as they were assumed to be hyperelastic, isotropic and homogeneous. In reality, the leaflets are neither isotropic nor homogeneous and this is

likely to affect any computer simulations testing the leaflet functionality, as detailed by *Smuts et al. (2011).*

7.2 Balloon Pressure Analysis

During the previous simulations the pressure within the balloon was 0.3 MPa as it was found to be the approximate pressure required to fully deploy the device. During TAVI, the clinician fills the balloon with a specific volume of fluid; at which point, the balloon is known to have reached the correct diameter. As the volume of the balloon is not a control variable in the simulations presented in this thesis, the correct pressure to fully deploy the device must be calculated.

In order to calculate the correct pressure for deployment, the device was deployed into a computational model of an aortic root with a linearly increasing pressure in the balloon. The radius of the frame was measured and the pressure associated with full deployment was found. This simulation also offers further understanding into the correct pressure to accurately over-expand the device in post-deployment angioplasty, a common procedure used to treat PAR.

The pressure required to deploy the TAVI device is dependent on the aortic root model, a stiffer model will require a greater pressure. The simulations dependent on the balloon pressure calculated within this section use the final aortic root model (section 6.4), therefore the final aortic root model was used in this simulation also.

The TAVI device, and components used to represent the device are likely to alter the pressure required to achieve the target diameter. In section 7.3, both the SAPIEN XT, and SAPIEN 3 models, represented by just the frame and cuff, are deployed into the aortic root model. The balloon pressure for both of these cases must be calculated through simulation. In section 8.3, a complete SAPIEN XT model is deployed into an aortic root. The simulation must therefore be repeated again to calculate the deployment diameter of a full device. However, for the case of the complete TAVI device, the crimped diameter was 10 mm, as opposed to 8 mm, in order to retain stability.

The components of the simulation included the final aortic root model, in which the delivery system (section 5.7) was positioned in the transapical deployment orientation. The SAPIEN XT model (section 5.6) was concentric to the balloon, and in line with the native leaflets and balloon centre. Contact definitions applied to the model were defined as *hard* and frictionless. The simulation was a two step process:

Step 1: The frame was crimped with a cylindrical surface that decreased in diameter to 8 mm (with exception to the case of a full TAVI device that was crimped to 10 mm) over a time period of 0.02 seconds. Simultaneously, the native aortic root leaflets were forced open with a bullet shaped surface

that was displaced through the valve. In order to inhibit the native aortic root from migrating due to the leaflet being forced open, an additional boundary condition was applied to the lower edge of the native aortic root inhibiting all degrees of freedom, this boundary condition was only active in this step.

Step 2: At the beginning of this step, contact definition pairings were removed between the native leaflets and the bullet shaped surface, as were contact pairings between the frame and the crimping surface. Contact definition pairings were implemented between the TAVI device and the native valve. The internal pressure of the balloon was linearly increased from 0 to 0.5 MPa over a time period of 0.05 seconds.

The frame diameter was calculated using a node tracking procedure. All the nodes in the frame were tracked in a plane to which the axis of the device was normal. The magnitude of displacement of the nodes in this plane were assumed to be the radial displacement of the device from which the average device diameter was calculated. If the frame rotated during the deployment procedure however, this would be an inaccurate measure. It was found that the device can locally rotate, however the gross frame will not rotate until balloon deflation. The calculated frame diameters, with reference to the balloon pressure are shown in Figure 77.

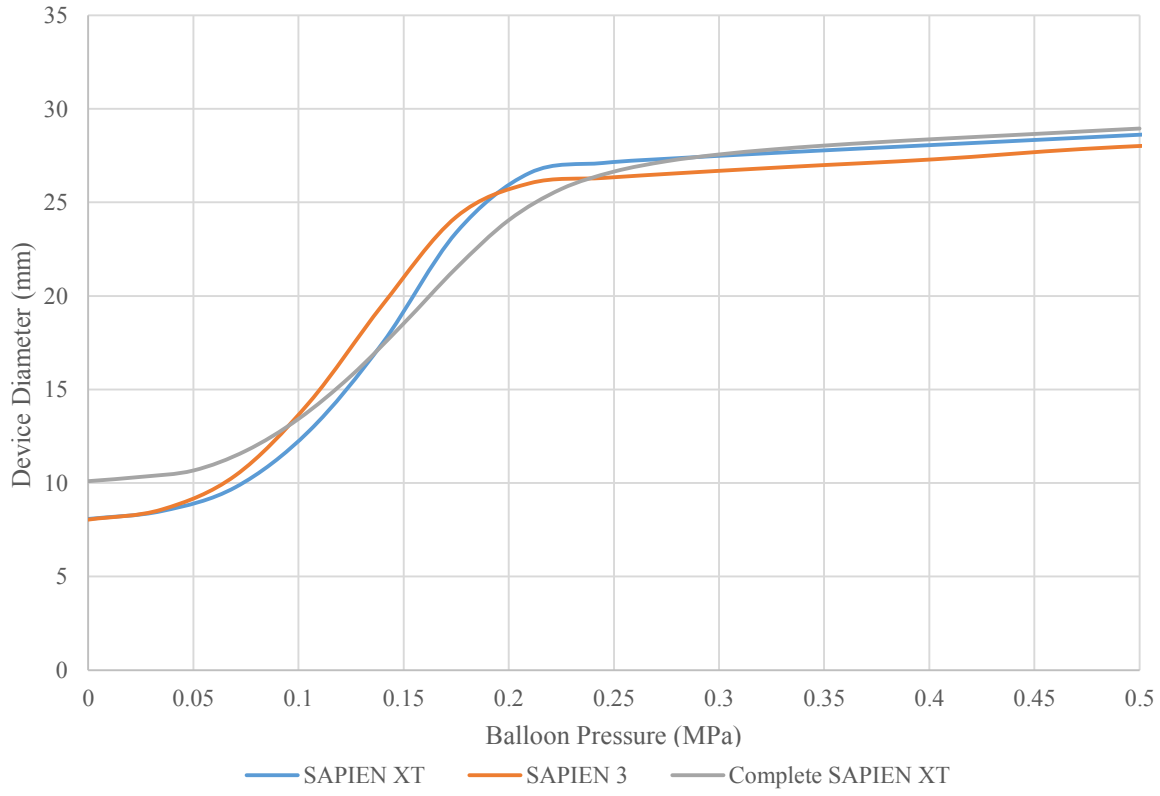

Figure 77. Expansion response to pressure of both a SAPIEN XT and SAPIEN 3 modelled as a frame and cuff, as well as a complete SAPIEN XT model.

The behaviour presented in Figure 77 shows the devices rapidly expanding until a diameter of approximately 26 mm, at which point the balloon has reached its full expansion. Beyond 26 mm, the balloon must also stretch in order to achieve greater diameters and as a result the rate of diameter increase is reduced.

This data was used to find the pressure required to expand the devices to the normal expansion diameter (26 mm) as well as two degrees of over-expansion (27 mm and 28 mm). The target diameters and relative pressures are summarised in Table 25.

Target Diameter	Pressure		
	SAPIEN XT	SAPIEN 3	Complete SAPIEN XT
26 mm	0.202 MPa	0.209 MPa	0.233 MPa
27 mm	0.236 MPa	0.351 MPa	0.266 MPa
28 mm	0.386 MPa	0.497 MPa	0.346 MPa

Table 26. Pressure required to achieve specific device target diameters.

7.3 Computational Aided Prediction of Paravalvular Aortic Regurgitation

PAR occurs when the TAVI device frame does not make an effective seal with the interior of the aortic root, therefore allowing blood to flow around the prosthetic valve. PAR has been linked to early mortality in TAVI patients. Reduction of the occurrence of PAR is an important area of research, and has significantly influenced device design. For instance the Edwards Lifesciences SAPIEN 3 features a unique cuff about the exterior of the valve which was introduced in order to create an effective seal against the interior of the aortic root. Alternatively, PAR could potentially be avoided if realistic simulation of device deployment could provide accurate prediction of PAR likelihood such that vulnerable patients could be identified and offered alternative treatment. Computational simulation can also be used to assess a novel devices resistance to PAR. In this section, an assessment is made of the capabilities to predict PAR using computational models. Furthermore, the ability of the SAPIEN XT to avoid PAR, with reference to the SAPIEN 3, will be explored.

7.3.1 Methods

In order to assess the ability of patient-specific computational simulation to predict PAR, a deployment simulation was constructed using the detailed patient-specific aortic root, featuring a non-uniform aortic root wall, calcified plaques and native leaflets (section 6.4). Both the SAPIEN XT and the SAPIEN 3 were deployed in separate simulations for comparison. Deployment was achieved through balloon expansion using a computational model of the NovaFlex+ delivery system (section 5.7). The devices were represented with the frame only as it was shown that the leaflets, clips and cuff had negligible impact on the final frame position post deployment.

Similarly to the procedure described in section 7.1, the balloon and devices were orientated for transapical deployment. The balloon was constrained at the upper free edge, as well as the lower free edge using boundary conditions to restrict motion. The contact between components was defined as *hard* normal behaviour and frictionless tangential behaviour. The contact pairings are shown in Table 26. The most common treatment for PAR is post deployment angioplasty with the intent of over expansion of the TAVI device. To represent the procedure, the TAVI device was deployed to the over-expanded state immediately, at pressures detailed in Table 27. This is unlikely to create inaccuracies as the device orientation relative to the native tissue did not change in either circumstance. The reason this method is used is because it is computationally more efficient. Two degrees of over-expansion were explored (as well as the standard target diameter of 26 mm): 27 mm and 28 mm.

As before, the native aortic valve was opened using a bullet shaped surface in order for the delivery system and TAVI device to fit. Also, the TAVI device was again crimped through means of a cylindrical surface that was contracted radially.

Contact Pairs\Step	Step 1	Step 2	Step 3
Balloon – Balloon	Active	Active	-
Balloon – Wire	Active	Active	-
Balloon – Frame	Active	Active	-
Balloon – Aortic Root	Active	Active	-
Native Leaflets – Native Leaflets	Active	Active	Active
Native Leaflets – Bullet Surface	Active	-	-
Native Leaflets – Aortic Root	Active	Active	Active
Crimping Surface – Frame	Active	-	-
Plaque – Native Leaflets	Active	Active	Active
Plaque – Aortic Root	Active	Active	Active
Frame – Frame	Active	Active	Active
Balloon – Native Leaflets	-	Active	-
Balloon - Plaques	-	Active	-
Frame - Plaques	-	Active	Active

Table 27. Contact pairs throughout the deployment simulation.

The simulation comprised three steps which are described below.

Step 1: In the first step the TAVI device was crimped to a diameter of 8 mm. Simultaneously, a bullet shaped surface was displaced through the native leaflets forcing them open. This step was modelled over a 0.02 second time step.

Step 2: At the beginning of this step, the contact definitions between the bullet shaped surface and native valve, and the crimping surface and the frame were removed. Therefore allowing the frame and native valve to elastically recoil. The boundary condition on the lower edge of the aortic root was also removed. Simultaneously, the deployment pressure was applied to the internal surface of the balloon (the magnitude of which is dependent on both the device undergoing deployment and the target diameter as summarised in Table 25). The duration of this step is dependent on the target pressure, the pressure was applied at a rate of 10 MPa/s and the step ended as the target pressure was achieved.

Step 3: All contact definitions associated with the balloon were removed, and the pressure within the balloon was also instantaneously reduced to zero. This step was modelled as a 0.005 second period.

7.3.2 Results

The deployment simulation for the case of the SAPIEN 3 frame deployed to a target diameter of 26 mm is shown in Figure 78. The frame experienced elastic recoil. The peak pressure diameter and recoiled diameter are detailed in Table 28

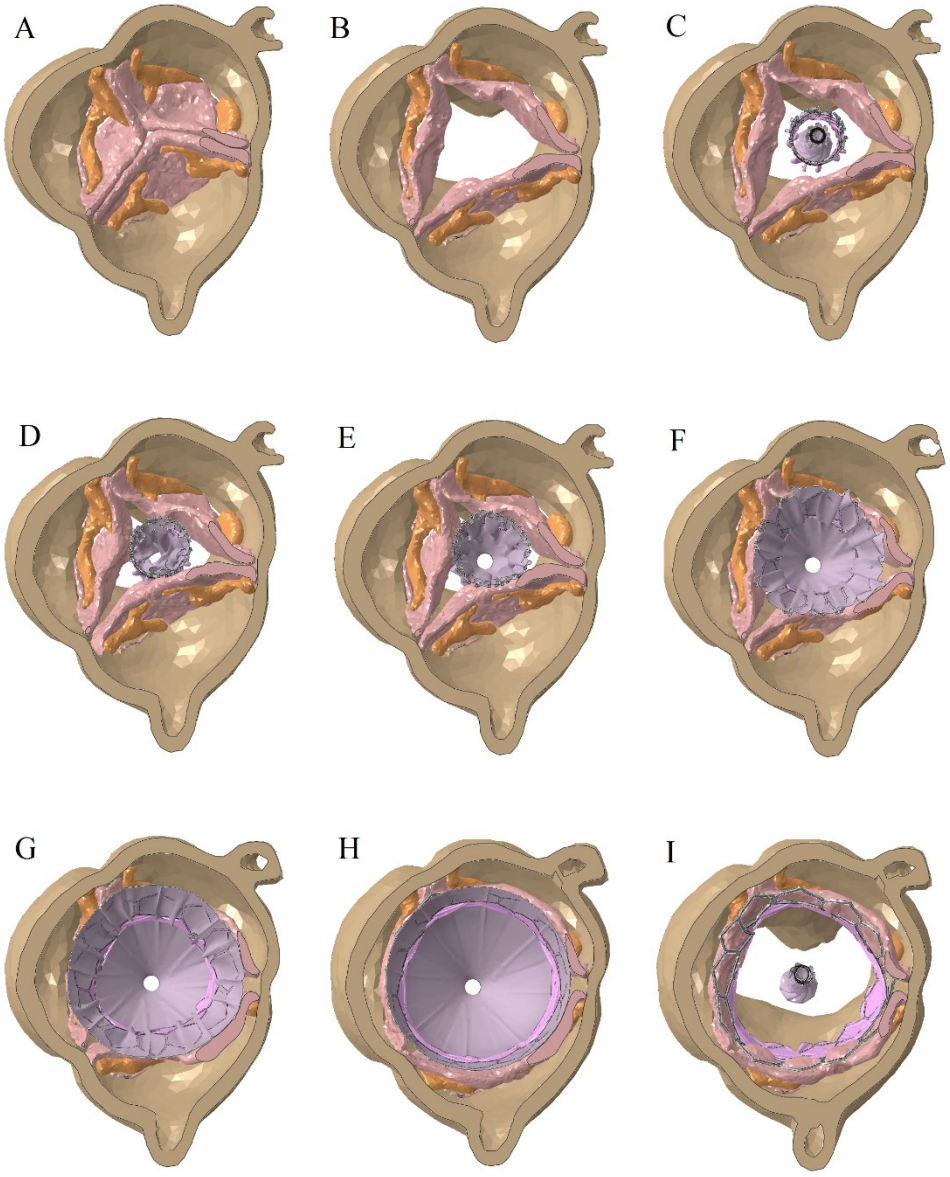

Figure 78. Deployment simulation of a SAPIEN 3 device (frame and cuff only) into a patient-specific aortic root model (with a section cut away to reveal the aortic root within). Each simulation step is visible in the simulation: the native valve is being pushed open by a surface (not pictured) (A-B), balloon inflation (C-H) and balloon deflation (H-I).

Target Diameter	SAPIEN XT Diameter		SAPIEN 3 Diameter	
	Achieved	Final	Achieved	Final
26 mm	26.25 mm	24.82 mm	25.98 mm	24.87 mm
27 mm	27.03 mm	25.42 mm	27.00 mm	25.67 mm
28 mm	27.98 mm	26.12 mm	27.98 mm	26.45 mm

Table 28. Maximum achieved diameter, and the final recoiled diameter of TAVI devices.

All devices deployed to a diameter within 0.03 mm of the target diameter with exception to the SAPIEN XT 26 mm device that over-expanded by 0.25 mm. The reason for the device over-expansion is unknown, and is a limitation that must be considered when analysing the value of over-expanding TAVI devices.

7.3.3 Discussion

A noticeable difference between the SAPIEN XT and SAPIEN 3 is the elastic recoil associated with each. The average recoil, as a percentage of the target diameter, for the SAPIEN XT and SAPIEN 3 was 6.0% and 4.9% respectively. This suggests that the SAPIEN 3 can retain a larger orifice area for a given target diameter. Although over-expansion can be used to achieve a larger orifice area in the SAPIEN XT, it would result in increased stress within the aortic root and plaques, therefore increasing the risk of aortic rupture and embolism.

Both the SAPIEN 3 and the SAPIEN XT displayed imperfect frame geometries post deployment, an example of which is shown in Figure 79. Figure 79(C-D) shows a dent in both frames in the upper left hand corner of the image, which was particularly prominent in the SAPIEN 3, where the cells in the local area failed to fully open. The imperfection in the frame is caused by a large plaque that lies across the base of the non-coronary leaflet. The pressure within the balloon was not only sufficient to fully expand the TAVI device, but also achieve a circular cross section. The stiff material properties of the balloon will not allow it to significantly stretch, even under the deployment pressure, as a result it will eventually find a circular cross section. However, when the balloon has deflated, the TAVI devices frame lacks the stiffness to withstand the forces exerted on it by the aortic root and partially collapses. Furthermore, the calcified plaques create an irregular distribution of force acting upon the frame, as a result the collapsed frame is no longer circular in cross section, as shown in Figure 80.

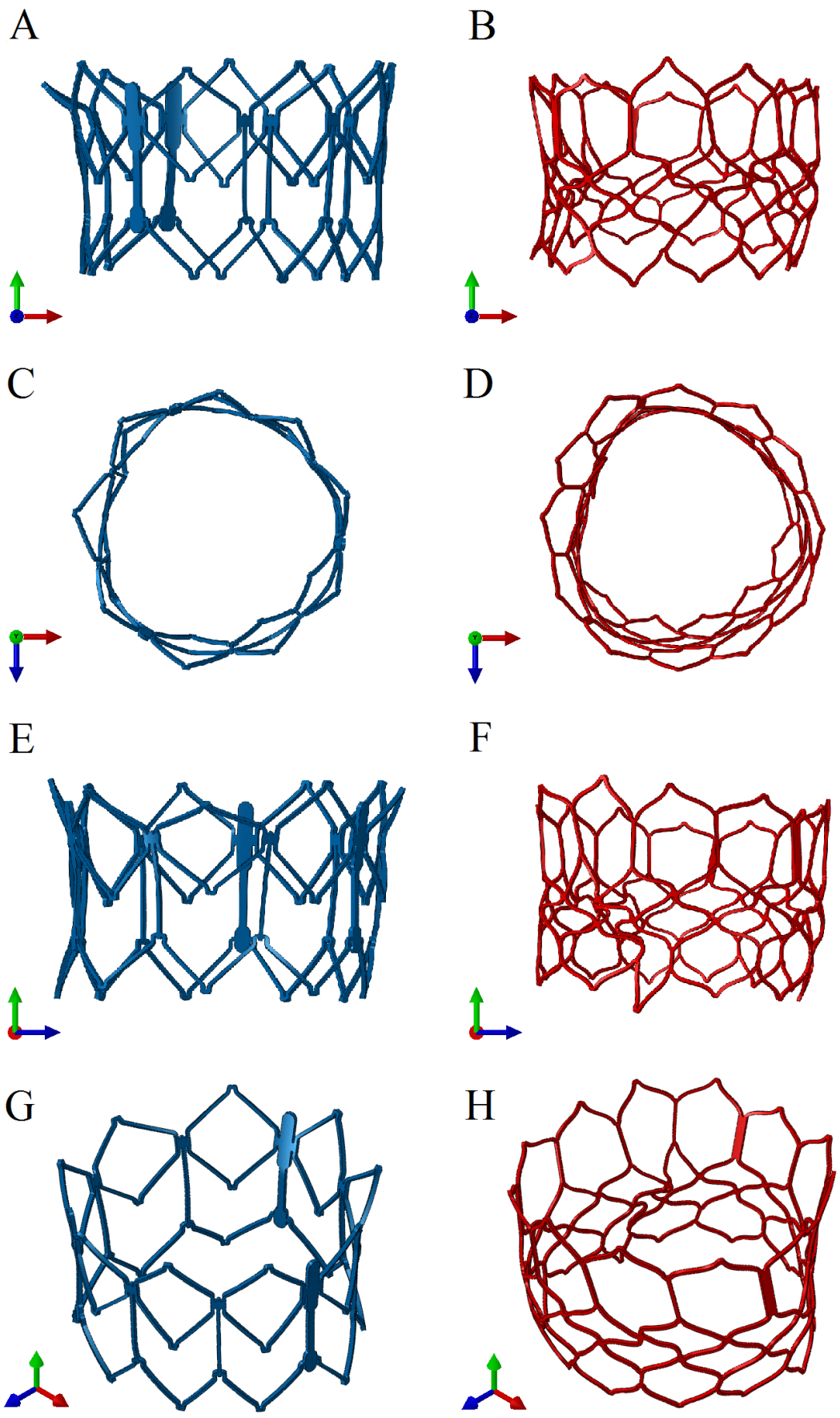

Figure 79. Comparison between the SAPIEN XT frame (blue) and SAPIEN 3 frame (red) post deployment.

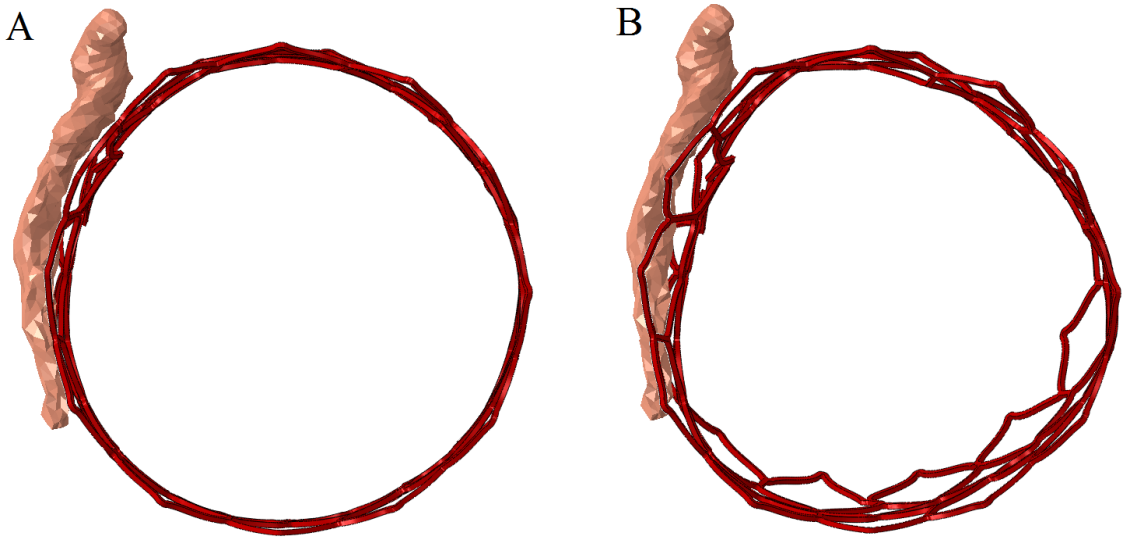

Figure 80. The SAPIEN 3 frame undergoing deployment, with a large calcified mass present, pictured during peak balloon pressure (A) and post balloon deflation (B).

Visual inspection was used to identify areas of PAR, made evident by cavities between the frame and the native tissue. The thickened native leaflets create narrow channels in the commissures which the TAVI devices fail to effectively seal. These initial areas of ineffective sealing allow the blood to flow behind the cuff, which would otherwise inhibit its flow. Figure 81 shows the result of the deployment simulation, where these channels are labelled with blue arrows. The channels in the simulation, however, may not be completely representative of a real life deployment. The channels are created because the tissue cannot effectively bend through 90 degrees and flatten against the aortic root wall. This may not be a geometric property so much as a limitation of the model. The tie constraints used to attach the leaflets to the aortic root could be artificially stiffening the tissue directly surrounding the interface. This would inhibit the leaflets from manipulating themselves away from the commissure. Furthermore, the material properties used to model the native leaflets are hyperelastic, isotropic and homogeneous as opposed to the actual material properties of hyperelastic, anisotropic and inhomogeneous. These simplifications of the native tissue may result in the channels that are visible in the simulation.

Other than the tie constraints, the channels could be induced through the placement of plaques. The right-coronary sinus contains a plaque (labelled with a green arrow in Figure 81) that falls within the native leaflet, next to the commissure between the left and right coronary sinuses. When the leaflet is fully opened by the TAVI device, the leaflet must wrap around this plaque before making contact with the sinus wall. The channel in the commissure between the left-coronary leaflet and the right-coronary leaflet is likely to be due to the plaque, as opposed to artificial stiffening. The leaflets position relative to this plaque is consistent across all six simulations, increasing the target diameter or changing the device did not alter the behaviour.

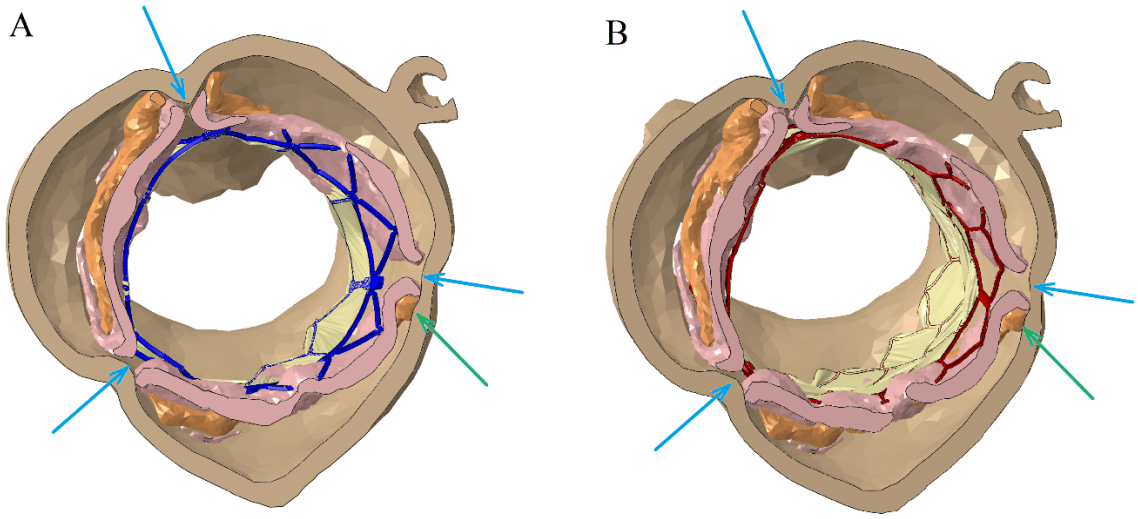

Figure 81. Both the SAPIEN XT (A) and SAPPIEN 3 (B) deployed (with a target diameter of 26 mm) demonstrate poor seals at the native valve commissures (labelled with blue arrows). A piece of plaque (labelled with a green arrow) increases the gap between the frame and the native tissue.

In order to inhibit PAR, it is crucial that the frame of the device makes an effective seal with the aortic root wall below the leaflets in order to seal the lower region from blood that has passed through any channels in the commissures. The presence of plaques in the native leaflet attachment lines create a step that the TAVI devices struggle to conform around. The plaque pulls the lower edge of the TAVI frame away from the wall of the LVOT creating gaps on either side of the plaque. The non-coronary leaflet contains such a plaque (as seen in Figure 80 and Figure 81(B-D)), and to a lesser extent so did the left-coronary leaflet. The right-coronary leaflet also had calcified masses, although none of them were situated at the base of the leaflet and the devices achieved an effective seal in this region (Figure 82 (A, C)). If these plaques, formed at the leaflet attachment lines, were not present, it is likely that the frame would be able to make an effective seal within the aortic root.

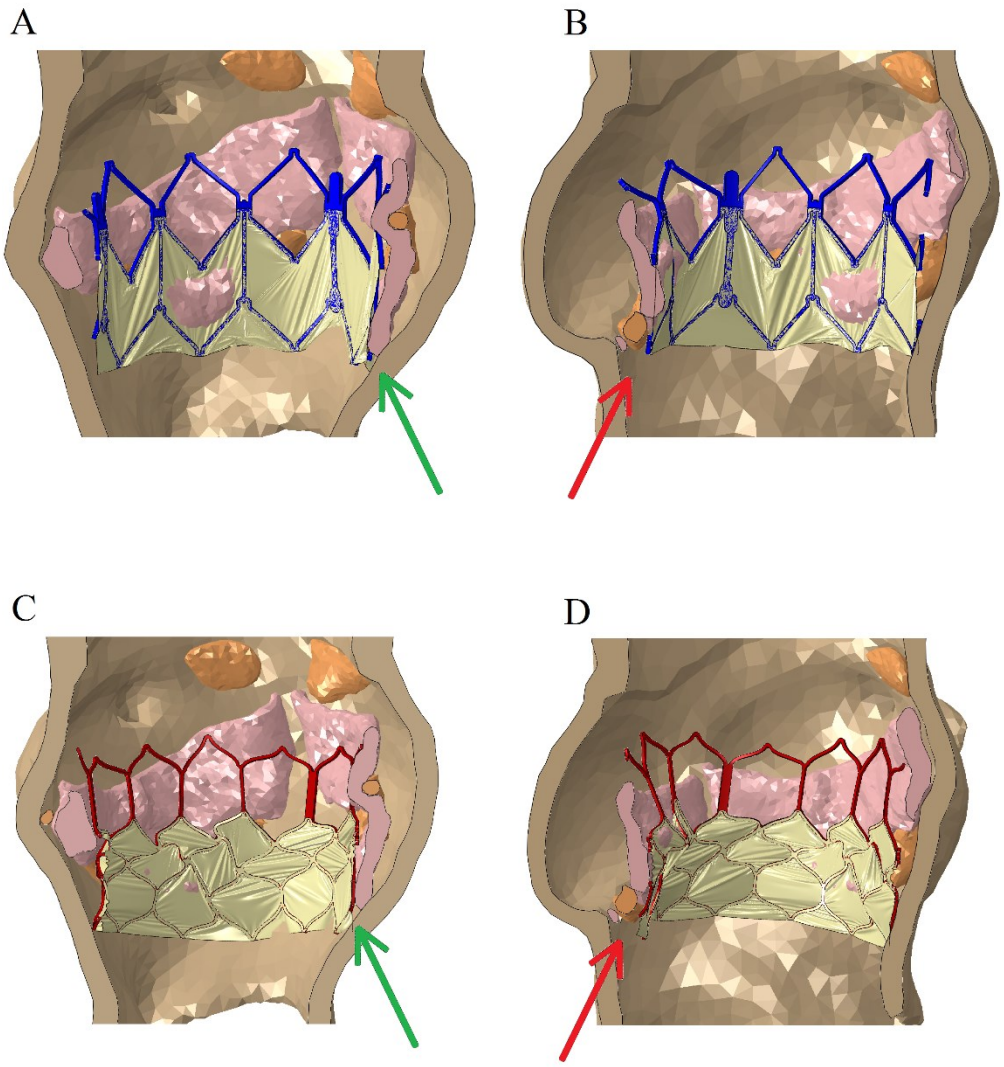

Figure 82. Both the SAPIEN XT (A, B) and SAPIEN 3 (C, D) struggled to create an effective seal underneath a native leaflet if the base of the leaflet was calcified (red arrows), as opposed to non-calcified leaflets (green arrows).

The significance of the plaques at the native leaflet attachment lines has been previously documented. *Ewe et al. (2011)* used a multilayer CT scanner to locate plaques within patients prior to TAVI, and then correlated the plaque location with the incidence of PAR. The image shown in Figure 83 is the map that was superimposed onto the CT scan images of the aortic root and used to classify the locations of the plaques. Six sites of PAR were identified in the vicinity of the three commissures, and the regions below each of the three native leaflets. The location of calcified masses was then matched with areas of PAR using receiver operating characteristic curves (Figure 84). PAR at a commissure was strongly associated with plaques at the respective commissure, while PAR below the native leaflets was associated with masses at the aortic wall.

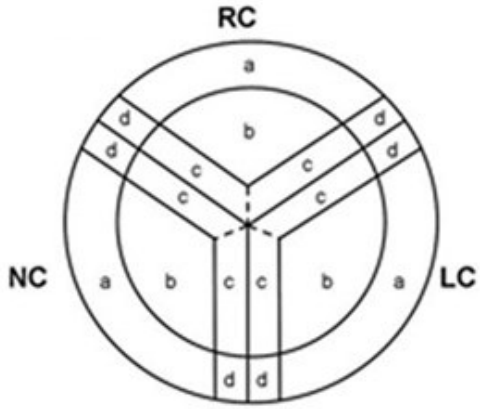

Figure 83. Clarification map of calcified plaques within the aortic root. a – aortic root wall, b – leaflet body, c – leaflet edge, d – commissure (Ewe et al. 2011).

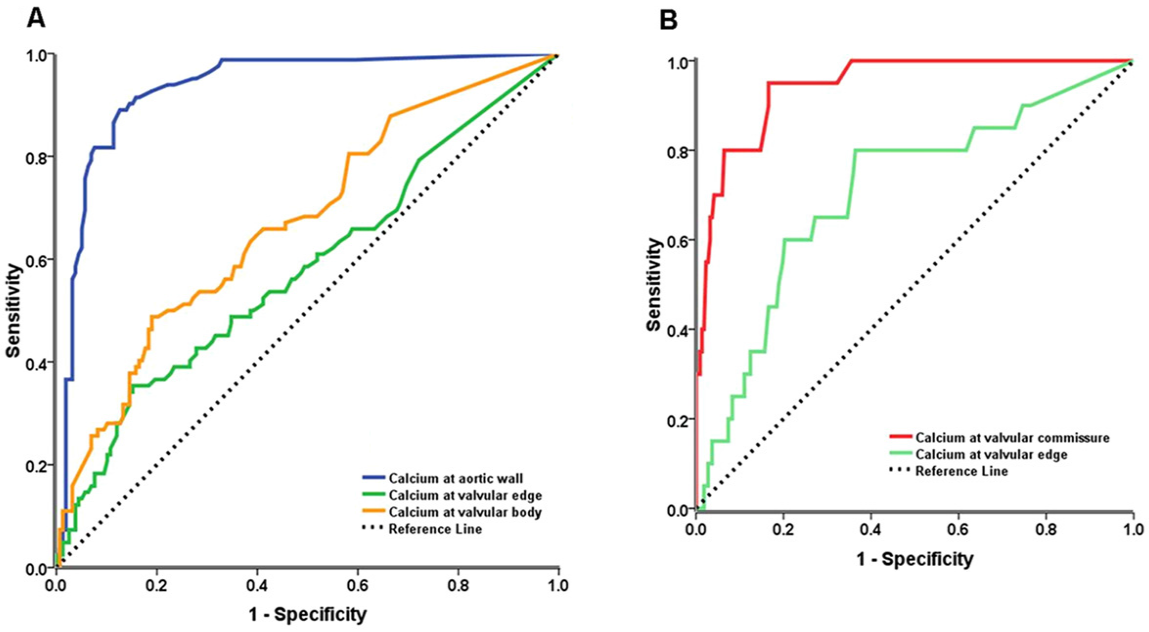

Figure 84. Receiver operating characteristic curves of calcified mass location as a predictor of PAR below the native leaflets (A) and at the commissures (B) (Ewe et al. 2011).

The simulation results correlate with the statistical analysis carried out by *Ewe et al. (2011)*. A plaque in the commissure can be seen inhibiting the motion of a leaflet resulting in a channel inside the commissure. Plaques at the base of the leaflets would be classified as plaques on the aortic root wall through the classification procedure described in Figure 83. These plaques were found to be statistically most likely to induce PAR below the native leaflets and are shown in the simulation pulling the frame away from the native tissue of the LVOT.

Unfortunately, the research presented by *Ewe et al. (2011)* did not consider the plaques on the commissures inducing PAR below the body of the native leaflets. Although it was shown that plaques on the aortic root wall (or base of the leaflets) was strongly associated with PAR, this area would

only create a channel where blood re-emerges from below the cuff, but the manner to which the blood initially circumnavigates the cuff was not identified. The simulations presented here suggest that blood would initially flow behind the cuff at the commissures because there was little or no gap between the frame and the underside of the native leaflets.

It is concluded that if PAR were to be present in this patient-specific case after TAVI, the path the blood would flow would most likely be through the plaque induced channel in the commissure between the left-coronary and right-coronary leaflets. The flow would then pass below the left-coronary native leaflet and out below the frame. The path is shown in Figure 85. Although this is not the only path blood could potentially flow through, it is the only path that exploits the channel between the left-coronary and non-coronary commissure that is induced by plaque position, as opposed to potentially being generated through computational inaccuracies associated with tie constraints.

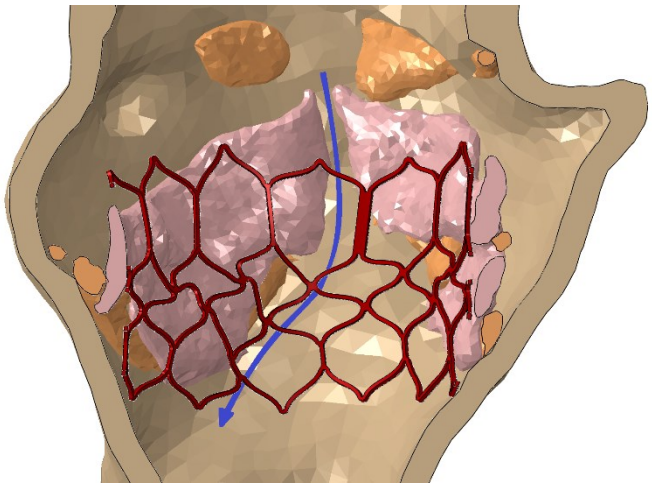

Figure 85. Computational simulation suggests PAR is most likely to originate in the commissure between the left-coronary and right-coronary leaflet before travelling below the left-coronary leaflet.

The two factors associated with PAR are the ability for the TAVI device to close the channels in the commissures and to create a seal below the native leaflets. These two areas will be used to compare the results from simulations in which the devices were deployed to different diameters. Two planes were selected for analysis, the first (plane 1) was 7.4 mm below the upper crowns of the device frames. This first plane was used to observe the size of channels between the commissures. In all cases, the plane was partially or fully above the cuff. The second plane (plane 2) was 17 mm below the upper crowns of the frames and visualises the frames ability to create a seal below the native leaflets. These two planes are graphically shown in Figure 86. The resultant sections for all cases are shown in Figure 87. Figure 88 shows the outlines of the anatomical features and frames, for both planes, with each simulation of varying target diameter superimposed over the other.

Increasing the target diameter of the SAPIEN XT did not improve the frames position relative to the native tissue. Although the frame reaches greater diameters, the gap between the frame and the native tissue remains the same. The SAPIEN 3, however, did show some improvements, which are particularly evident in Figure 88(D). As the frame over-expands in the lower section, the frame-tissue gap is reduced. The shape of the plaques does not change post deployment, only the plaque orientation changes. This suggests that the improvements the SAPIEN 3 frame experiences is due to the frame manipulating itself about the plaques as opposed to the plaques yielding.

During TAVI, if PAR is detected using TOE Doppler analysis, two immediate treatment options are available: post deployment angioplasty to over-expand the device or deployment of a second valve. Both treatments have been shown to reduce the incidence of PAR in the SAPIEN XT and SAPIEN 3 (Nombela-Franco et al. 2012). The marginal improvement seen in this simulation suggests that it does not accurately capture the behaviour of prosthetic valve deployment. The missing behaviour is the plaque deformation and damage. Although the plaques are very hard relative to the surrounding tissue, the plaques can still crack or rupture and neither behaviours are considered in this simulation. This suggests that the majority of the improvement associated with balloon over-expansion would be related to damaging the plaques which will unfortunately increases the risk of embolism in the patient.

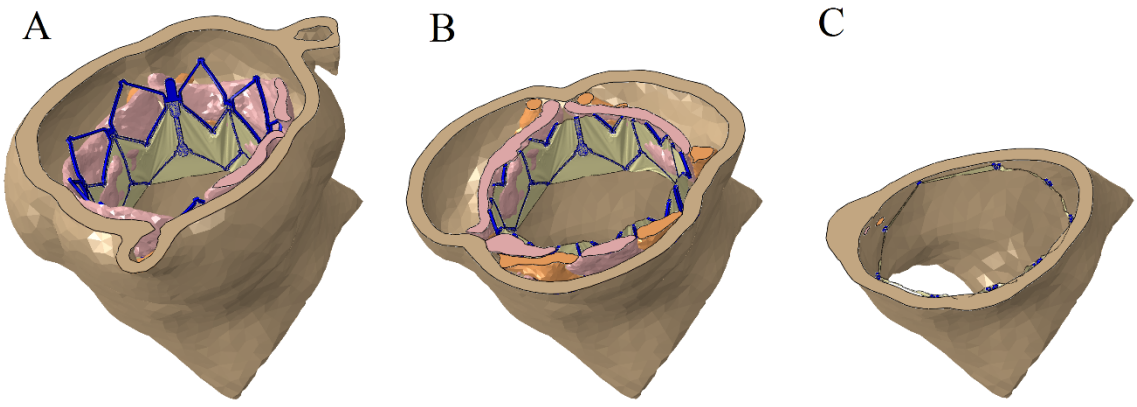

Figure 86. Final position of a SAPIEN XT frame deployed to 26 mm, with sections cut away: A generic section cut away to reveal the device (A), Plane 1 acting as the cutting plane (B) and Plane 2 acting as the cutting plane (C).

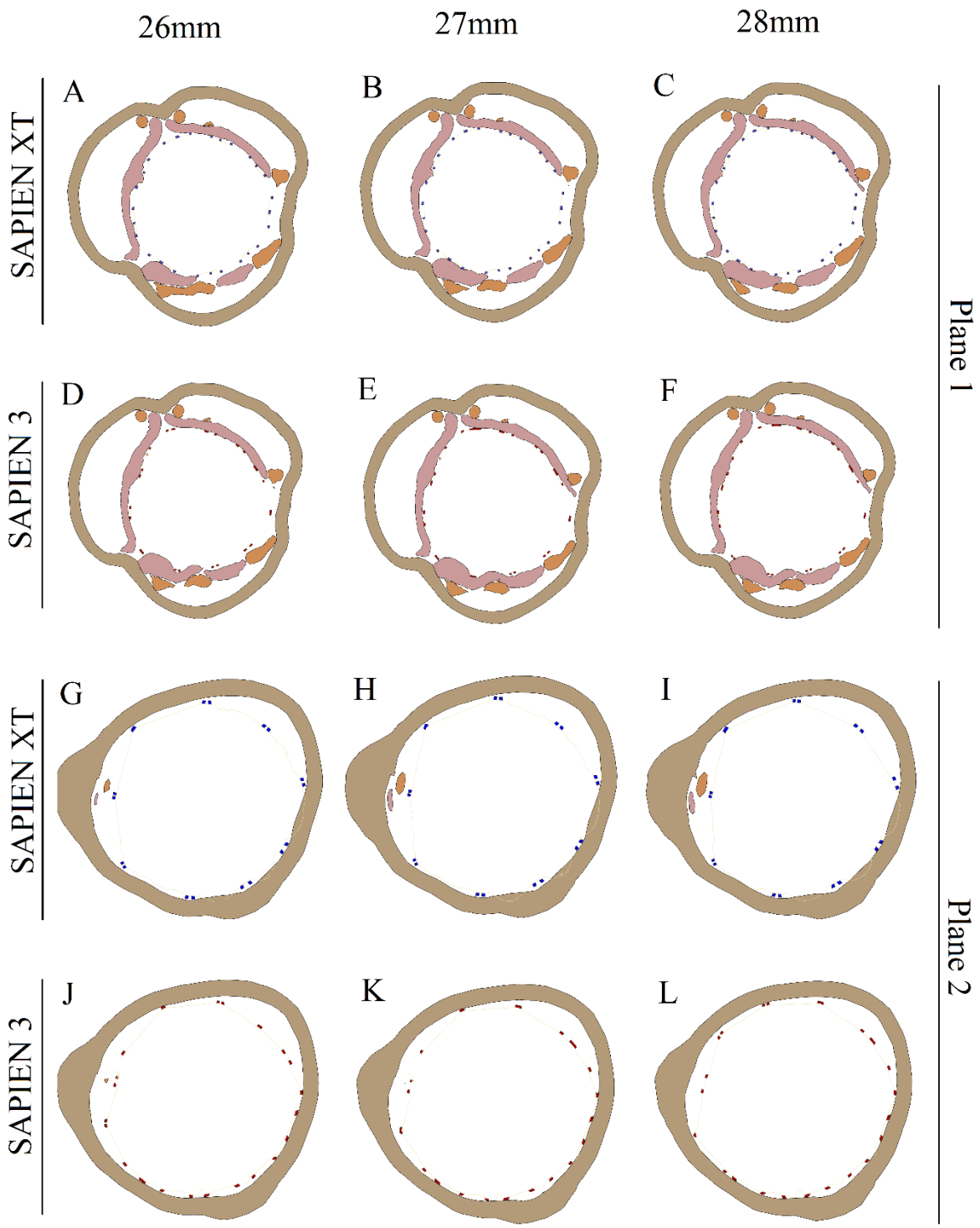

Figure 87. Two sections of the aortic root post deployment, showing the TAVI device frame position. A comparison between the target deployment diameters, as well as TAVI devices (SAPIEN XT and SAPIEN 3) can be made.

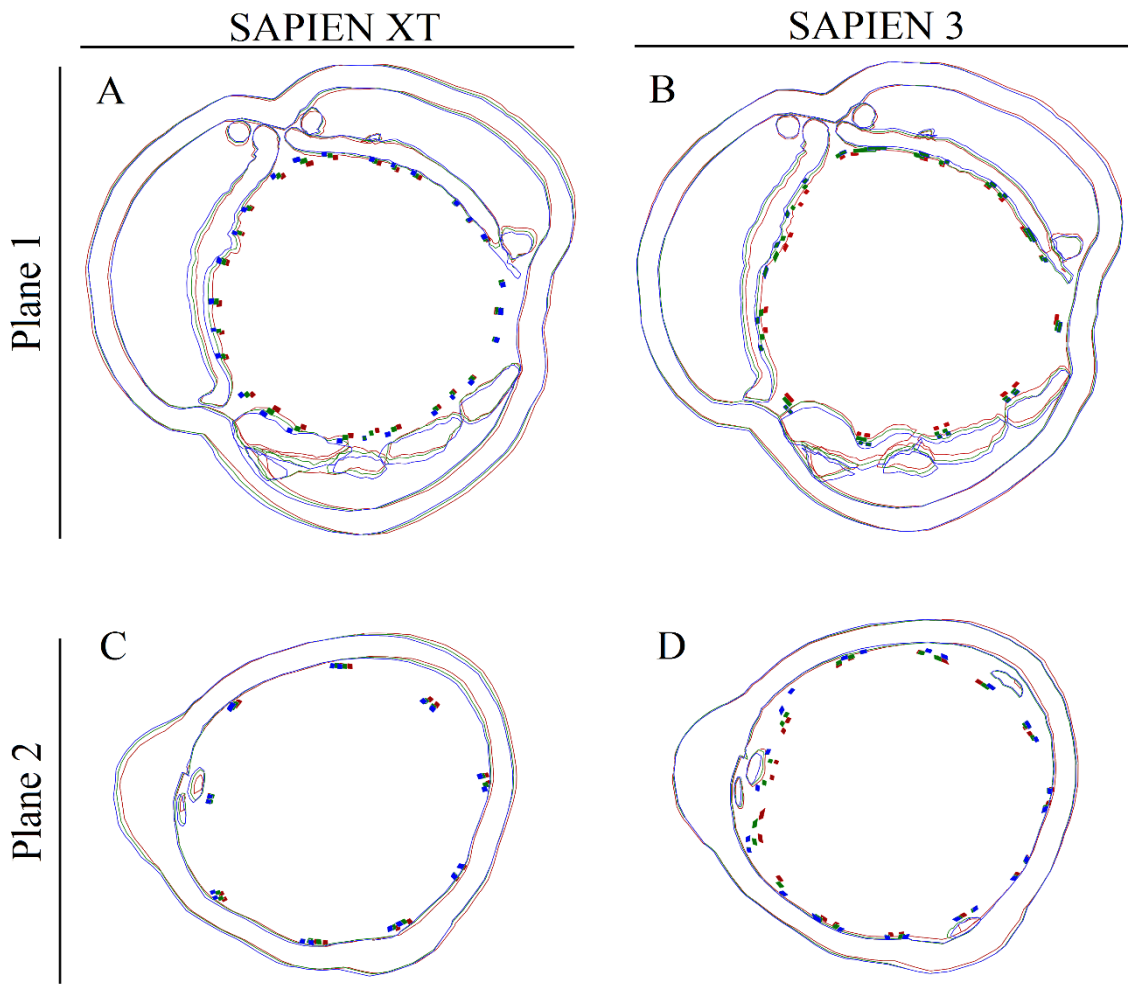

Figure 88. Sections of plane 1 and plane 2 showing the outlines of anatomical features and the device frames. Each plot features the three different deployment diameters superimposed in different colours: 26 mm is red, 27 mm is green and 28 mm is blue.

The channels associated with the commissures are significantly larger for the case of the SAPIEN XT as opposed to the SAPIEN 3. The SAPIEN 3 adopts a non-circular shape with a flattened section below the non-coronary sinus. The flattened section has two corners that fall into the commissures of the non-coronary leaflet, which reduces the size of the channels. The frame of the SAPIEN 3 is unusually damaged, far more than seen in images of deployed devices (Garcia et al. 2014, Mark et al. 2015) . The source of this inaccuracy is thought to be associated with the strut cross sections of the SAPIEN 3 model. The struts of the SAPIEN 3 frame model feature a square cross section. This is likely to be an inaccuracy in the model as a square cross section is more liable to twist. The excessive distortion seen could be associated with the inability of the struts to withstand torsion.

Again, the primary limitation of this study was the aortic root model. Although geometry is sufficiently accurate to the patient to be considered reliable, the material properties applied to the tissue (with exception of the plaque) were hyperelastic, homogeneous and isotropic, a simplification of reality in which the tissue is hyperelasitic anisotropic and inhomogeneous. The gross behaviour

of the aortic root is determined by the in plane material properties of the tissue, which is almost orthotropic. As a result, assuming the tissue to be isotropic is not unreasonable. The softer off plane material properties of the native tissue may allow the frame to imbed into the tissue, reducing the gap between the frame and the native tissue. The plaques were assumed to be linear elastic. However, no model of failure capable of modelling rupture was assigned to the plaques. Since plaque failure can potentially be exploited to reduce PAR through over-expansion (and undoubtedly occurs in standard-expansion as well) it would be useful to develop a material for this behaviour in future work. For now, it is useful to simply consider the implications for plaque embolization.

Finally, the tie constraints, that hold the native aortic root model together, artificially stiffen the tissue. If the number of tie constraints were reduced, the predicted route of PAR would be more credible as the artificial stiffening would be reduced. A method for achieving this is to have a native aortic root constructed from a single mesh; different tissues would be represented by different material properties applied to element sets.

The true value of computational simulation of TAVI exceeds PAR prediction, and ventures into the ability to advise on how to avoid or treat PAR. Simulations could be used to predict the outcome of device deployment at multiple locations and identify the safest deployment zone, or identify the best treatment for PAR, such as valve-in-valve deployment, or over-expansion of the device. However, due to the poor material property applied to the plaques, plaque damage cannot be modelled and therefore advanced simulations surrounding treatment of PAR are currently unavailable.

7.4 Computational Prediction of Embolism

Although TAVI is known to be procedurally safer than either SVR or non-surgical intervention, it has an increased incidence of embolism. During SVR, any plaques that are likely to rupture and produce debris, are scraped away with a scalpel; a technique that is not feasible during TAVI. Furthermore the delivery system of TAVI devices is clumsy and could agitate plaques, inducing debris release. In this section, the previously described simulations are repurposed to assess the possibilities of predicting embolization.

7.4.1 Emboli Release Associated with Balloon Expansion

Previously, the balloon deployment phase of TAVI has been identified as the most likely phase to produce debris (Drews et al. 2011). This is hypothesized to be associated with the balloon exerting stresses upon the plaques which are far greater than these experienced during the cardiac cycle. If the

balloon is over-expanded, the stress within the plaques will be increased, although the extent to which the risk of emboli release increases is unknown. Previously (in section 7.2) a simulation was described that identified the pressure required within the balloon to deploy the TAVI device. In summary, a TAVI device frame and cuff was expanded into an aortic root by means of a balloon with a linearly increasing pressure. The device is over-expanded until the simulation fails due to excessive element distortion. This same simulation can be used to examine the stresses within the plaques during balloon expansion and over-expansion. This will allow for the plaques that are at greatest risk to be identified. Furthermore, a sudden increase in stress within the plaques during over-expansion could represent an increase in risk of debris release.

The manner to which plaques fail is not fully understood. It is a highly complex problem as the plaques comprise solid calcified masses within a fibrous tissue matrix. It is thought that plaque fracture is led by the maximum principal stress. Therefore, the following analysis focusing on the plaques will be in terms of maximum principal stress.

The average principal stress within the plaques, associated with both the SAPIEN XT and SAPIEN 3, is shown in Figure 89. The stress within the plaques initially decreases as the leaflets were forced open and then released onto the delivery device in order to avoid volumetric intersection at the beginning of the simulation. After this point, the stress in the leaflet increase, in a near linear fashion, to a maximum. There was limited variation in plaque stress between the SAPIEN XT and SAPIEN 3.

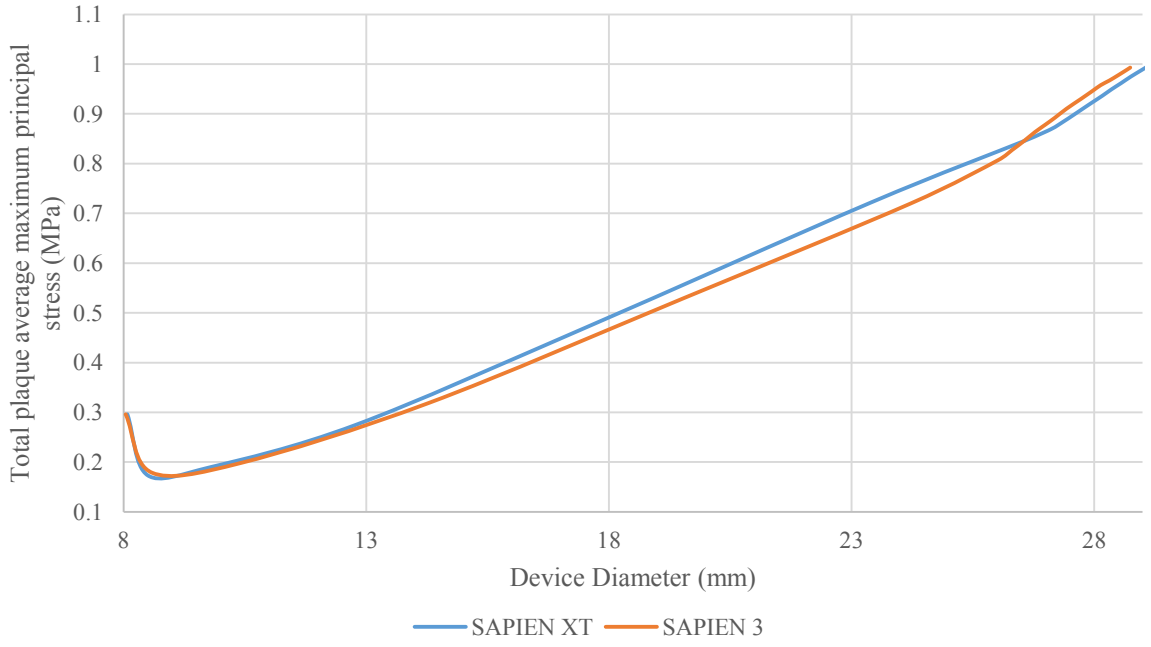

Figure 89. Relationship between von Mises stress within aortic plaques and device deployment diameter (mm).

During TAVI, the device will recoil as the balloon is deflated, resulting in a reduced stress within the plaques. Although the predominant amount of emboli release is likely to be associated with the balloon deployment, debris can still be released in the days after the procedure. The stress exerted in the plaques during this period is likely to be a key factor to this debris release.

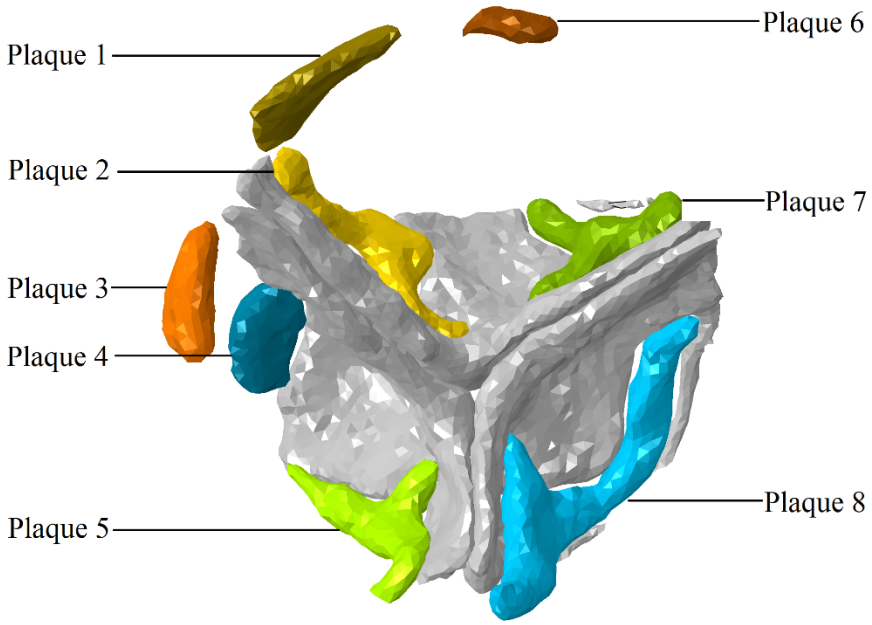

Figure 90. Computational model of the native leaflets (grey) surrounded by the plaques present within the native valve.

Within the model of the native aortic root there are eight individual masses of plaque, as seen in Figure 90. The stresses within the plaques, for the case of the SAPIEN XT, are shown in Figure 91.

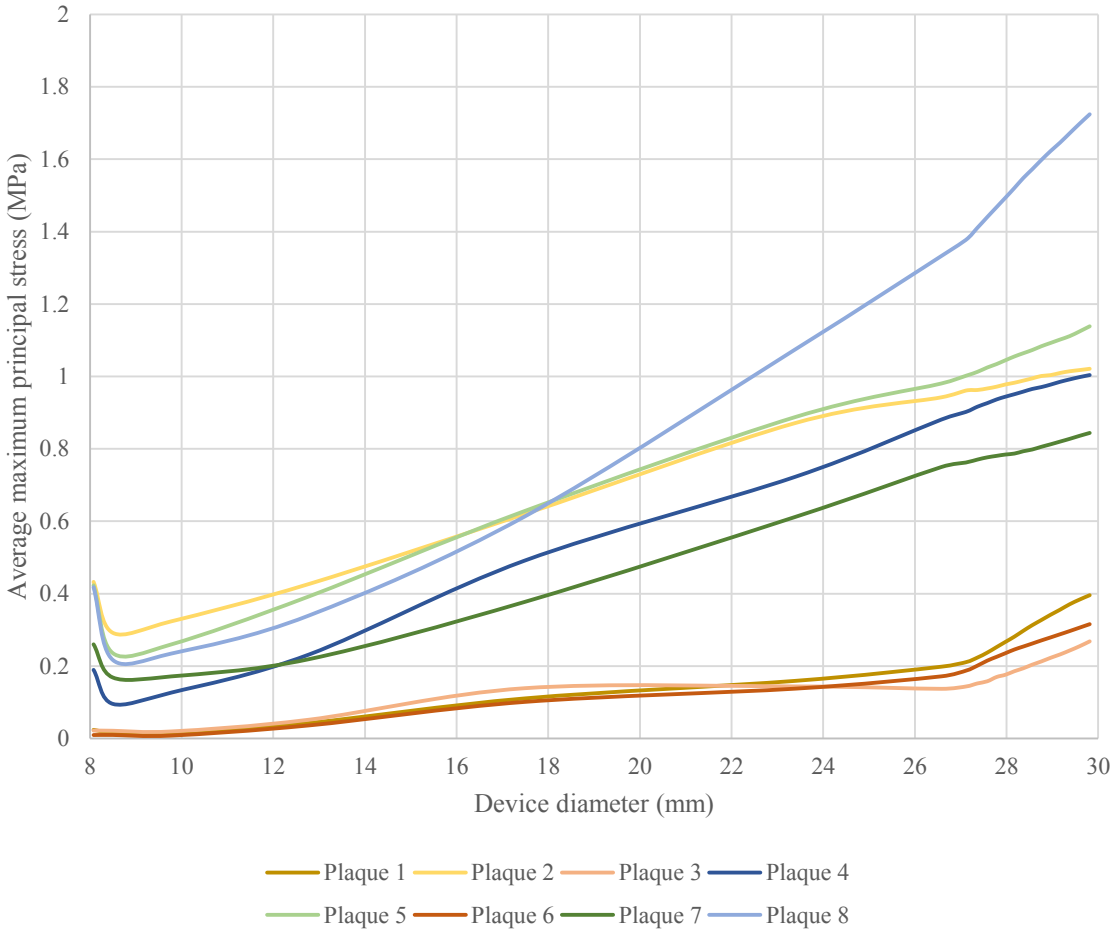

Figure 91. Average stress within each mass of plaque.

Three of the plaques (plaque 1, 3 and 6) are not in contact with the aortic valve (are attached to the aortic root wall). Because these plaques are not in contact with the aortic valve, the motion of the valve opening does not apply additional stress to the plaques. This is evident in Figure 91 as plaques 1, 3 and 6 do not demonstrate an initial unloading. The balloon makes initial contact with plaques 1, 3 and 6 almost immediately, but it cannot exert a large stress upon them as the device restrains the balloon. When the device has reached a large enough diameter, and the pressure within the balloon is sufficient to stretch the material, the stress within the plaques sharply increases; this occurs at a device diameter of approximately 27 mm.

Due to the reduced stress levels, it is unlikely that plaque 1, 3 and 6 will rupture without additional loading. Plaques 2, 4, 5 and 7 demonstrated a variance in that remained approximately constant throughout the simulation. Plaque 8 however had a comparable stress to plaque 2, 4, 5 and 7 during the early stages of the simulation before the stress levels rose beyond that experienced by its peers. It is unknown why this plaque suffered a significantly increased stress, however there was no numerical error evident after reviewing the data. This suggests that plaque 8 is most likely to rupture during deployment.

7.4.2 Emboli Release Post Balloon Expansion

Although it is known that the probability of stroke is greatest during balloon deployment, an increased rate of stroke in TAVI patients relative to other treatment options is reported at 30 days and 1 year post implantation (Leon et al. 2010, Smith et al. 2011). The plaque stress post deployment is likely to be a good indicator of plaque rupture post deployment.

The final, average maximum principal stresses within the plaques for the case of the SAPIEN XT were calculated and presented in Figure 92.

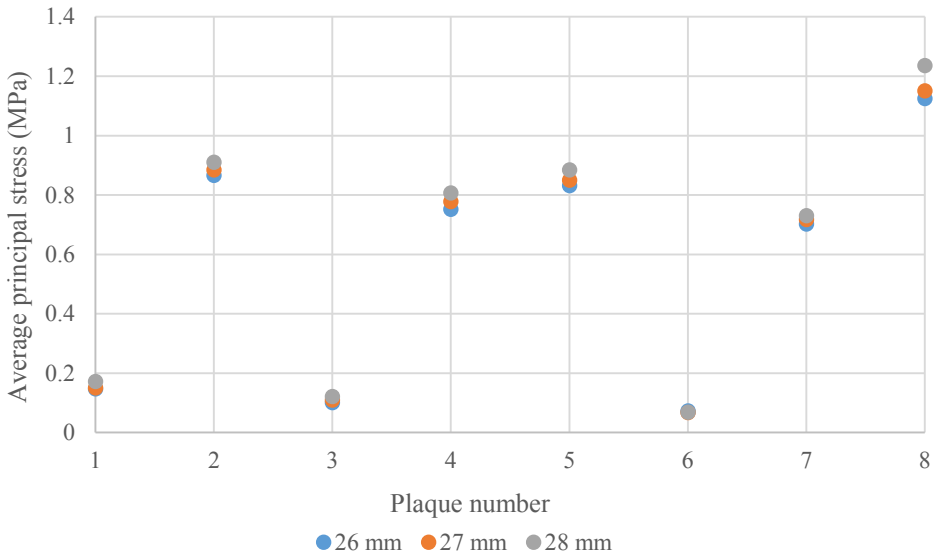

Figure 92. Average stresses within plaques post device deployment to three diameters: 26, 27 and 28 mm.

Similarly to the results of section 7.4.1, plaques 1, 3 and 6 had a reduced stress relative to the other plaques. Interestingly, the final stresses within these plaques was not zero. The geometry of the aortic root wall has been distorted by the TAVI device frame, which in turn distorts the plaques resulting in a stress above zero. This behaviour could be induced by the tie constraints used to attach the plaque to the aortic root wall creating an artificially stiff interface which generates increased stresses.

Over expanding the device was shown to increase the average principal stress in the leaflets by an average of 10.8% (between a deployment diameter of 26 mm and 28 mm). The greatest increase in average principal stress was experienced by plaque 3 which underwent a 12% increase (again, between deployment diameter of 26 mm and 28 mm). This increase in average principal stress may well be significant enough to increase the risk of rupture.

These results only consider the plaques to be immovable masses and do not consider any failure material model. It is therefore impossible to determine which of the plaques are most likely to embolise. Further work is required to improve the material model of the plaques.

7.5 Improvements on Current Transcatheter Aortic Valve Implantation Device Design

A major fault in the design of the SAPIEN XT 26 mm is that once blood has found an opening behind the cuff, the only area that can create a seal is the lower edge of the device. That is, the SAPIEN XT 26 mm has only two lines of defence. The SAPIEN 3 however has up to three cells that the blood must penetrate before a viable route of PAR would be achieved. These multiple additional barriers featured in the SAPIEN 3 will aid in reducing PAR. The design of the SAPIEN XT 26 mm could be improved by adding more cells (such as the case of the SAPIEN XT 29 mm, pictured in Figure 8).

As opposed to increasing the number of struts in the SAPIEN XT 26 mm, the area the cuff covers could be increased. This would increase the number of struts that are capable of blocking PAR, as the upper cells of the device would be spanned by the cuff also. This technique could be also applied to the SAPIEN 3 as the upper cells are also open. The reason TAVI devices tend to have open upper cells, is fear of blocking the coronary arteries which would result in cardiac arrest. However, if the devices rotational orientation is known, open areas in the cuff could be lined up with the coronary arteries allowing blood to flow through.

Increasing the area the cuff spans is hypothesised to also reduce the rate of embolism. The cuff has always been considered to have two functions:

1) Retain the lower edge of the prosthetic leaflets to the device.
2) Reduce the incidence of PAR.

There is also a third function: trapping debris post deployment. If a plaque is in contact with the cuff, and ruptures, the cuff may be able to offer a sufficient seal to contain the debris. As the cuff is expanded about the frame of the TAVI device, it also increases the area of potential emboli capture.

Due to concern for coronary occlusion, some cells of the TAVI device have been left open. These cells will have to be aligned with the coronary arteries. It has been computationally shown that the TAVI device does not rotate during deployment. The lack of device rotation can also be observed through fluoroscopy imaging. Provided the orientation of the device can be monitored predeployment, the final position of the device can be controlled.

During TAVI deployment, the two primary delivery methods are transfemoral and transapical deployment routes (section 2.6). In the case of transfemoral, the delivery catheter must contort itself around the femoral arteries, up the ascending aorta and around the aortic arch. Due to the contortions the catheter undergoes, it may be difficult to control the orientation of the TAVI device. During

transapical deployment however, the catheter is nearly straight, in which case it would be relatively easy to rotationally orientate the TAVI device.

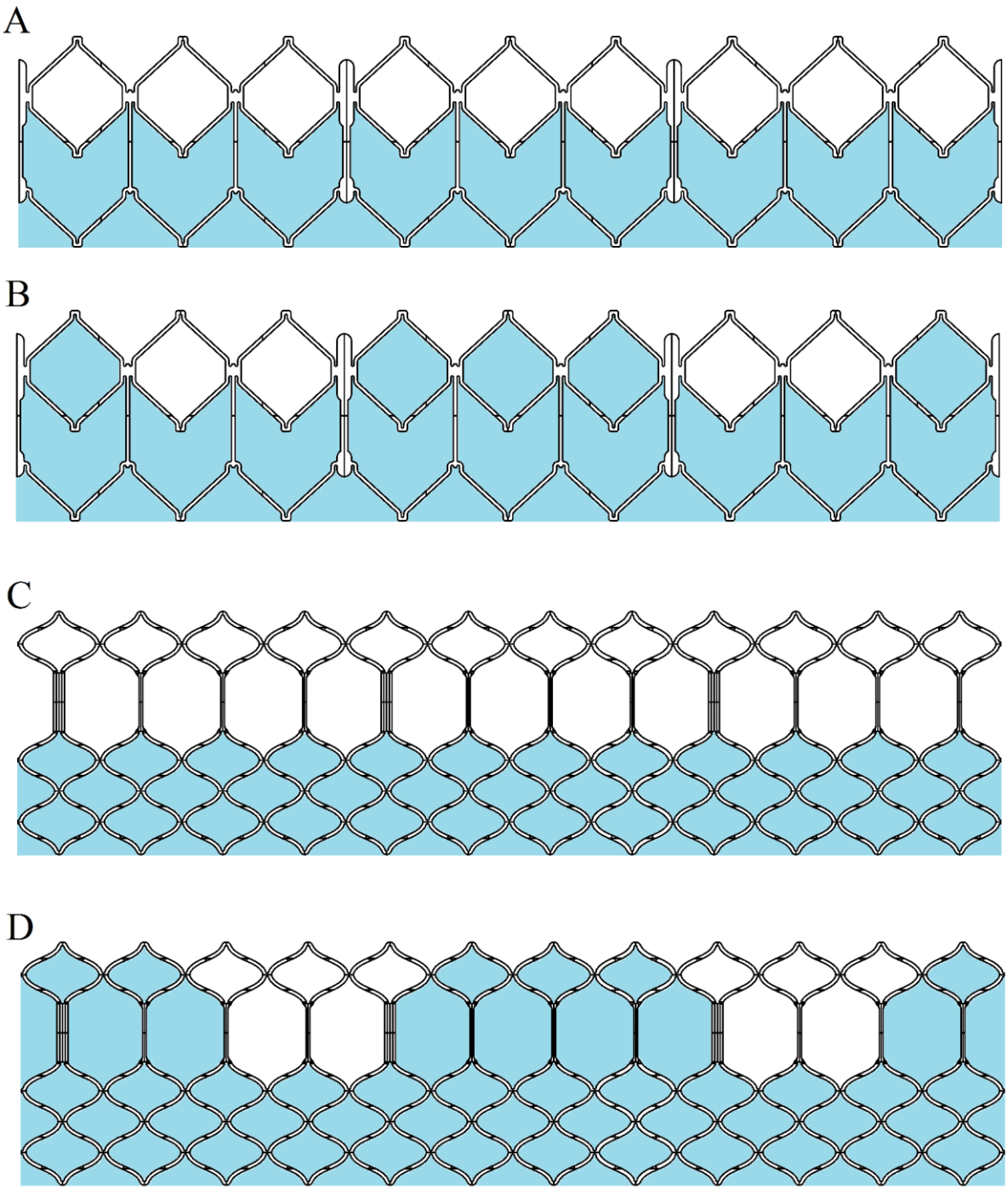

Figure 93. TAVI devices with current and proposed cuff coverage areas. A: Current SAPIEN XT 26 mm, B: Proposed SAPIEN XT 26 mm, C: Current SAPIEN 3, D: Proposed SAPIEN 3.

The device orientation cold be monitored through two methods:

1) Adding radiopaque markers onto the device so orientation can be calculated through fluoroscopy.
2) The device orientation relative to the handle is known, the handle can then be orientated appropriately.

The first method may be suitable for transfemoral delivery, as the second method requires the delivery catheter to remain straight. For the case of transapical delivery, either method is suitable. If this reasoning is correct, future generations of TAVI devices will feature rotational orientation mechanisms.

7.6 Conclusion

In this chapter a multitude of simulations were performed in order to find the required level of device model detail, correct balloon pressure for full expansion, analyse PAR and embolism. The key findings in this chapter are:

1) Computational simulations can identify sites that are susceptible to PAR.
2) Including prosthetic leaflets in the device model does not alter the simulated frame position post deployment.
3) Plaques that are most likely to rupture can be identified through computational simulation.
4) Post-deployment balloon angioplasty reduces the degree of PAR by damaging plaques.

In section 7.3 it was shown that it is possible to detect areas that are likely to be susceptible to PAR by means of computational analysis. For this case, the origin of PAR was a channel in the commissure between the left-coronary and right-coronary leaflets. The channel is believed to be the product of plaque placement in the near vicinity. The regurgitation path then flowed below the left-coronary leaflet where the frame failed to create an effective seal against the aortic root wall due to a second calcified mass.

The exploratory simulations presented in section 7.1 suggest that the leaflets are not required for accurate simulation of TAVI deployment. Furthermore, the greatest discrepancy was associated with the cuff for which, the associated ANPD was 0.263 mm (1.01% of the device diameter). This is still a small discrepancy and as a result, it was concluded that the only part of the TAVI device required for PAR assessment is the frame. This is an important result as to some extent, it reinforces the simplifications of leaflet exclusion in many previous papers in the subject, as well as providing a justifiable means for reducing the computational time by removing irrelevant components (Capelli et al. 2012, Wang, Sirois, and Sun 2012, Russ et al. 2013, Auricchio et al. 2014, Gunning, Vaughan, and McNamara 2014, Morganti et al. 2014).

The aortic root model includes eight individual bodies of plaque. Through the analysis presented in section 7.4, it was found that of the eight plaques there were three groups, five plaques that were highly stressed and three that were not. The highly stressed plaques were situated on the native leaflets while the plaques that experienced reduced stress were situated in the aorta. This is a predictable result as the plaques in the aorta are only influenced by the delivery balloon, the prosthetic valve will not make contact with them. Of the five highly stressed plaques, a single plaque experienced a significantly increased level of principal stress in the latter stages of the simulation and is thought to be most likely to rupture. It was also shown that increasing the device diameter increased the stress within the plaques. The average stress increase experience by the plaques between a device deployed to 26 mm and 28 mm was 10.8%.

Finally, the simulations of section 7.3 offered further insight into how post deployment balloon angioplasty and over inflation can reduce PAR: by damaging plaques as opposed to improving frame conformity. This raises questions surrounding the benefit of post deployment angioplasty against the possibility of emboli release.

Chapter 8: Leaflet Damage and Operating Stress

As TAVI matures, the envelope of patients that are considered suitable increases. TAVI is now being performed on patients free from AS, and as young as 20 years old (Faria et al. 2013, Urena et al. 2014). Low-risk patients tend to have a longer life expectancy that the TAVI devices must also satisfy so as to avoid repeat implantation, which would result in both increased risk of mortality and expense. Once deployed a TAVI device will become ineffective over time due to restenosis. Restenosis is associated with damaged collagen fibres which reveal specific protein structures to which calcium can be deposited. In order to inhibit the collagen fibres from being damaged, the mean and amplitude of stress variation of the valve must be reduced to a minimum. There are two major contributing factors to increased stress within the prosthetic leaflets:

1) The leaflets are damaged during the delivery process resulting in a weaker structure.
2) The frame is in a non-optimal position which alters the leaflet operating dynamics and stress within the leaflets.

Both of these occurrences are addressed in this chapter.

Throughout this chapter the stress within the leaflets is represented by the von Mises stress. Damage to the collagen fibres within the leaflets, which could potentially lead to early restenosis will most likely be associated with change in shape, as opposed to volume. As a result von Mises stress is a good measure of failure as it is primarily concerned with shape change, as opposed to volume change.

8.1 Leaflet Damage during Deployment

TAVI leaflets have been shown to be damaged in two stages of the deployment process; i.e., in crimping and balloon deployment (Alavi, Groves, and Kheradvar 2014, de Buhr et al. 2012). In previous articles found in the literature, the leaflets were not included in the deployment simulation. If the leaflets were considered at all, a mapping technique was used to align the leaflets with the frame post-deployment (Gunning, Vaughan, and McNamara 2014, Auricchio et al. 2014, Morganti et al. 2013). As a result there has not been any computational analysis performed on the leaflets during the crimping or expanding procedure. The leaflets developed in this project (section 5.5) are capable of undergoing deployment due to the highly regular hexahedral mesh. Furthermore, the hexahedral elements offer greater accuracy but the results need to be validated. Two simulations were constructed. The first focused on the stress within the leaflets during crimping (section 8.1.1), and the second simulation focused on balloon expansion (section 8.1.2).

8.1.1 Leaflet Damage Associated with Crimping

It has been shown that leaflets are damaged during the crimping procedure and the extent of damage is dependent upon the diameter to which the device was crimped (Alavi, Groves, and Kheradvar 2014). In the analysis now described, a computational SAPIEN XT TAVI model (section 5.6) was crimped about a balloon (section 5.7) and data on the stress within the leaflets was incrementally recorded at different diameters. The device was crimped by means of a cylindrical surface that radially contracts about the frame, crimping it to the balloon. The cylindrical surface linearly reduces in diameter from 26 mm to 2 mm over a time period of 0.05 seconds. The final diameter of the device is known to be beyond that of which the model is capable of achieving, therefore producing the most data possible.

The simulation failed due to excessive element distortion at a diameter of 4.5 mm. However, in order to retain simulation stability for as long as possible, contact pairings between the cuff and the other components were removed. The cuff does not contribute to the crimping procedure other than restricting motion of the lower edge of the leaflet. Therefore, removing the contact pairings associated with the cuff had a negligible effect on the simulation. Contact pairings between all the remaining components of the simulation remained instated. The normal contact definition was *hard* while the tangential definition employed a penalty friction model with a coefficient of friction of 0.2.

The crimping procedure is graphically shown in Figure 94. The average von Mises stress within each leaflet was calculated, and is plotted in Figure 96.

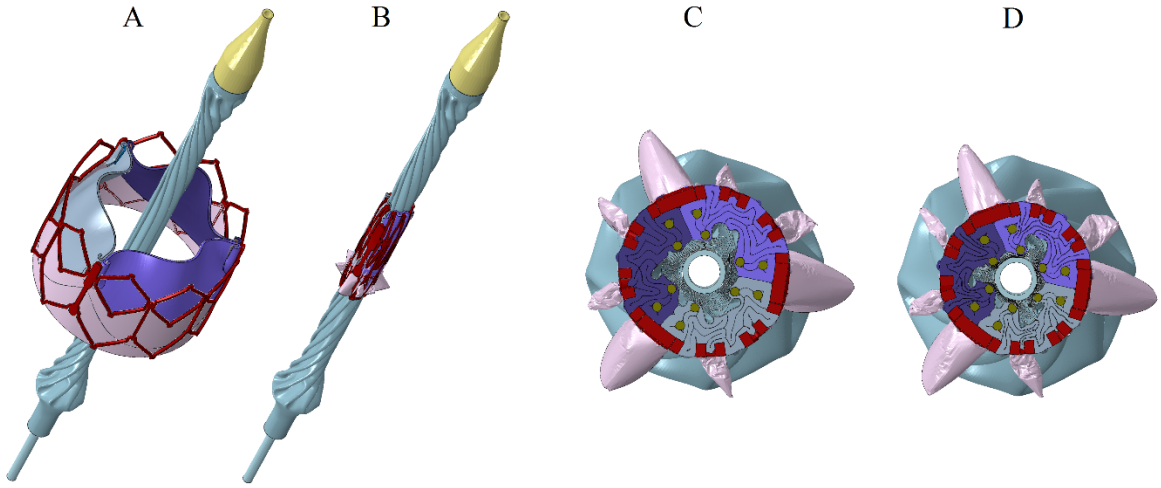

Figure 94. Computational model of the SAPIEN XT device being crimped towards a target diameter of 2 mm. The device pre-crimping (A), the device post crimping (4.5 mm diameter) (B), a cross section of the crimped device crimped to a diameter of 5.25 mm, the deployment diameter of an actual SAPIEN XT (C) and a cross section of the crimped device at the final diameter before failure (D, 4.5 mm diameter).

Throughout the remainder of this thesis, the leaflets are numbered for reference. The leaflet numbering is defined in Figure 95.

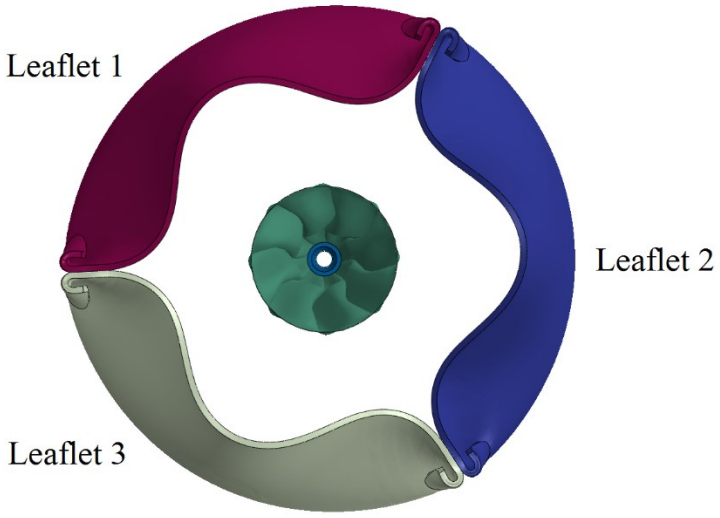

Figure 95. Leaflet labels.

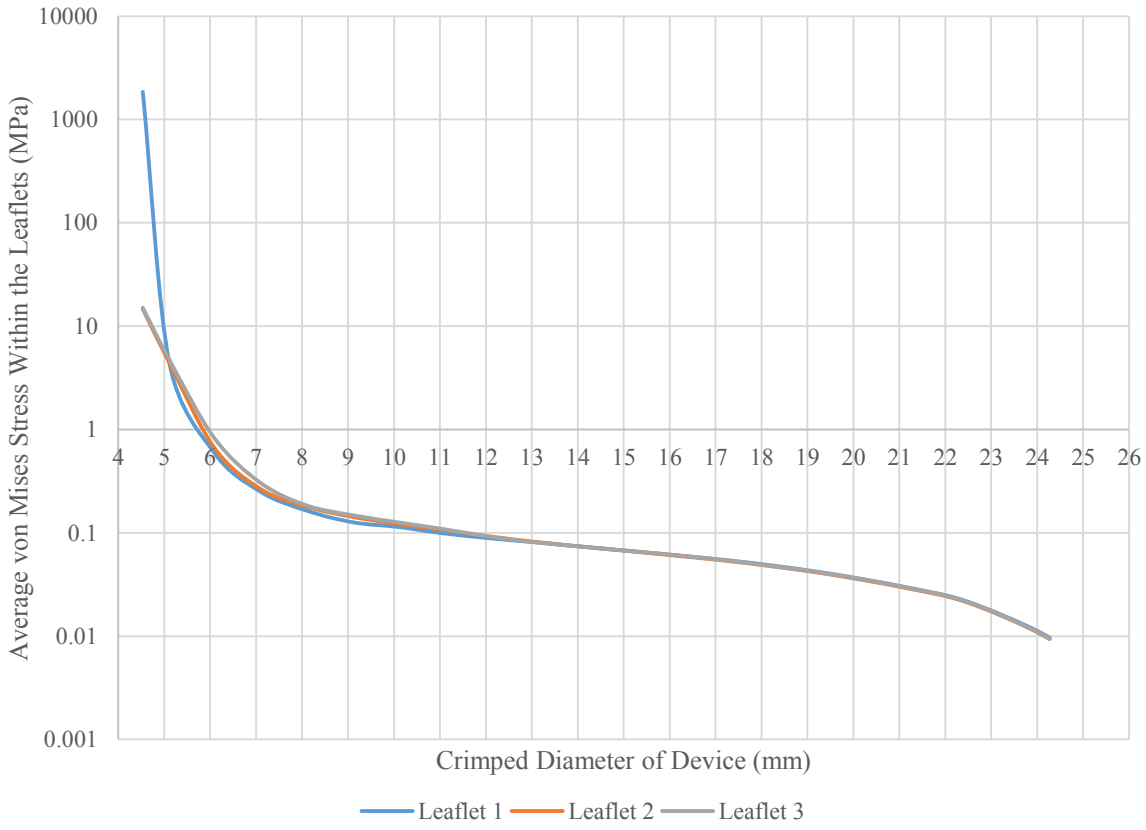

Figure 96. Average von Mises stress within each leaflet during the crimping procedure at different diameters.

Simulation failure was associated with an element in Leaflet 1 severely distorting. This may seem counterintuitive as the simulation appears to be symmetrical. However the valve has an order of

symmetry three while the balloon an order of symmetry eight. This acute variation is enough to destabilise just a single leaflet. The results show that as the device diameter decreases the stress within the leaflets increases. If the device diameter is greater than approximately 9 mm, the stress is a relatively steady increase. However as the device diameter decreases below 9 mm, the stress increase becomes near exponential. The sudden increase in stress is attributed to the leaflets being pinched between the frame struts. In the final frame of the simulation, the average von Mises stress within Leaflet 1 had increased to 1.85 GPa, which indicates a singularity had occurred, possibly due to the leaflet being pinched between the frame struts and then excessively distorting. The 26 mm SAPIEN XT is supposed to be crimped to a diameter of 5.25 mm (determined through measuring a crimping device), a device crimped to that extent is shown in Figure 94(c). It is visually evident that the leaflets at this point have been pinched by the frame. However, the stress within the leaflets is not reliable as the mesh had severely degraded, resulting in poor stress calculations.

While Figure 96 shows the average stress within the leaflets, this is not a good measure of potential leaflet damage as only a small proportion of the leaflets are exposed to elevated stress. By measuring the stresses within high stress elements, the stresses within the pinched areas of the leaflets became more prominent. The 5% of elements with the greatest stress were selected, from which the average von Mises stress was taken and the result is shown in Figure 97. The resultant plot of highly stressed elements demonstrates a sharp increase in stress as the device is crimped beyond a diameter of 7 mm. This is a concerning finding as the SAPIEN XT is crimped to a diameter of 5.25 mm. The stress within the highly stressed elements at a diameter of 5.25 mm was approximately 50 MPa. The areas of elevated stress that are being pinched by the frame will most likely be damaged as the stress is well beyond that of which soft tissue can withstand.

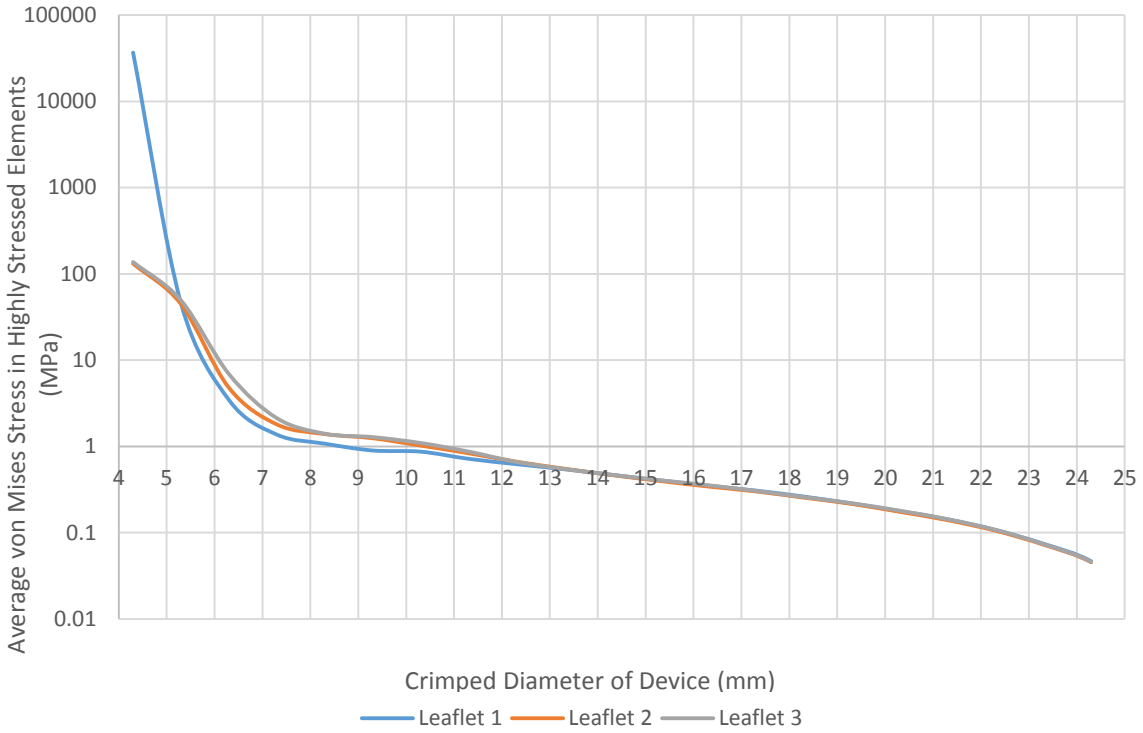

Figure 97. Average von Mises stress of highly stressed elements within leaflet during the crimping procedure at different diameters.

The location of the highly stressed elements is consistent across all three leaflets. Three stress intensities are visible within the body of the leaflet (Figure 98). These stress intensities align with the upper row of cells, where the leaflet migrated between the frame struts and were pinched. There are an additional pair of stress intensities on either side of the leaflet at the commissures, where the leaflets were crushed by the clips. Due to the constraints used, the clips were rigid to the frame in these simulations, which is unrealistic as the leaflets are actually stitched to the frame and will have a degree of flexibility. Therefore, the predicted stress intensities associated with the clips are greater in the simulation than in reality. The three stress intensities within the body of the leaflet, however, are likely areas of leaflet damage.

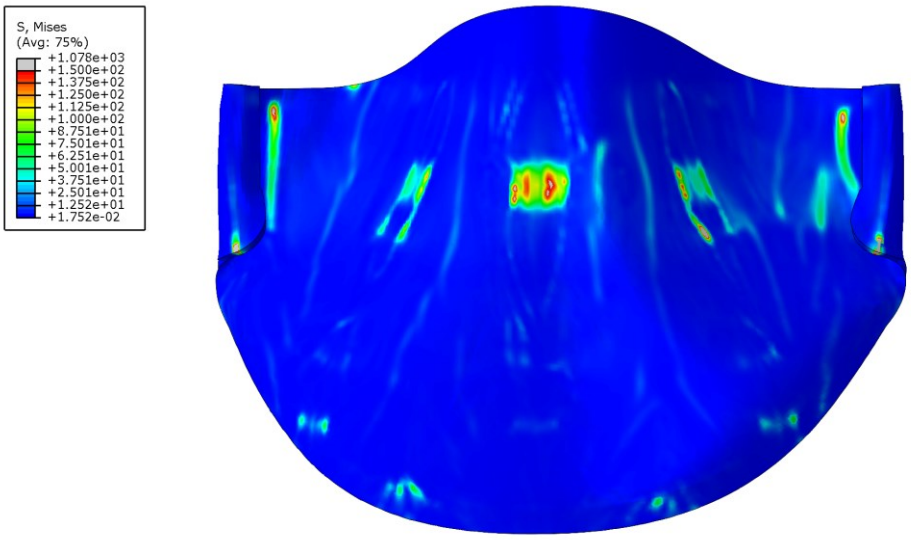

Figure 98. Von Mises stress distribution within a leaflet (displayed in its non-deformed state) that has been crimped to a diameter of 5.3 mm.

8.1.2 Leaflet Damage Associated with Balloon Expansion

During balloon-expansion, the frame is forced to plastically deform and expand. Since, the leaflets are situated directly between the frame and the balloon the leaflets are subjected to high stresses. These stresses have been shown to be orientated about the frame structure, resulting in damage to the collagen fibres (de Buhr et al. 2012). The simulations in this section were constructed to detect the stresses within the leaflets.

The simulations included the complete SAPIEN XT model (section 5.6) undergoing crimping, before balloon expansion. The aortic root model is unnecessary for this analysis, therefore it was excluded in the simulation and the prosthetic device underwent free expansion. Similarly to this analysis in section 8.1.1, multiple simulations were performed, in each simulation the device was crimped to a different diameter: 10 mm, 8 mm and 6 mm. The crimping procedure was modelled as a 0.03 second process. The balloon was then expanded using a linearly increasing internal pressure of 0.5 MPa, a sufficient pressure to over-expand the prosthetic device. This step was modelled as a 0.05 second process. Snapshots of the simulation are shown in Figure 99.

The simulation in which the device was crimped to 6 mm diameter was not completed, rather the simulation failed due to excessively distorted elements within the leaflet meshes.

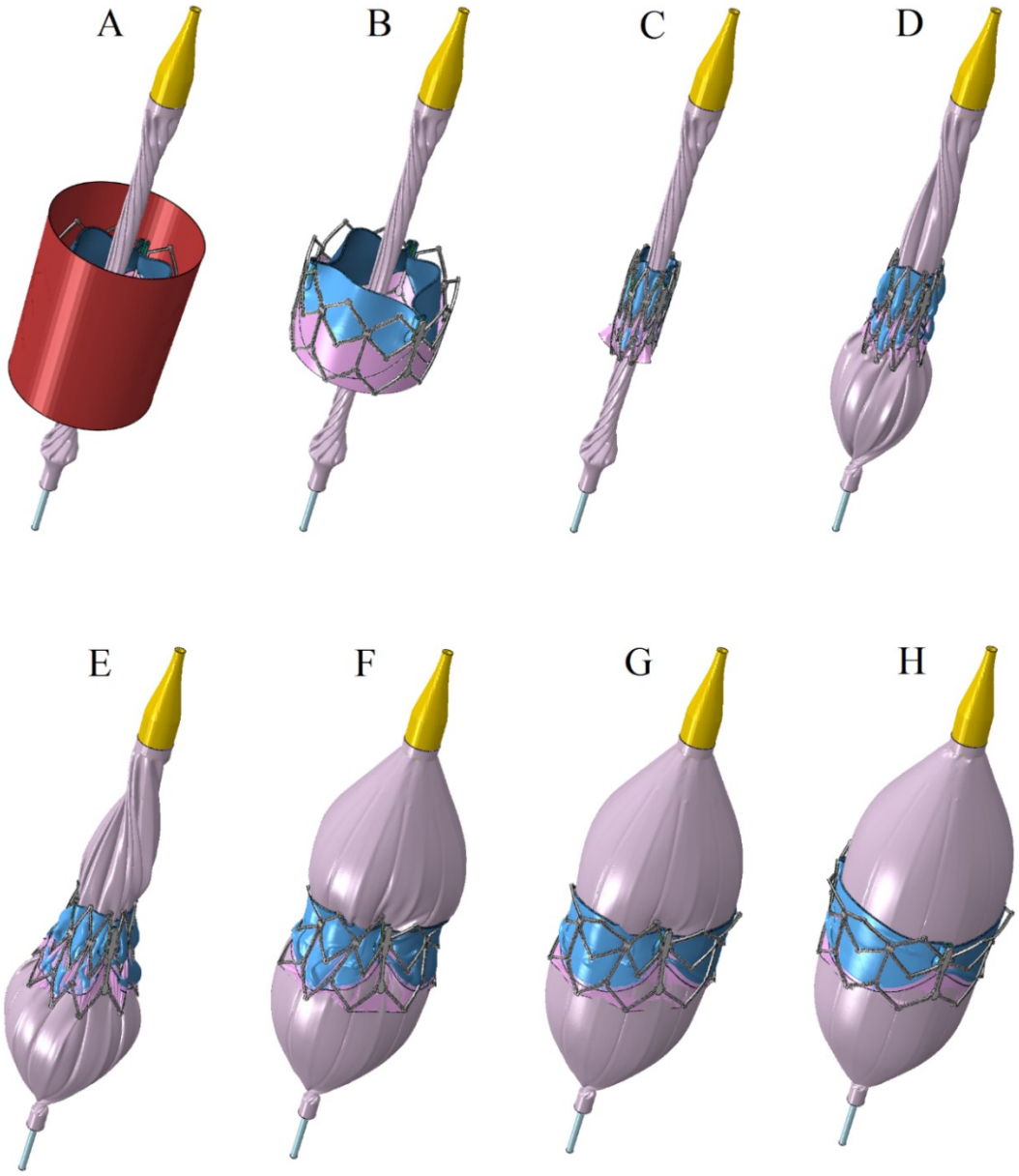

Figure 99. Complete SAPIEN XT model undergoing crimping and free balloon expansion. (A): The full model including the crimping surface. (B-C): Before and after crimping (crimping surface removed). (C-H): Balloon inflation (crimping surface removed).

The radius of the device was calculated as the average distance of each node from the centre of the device, from which the diameter was calculated. It was shown that the pressure required to fully deploy the device (having an average diameter of 26 mm) was dependent on the crimped diameter of the device (Figure 100). A device crimped to a diameter of 10 mm required an internal balloon pressure of 0.225 MPa, while a device crimped to 8 mm diameter required 0.263 MPa.

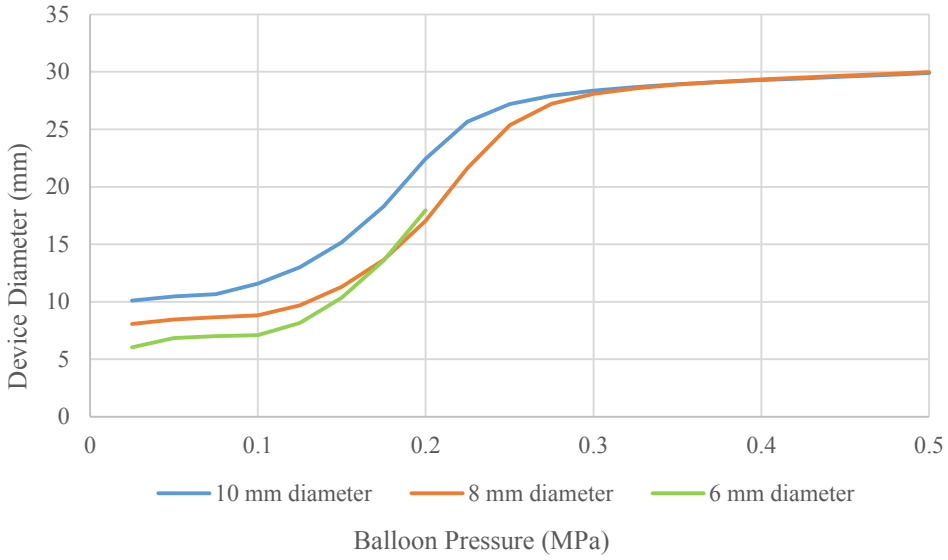

Figure 100. Balloon pressure and the device diameter achieved with reference to devices with carrying initial diameters.

The simulation that modelled the device being deployed from a diameter of 6 mm prematurely ended as elements within Leaflet 2 became excessively distorted. The other two simulations completed successfully.

The von Mises stress within the leaflets is depicted in Figure 101 for the case of a device crimped to a diameter of 8 mm. The imprint of the frame is visually identifiable within the plot, which correlates with previous findings in which balloon expansion was observed to imprint of the frame upon the leaflets post deployment (de Buhr et al. 2012). Stress concentrations were also identifiable about the clips and this is likely to be associated with the boundary conditions implemented on the clips as the conditions are completely rigid, as explained in section 5.6.

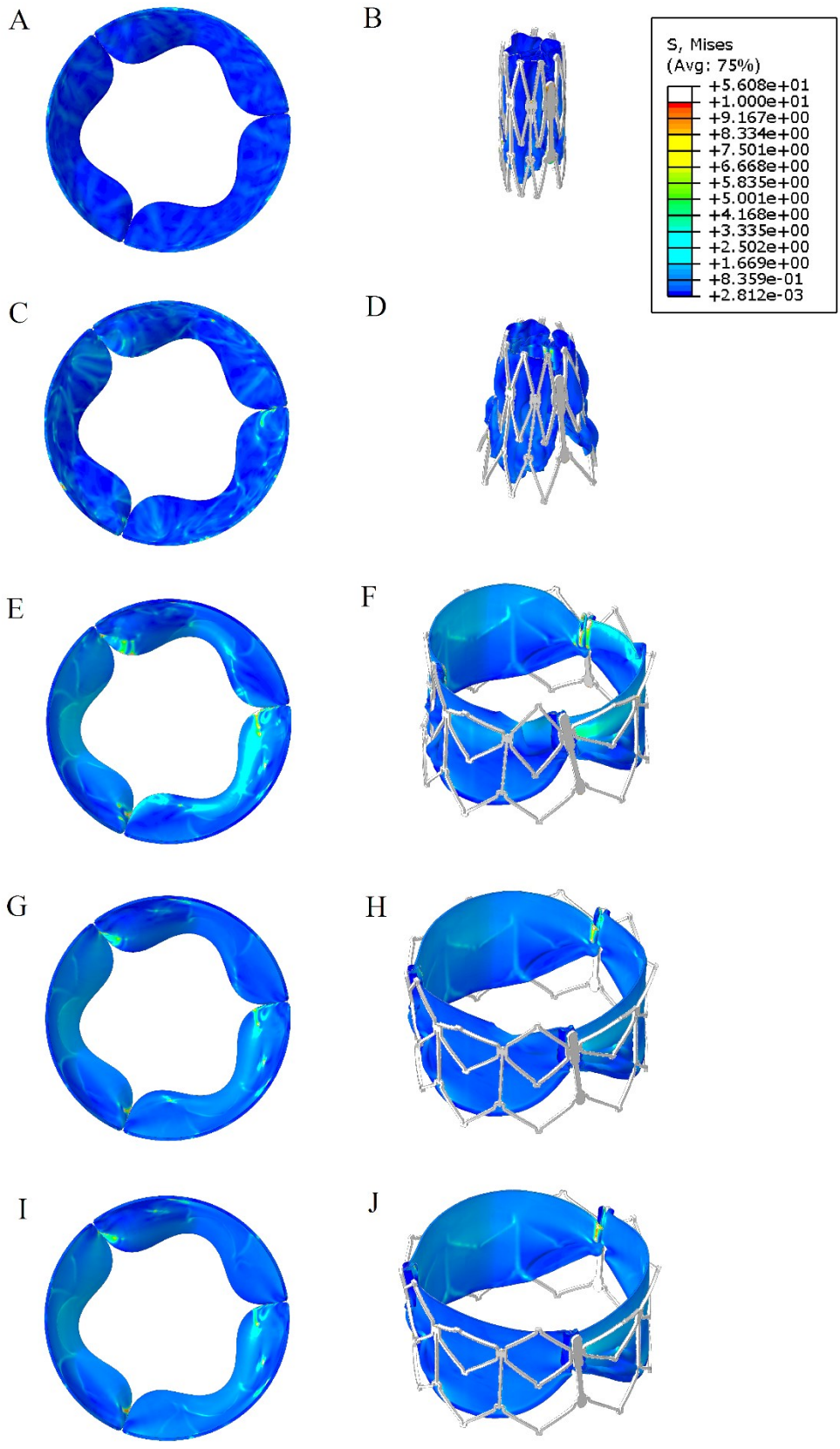

Figure 101. Von Mises stress within the leaflets of a device crimped to a diameter of 8 mm during free balloon expansion. Both undeformed (A, C, E, G and I) and deformed (B, D, F, H and J) are plotted. Data is displayed at five intervals determined through balloon pressure (MPa): 0 (A and B), 0.125 (C and D), 0.25 (E and F), 0.375 (G and H) and 0.5 (I and J).

Visual inspection of the deployment simulation also identified another cause of elevated stress; creases within the leaflets. Figure 102 shows Leaflet 1 (left) and Leaflet 3 (right) of the device that was crimped to a diameter of 10 mm. Leaflet 1 has migrated across the commissure and partially lies across leaflet 3. This creates a fold in the leaflet that increases the stress, as well as further increases the stress associated with the clips. As the balloon inflated, it trapped the fold of Leaflet 1 which effectively decreased the free edge length of the leaflet relative to the frame diameter, this stretched the leaflet leading to a global increase in stress within the leaflet. The average von Mises stress in leaflet 1 is 1.19 MPa, as opposed to the average stresses within leaflet 2 and 3 which were 0.577 MPa and 0.625 MPa respectively. The average von Mises stresses within the leaflets is shown in Figure 103-106.

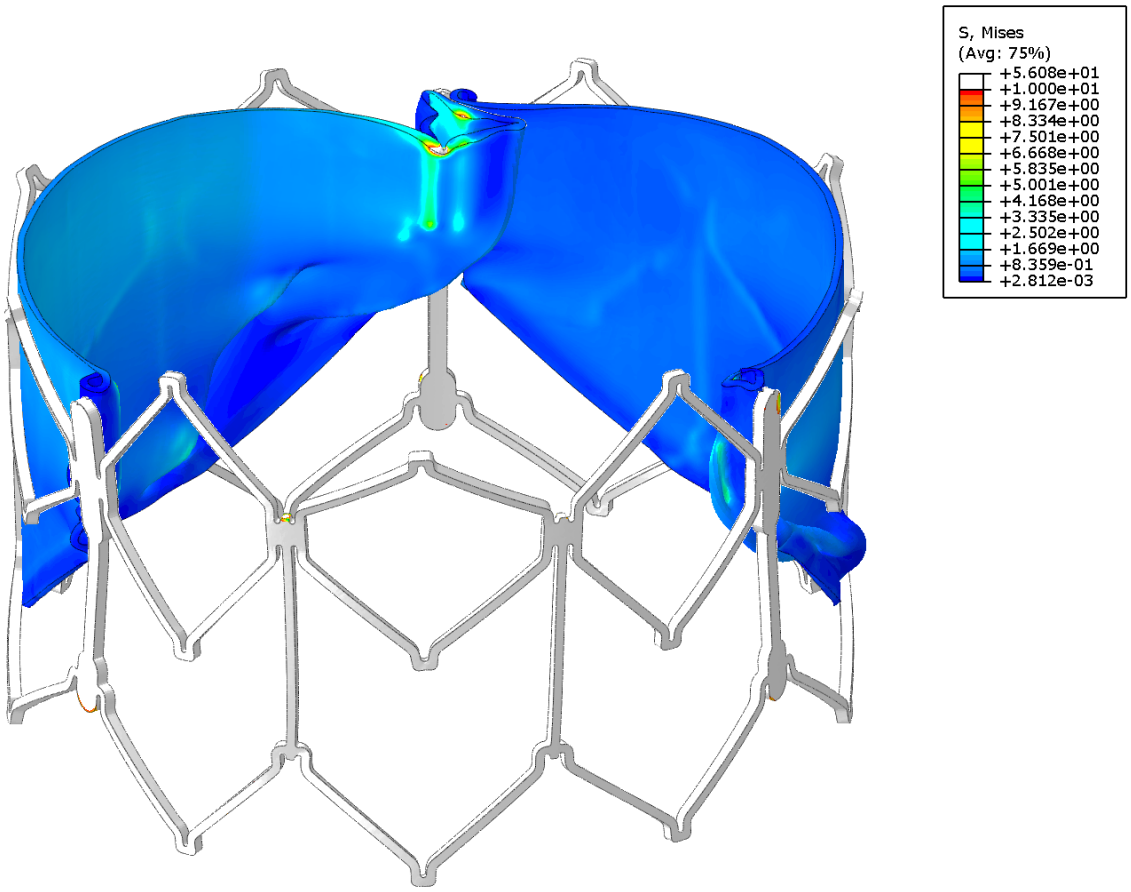

Figure 102. Von Mises stress within a computational model of a fully expanded TAVI device before the balloon has been deflated (with a leaflet removed). The leaflet on the left has folded back upon itself that locally, and globally increases stress within the leaflet.

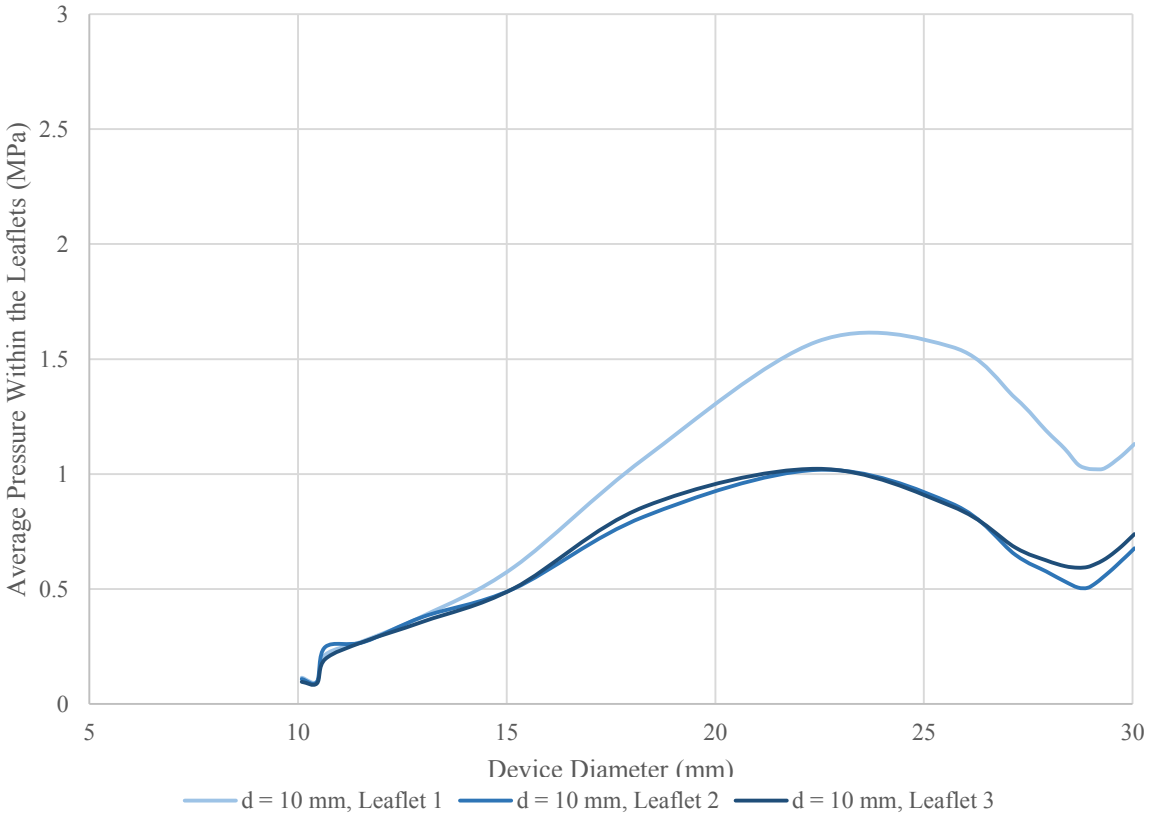

Figure 103. Average stress within the leaflets of devices crimped to 10 mm.

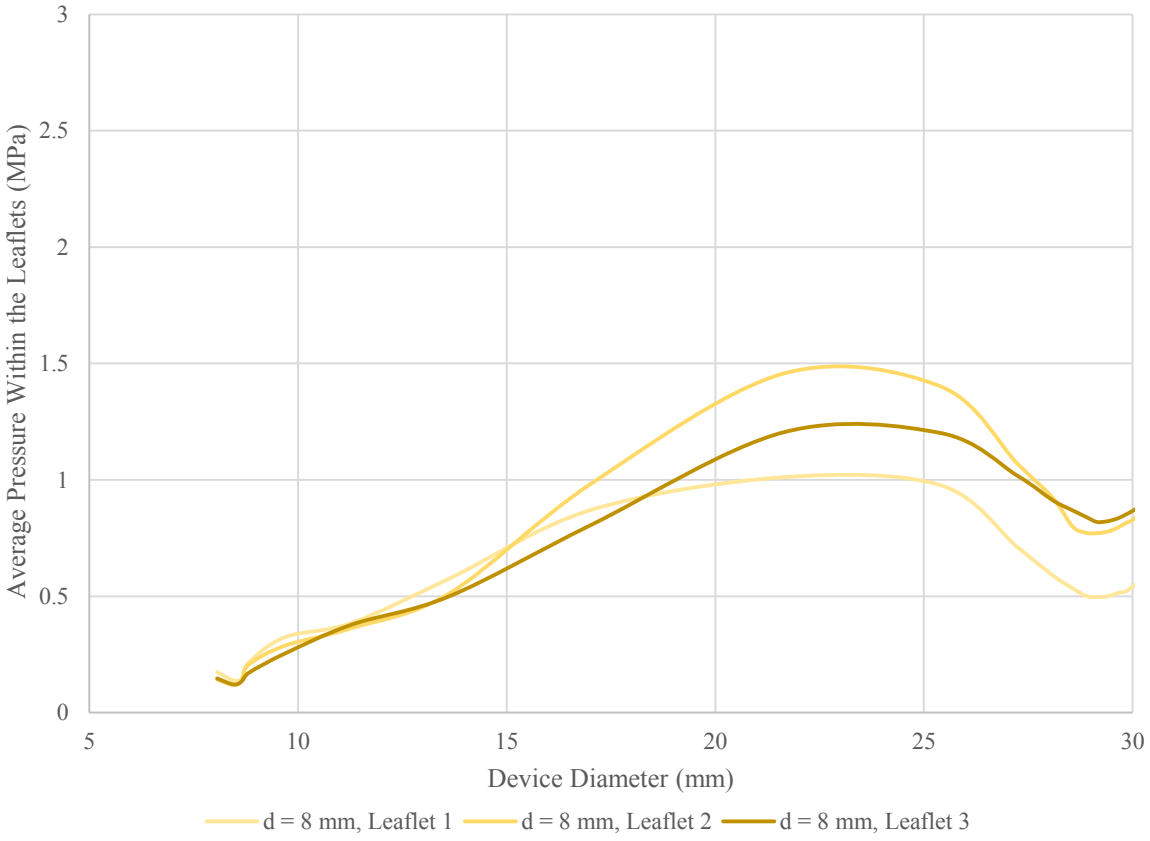

Figure 104. Average stress within the leaflets of devices crimped to 8 mm.

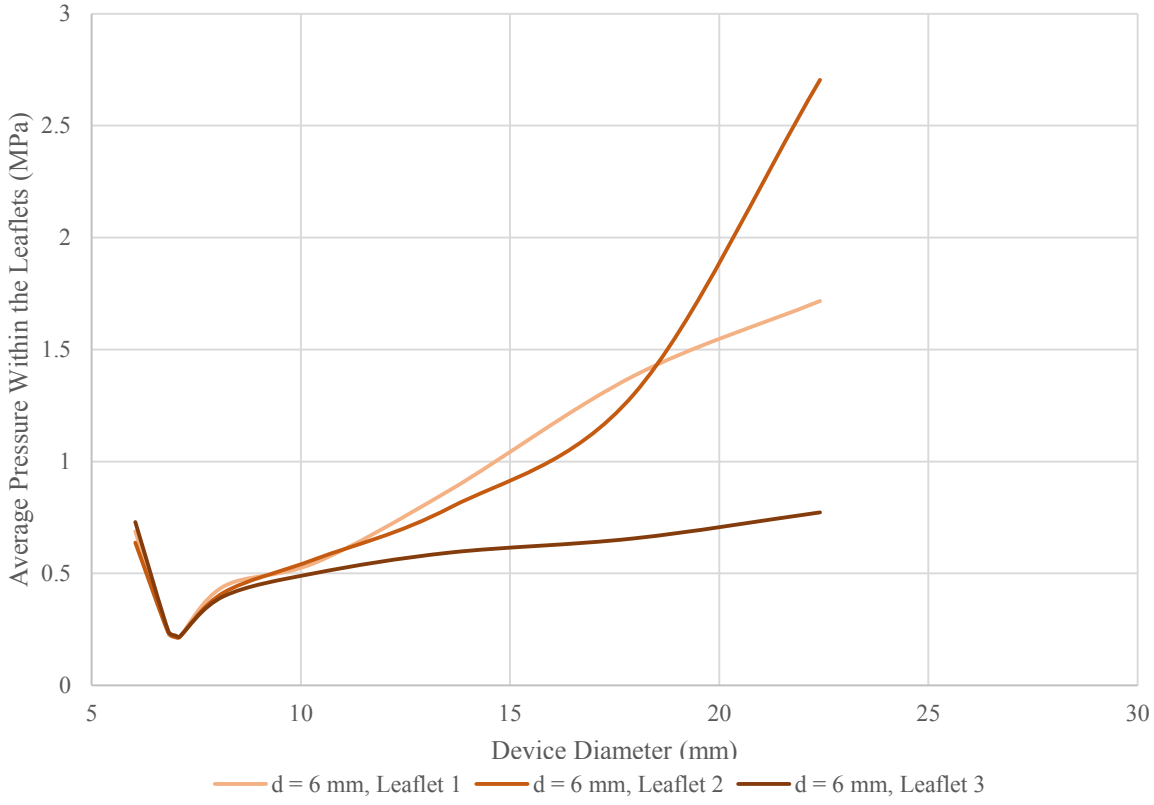

Figure 105. Average stress within the leaflets of devices crimped to 6 mm.

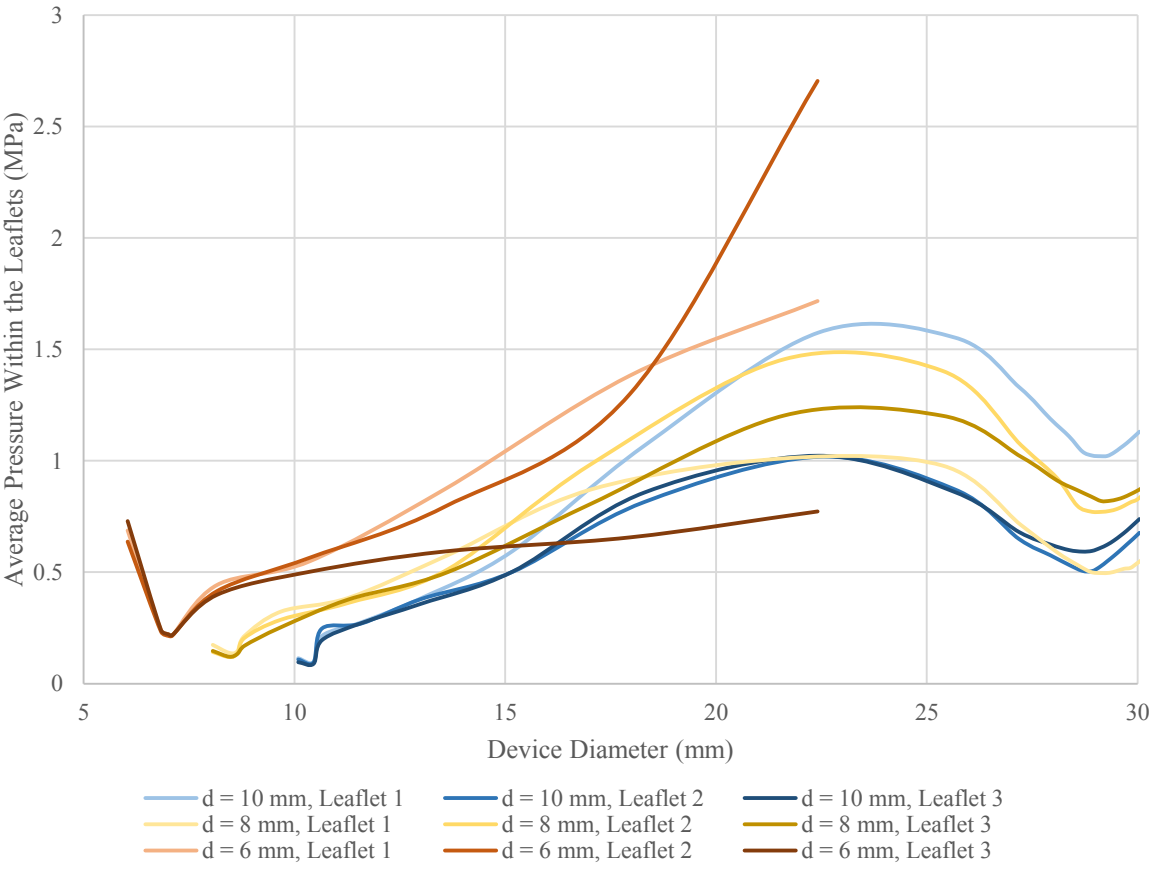

Figure 106. Average stress within the leaflets of devices crimped to varying diameters during balloon expansion.

Initial stress within the leaflets was a resultant of the crimping procedure, as opposed to the balloon expansion. In the initial stages of the expansion step, the device frame elastically recoils, alleviating some of the stress within the leaflets. After the devices recoil, the balloon made contact with the leaflets and began expanding the frame. The stress in the leaflets reached a maximum when the device was at an approximate diameter of 23 mm, after which the stress decreases. This peak in stress was caused by the leaflets unfolding while under load from the balloon. It was also found that if a fold was retained in the leaflet body, or the leaflet moved across the commissure, the stress is greatly increased (shown in Figure 102). Within the simulations, three leaflets ventured across the commissure: from the device crimped to 10 mm, leaflet 1 crossed the commissure, as did leaflet 2 and 3 from the device crimped to 8 mm. All three of these leaflets demonstrated elevated stress levels relative to the remaining leaflets in the valve, as shown in Figure 103 and Figure 104. It is possible that the diameter to which the device is crimped to affects the probability of the leaflets crossing the commissure and should be investigated in future work.

A limitation of this study is the material properties used to model the leaflets. The material model was hyperelastic, while in reality the leaflets are hyperelastic, anisotropic and inhomogeneous. The in-plane material properties of the leaflets are almost uniform, as a result the leaflets can be described as near orthotropic. The hyperelastic material model used in the simulation was based on the stiffer in-plane material properties, allowing the simulation to accurately capture valvular function. This stiffened material properties may not be accurate at calculating the stresses within areas of the leaflet that are being pinched between the frame struts.

8.2 The Requirements of Friction on Leaflet Operating Simulations

The previous simulations analysed stress within the leaflets during the crimping and deployment procedures. Friction is important to these simulations and if it is neglected the leaflet behaviour dramatically changes. In section 8.1.2 it was found that folds in the leaflets during deployment dramatically increase the stress within the leaflets. However, if friction is neglected in the simulation the folds are no longer present, therefore reducing the perceived stress.

In the later sections of this chapter, the full TAVI device is simulated undergoing deployment into the realistic aortic root model. The objective of the simulation is to monitor stress within the leaflets undergoing a cardiac cycle, while the frame is in an imperfect operating condition. Unfortunately, including a friction model decreases the stability of the simulation. In this section the effects of a friction model on the leaflet operating stress was explored.

In section 5.5.1 a triplet of leaflets were loaded with a uniform pressure load to simulate the blood pressure experienced by the leaflets during the cardiac cycle. The ability of the leaflets to effectively

close was monitored. The simulation included three leaflets that were rotated to form a valve, and six clips, two for each leaflet. The clips and the lower edges of the leaflets (Figure 46), were stitched to the frame. Rather, along with the cuff they were constrained in all degrees of freedom. A pressure load was applied to the top surface of the leaflets representing the pressure experienced during the cardiac cycle. A typical loading profile experienced by the aortic valve during the cardiac cycle is shown in Figure 47 (Kim et al. 2008).

Two simulations were performed with *hard* normal contact behaviour. In the first simulation the frictional model was frictionless, while a penalty friction model was applied to the second simulation with a coefficient of friction of 0.2.

The average von Mises stress within the leaflets was calculated over the duration of both simulations. And the results are plotted in Figure 107.

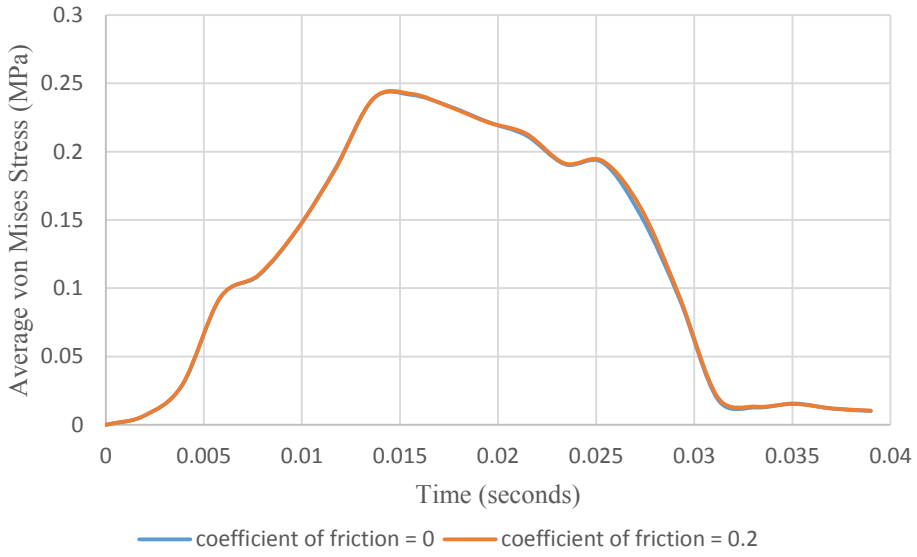

Figure 107. The effect of including a friction model in the average von Mises stress within the leaflets of TAVI devices.

The average discrepancy between the stresses with in the leaflets was 1.4%. This discrepancy is considered sufficiently small to use frictionless simulations to analyse the stress within the leaflets.

8.3 Leaflet Operating Stress within an Imperfect Frame

TAVI device frames do not achieve perfect deployment, and often feature non-circular lumens or irregular struts. These imperfections may alter the manner in which the leaflets close, as the shape of the leaflet attachment line, and clip placement is dependent upon the frame topology. Variation in leaflet closing dynamics will undoubtedly alter the operational stress. When this is the case the life expectancy of the devices may be lower than predicted through experimental analysis. Experimental fatigue analysis is generally performed on TAVI devices. However, as the analysis was *in vitro,* an idealised frame was likely employed for the experimental analysis.

In section 7.3, a simulation demonstrated how a large plaque locally disrupted the frame's shape. The orientation of the leaflets to this local distortion is hypothesised to be important as the leaflet attachment line can be locally altered due to the distortion. In order to validate this hypothesis, multiple simulations were performed, each with the TAVI device in a different orientation relative to the native valve and plaque.

8.3.1 Methods

The simulations developed to analyse post-deployment leaflet operating stress has two phases: simulated deployment (based on the simulation described in section 7.3) and simulated cardiac cycles (based on the simulation described in section 5.5.1). During the first phase, the SAPIEN XT computational model (section 5.6) underwent deployment by means of the NovaFlex+ delivery system (section 5.7) into a native aortic root (section 6.4). The delivery balloon was positioned in a transapical deployment orientation within the native aortic root model, such that the centre of the balloon passes through the centre of the valve, and no part of the delivery system is in contact with the aortic root model. The SAPIEN XT model was positioned concentrically with the balloon where the device lined up with the native aortic root and the centre of the balloon. During the second phase, pressure applied to the device leaflets followed a load profile as shown in Figure 47.

Similarly to the simulation described in section 8.2, a bullet shaped surface was included in the model that was used to open the native aortic valve. Boundary conditions were also applied to the upper and lower edge of the aortic root inhibiting motion in all degrees of freedom. The contact properties were defined as *hard* normal behaviour and frictionless tangential behaviour. The simulation constitutes four steps which are described below and the contact pairs defined in each step are shown in Table 29.

Contact Pairs\Step	Step 1	Step 2	Step 3	Step 4	Step 5
Balloon – Balloon	Active	Active	Active	-	-
Balloon – Wire	Active	Active	Active	-	-
Balloon – TAVI leaflets	Active	Active	-	-	-
Balloon – Frame	Active	Active	Active	-	-
Balloon – Aortic Root	Active	Active	Active	-	-
Device Leaflets – Clips	Active	Active	Active	Active	Active
Device Leaflets – Device Leaflets	Active	Active	Active	Active	Active
Device Leaflets – Frame	Active	Active	Active	Active	Active
Native Leaflets – Native Leaflets	Active	Active	Active	Active	Active
Native Leaflets – Bullet Surface	Active	-	-	-	-
Native Leaflets – Aortic Root	Active	Active	Active	Active	Active
Crimping Surface – Frame	Active	-	-	-	-
Plaque – Native Leaflets	Active	Active	Active	Active	Active
Plaque – Aortic Root	Active	Active	Active	Active	Active
Frame – Frame	Active	Active	Active	Active	Active
Balloon – Native Leaflets	-	Active	Active	-	-
Balloon - Plaques	-	Active	-	-	-
Frame - Plaques	-	Active	Active	Active	Active

Table 29. Contact pairs throughout the deployment simulation.

Step 1: In the first step the TAVI device was crimped by means of the cylindrical surface. Displacement boundary conditions reduced the diameter of the cylinder from 26 mm to 10 mm, thus reducing the diameter of the frame to 10 mm at its widest point. Simultaneously, a bullet shaped surface was displaced through the native leaflets forcing them open. This step was modelled over a 0.02 second time step.

Step 2: At the beginning of this step, two contact pairings were removed: the first was the pairing between the bullet shaped surface and the native valve, the second was between the crimping surface and the frame. This allowed the frame and native valve to elastically recoil. The boundary condition on the lower edge of the aortic root was removed at the beginning of this step also. Simultaneously, a pressure load of magnitude 0.233 MPa was applied to the internal surface of the balloon, as determined in section 7.2. This step was modelled as a 0.0233 second process.

Step 3: The pressure within the balloon was reduced from 0.233 MPa to zero over a time period of 0.01 seconds, allowing the balloon to elastically recoil to an orientation similar to its original position. All contact pairings featuring the delivery apparatus were removed.

Step 4: During this step a pressure load was applied to the aortic side of the prosthetic leaflets to simulate a cardiac cycle. This step time was determined by the loading profile: 0.039 seconds.

A major discrepancy between the simulation described above, and the simulation described in section 7.3 is the absence of the relaxation step between the crimping step and the expansion step. The step served to gently unload the frame and native leaflets. However, it was found that the simulations described in this section retained stability if instantaneous unloading was used. Since the step did not serve any purpose, it was removed for computational efficiency.

In order to find any significance of plaque placement relative to the TAVI device, the simulation was repeated eight times, each with a different device rotational orientation. The orientation of the device was defined as the clockwise angular rotation, θ, of the device leaflets relative to the native leaflets. The angle is defined in Figure 108. The angles simulated were: 0, 15, 30, 45, 60, 75, 90 and 105 degrees.

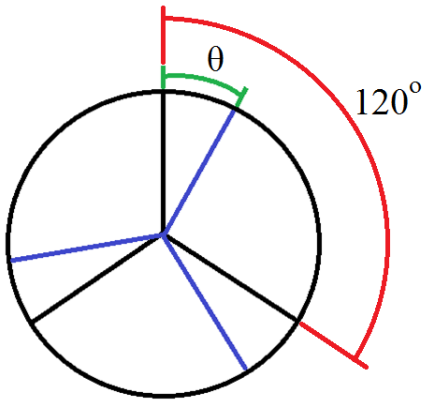

Figure 108. The angle of rotation of the TAVI device leaflets (blue) relative to the native tissue leaflets (black) is defined in green.

8.3.2 Results

Of the eight simulations, seven completed successfully. The simulation with a device orientation of 75 degrees failed due to an element in one of the prosthetic leaflets undergoing excessive distortion. This is a demonstration of the instability of these simulations, if the leaflet loading is acutely changed by altering the device orientation, it can induce premature numerical failure. Of the simulations that completed, all of the frames suffered from varying degrees of noncircular distortion. In section 7.3 it was shown that a single plaque was responsible for the most significant distortion in the frame. This

same plaque was again responsible for the most significant distortions in the frames here. A sample of the resultant frames, with the plaque associated with frame distortion, is shown in Figure 109.

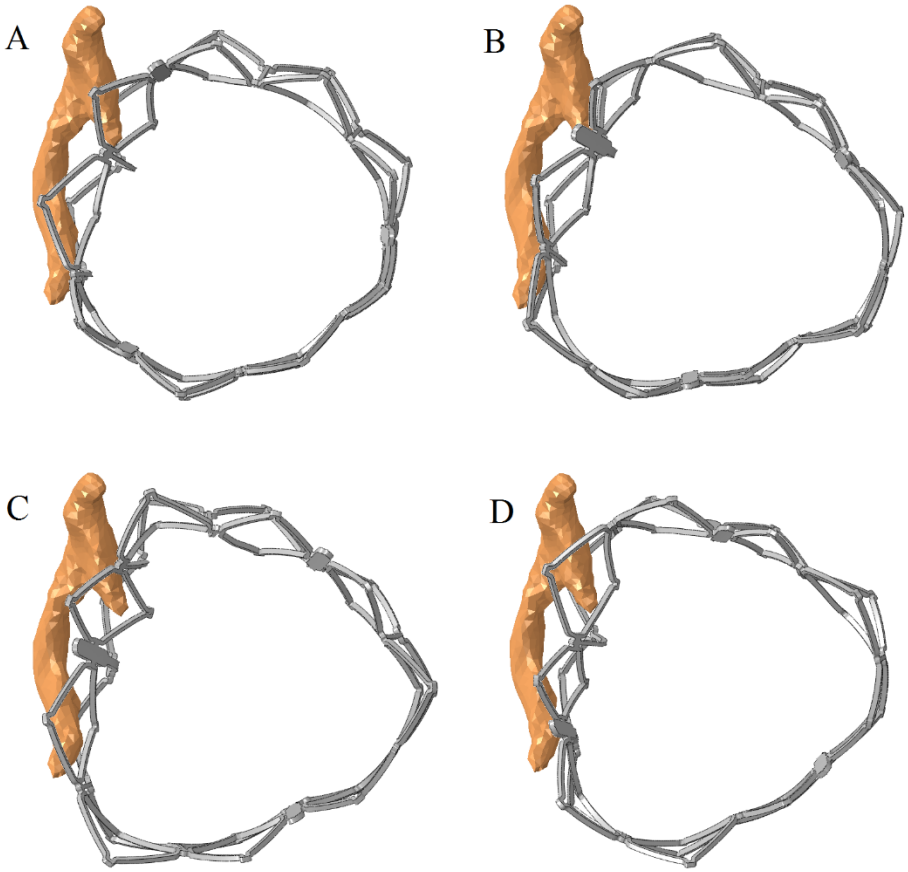

Figure 109. Distortion of the TAVI device frame occurred irrespective of orientation: θ = 0 (A), 30 (B), 60 (C) and 90 (D) degrees.

In all cases, the frames were noticeably non-circular irrespective of device orientation. Furthermore, as the orientation of the TAVI device changed, the leaflet attachment line also changed. This alteration to the leaflet attachment line changed the leaflets closed configuration (Figure 110). Figure 110(B) shows one of the leaflets has an additional fold along the upper edge suggesting it is much too large for the orifice area that the TAVI device is spanning. There was a small hole running through the centre which may have been capable of creating a source of transvalvular leakage.

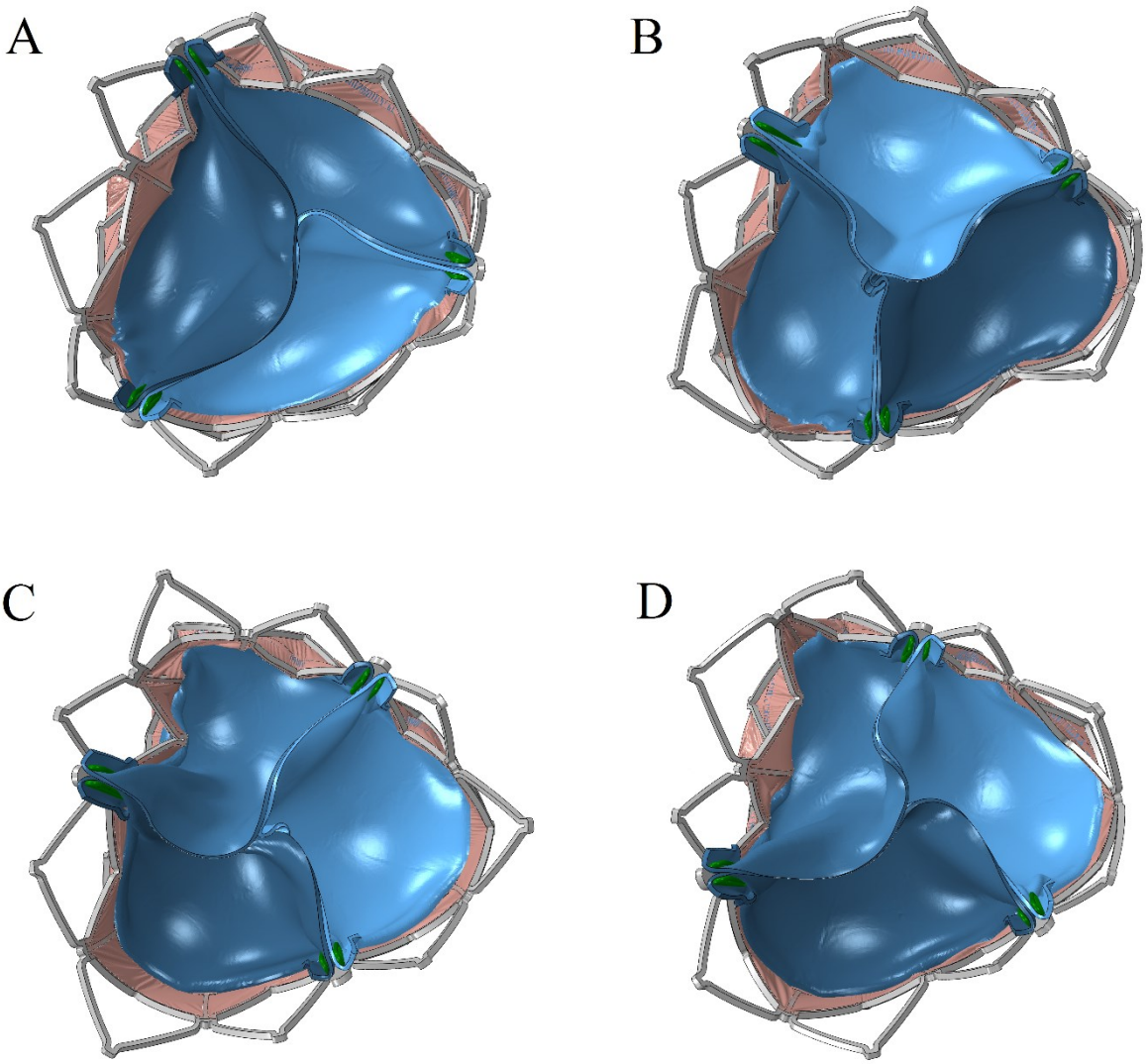

Figure 110. Closed leaflet orientation associated with device deployment orientation: θ = 0 (A), 30 (B), 60 (C) and 90 (D) degrees.

The stress within the leaflets predictably changes throughout the cardiac cycle depending on the closing formation. The stresses within all the leaflets was calculated to find the average von Mises stress, which is plotted in Figure 111-113. For comparative purposes, Figure 111-113 also includes the average von Mises valvular stress of the idealised valve over a cardiac cycle, which was simulated in section 5.5.1.

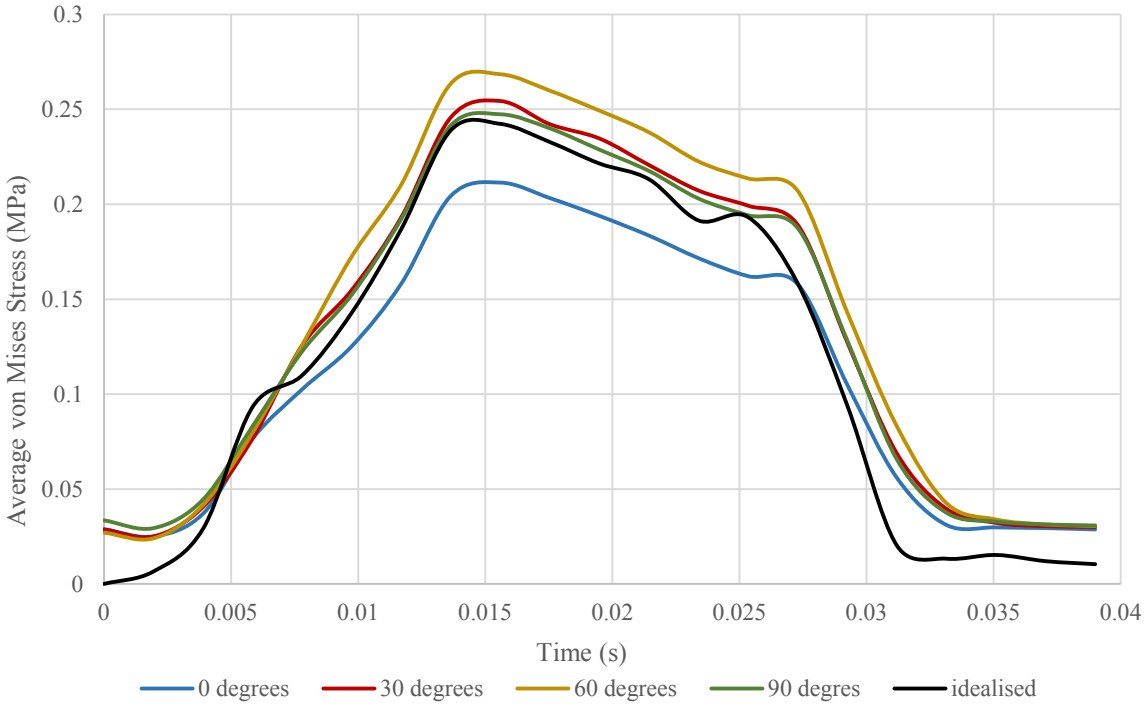

Figure 111. Average valvular stress within a device deployed to a diameter of 26 mm, over a cardiac cycle, with reference to device orientation during deployment. The valvular stress of a circular device is also included for comparison.

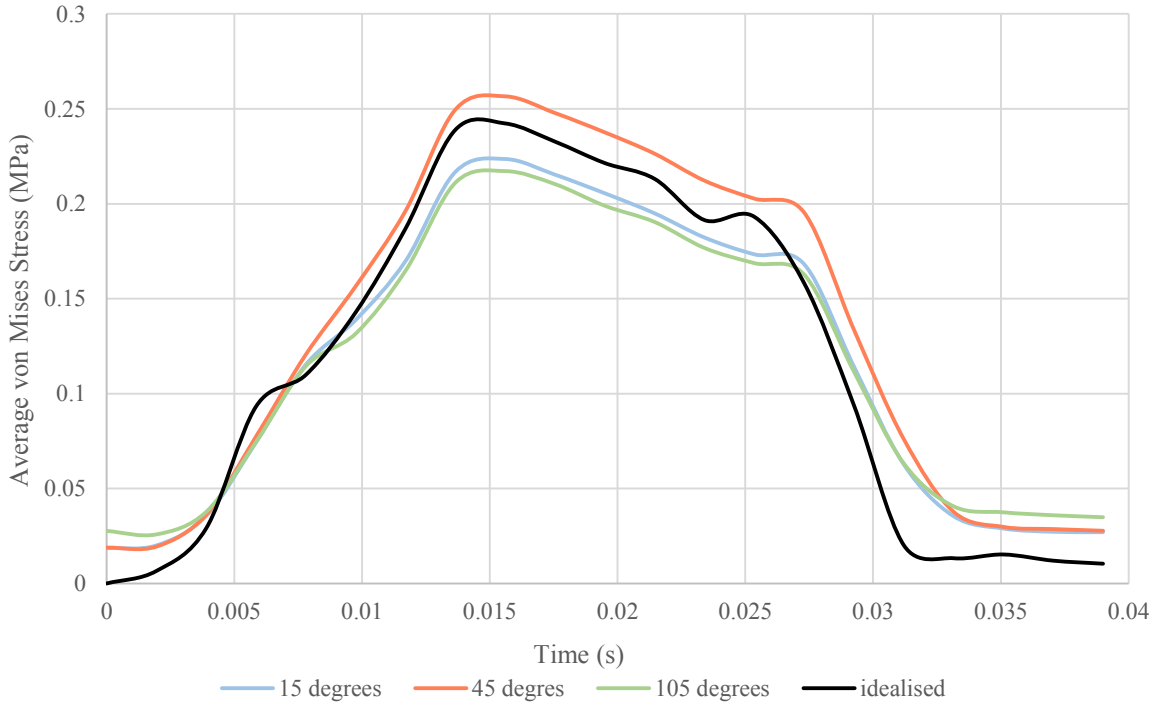

Figure 112. Average valvular stress within a device deployed to a diameter of 26 mm, over a cardiac cycle, with reference to device orientation during deployment. The valvular stress of a circular device is also included for comparison.

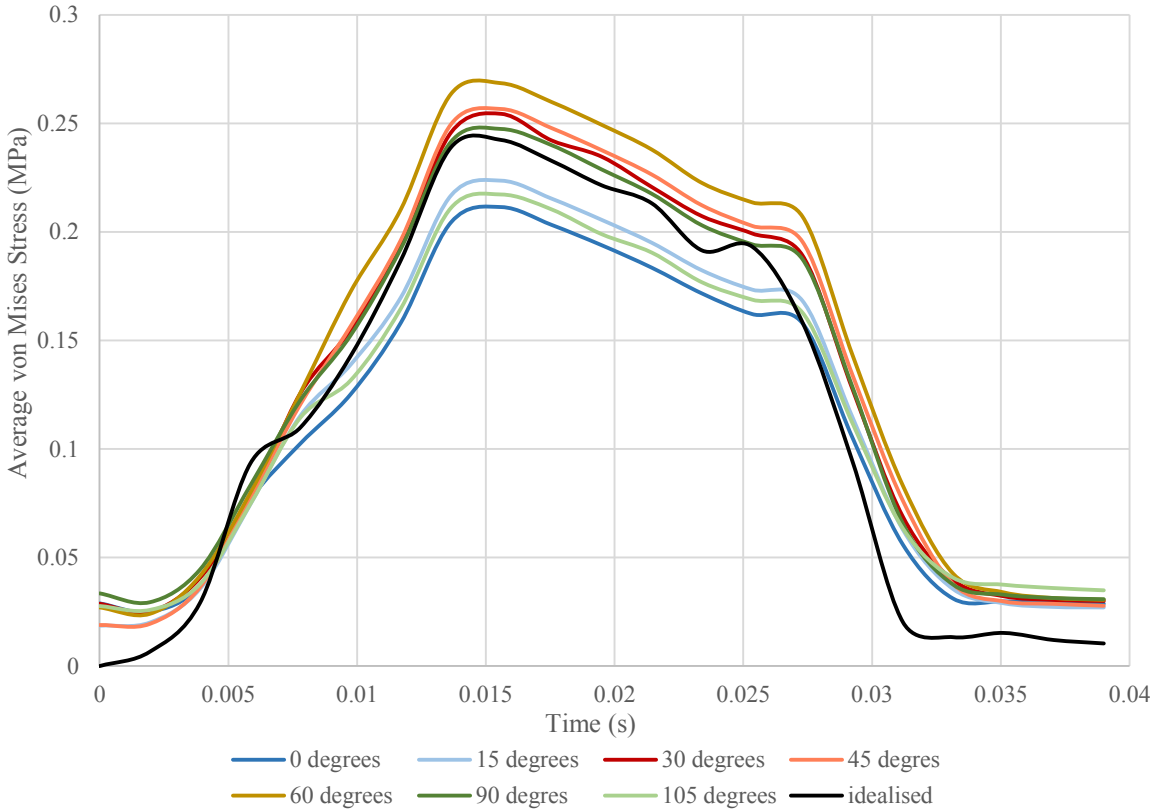

Figure 113. Average valvular stress within a device deployed to a diameter of 26 mm, over a cardiac cycle, with reference to device orientation during deployment. The valvular stress of a circular device is also included for comparison.

8.3.3 Discussion

In order to quantify the degree of frame distortion, the deviation from a perfect cylinder (σ_{DPC}) was calculated. The average frame diameter was calculated through node tracking techniques (as described in section 7.2). The standard deviation of each node's position from the average diameter was then calculated by

$$\sigma_{DPC} = \sqrt{\sum \frac{(R - \bar{R})^2}{n}} \qquad [26]$$

where n is the number of nodes in the frame, R is the distance of an individual node from the centre of the device and $\bar{R}$ is the average distance of all the nodes to the centre of the device. The σ_{DPC} for each simulation is shown in Table 30. All of the simulations demonstrated elastic recoil of the frame to some degree, the target diameter, maximum achieved diameter, and estimated recoiled diameter of the frame is also shown in Table 30.

Device Angle	Target Diameter	Achieved Diameter	Recoiled Diameter	σ_{DPC}
0	26	26.06 mm	23.73 mm	1.066 mm
15	26	26.00 mm	23.53 mm	1.280 mm
30	26	26.00 mm	23.95 mm	1.287 mm
45	26	25.97 mm	23.93 mm	1.368 mm
60	26	25.89 mm	23.86 mm	1.500 mm
75	26	-	-	-
90	26	25.95 mm	23.78 mm	1.346 mm
105	26	26.05 mm	23.60 mm	1.233 mm

Table 30. Deployed frame metrics with reference to device orientation.

The σ_{DPC} values were very small, it was initially thought that there was an error with the calculation. However, when a frame was imaged with circles representing the average diameter, upper standard deviation, and lower standard deviation, it became evident that the values are realistic (Figure 114).

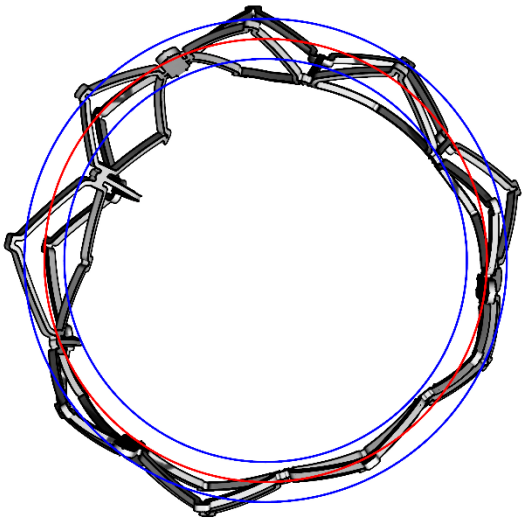

Figure 114. A post-deployment frame orientated at 0 degrees, with a target diameter of 26 mm. The red circle represents the average diameter, while the blue circle represents the standard deviation of the frame from the average diameter.

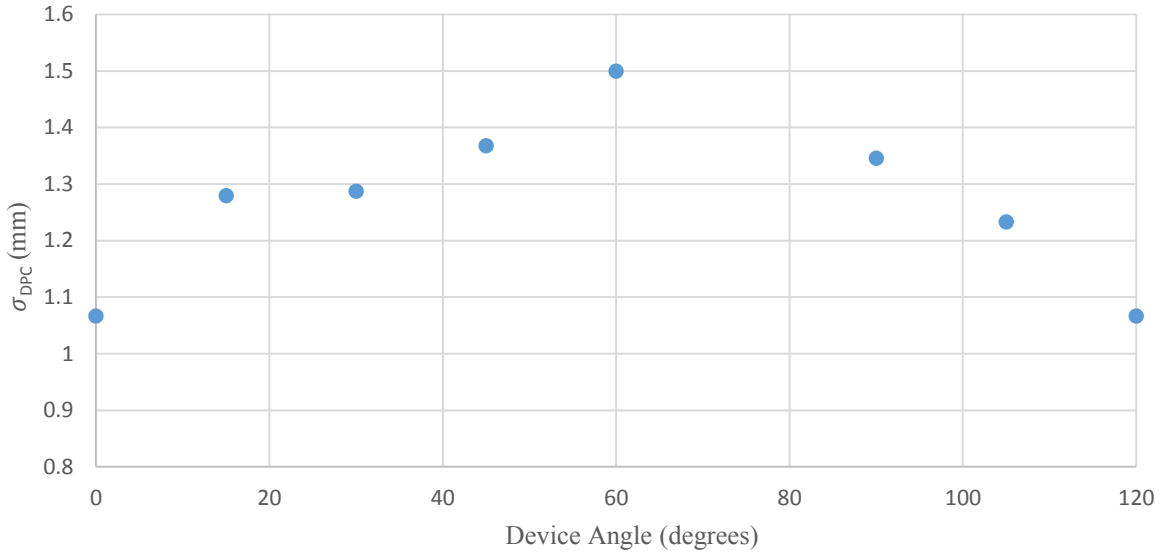

Figure 115. Relationship between device orientation, and σ_{DPC}.

The σ_{DPC} varied with the device orientation. Figure 115 shows the σ_{DPC} plotted against the device angle, revealing a trend: σ_{DPC} is at a minimum when the native leaflets and prosthetic leaflets are in phase (0 and 120 degrees), while σ_{DPC} reaches a maximum when the leaflets are out of phase (60 degrees).

This variation σ_{DPC} could potentially be associated with the presence of the clips. The constraints that hold the clips to the frame are completely rigid. As a result, the balloon applies a non-uniform load onto the frame as it must also conform about the rigid clips. However, section 7.1 shows that the clips do not have a large affect on the frame position. Inclusion of the clips was assocaited with an average nodal position discrepancy of 0.0343 mm, approximately 10% of the device's strut width.

The average stress within the leaflets varied with device orientation, as shown in Figure 111-113. The results from a simulation of a TAVI device within a circular frame are also plotted for comparison. Figure 111-113 show that a positive σ_{DPC} does not necissarily have a negative effect on the valvular stress; devices orientated at 0, 15 and 105 degrees experienced reduced stress levels throughout the cardiac cycle.

Peak stress is a better measure of device damage as it is the highly stressed areas that are likely to fail first. A measure of peak stress is the standard deviation of stress within the nodes from the average valvular stress, as defined by

$$\sigma_{vM} = \sqrt{\sum \frac{(\sigma - \bar{\sigma})^2}{n}} \qquad [27]$$

where σ is the nodal von Mises stress, $\bar{\sigma}$ is the average von Mises stress and n is the number of nodes. The greatest average stress occurs at 0.015 seconds into the cardiac cycle. As a result, the standard deviation of stress for each valve was calculated at this time point for each simulation; the results are plotted in Figure 116.

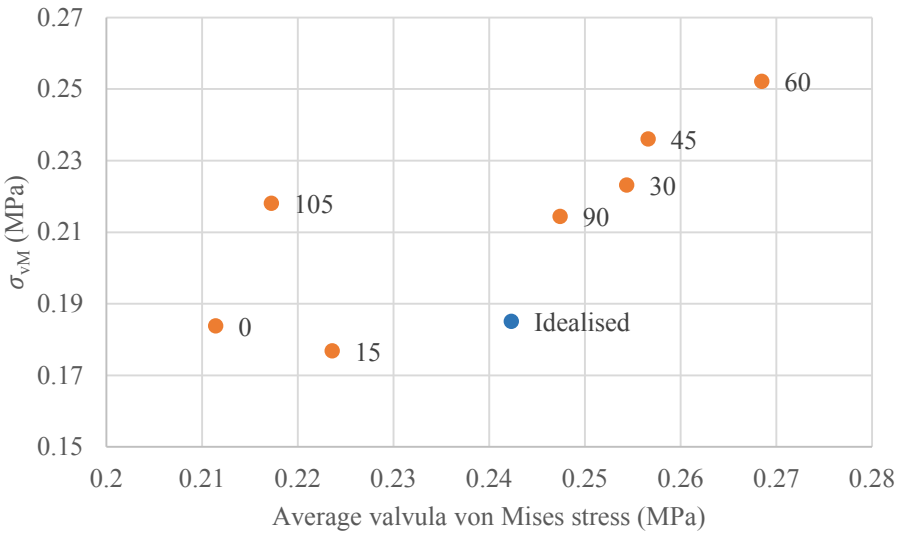

Figure 116. σ_{vM} and average valvular von Mises stress (data labels indicate device orientation).

A valve orientation between 30 and 90 degrees resulted in an average stress, and σ_{vM}, that was greater than the idealised frame. Devices that are deployed in this orientation are therefore likely to fail before an idealised device. A device orientated at 105 degrees had a lower average stress but a greater σ_{vM}, it is not clear if this device will fail before or after the idealised device through fatigue. Devices orientated at either 15 and 0 degrees had both a lower average stress, but also a lower σ_{vM}, which suggests they would have a superior life expectancy relative to an idealised device. Visually, it is apparent that the stress concentrations are in the commissures of the valve, as shown in Figure 117.

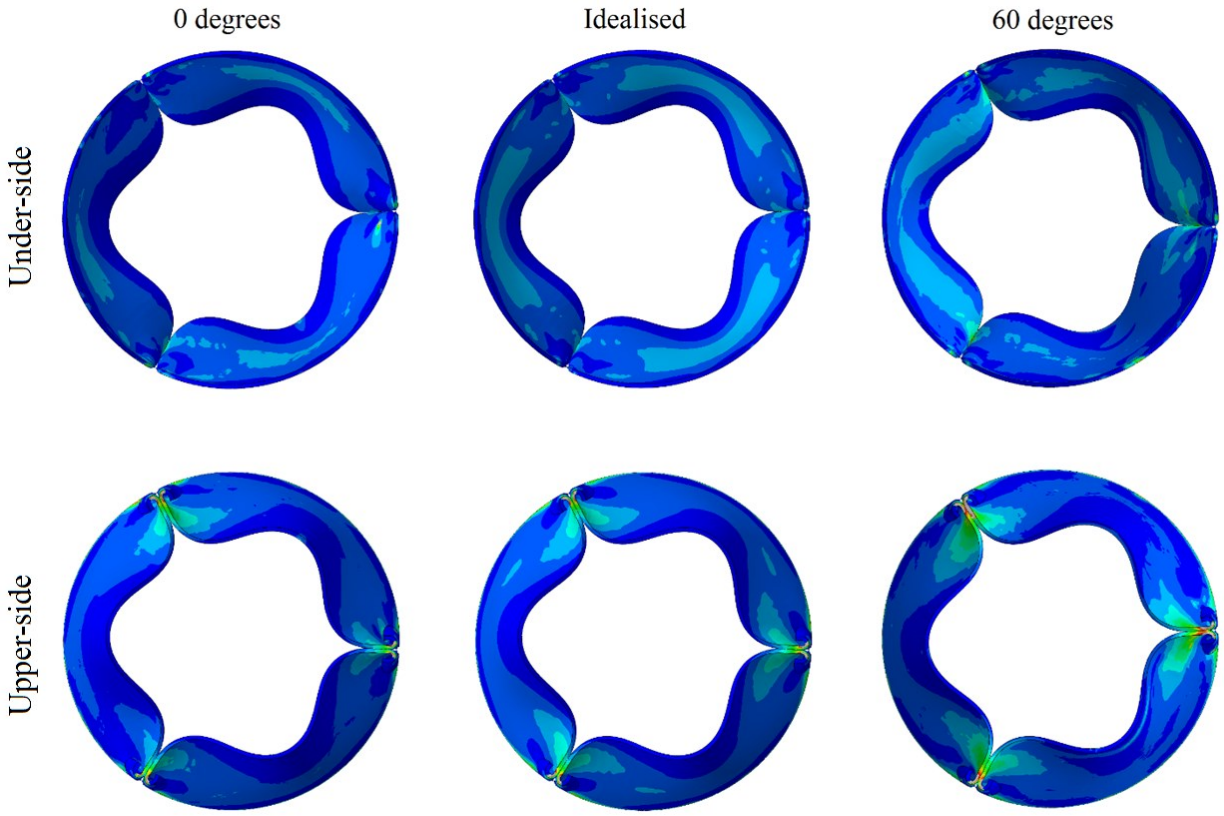

Figure 117. Von Mises stress on the upper- and under-side of the leaflets (displayed in the nondeformed state) at peak load during the cardiac cycle.

The stress within the leaflets again follows a familiar trend. As the orientation of the TAVI device leaflets deviates from in-phase with the native valve, the stress within the leaflets increases. There is also a linear relationship between σ_{DPC} and average von Mises stress within the valves. For the case of 0.015 seconds into the cardiac cycle simulation, the relationship is shown in Figure 118. A linear trend line has been added to the data that has a correlation coefficient of 0.768.

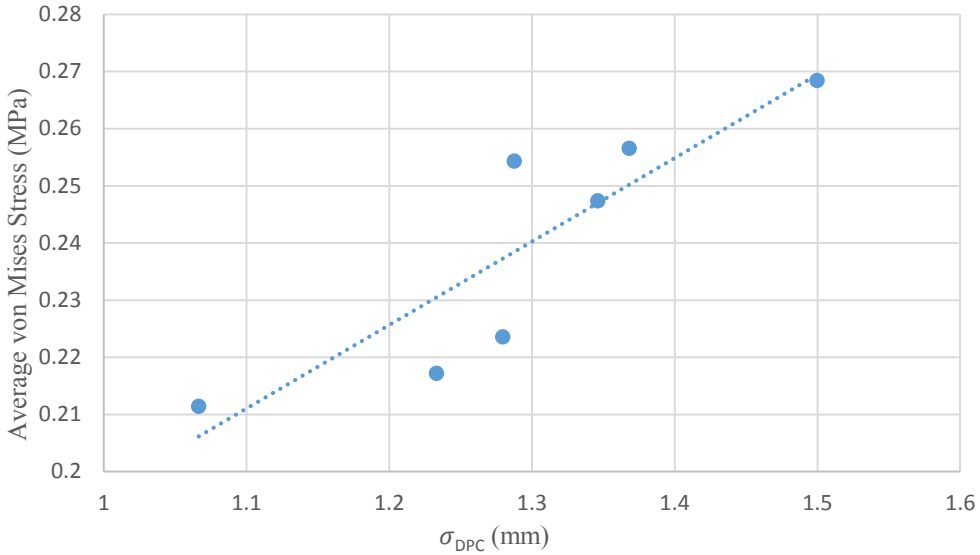

Figure 118. Relationship between σ_{DPC} and average stress within the leaflets.

The maximum average valvular stress varied from 0.211 MPa (0 degrees) to 0.264 MPa (60 degrees), an increase of 25%. This is likely to decrease the life span of the device considerably due to fatigue, the extent of which is unknown, but a valuable area of future research. For this specific patient case, device orientation is therefore important if the device is to be deployed to a diameter of 26 mm; the device should be deployed at, or as close to, an angle of 0 degrees. Controlling the rotational orientation of the device during deployment would be advantageous for increasing the device life span. The idea has already been discussed in section 7.5 as it was thought that it would also allow for devices to be developed that have increased resistance to both PAR and embolism.

All the simulations within this chapter included elastic recoil post dilation, and presented large frame distortions. It is likely that post-deployment angioplasty would be used in an attempt to increase the device diameter, and reduce σ_{DPC}. As a result, the device was modelled undergoing deployment in eight further simulations, in which over-expansion of the device was explored. Deployment and post-deployment angioplasty was modelled as a single balloon inflation to an increased pressure, resulting in a maximum device diameter of 28 mm. The rotational device orientation was again 0, 15, 30, 45, 60, 75, 90 and 105 degrees.

All eight simulations completed successfully, and all of the frames experienced varying degrees of frame distortion. The frames post deployment are shown in Figure 119.

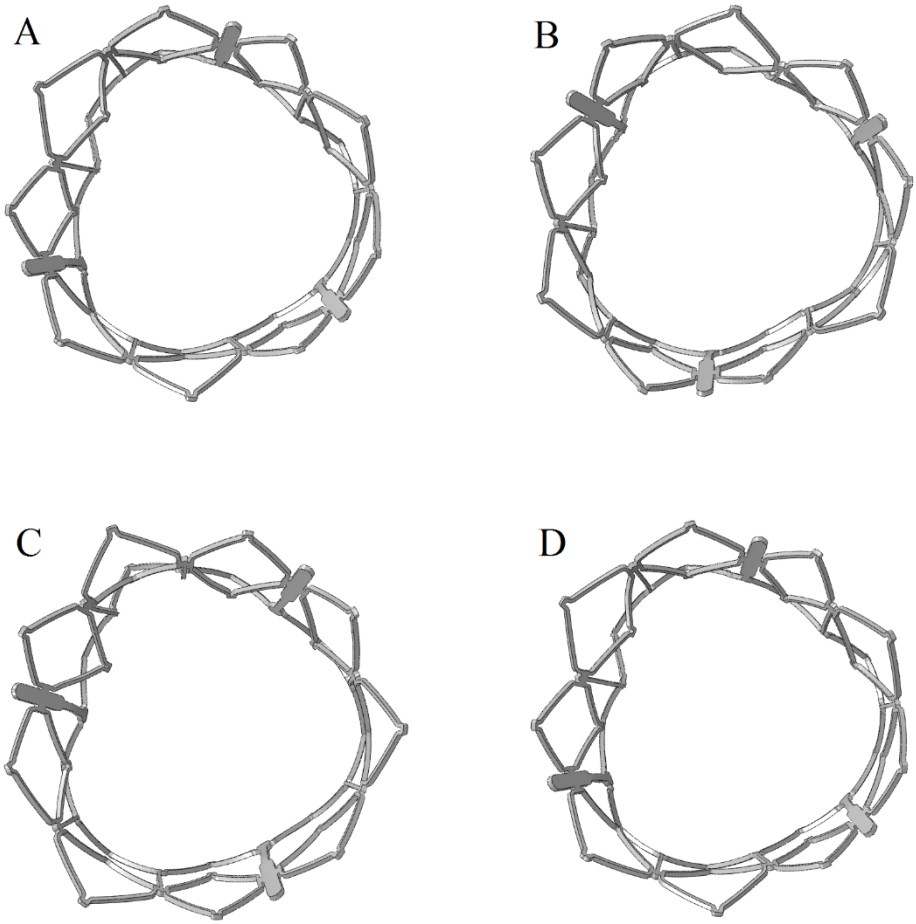

Figure 119. Post deployment TAVI frames that were deployed to a target diameter of 28 mm, each at a different orientation: 0 (A), 30 (B), 60 (C) and 90 (D) degrees.

As before, the final frame geometry affects the leaflets closing orientation. The leaflets under peak pressure for each simulation are shown in Figure 120. In Figure 110(B), the device deployed at an orientation of 30 degrees demonstrated an additional fold in one of the leaflets, suggesting the valve was susceptible to transvalvular leakage. This fold is no longer present in the over-expanded devices, as shown in Figure 120(B). This suggests the use of post deployment angioplasty can protect from transvalvular leakage.

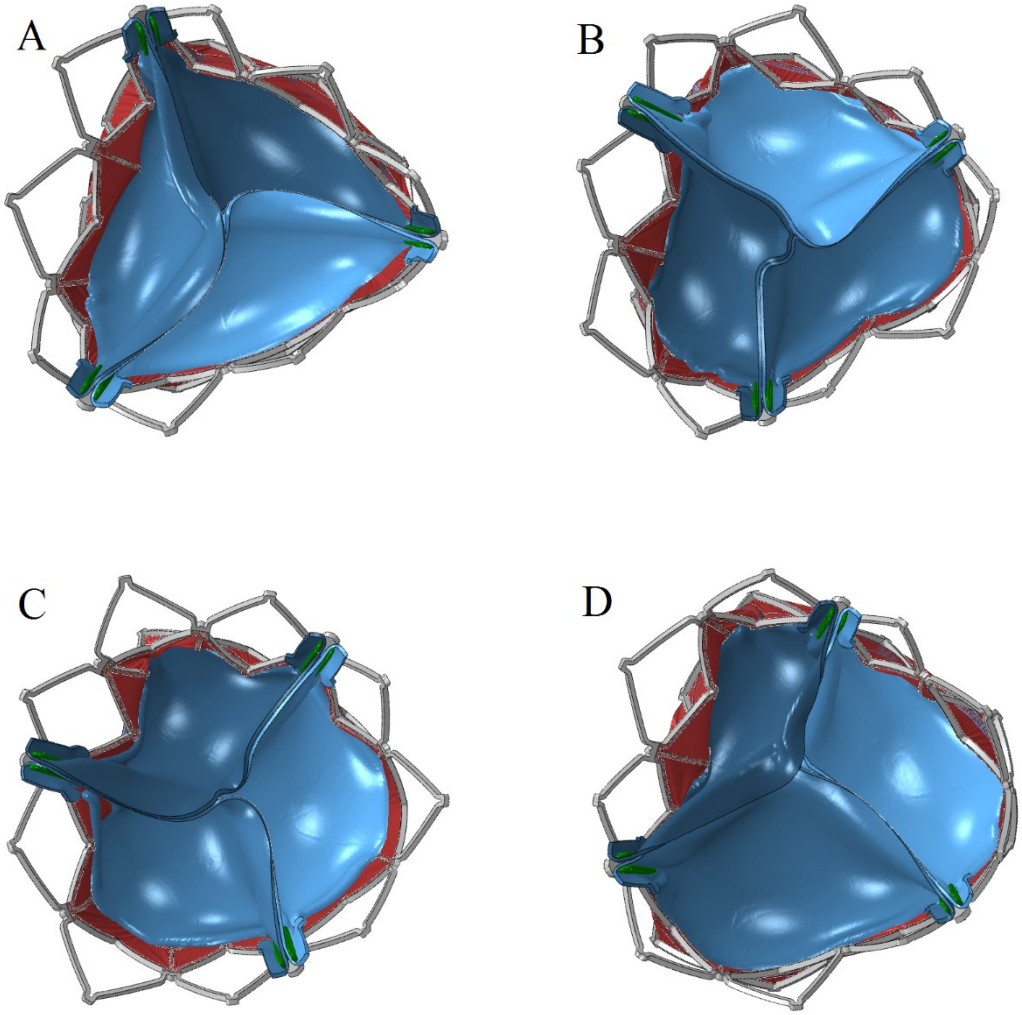

Figure 120. Closed Leaflet orientation associated with device deployment orientation. A: 0 degrees, B: 30 degrees, C: 60 degrees, D: 90 degrees.

The achieved diameter, recoiled diameter and σ_{DPC} for these eight simulations is shown in Table 31. All of the devices were deployed to within 0.2 mm of the target diameter. The σ_{DPC} decreased in all the simulations when the device was deployed to a diameter of 28 mm, with exception to the device orientated at 0 degrees, in which the σ_{DPC} increased by 26%. The recoiled diameter of the model deployed at 0 degrees was significantly greater than all other models. This unusual behaviour was caused by volumetric intersection of the device frame and deployment balloon. As the balloon deflated, it pulled the device inwards. If the results associated with the 0 degree orientation are ignored, the computational simulations demonstrate that in most cases over-expansion reduces frame distortion.

Device Angle	Target Diameter	Achieved Diameter	Recoiled Diameter	σ_{DPC}
0	28	27.99 mm	24.93 mm	1.434 mm
15	28	28.03 mm	25.89 mm	0.637 mm
30	28	27.88 mm	25.91 mm	1.084 mm
45	28	27.86 mm	25.94 mm	1.110 mm
60	28	27.88 mm	25.96 mm	1.183 mm
75	28	27.83 mm	25.83 mm	1.139 mm
90	28	28.00 mm	26.04 mm	1.100 mm
105	28	28.03 mm	25.92 mm	1.162 mm

Table 31. Deployed frame metrics with reference to device orientation.

The resultant stresses in the valves over a cardiac cycle is shown in Figure 121-123. All of the simulations demonstrated stress levels throughout the cardiac cycle that were greater than the case of a circular frame. Furthermore, the frames also recoiled to approximately 26 mm, the same diameter as the idealised device. This increase in stress is therefore associated with imperfect frames, as opposed to an increased orifice area. The stress in the valves deployed to 28 mm were also greater than those deployed to 26 mm; a sample of device orientations was selected for comparison and is shown in Figure 124 and Figure 125.

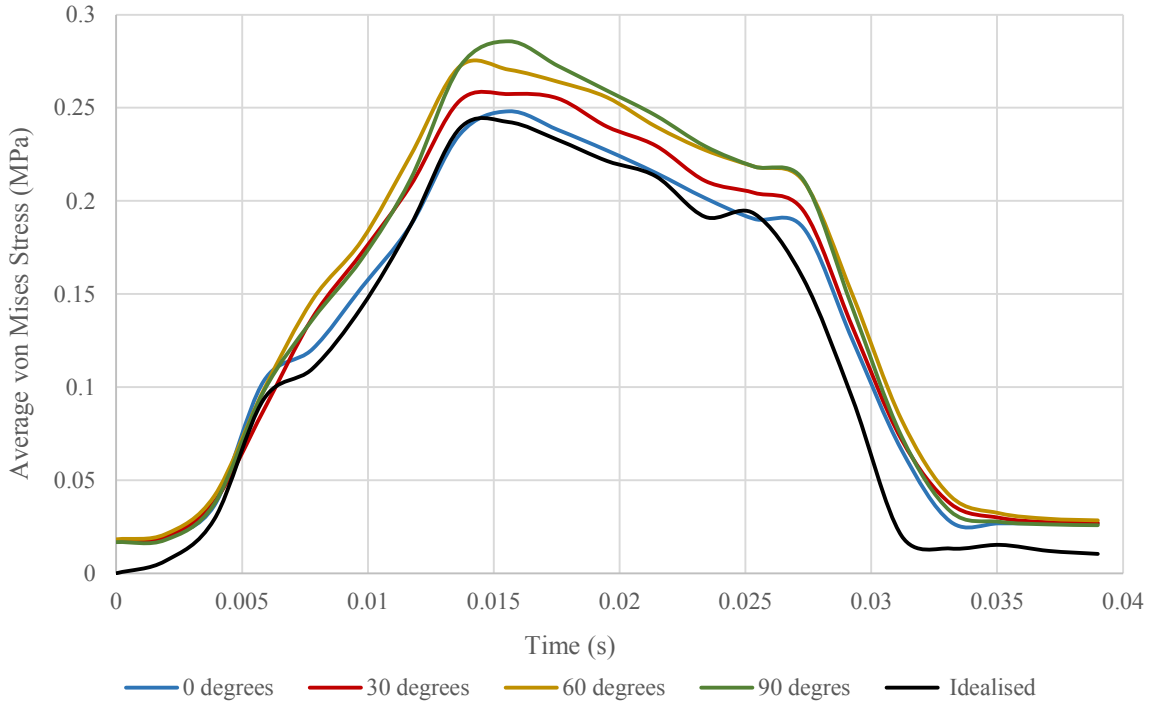

Figure 121. Average von Mises stress in devices deployed to a diameter of 28mm over a cardiac cycle, with reference to device orientation during deployment. The valvular stress of an idealised device is also included for comparison.

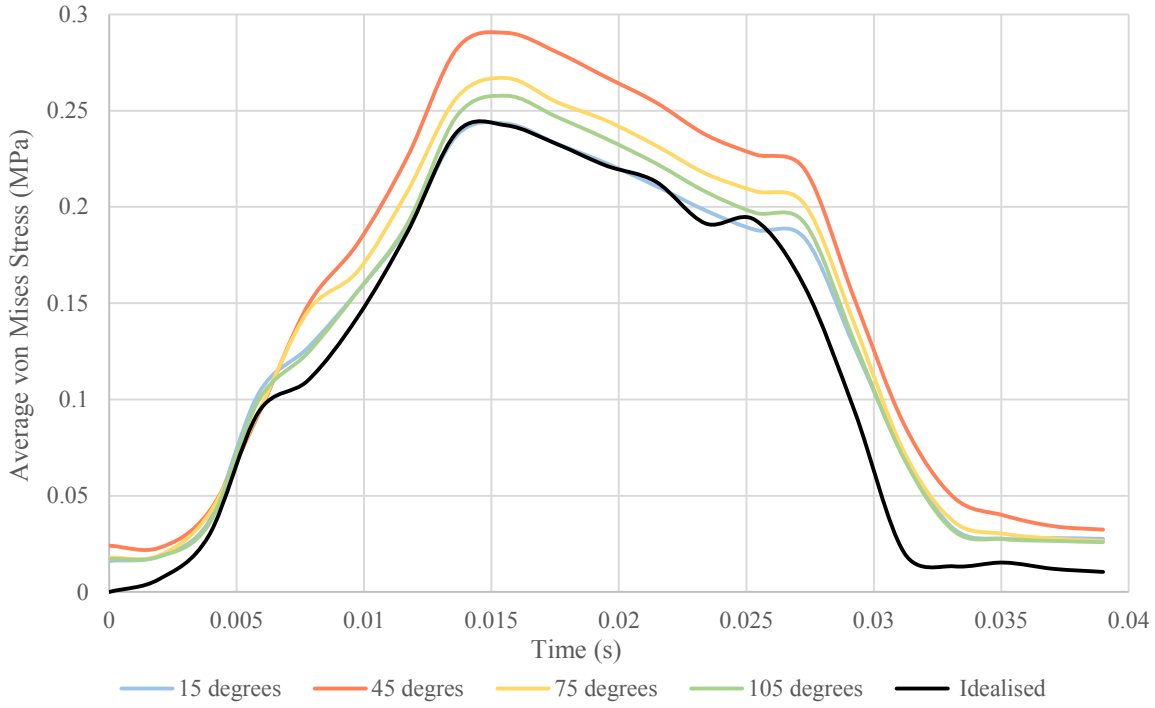

Figure 122. Average von Mises stress in devices deployed to a diameter of 28 mm over a cardiac cycle, with reference to device orientation during deployment. The valvular stress of an idealised device is also included for comparison.

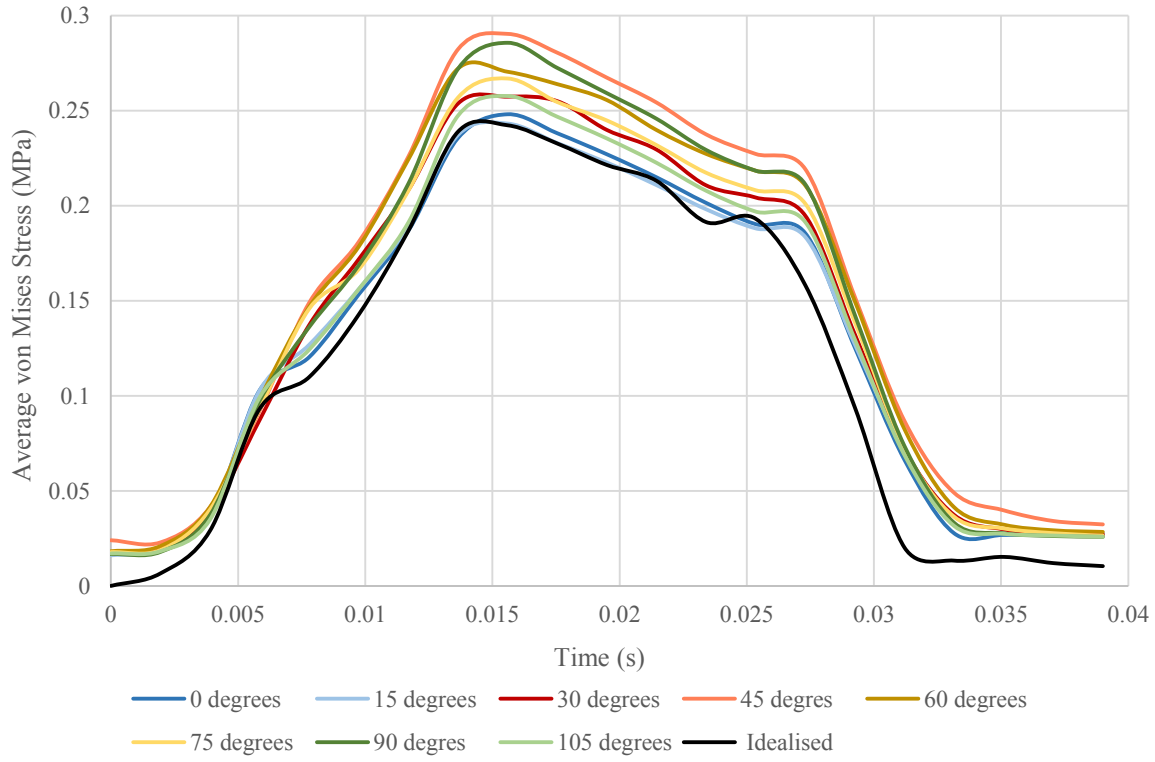

Figure 123. Average von Mises stress in devices deployed to a diameter of 28 mm over a cardiac cycle, with reference to device orientation during deployment. The valvular stress of an idealised device is also included for comparison.

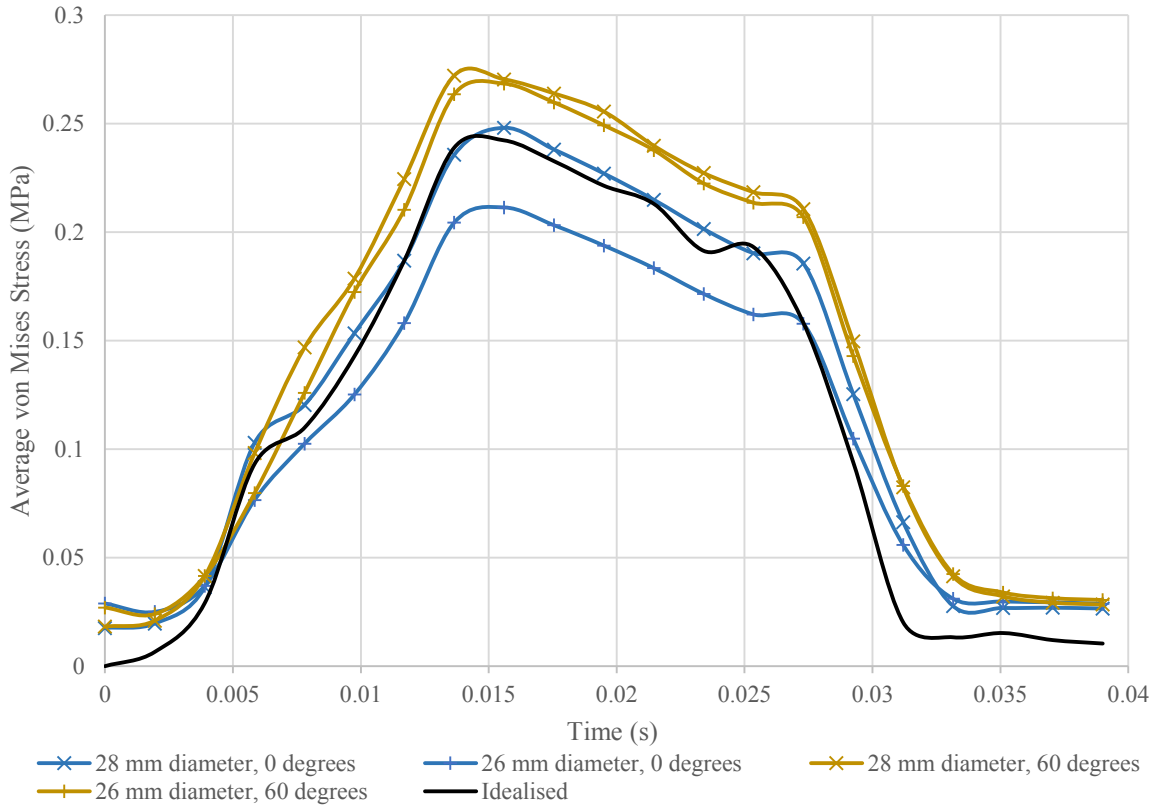

Figure 124. Average von Mises stress within TAVI valves with reference to device orientation and diameter to which the device was deployed.

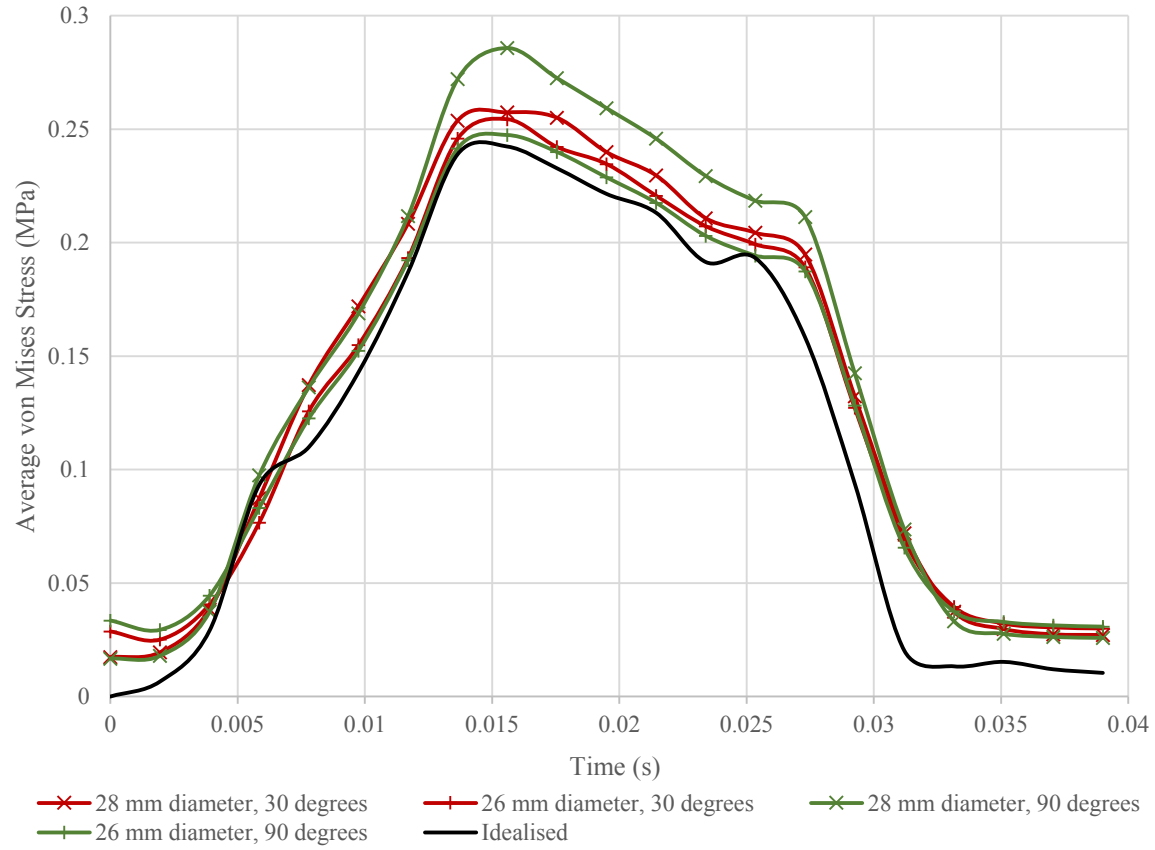

Figure 125. Average von Mises stress within TAVI valves with reference to device orientation and diameter to which the device was deployed.

The increased diameter of the TAVI device increased the stress within the leaflets in all cases. The deviation of stress from the average was also greater in devices that were deployed to 28 mm, as opposed to 26 mm, as shown in Figure 126.

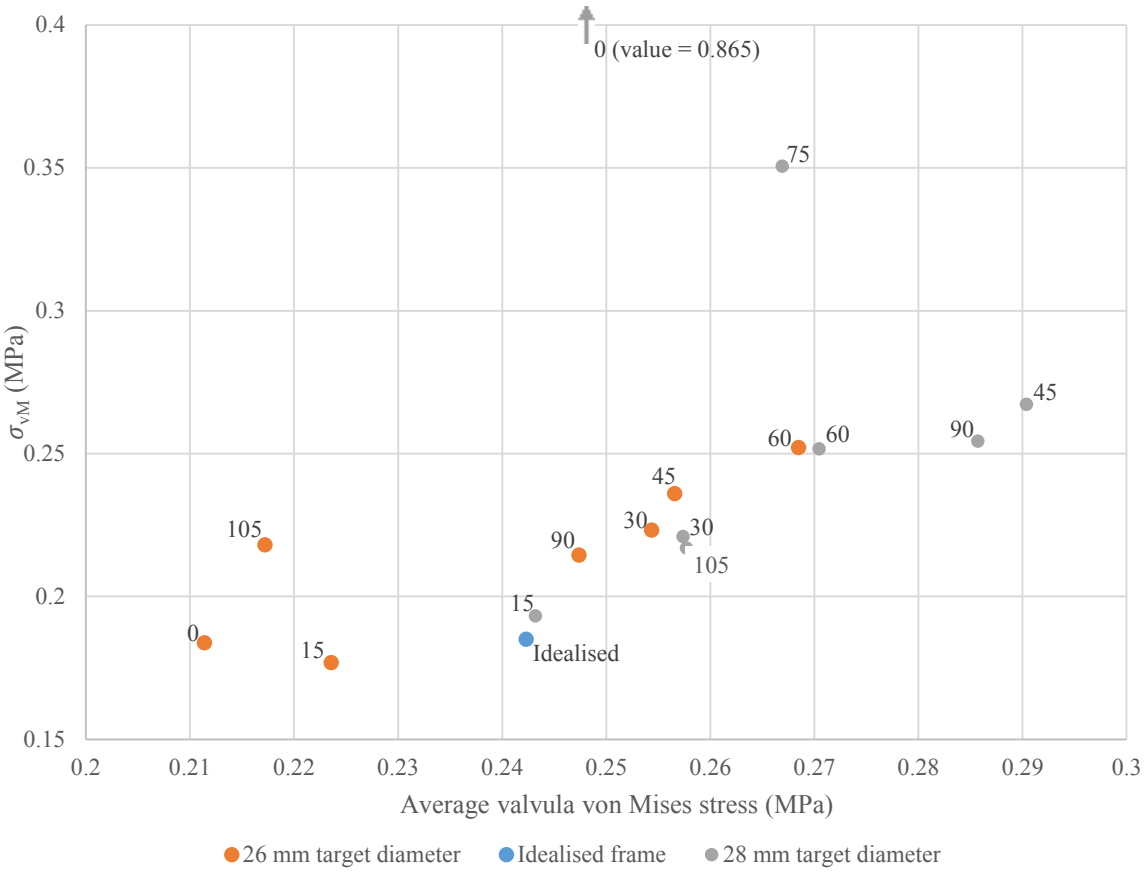

Figure 126. σ_{vM} and average valvular von Mises stress for devices deployed to a target diameter of 26 mm and 28 mm as well as the idealised frame (data labels indicate device orientation).

The device that was deployed to 28 mm with an orientation of 0 degrees, had a significantly greater σ_{vM}. This is because a second volumetric intersection had occurred between the frame and one of the leaflets. The node of the leaflet that had intersected the frame had a stress of 373 MPa, significantly greater than highly stressed elements in other simulations (peak stress in the leaflets was typically between 6 and 9 MPa).

TAVI devices are available in a small number of sizes. Each size has a recommended envelope of native valve dimensions in to which it can be deployed. However, there are ranges of aortic root sizes where no device is ideal. If the aortic root model was between TAVI device sizes, from a life span expectancy perspective, deploying the larger of the two available devices would be recommended as the operating stress is likely reduced. Deploying a larger valve is also thought to aid in reducing the incidence of PAR (Leber et al. 2013). However, deploying the larger of the two valves may induce aortic root rupture.

In order to increase simulation stability, the system is assumed to be frictionless. This has been shown to have a limited effect on the stress within the leaflets during the cardiac cycle (as shown in section 8.2), however, it may have an effect on the frames position post deployment. As friction was neglected in all the simulations in this section, the results are still comparable.

The material model used to simulate the plaques has been simplified to a linear elastic model. In reality the plaque is highly inhomogeneous, anisotropic and hyperelastic, with complex failure. The material properties of the plaque is unique to each mass, and accurately modelling them is beyond current capability. The plaque can visually be seen acting as rigid masses that can crack. Although the plaque within this study was modelled as a rigid mass, plaque failure behaviour was not captured.

8.4 Conclusion

As our experience with percutaneous treatment of AS increases, so does the envelope of patients that are considered suitable. Initially the treatment was reserved for high risk patients, however lower risk patients are now considered for treatment. As the risk of patient decreases, life expectancy increases, which the prosthetic devices must meet. Reducing the operating stress of the device valve and the extent to which the leaflets are damaged during deployment was thought to improve life expectancy. In this chapter, computational analysis was performed in order to identify any adverse operating stresses associated with imperfect deployment. Furthermore, the stresses within the leaflets during the deployment process was analysed in order to identify any areas that may be damaged. The following conclusions were made:

1) If the TAVI device frame is distorted post-deployment, the average valvular operating stress was found to be increased in 80% of cases.
2) If the frame is distorted, the rotational orientation of the TAVI device will affect the average operating stress within the leaflets by as much as 25%.
3) The extent to which the frame is distorted is related to the average valvular operating stress.
4) Computational simulation can be used to determine the most appropriate TAVI device size for a patient with respect to average valvular operating stress.
5) Leaflet migration across the commissures during balloon expansion greatly increases stress within the leaflets during deployment, potentially resulting in damage.
6) Computational simulation can accurately predict the areas of the leaflets that are likely to be damaged during the crimping procedure.

Within this chapter, a complete TAVI device was successfully simulated undergoing deployment fifteen times, with varying device orientations and deployment diameters. All devices post deployment featured distorted frames. In twelve of the fifteen simulations the post-deployment

average valvular operating stress was greater than the stresses experienced by a valve with a perfectly circular frame. This increase in stress will likely decrease life expectancy of the device due to fatigue.

Frame damage is caused by large plaques that exert additional force onto the frame post deployment. The device orientation, relative to these plaques alters the distortion experienced by the device frame. As the rotational orientation of the device changes relative to the plaques, the average valvular operating stress also changes. A trend was identified relating device orientation and average operating stress: The lowest average operating stress occurred in the TAVI device model that was in-phase with the native leaflets. As the device deviated from the in-phase orientation, the stress within the leaflets increased to a maximum (a 25% increase) at an orientation of 60 degrees.

Quantifying the frame distortion as the standard deviation of the frame from a perfect cylinder was shown to be approximately linearly proportional (correlation coefficient of 0.768) to the average von Mises stress within the valves during a cardiac cycle. As distortion of the frame increased, the stress within the leaflets increased.

If the valve is over-expanded to 28 mm (and then allowed to relax to approximately 26 mm), the average stresses within the leaflets increases, as does the deviation of stress. Given a choice between an over-expanded small device, and an under-expanded large device, the larger device would likely have a lower operating stress. This is the first step towards computational simulation aided device selection.

During the deployment process, the stress experienced by the leaflets was shown to be greatly increased if the leaflets cross the commissures into their neighbouring sinus. This effectively decreases the free edge length, as well as introducing a fold into the leaflets. We hypothesise that the increased stress associated with this phenomena could result in local leaflet damage. In which case, inhibiting this behaviour could decrease the risk of premature device failure.

Simulations revealed that as the TAVI device is crimped, the leaflets were found to be liable to fall between the struts of the frame and be subsequently crushed. The extent of damage increased as the diameter of the device decreased. Unfortunately, reducing the deployment diameter for TAVI is a manufacturer's objective since smaller diameters allow for TAVI through fragile femoral arteries, increasing the envelope of patients suitable for the procedure. The resultant damage to the leaflets could be reduced if the leaflets are inhibited from migrating between the struts of the frame.

Chapter 9: Conclusion

The main objective of this research was to explore how valvular function can be compromised by heavily calcified aortic roots. Through completion of this objective, the application of computational patient-specific deployment simulation was also observed. The first complete model of a TAVI device (the Edwards Lifesciences SAPIEN XT) was developed that is capable of undergoing deployment, along with its deployment apparatus. A patient-specific aortic root model was also derived from medical CT data. The model featured native leaflets and plaques, a level of detail yet to be demonstrated in the literature. A series of FEA simulations were produced including the deployment of the complete SAPIEN XT model into the patient-specific native aortic root model. From these simulations, the following conclusions could be drawn:

1) If the TAVI device frame is distorted post-deployment, the average valvular operating stress was found to be increased in 80% of cases.
2) If the frame is distorted, the rotational orientation of the TAVI device will affect the average operating stress within the leaflets.
3) The extent to which the frame is distorted is related to the average valvular operating stress in a potentially linear manner.
4) Computational simulations can identify sites that are susceptible to PAR, or potentially PAR itself in future.
5) Computational simulation could potentially be used to determine the most appropriate TAVI device size for a patient with respect to average valvular operating stress.
6) Including prosthetic leaflets in the device model does not alter the simulated frame position post deployment.
7) Our simulations suggest leaflet migration across the commissures during balloon expansion greatly increases stress within the leaflets during deployment, potentially resulting in damage.
8) Computational simulation have been used to estimate the areas of the leaflets that are likely to be damaged during the crimping procedure.
9) Plaques that are most likely to rupture can be identified through computational simulation.
10) Post-deployment balloon angioplasty reduces the degree of PAR by damaging plaques.

In section 8.3, a complete SAPIEN XT model was successfully simulated undergoing deployment fifteen times, with varying device orientations and deployment diameters. Each of the post deployment frames featured a distorted frame of varying degree, due to a large plaque embedded in the base of the non-coronary leaflet. Of these fifteen devices simulated undergoing deployment, twelve devices were found to be less efficient post-deployment than a device with a cylindrical frame. The increase in stress throughout the cardiac cycle that the frame experiences will likely decrease the lifespan of the device due to fatigue. Previously distorted frames have been associated with an

increased risk of PAR, however if there is no PAR present, the imperfect frame deployment is assumed to be acceptable.

Frame damage is caused by large plaques that exert additional force onto the frame post deployment. The device orientation, relative to these plaques alters the location, and degree of distortion experienced by the device frame. In section 8.3 it was shown that the variation in location and degree of distortion affected the average leaflet operating stress. A trend was identified relating device orientation and average operating stress: The lowest average operating stress occurred when the TAVI device model was in-phase with the native leaflets. As the device deviated from this orientation, the stress within the leaflets increased to a maximum (a 25% increase) at an orientation of 60 degrees. Originally patient specific deployment simulations were only thought to have application in identifying patients that are at a greater risk of PAR, however, this research shows that finding the optimal device orientation is another application.

The degree to which the device frame deviated from an idealised shape was quantified through measuring and averaging the distance the nodes deviated from a perfect cylinder (σ_{DPC}). As σ_{DPC} increased, as did the average stress within the leaflets. In section 8.3, it was found that the σ_{DPC} was in fact linearly proportional to the average valvular operating stress with a correlation coefficient of 0.768. It may therefore be possible to estimate the extent to which the leaflets operating stress is increased, by quantifying the degree of frame distortion using post-deployment CT scan data.

It was found that computational simulation of device deployment can identify areas that are likely to be vulnerable to PAR (section 7.3). The plaque placement that was responsible for creating the channel through which the blood might flow correlated with experimental analysis. For this case, the origin of PAR was a channel in the commissure between the left-coronary and right-coronary leaflets. The channel is believed to be the product of plaque placement in the near vicinity. The regurgitation path then flowed below the left-coronary leaflet where the frame failed to create an effective seal against the aortic root wall due to a second calcified mass. There were, however, possible errors in the results at the commissures of the native valve, where channels were created. It is difficult to determine whether these channels are associated with the method of model construction or PAR. This thesis contains the most sophisticated PAR prediction simulations which we hope will mature into an active part of TAVI planning.

Over-expansion of TAVI devices is common practice as it can reduce PAR. In section 8.3, it was found that if the devices are over-expanded to 28mm, the average operating stress within the leaflets increases, as does the deviation from the average stress. Post-deployment angioplasty may therefore reduce the device lifespan. TAVI devices are available in different sizes, with a recommended bracket of aortic root sizes to which each can treat. If a patient had an aortic root that fell between the recommended sizes for two devices, under-expanding the larger device would be recommended as the valvular operating stress would likely be reduced. However, these findings may be patient

specific; in which case TAVI device selection is another application of patient specific computational simulation of TAVI.

The exploratory simulations presented in section 7.1 demonstrates that the leaflets are not required for accurate simulation of TAVI frame deployment. A measure of discrepancy between frame positions is the average nodal position discrepancy, which showed that if the leaflets were neglected, the discrepancy created was 0.0613 mm, or 0.0236% of the device diameter. This allows for simulations aimed at finding likely sites of PAR to be significantly more efficient as the leaflets can be neglected. This result also demonstrates that the lack of leaflets in other research groups work is not a source of significant error or limitation (Capelli et al. 2012, Wang, Sirois, and Sun 2012, Russ et al. 2013, Auricchio et al. 2014, Gunning, Vaughan, and McNamara 2014, Morganti et al. 2014).

Section 8.1.2 analysed the stress within the leaflets during the balloon expansion process. The analysis revealed that the stress within the leaflets during balloon expansion was greatly increased if the leaflets migrated across a commissure. In the event that the leaflets did migrate across a commissure, the free edge length of the leaflet is effectively reduced which increases stress within the body of the leaflet, as it is stretched taught by the balloon. Furthermore, a crease will be formed in the leaflet which increases the stress in the leaflet along the edge of the fold. This increased stress associated with the fold may be significant enough to disrupt collagen fibres within the valve which would reduce the device lifespan due to restenosis.

The simulations of section 8.1.1 revealed that as the TAVI device is crimped, the leaflets were found to be liable to fall between the struts of the frame and be subsequently crushed. The stress within the leaflets associated with these pinches exponentially increased if the device was crimped below 8 mm. Inhibiting the leaflets from migrating between the frame struts would reduce the damage to the leaflets to a minimum, and increase the life expectancy of the device. If this cannot be achieved, increasing the diameter to which the device is crimped to a minimum of 8 mm is advisable. This may have implications for frail patients as devices with a large diameter are often too wide to travel through diseased femoral arteries.

It has been shown that most emboli debris is released after the balloon-expansion phase of the deployment process (Drews et al. 2011). This is because the balloon disrupts the plaque, but while inflated, also traps the debris. In section 7.4.1 the stress within the plaques during balloon expansion was calculated. Of the eight bodies of plaque present in the aortic root model, five became highly stressed, while three others experienced a lower level of stress. The five highly stressed bodies of plaque were all situated on the native leaflets or sinuses, while the lesser stressed plaques were all within the aorta. Of these five bodies of plaque, a single plaque experienced a significantly elevated level of stress and is most likely to rupture. This shows that to some extent, computational simulation of TAVI can identify the plaques that are at most risk of rupturing. Furthermore, it was found that the stress experienced by the plaques increases with over expanding a 26 mm prosthetic device to 28

mm by an average of 10.8%. This increase in stress, although low, may be capable of rupturing plaques. Further research into the rupture mechanics of plaques is required before a simulation capable of determining the probability of plaque rupture can be developed.

It is known that device over-expansion reduces the incidence of PAR, computational simulation of over-expansion (section 7.3) did not improve the contact between the frame and the native tissue for the case of the SAPIEN XT. For the case of the SAPIEN 3, minor improvements were visually evident, but not significant enough to reduce the degree of PAR. Simulations demonstrated that increasing the diameter of the device does not directly improve PAR. PAR reduction associated with over-expansion is therefore likely achieved through damaging the plaques to change their geometry. This will unfortunately increase the risk of embolism to the patient. Plaque damage was not considered in this work as the material model has not been derived, but is an important topic of further work.

This work is by no means complete and there are multiple areas of research which can be furthered.

The main conclusion of this thesis is that frame distortion can affect the efficiency of the prosthetic valve. This drop in efficiency is likely to reduce the device lifespan due to fatigue. However, as of yet, frame distortion is not associated with decreased device lifespan. Further work is required to strengthen the results presented in this thesis and also increase publicity of these finding.

In section 7.3 it was demonstrated that a computational simulation can predict areas of a patient's aortic root that are susceptible to PAR. This research should be reinforced with more cases, and validated with post-deployment TOE. Furthermore, it is thought that there are possible errors in the commissures of the native valve. Channels are evident, but it is unknown whether they are a location of PAR, or a product of the model development technique. Further model development techniques may be required if the latter is true.

It has been shown that distortion to the frame can alter the stress within the leaflets. The only study that examines the incidence of frame distortion had a small sample size (30) from which no credible conclusion can be drawn (Schultz et al. 2009). It is therefore advisable that a larger study is conducted in order to clarify the incidence of frame distortion within modern TAVI devices.

The extent to which the elevated operating stresses within the valves affects the life span of the device is unknown. This should be studied through either experimental, or computational fatigue analysis. However, it is extremely difficult to calculate as the human immune system must be taken into account, as it can decrease the life expectancy of a device by triggering an inflammatory response.

Although the lifespan of TAVI devices is unknown, and it is also unknown how the lifespan will be affected by distorted frames, the next generation of devices can still be prepared to be resistant to premature fatigue associated with distortion. A robust design optimisation study should be performed

on the device leaflets in order to reduce the operating stress within optimal, and suboptimal frames in order to maximise the device lifespan.

A constant limitation within this thesis was the material properties associated with the plaques. A material property analysis study could be performed to further the computational models, and improve the reliability of the results.

Finally, it was found that if the prosthetic leaflets are folded during deployment, the stress within the leaflets is increased. It is thought that this increase in stress could reduce the device lifespan. It is possible that the diameter to which the device is crimped to alters the probability of a fold occurring, however, there was insufficient simulations performed in the area to create a clear picture. Further simulations are required to produce further evidence.

The research presented in this thesis is not complete. As only a single patient specific case has been analysed it is impossible to say if the trends identified are globally true or patient specific. However, there is still application for the techniques and models developed.

These are some of the first steps towards patient specific procedural simulations. These simulations will one day be used to predict any adverse outcomes to TAVI such as PAR and embolism release. This will be an invaluable tool for determining which patients are suitable for TAVI and could further reduce the mortality rates associated with AS.

Simulations of this nature have further application in device development. Currently when a new device is developed it undergoes vivisection trials. We hope that the computational simulations, such as those presented in this thesis, will one day be sophisticated enough to accurately represent TAVI, such that the extent to which vivisection is incorporated into the design process is reduced.

The method developed to model the leaflets undergoing TAVI simulation has application within leaflet design. It is an effective method of converting simple 2D geometries into complex 3D geometries. This makes it significantly easier to develop CAD models of TAVI leaflets. Furthermore, this leaflet modelling technique allows insight into the stresses the leaflets undergo during deployment which may be a design objective in the future of TAVI.

Finally, the occurrence of imperfect frames has been identified to affect the manner to which the leaflets close and the stresses within. Whether or not the increased stress is sufficient to decrease the life expectancy of the device is unknown. Irrespectively, we would expect device manufacturers to consider experimental fatigue analysis of imperfect devices to ensure the next generation of TAVI devices can withstand the test of time, even in less favourable circumstances.

Appendix

Mass Scaling Analysis

In order to calculate the correct mass scaling value, a simple simulation was developed that was repeated multiple times with different time increments (10^{-6}, 10^{-7}, 10^{-8} and 10^{-9}). A small section of the SAPIEN XT frame (section 5.2) was simulated being expanded from a diameter of 16 mm to a diameter of 26 mm by means of a cylindrical surface (Figure 127). The frame expansion was modelled over a time period of 0.03 seconds. After the frame is deployed the cylindrical surface radially contracts. As mass scaling analysis can be extremely computationally demanding, the number of elements was reduced as much as possible by using a small portion of the SAPIEN XT (section 5.2) as opposed to the entire device (Figure 127). The subsection of the frame was meshed with a target element length of 0.08 mm resulting in 38,170 hexahedral elements (reduced from 168,735 elements).

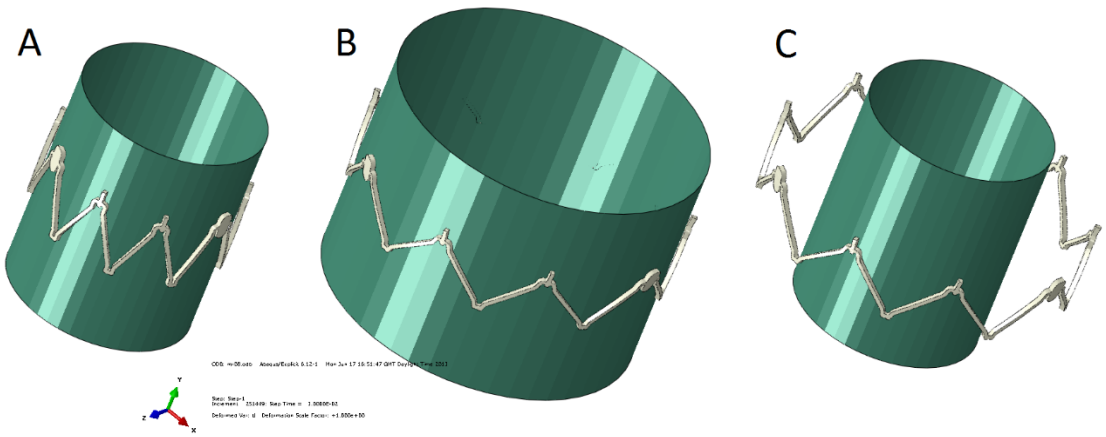

Figure 127. Deployment of a partial SAPIEN XT frame by means of a cylindrical surface.

The displacement of the frame was calculated and shown in Figure 128 while the computational times are tabulated in Table 32.

Target Time Increment (seconds)	Computational Time (minutes)
10^{-6}	17
10^{-7}	264
10^{-8}	810
10^{-9}	NA

Table 32. Computational time variation associated with mass scaling.

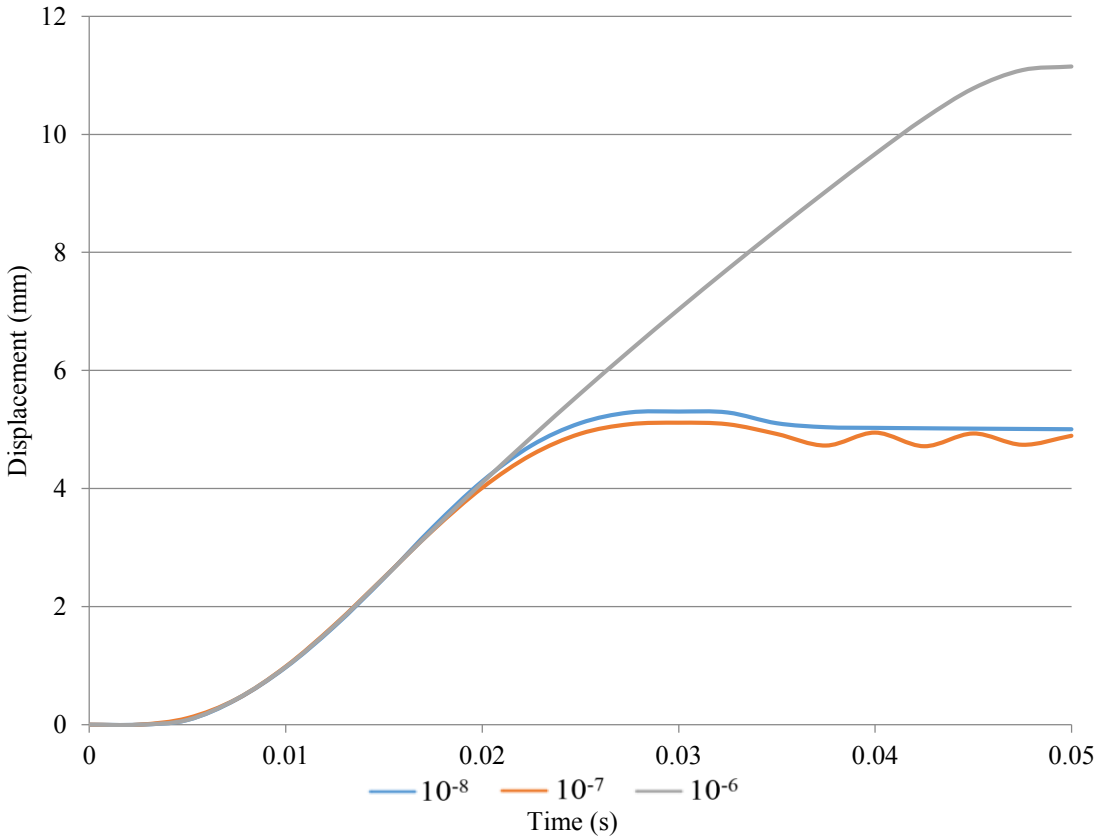

Figure 128. Frame displacement associated with different time increments.

As the time increment decreased, the computational time increases (Table 32). Despite the simplicity of the model, the simulation using a time increment of 10^{-9} did not complete within a reasonable amount of time (10 days), therefore it was manually terminated.

The displacement of the elements within the simulation is shown in Figure 128. For the case of the simulation with a target time increment of 10^{-6}, the frame continued to expand as the time increment was too large to effectively model momentum. The simulation with a time increment of 10^{-7} demonstrated an oscillatory response that can be supressed through damping. Despite the damping, the simulation results were very similar to that of a simulation with a time increment of 10^{-8} and did not show any signs of ineffective momentum calculations.

It was concluded that a time increment of 10^{-7} was most suitable as it computed quickly with a relatively high accuracy, despite the oscillatory response. For the remainder of the simulations presented in this thesis, the target time increment of 10^{-7} will be used.

Frame Damping Analysis

It was observed that the frame is susceptible to vibration after unloading (Figure 128). In order to effectively remove the oscillatory response without damaging the accuracy of the simulation through over-damping, damping analysis was performed. Damping in Abaqus is implemented through the Rayleigh damping factor, which was discussed in section 5.1. In order to calculate the α coefficient, a fast Fourier transform was performed on the oscillatory responses. The oscillatory response can be seen between t = 0.035 and 0.06 seconds of Figure 128 (for the case of the target time increment equal to 10^{-7}). The time-domain displacement evolution was converted to frequency domain by means of a fast Fourier transform, shown in Figure 129.

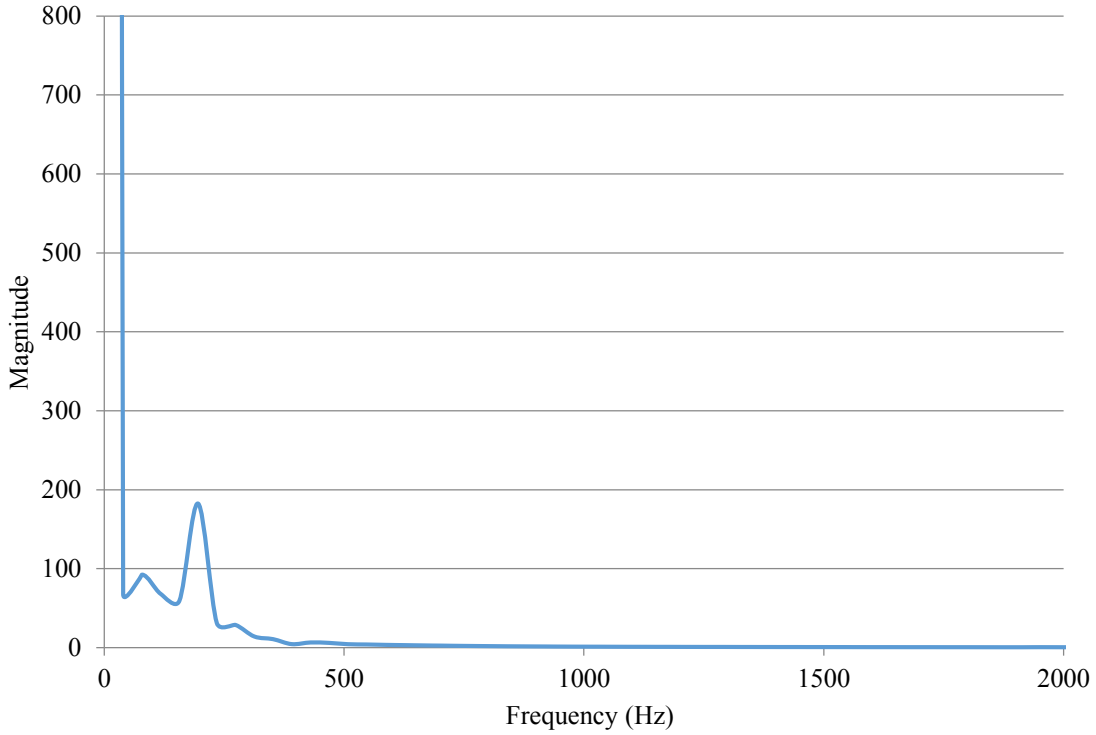

Figure 129. Fourier analysis of the oscillatory response observed by the SAPIEN XT frame.

The response of the frame in the frequency domain shows a peak at 195 Hz which was identified with its resonant frequency. Further analysis was performed to ensure the system was not over damped by implementing different damping factors (ζ= 1.5, 1, 0.5, 0.25 and 0.125) before the analysis was repeated and the oscillatory response of the model was measured (Figure 130).

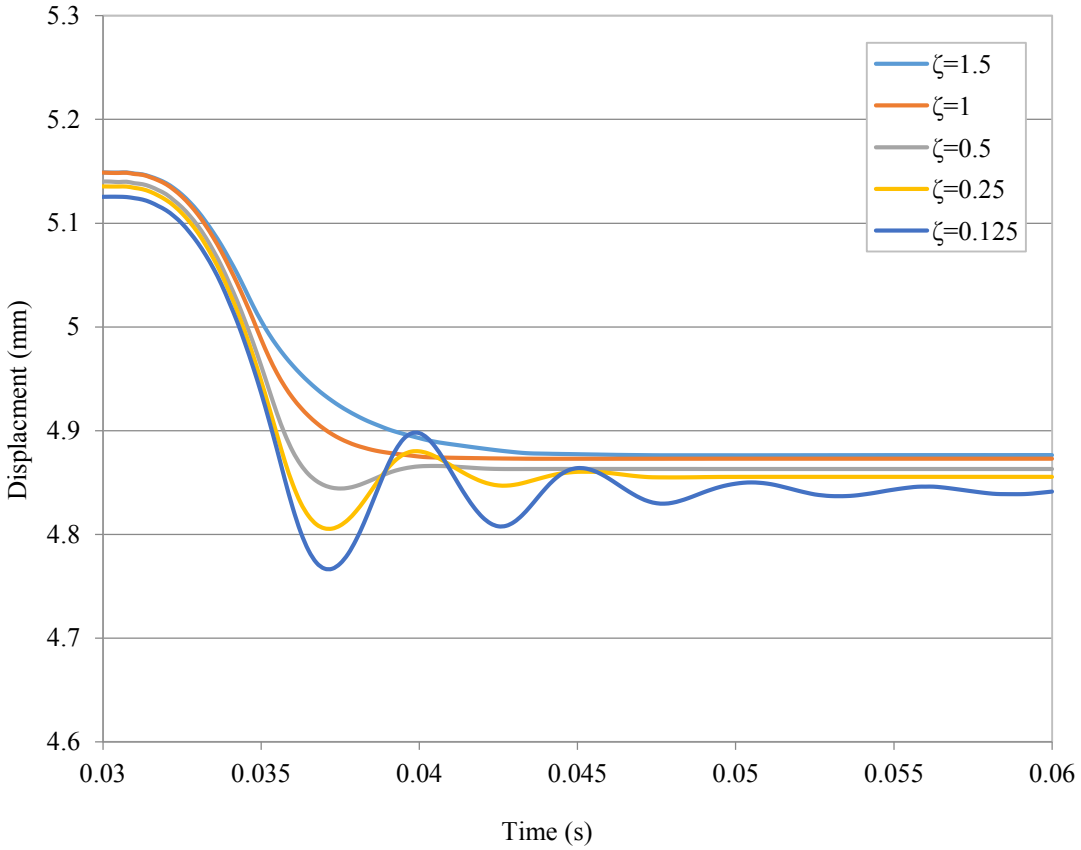

Figure 130. The oscillatory response of a SAPIEN XT frame with different damping factors applied.

The oscillatory response was alleviated as ζ approached unity (critical damping). As ζ supersedes unity, the time required for the system to reach steady state increases which demonstrates over damping. Furthermore, as ζ is increased, the elastic recoil decreases which is a superior representation of the actual device. As a result, critical damping (ζ = 1) was applied to the device frame in all further simulations presented in this research unless started otherwise, by means of an equivalent value of α (=2450).

Device Frame Mesh Refinement

The accuracy of a FEA model strictly depends on the number of elements used to discretise the domain. However, this negatively impacts the computational efficiency as the time to solve the equations increases too. As a consequence, a trade-off must be found between mesh resolution and computational time. In order to ensure the simulations that were used in this research are accurate and as fast as possible, a mesh convergence analysis was undertaken. A frame was meshed four times with different element target lengths (0.16 mm, 0.08 mm, 0.04 mm and 0.02 mm), the number of elements in each mesh are shown in Table 33. Again, a subsection of the frame was used to reduce the computational time (Figure 127). The test simulation described in the *Mass Scaling Analysis* section of the Appendix was then repeated four times, each with a different mesh resolution (and a target time increment of 10^{-7}).

The oscillatory response is dependent upon the element size. As a result the analysis described in the *Frame Damping Analysis* section of the Appendix was repeated for each target element size. Once the damping coefficient α was computed, the simulation was repeated with damping implemented. The target element size, number of elements, value of α and computational time is shown in Table 33. The frames displacements are shown in Figure 131.

Target element size	Number of elements	α	Computational time
0.16 mm	7881	3430	18 minutes
0.08 mm	38170	2450	98 minutes
0.04 mm	298120	1219	713 minutes
0.02 mm	2287224	26	5978 minutes

Table 33. Target element sizes and the associated number of elements, α coefficient (for critical damping) and computational time.

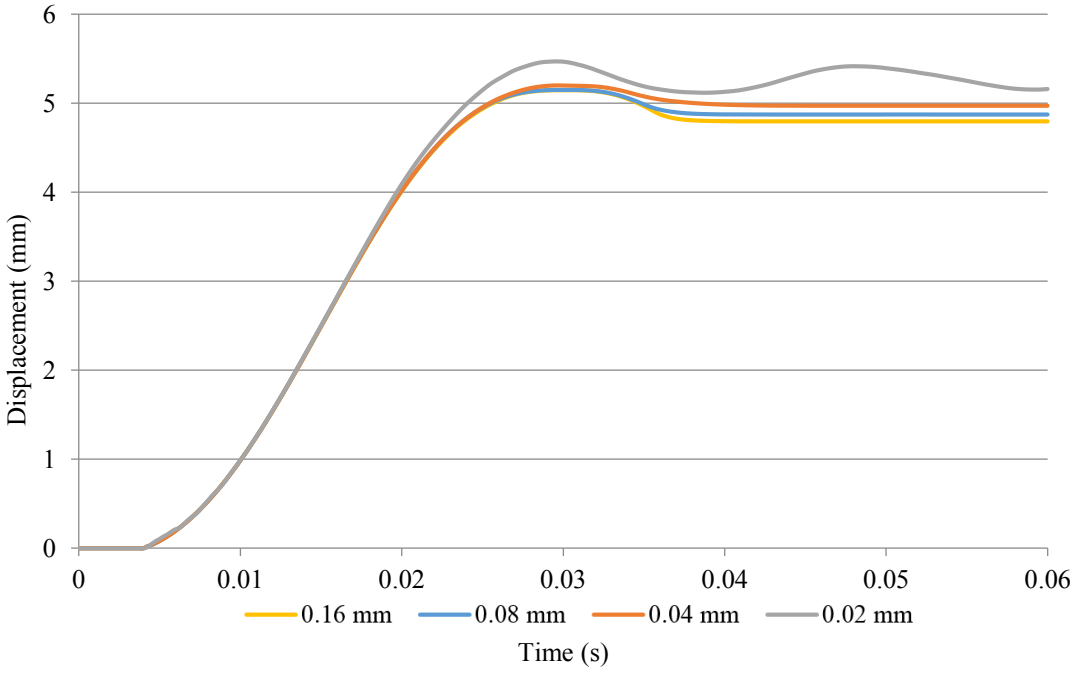

Figure 131. Frame displacement relative to target element size of mesh.

There was a discrepancy in the results, most surprisingly; the 0.02 mm plot still had an oscillatory response. This is likely due to the elements requiring a lower target value for the mass scaling. Since the computational time was approximately 100 hours, it is deemed too expensive and will not be pursued. The model with a target mesh resolution of 0.04 mm is likely the most accurate as it is the finest mesh that did not succumb to instability. The target mesh resolution will be 0.08 mm in further studies as, although there are discrepancies in the results, it does compute in a reasonable time and the discrepancy between that and the most accurate model (target element length of 0.04 mm) is only 1.84% (determined through final frame position).

Leaflet Damping Analysis

An acute oscillatory response was observed with in the leaflets. In order to remove it, Rayleigh damping was applied. In order to find the correct value of α for the Rayleigh damping, a cardiac cycle was simulated (as described in 5.5.1) multiple times. Each simulation had a different α coefficient with values 0, 500, 1000 and 1500. Conventionally the displacement is monitored in order to identify if a system is over or under damped. However, in this case the stresses within the leaflets are of interest, so the average valvular von Mises stress was monitored instead (Figure 134).

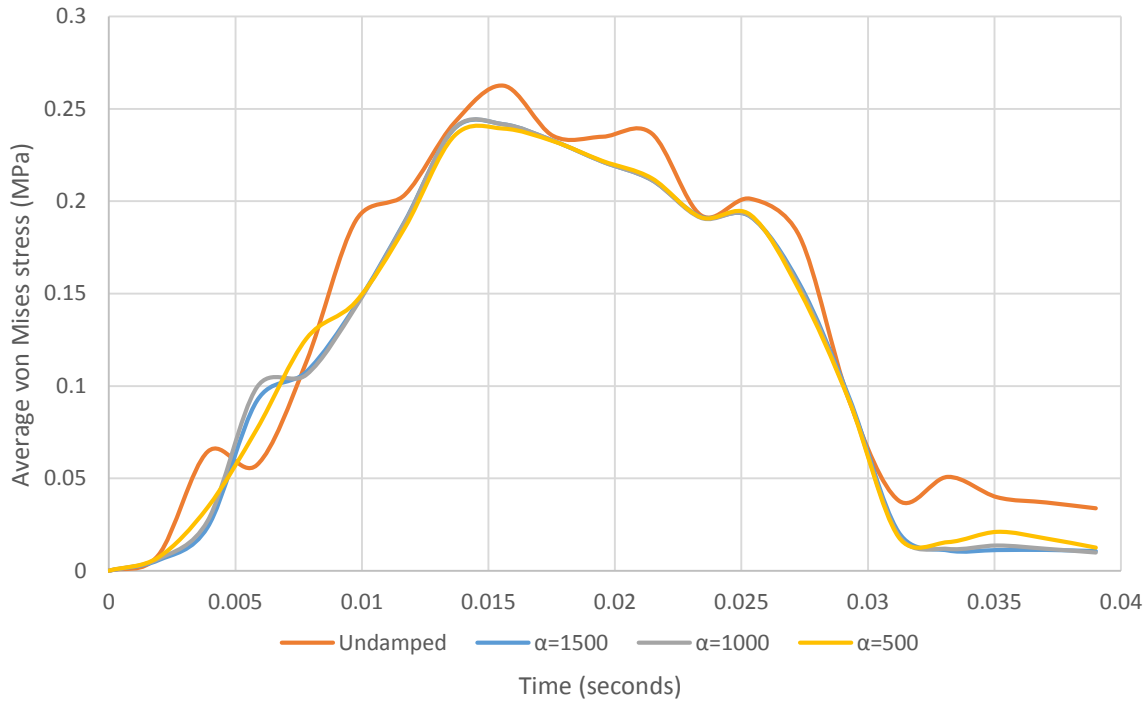

Figure 132. Average von Mises stress within valves that are simulated with varying degrees of damping.

The undamped system demonstrated a severe oscillatory response, however as damping was added the oscillatory response diminished. The oscillatory response is not noticeable in the plot of $\alpha = 1000$, which also showed a strong correlation with the plot of $\alpha = 1500$, suggesting the values had converged. It was decided that a value of $\alpha=1500$ will be used throughout the simulations as the oscillations in the response were removed and additional damping would contribute to the stability of the system by reducing the kinetic energy of the system.

Additional Components of the Deployment System

The deployment device used to deploy the SAPIEN XT is the NovaFlex+ deliver catheter, which the deployment device in this study is based on. The geometry of the balloon is described in section 5.7. There are however additional components which are shown in Figure 133.

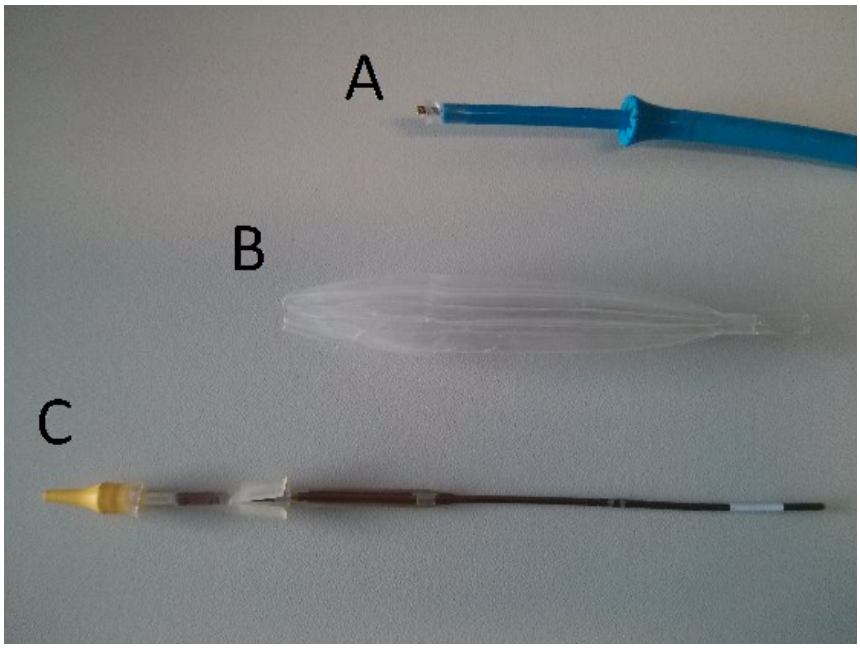

Figure 133. Disassembled NovaFlex+ delivery system (26mm). The catheter body and the shunt that can push the device forward is visible (A). The clear balloon in a semi expanded state (B). The tube that is revealed upon removal of the balloon with the yellow cone and two additional plastic components (C).

Figure 133(A) is the catheter body comprising two components, an external tube with a flanged end and an interior tube. The exterior tube can move forwards and backwards relative to the internal tube. During transapical deployment the TAVI device is crimped to the internal tube, then the external tube pushed the device forwards on to the balloon. For the simulation, this component is represented by a boundary condition along the lower edge of the balloon. The lower edge of the balloon is constrained in such a manner that it must remain circular in cross section and not deviate from the original plane.

Figure 133(C) shows the internal components of the device that are normally obscured from view by the balloon. There is a tube running through the centre that appears to be a metallic braid that has been set in a resin. A series of silver metal rings can be seen along its length, which are radio opaque markers that aid in gauging the deployment location. The tube is in fact hollow, the reason for this is that it accommodates a guide wire through the centre. This tube is modelled as a simple solid tube in Abaqus, the geometry is derived from actual measurements. The external diameter is 1.34 mm and an internal diameter of 1 mm. The wire was 94.52 mm long; this allowed it to attach to the cone, and

protrude 20 mm below the balloon. Although the wire is relatively stiff, in order to minimize migration of components, the material properties used to model the wire were the same as that from the frame. That is cobalt chromium allow MP35N, the properties are: elastic modulus: 232 GPa, Poisson's ratio: 0.3, Yield stress: 379 MPa, and a density of 8.4 g/cm^3.

A yellow plastic cone is seen at one end. The balloon is attached to the outer surface of the cone creating a seal. Again the cone has a hole running through the centre of it to accommodate a guide wire. The cone appears to be manufactured from a rubber like material. During the deployment procedure the cone is unlikely to deform as it is significantly stiffer than the balloon. As a result it was assigned exceedingly stiff material properties, that again of, cobalt chromium MP35N. This will ensure the cone will not deform throughout the analysis. The geometry of the cone was measured using a calliper, the measured (and modelled) geometry is shown in Figure 134.

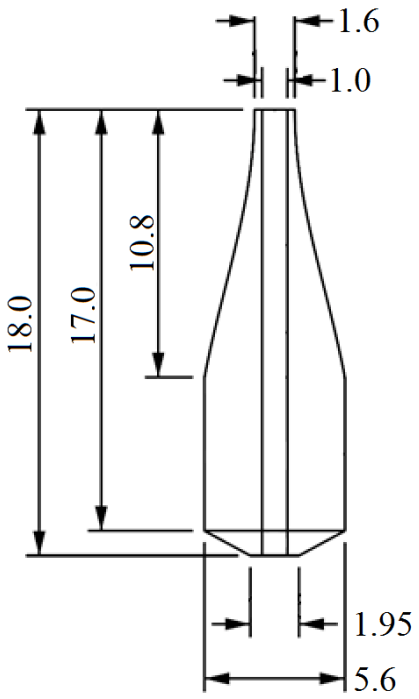

Figure 134. A cross section of the cone showing its geometry.

Glossary of Terms

Anisotropic – A body that has variable material properties dependent on the orientation to which it was measured.

Angina – Chest pain associated with lack of blood flow to the heart.

Angioplasty – The percutaneous procedure of unblocking or increasing the lumen area of a segment of the cardiovascular system.

Balloon Valvuloplasty – A medical procedure, in which a balloon is used to open a narrowed heart valve.

Bicuspid – Referring to human anatomy, a bicuspid valve is a valve that comprises two leaflets.

Commissure – The joint or area between two neighbouring leaflets within a valve.

Cerebral Lesion – An area of the brain that has been damaged.

Computer Tomography – A form of imaging technique in which a series of images all of which have a common line, are aggregated together to create an image normal to all of the initial images.

Congenital – A disease present from birth.

Cuff – With reference to TAVI devices, the cuff is a thin film that spans select cells of the device. The cuff inhibits motion of the lower edge of the leaflets.

Echocardiography – A medical procedure that uses ultrasound waves to investigate the function of the heart.

Embolism – Obstruction of part of the cardiovascular system by a foreign body.

Extracorporeal Circulation Machine – A machine that both bypasses, and functionally replaces the heart.

Fluoroscopy – A medical imaging technique which uses a continuous source of radiation to create a live stream of images.

Gaetano – A Reader in Biomedical Engineering, not to be confused with gelatino, which is a small ice cream.

Gravity Gun – Zero point energy field manipulator.

Homogeneous – A body that has uniform material properties irrespective of the location of measurement in the body.

Hyperelastic – Referring to constitutive material laws, a hyperelastic material is one that responds elastically when subjected to large strains.

Imperfect Frame – A prosthetic device frame that is not the same as the intended design.

Inhomogeneous – A body whose material properties are dependent on the location of measurement.

Intercostal Space – The gap between the ribs comprising soft tissue.

Intima – The inner lining of the heart.

Isotropic – A body that has uniform material properties irrespective of the orientation to which it is measured.

Leaflet Attachment Line – The line to which the leaflets attach to either the native tissue or a prosthetic device.

Lumen – The central cavity of a vessel within the cardiovascular system.

NovaFlex+ - A delivery system for the SAPIEN range of TAVI devices, developed by Edwards Lifesciences.

Paravalvular Aortic Regurgitation – A condition unique to TAVI patients, in which blood flows around the prosthetic valve during diastole.

Particle Image Velocimetry – An optical method of visualising flow within a body of fluid.

Percutaneous – A minimally invasive surgical procedure, frequently employing catheters.

Pericardium – The fibrous membrane enveloping the heart.

Prosthetic – A man made organ.

Purse String Sutures – A ring of sutures that visually and functionally resembles the string around the free edge of a handbag or purse.

Quadricuspid – Referring to human anatomy, a quadricuspid valve is a valve that comprises four leaflets.

Restenosis – Reoccurrence of stenosis, often associated with prosthetic heart valves.

SAPIEN 3 – A third generation TAVI device produced by Edwards Lifesciences.

SAPIEN XT – A second generation TAVI device produced by Edwards Lifesciences.

Sclerosis – A medical condition in which the tissue in question becomes both hardened and stiffened.

Stereo Photogrammetry – The practice of measuring the location of objects through analysis of photographs.

Stenosis – A medical condition in which calcified plaques are deposited in the cardiovascular system, decreasing the lumen at the point of the plaque.

Sternotomy – An incision into, or through the sternum.

Sternum – The ventral plate of bone in the human skeleton.

Stroke – A cerebral embolism.

Transapical – A type of TAVI, in which the catheter route is through the apex of the heart.

Transcatheter – A procedure performed through a catheter.

Transfemoral – A type of TAVI, in which the catheter route is through the femoral artery.

Transvalvular Aortic Regurgitation – A condition in which blood flows through the aortic valve during diastole.

Tricuspid – Referring to human anatomy, a tricuspid valve is a valve that comprises three leaflets.

Zelda – With reference to the video game *The Legend of Zelda*, Zelda is a princess, often confused with the games main protagonist Link.

List of References

Abdel-Wahab, M., R. Zahn, M. Horack, U. Gerckens, G. Schuler, H. Sievert, H. Eggebrecht, J. Senges, and G. Richardt. 2011. "Aortic Regurgitation After Transcatheter Aortic Valve Implantation: Incidence and Early Outcome. Results from the German Transcatheter Aortic Valve Interventions Registry." *Heart* no. 97 (11):899-906. doi: 10.1136/hrt.2010.217158.

Alavi, H., E. Groves, and A. Kheradvar. 2014. "The Effects of Transcatheter Valve Crimping on Pericardial Leaflets." *The Annals of Thoracic Surgery* no. 97 (4):1260-1266. doi: http://dx.doi.org/10.1016/j.athoracsur.2013.11.009.

ALS. 2014. "Centre for Anatomical Learning Sciences " *The University of Southampton*.

Arcidiacono, G., A. Corvi, and T. Severi. 2005. "Functional Analysis of Bioprosthetic Heart Valves." *Journal of Biomechanics* no. 38 (7):1483-1490. doi: http://dx.doi.org/10.1016/j.jbiomech.2004.07.007.

Auricchio, F., M. Conti, S. Morganti, and A. Reali. 2014. "Simulation of Transcatheter Aortic Valve Implantation: a Patient-Specific Finite Element Approach." *Comput Methods Biomech Biomed Engin* no. 17 (12):1347-57. doi: 10.1080/10255842.2012.746676.

Auricchio, F., A. Ferrara, and S. Morganti. 2012. "Comparison and critical analysis of invariant-based models with respect to their ability in fitting human aortic valve data." *Annals of Solid and Structural Mechanics* no. 4 (1):1-14. doi: 10.1007/s12356-012-0028-x.

Azadani, A., S. Chitsaz, P. Matthews, N. Jaussaud, J. Leung, T. Tsinman, L. Ge, and E. Tseng. 2012. "Comparison of Mechanical Properties of Human Ascending Aorta and Aortic Sinuses." *The Annals of Thoracic Surgery* no. 93 (1):87-94. doi: http://dx.doi.org/10.1016/j.athoracsur.2011.08.002.

Azzalini, L., B. Ghoshhajra, S. Elmariah, J. Passeri, I. Inglessis, I. Palacios, and S. Abbara. 2014. "The Aortic Valve Calcium Nodule Score (AVCNS) Independently Predicts Paravalvular Regurgitation After Transcatheter Aortic Valve Replacement (TAVR)." *Journal of Cardiovascular Computed Tomography* no. 8 (2):131-140. doi: http://dx.doi.org/10.1016/j.jcct.2013.12.013.

Bagur, R., J. Rodés-Cabau, D. Doyle, R. De Larochellière, J. Villeneuve, J. Lemieux, S. Bergeron, M. Côté, O. Bertrand, P. Pibarot, and É. Dumont. 2011. "Usefulness of TEE as the Primary Imaging Technique to Guide Transcatheter Transapical Aortic Valve Implantation." *JACC: Cardiovascular Imaging* no. 4 (2):115-124. doi: http://dx.doi.org/10.1016/j.jcmg.2010.10.009.

Bailey, J., N. Curzen, and N. W. Bressloff. 2015. "Assessing the impact of including leaflets in the simulation of TAVI deployment into a patient-specific aortic root." *Comput Methods Biomech Biomed Engin*:1-12. doi: 10.1080/10255842.2015.1058928.

Balguid, A., N. J. B. Driessen, A. Mol, J. P. J. Schmitz, F. Verheyen, C. V. C. Bouten, and F. P. T. Baaijens. 2008. "Stress Related Collagen Ultrastructure in Human Aortic Valves—Implications for Tissue Engineering." *Journal of Biomechanics* no. 41 (12):2612-2617. doi: http://dx.doi.org/10.1016/j.jbiomech.2008.06.031.

Bapat, V., and R. Attia. 2012. "Transaortic Transcatheter Aortic Valve Implantation: Step-by-Step Guide." *Seminars in Thoracic and Cardiovascular Surgery* no. 24 (3):206-211. doi: http://dx.doi.org/10.1053/j.semtcvs.2012.06.004.

Bapat, V., R. Attia, S. Redwood, J. Hancock, K. Wilson, C. Young, and M. Thomas. 2012. "Use of Transcatheter Heart Valves for a Valve-in-Valve Implantation in Patients with Degenerated Aortic Bioprosthesis: Technical Considerations and Results." *The Journal of Thoracic and*

Cardiovascular Surgery no. 144 (6):1372-1380. doi: http://dx.doi.org/10.1016/j.jtcvs.2012.07.104.

Bapat, V. N., R. Q. Attia, and M. Thomas. 2012. "Distribution of Calcium in the Ascending Aorta in Patients Undergoing Transcatheter Aortic Valve Implantation and Its Relevance to the Transaortic Approach." *JACC: Cardiovascular Interventions* no. 5 (5):470-476. doi: http://dx.doi.org/10.1016/j.jcin.2012.03.006.

Barbanti, M., A. S. Petronio, F. Ettori, A. Latib, F. Bedogni, F. De Marco, A. Poli, C. Boschetti, M. De Carlo, C. Fiorina, A. Colombo, N. Brambilla, G. Bruschi, P. Martina, C. Pandolfi, C. Giannini, S. Curello, C. Sgroi, S. Gulino, M. Patanè, Y. Ohno, C. Tamburino, G. F. Attizzani, S. Immè, A. Gentili, and C. Tamburino. 2015. "5-Year Outcomes After Transcatheter Aortic Valve Implantation With CoreValve Prosthesis." *JACC: Cardiovascular Interventions* no. 8 (8):1084-1091. doi: http://dx.doi.org/10.1016/j.jcin.2015.03.024.

Ben-Gal, Y., and M. Williams. 2011. "Transapical Transcatheter Aortic Valve Implantation." *Operative Techniques in Thoracic and Cardiovascular Surgery* no. 16 (1):41-61. doi: http://dx.doi.org/10.1053/j.optechstcvs.2010.12.004.

Bertolini, G., and M. Prokop. 2011. "Multidetector-Row Computed Tomography: Technical Basics and Preliminary Clinical Applications in Small Animals." *The Veterinary Journal* no. 189 (1):15-26. doi: http://dx.doi.org/10.1016/j.tvjl.2010.06.004.

Bertrand, M. E., J. M. LaBlanche, P. Y. Tilmant, F. P. Thieuleux, M. R. Delforge, and A. G. Carre. 1981. "Coronary Sinus Blood Flow at Rest and During Isometric Exercise in Patients with Aortic Valve Disease. Mechanism of Angina Pectoris in Presence of Normal Coronary Arteries." *Am J Cardiol* no. 47 (2):199-205.

Butchart, E. G., H.-H. Li, N. Payne, K. Buchan, and G. L. Grunkemeier. 2001. "Twenty years' experience with the Medtronic Hall valve." *The Journal of Thoracic and Cardiovascular Surgery* no. 121 (6):1090-1100. doi: http://dx.doi.org/10.1067/mtc.2001.113754.

Calle, E. E., M. J. Thun, J. M. Petrelli, C. Rodriguez, and C. W. Heath. 1999. "Body-Mass Index and Mortality in a Prospective Cohort of U.S. Adults." *New England Journal of Medicine* no. 341 (15):1097-1105. doi: doi:10.1056/NEJM199910073411501.

Capelli, C., G. M. Bosi, E. Cerri, J. Nordmeyer, T. Odenwald, P. Bonhoeffer, F. Migliavacca, A. M. Taylor, and S. Schievano. 2012. "Patient-Specific Simulations of Transcatheter Aortic Valve Stent Implantation." *Medical & Biological Engineering & Computing* no. 50 (2):183-192. doi: 10.1007/s11517-012-0864-1.

CD-adapco. 2014. "STAR-CCM+." *http://www.cd-adapco.com/products/star-ccm%C2%AE*.

Cheung, A. W., R. Gurvitch, J. Ye, D. Wood, S. V. Lichtenstein, C. Thompson, and J. G. Webb. 2011. "Transcatheter Transapical Mitral Valve-in-Valve Implantations for a Failed Bioprosthesis: A Case Series." *The Journal of Thoracic and Cardiovascular Surgery* no. 141 (3):711-715. doi: http://dx.doi.org/10.1016/j.jtcvs.2010.11.026.

Clarke, A., P. Wiemers, K. K. C. Poon, C. N. Aroney, G. Scalia, D. Burstow, D. L. Walters, and P. Tesar. 2013. "Early Experience of Transaortic TAVI—The Future of Surgical TAVI?" *Heart, Lung and Circulation* no. 22 (4):265-269. doi: http://dx.doi.org/10.1016/j.hlc.2012.11.002.

Cocchetti, G., M. Pagani, and U. Perego. "Selective Mass Scaling and Critical Time-Step Estimate for Explicit Dynamics Analyses with Solid-Shell Elements." *Computers & Structures* (0). doi: http://dx.doi.org/10.1016/j.compstruc.2012.10.021.

Cribier, A., H. Eltchaninoff, C. Tron, F. Bauer, and L. Gerber. 2006. "Percutaneous Implantation of Aortic Valve Prosthesis in Patients with Calcific Aortic Stenosis: Technical Advances,

Clinical Results and Future Strategies." *Journal of Interventional Cardiology* no. 19:S87-S96. doi: 10.1111/j.1540-8183.2006.00176.x.

D'Errigo, P., M. Barbanti, M. Ranucci, F. Onorati, R. D. Covello, S. Rosato, C. Tamburino, F. Santini, G. Santoro, and F. Seccareccia. 2012. "Transcatheter Aortic Valve Implantation versus Surgical Aortic Valve Replacement for Severe Aortic Stenosis: Results from an Intermediate Risk Propensity-Matched Population of the Italian OBSERVANT Study." *International Journal of Cardiology*. doi: http://dx.doi.org/10.1016/j.ijcard.2012.05.028.

Daneault, B., A. J. Kirtane, S. K. Kodali, M. R. Williams, P. Genereux, G. R. Reiss, C. R. Smith, J. W. Moses, and M. B. Leon. 2011. "Stroke Associated With Surgical and Transcatheter Treatment of Aortic Stenosis: A Comprehensive Review." *Journal of the American College of Cardiology* no. 58 (21):2143-2150. doi: http://dx.doi.org/10.1016/j.jacc.2011.08.024.

de Buhr, W., S. Pfeifer, J. Slotta-Huspenina, E. Wintermantel, G. Lutter, and W. A. Goetz. 2012. "Impairment of Pericardial Leaflet Structure from Balloon-expanded Valved Stents." *The Journal of Thoracic and Cardiovascular Surgery* no. 143 (6):1417-1421. doi: 10.1016/j.jtcvs.2011.11.001.

De Hart, J., F. P. T. Baaijens, G. W. M. Peters, and P. J. G. Schreurs. 2003. "A computational fluid-structure interaction analysis of a fiber-reinforced stentless aortic valve." *Journal of Biomechanics* no. 36 (5):699-712. doi: http://dx.doi.org/10.1016/S0021-9290(02)00448-7.

Détaint, D., L. Lepage, D. Himbert, E. Brochet, D. Messika-Zeitoun, B. Iung, and A. Vahanian. 2009. "Determinants of Significant Paravalvular Regurgitation After Transcatheter Aortic Valve Implantation: Impact of Device and Annulus Discongruence." *JACC: Cardiovascular Interventions* no. 2 (9):821-827. doi: http://dx.doi.org/10.1016/j.jcin.2009.07.003.

DICardiology. 2013. "JenaValve Image." *http://www.dicardiology.com/sites/default/files/imagecache/node_image/photo_article/JenaValve%20TAVI.jpg*.

Drews, T., M. Pasic, S. Buz, A. Unbehaun, S. Dreysse, M. Kukucka, A. Mladenow, and R. Hetzer. 2011. "Transcranial Doppler sound detection of cerebral microembolism during transapical aortic valve implantation." *Thorac Cardiovasc Surg* no. 59 (4):237-42. doi: 10.1055/s-0030-1250495.

Edwards LifeSciences. 2013a. "Edwards Lifesciences eSheath - Expandable Introducer Sheath." *http://www.edwards.com/eu/products/transcathetervalves/pages/esheath.aspx*.

Edwards LifeSciences. 2013b. "Edwards Lifesciences SAPIEN XT." *http://www.edwards.com/eu/products/transcathetervalves/pages/sapienxt.aspx*.

Edwards LifeSciences. 2013c. "Edwards LifeSciences SAPIEN XT image." *http://www.edwards.com/eu/products/transcathetervalves/pages/sapienxt.aspx*.

Edwards Lifesciences. 2013d. "MRI Data Safety Specification."12.

Edwards Lifesciences. 2014a. "Edwards Lifesciences NovaFlex+ Delivery System " *http://ht.edwards.com/scin/edwards/sitecollectionimages/products/transcatheter/novaflex-banner.png*.

Edwards Lifesciences. 2014b. "Edward Lifesciences Magna SVR device." *http://www.edwards.com/products/heartvalves/Pages/Magna.aspx*.

Edwards LifeSciences. 2015. "Edwards LifeSciences - Ascendra angioplasty kit." *http://www.edwards.com/eu/Products/TranscatheterValves/Pages/ascendraplus.aspx*.

Eggebrecht, H., and R. H. Mehta. 2016. "Transcatheter aortic valve implantation (TAVI) in Germany 2008-2014: on its way to standard therapy for aortic valve stenosis in the elderly?" *EuroIntervention* no. 11 (9):1029-33. doi: 10.4244/eijy15m09_11.

Ewe, S. H., A. C. T. Ng, J. D. Schuijf, F. van der Kley, A. Colli, M. Palmen, A. de Weger, N. A. Marsan, E. R. Holman, A. de Roos, M. J. Schalij, J. J. Bax, and V. Delgado. 2011. "Location and Severity of Aortic Valve Calcium and Implications for Aortic Regurgitation After Transcatheter Aortic Valve Implantation." *The American Journal of Cardiology* no. 108 (10):1470-1477. doi: 10.1016/j.amjcard.2011.07.007.

Faria, R., D. Caeiro, R. Fontes de Carvalho, F. Lima, J. C. Mota, A. Rodrigues, P. Braga, and V. Gama. 2013. "Transcatheter aortic valve implantation in a very young patient." *Revista Portuguesa de Cardiologia (English Edition)* no. 32 (10):827-831. doi: http://dx.doi.org/10.1016/j.repce.2013.10.023.

Fedak, P. W., S. Verma, T. E. David, R. L. Leask, R. D. Weisel, and J. Butany. 2002. "Clinical and Pathophysiological Implications of a Bicuspid Aortic Valve." *Circulation* no. 106 (8):900-4.

Fenoglio Jr, J. J., H. A. McAllister Jr, C. M. DeCastro, J. E. Davia, and M. D. Cheitlin. 1977. "Congenital Bicuspid Aortic Valve After Age 20." *The American Journal of Cardiology* no. 39 (2):164-169. doi: http://dx.doi.org/10.1016/S0002-9149(77)80186-0.

Foundation, C. C. 2014. "Aortic root image." *http://my.clevelandclinic.org/services/heart/heart-blood-vessels/aorta*.

Foundation, W. 2013. "Diagram of Human Heart." *http://upload.wikimedia.org/wikipedia/commons/thumb/6/67/Heart_diagram_blood_flow_en.svg/1000px-Heart_diagram_blood_flow_en.svg.png*.

Fung, Y. C. 1993. "Biomechanics: Mechanical Properties of Living Tissue." *Springer New York*.

Gao, Z. B., S. Pandya, N. Hosein, M. S. Sacks, and N. H. C. Hwang. 2000. "Bioprosthetic Heart Valve Leaflet Motion Monitored by Dual Camera Stereo Photogrammetry." *Journal of Biomechanics* no. 33 (2):199-207. doi: http://dx.doi.org/10.1016/S0021-9290(99)00165-7.

Garcia, E., L. Unzue, E. Garcia, J. Solis, R. Teijeiro, and B. Tarancon. 2014. "Initial experience with the low-profile percutaneous aortic valve SAPIEN 3." *Rev Esp Cardiol (Engl Ed)* no. 67 (11):953-4. doi: 10.1016/j.rec.2014.04.014.

Grande, K. J., R. P. Cochran, P. G. Reinhall, and K. S. Kunzelman. 1998. "Stress Variations in the Human Aortic Root and Valve: the Role of Anatomic Asymmetry." *Ann Biomed Eng* no. 26 (4):534-45.

Gundiah, N., K. Kam, P. B. Matthews, J. Guccione, H. A. Dwyer, D. Saloner, T. A. M. Chuter, T. S. Guy, M. B. Ratcliffe, and E. E. Tseng. 2008. "Asymmetric Mechanical Properties of Porcine Aortic Sinuses." *The Annals of Thoracic Surgery* no. 85 (5):1631-1638. doi: http://dx.doi.org/10.1016/j.athoracsur.2008.01.035.

Gunning, P. S., T. J. Vaughan, and L. M. McNamara. 2014. "Simulation of Self Expanding Transcatheter Aortic Valve in a Realistic Aortic Root: Implications of Deployment Geometry on Leaflet Deformation." *Ann Biomed Eng* no. 42 (9):1989-2001. doi: 10.1007/s10439-014-1051-3.

Hayashida, K., E. Bouvier, T. Lefèvre, B. Chevalier, T. Hovasse, M. Romano, P. Garot, Y. Watanabe, A. Farge, P. Donzeau–Gouge, B. Cormier, and M. C. Morice. 2013. "Transcatheter Aortic Valve Implantation for Patients with Elliptical Aortic Annulus." *Journal of the American College of Cardiology* no. 61 (10, Supplement):E1994. doi: http://dx.doi.org/10.1016/S0735-1097(13)61994-4.

Hayashida, K., T. Lefèvre, B. Chevalier, T. Hovasse, M. Romano, P. Garot, E. Bouvier, A. Farge, P. Donzeau-Gouge, B. Cormier, and M.-C. Morice. 2012. "Impact of Post-Procedural Aortic Regurgitation on Mortality After Transcatheter Aortic Valve Implantation." *JACC: Cardiovascular Interventions* no. 5 (12):1247-1256. doi: http://dx.doi.org/10.1016/j.jcin.2012.09.003.

Heart, K. 2015. "TriGuard Cerebral Protection Device." *http://www.keystoneheart.com/images/TriGuard_Cerebral_protection_Device_-_Covering_all_aortic_arches.jpg*.

Hendrik Treede, M. A. R., MD; Markus Ferrari, MD; Stephan Ensminger, MD, PhD;, and M. F.-W. M. Hans-Reiner Figulla, MD. 2012. "JenaValve." *Euro Intervention*.

Hokken, R. B., M. M. Bartelings, A. J. J. C. Bogers, and A. C. Gittenberger-de Groot. 1997. "Morphology of the Pulmonary and Aortic Roots with Regard to the Pulmonary Autograft Procedure." *The Journal of Thoracic and Cardiovascular Surgery* no. 113 (3):453-461. doi: http://dx.doi.org/10.1016/S0022-5223(97)70357-X.

Hounsfield, G. N. 1979. "Computed Medical Imaging." *Nobel lecture, 8 December*.

Ihlberg, L., A. Sahlman, J. Sinisalo, J. Rapola, and M. Laine. 2012. "Transaortic Valve-in-Valve Implantation After Previous Aortic Root Homograft." *The Annals of Thoracic Surgery* no. 94 (5):1718-1721. doi: http://dx.doi.org/10.1016/j.athoracsur.2012.03.111.

Iung, B., G. Baron, E. G. Butchart, F. Delahaye, C. Gohlke-Barwolf, O. W. Levang, P. Tornos, J. L. Vanoverschelde, F. Vermeer, E. Boersma, P. Ravaud, and A. Vahanian. 2003. "A Prospective Survey of Patients with Valvular Heart Disease in Europe: The Euro Heart Survey on Valvular Heart Disease." *Eur Heart J* no. 24 (13):1231-43.

John, D., L. Buellesfeld, S. Yuecel, R. Mueller, G. Latsios, H. Beucher, U. Gerckens, and E. Grube. 2010. "Correlation of Device Landing Zone Calcification and Acute Procedural Success in Patients Undergoing Transcatheter Aortic Valve Implantations with the Self-expanding CoreValve Prosthesis." *JACC Cardiovasc Interv* no. 3 (2):233-43. doi: 10.1016/j.jcin.2009.11.015.

Kaatze, U. 1995. "Fundamentals of Microwaves." *Radiat Phys Chem*

Keele, K. D., and Jane Roberts. 1983. "Leonardo da Vinci: Anatomical Drawings from the Royal Library, Windsor Castle." *The Metropolitan Museum of Art*.

Keeley, E. C., and C. L. Grines. 1998. "Scraping of Aortic Debris by Coronary Guiding Catheters: a Prospective Evaluation of 1,000 Cases." *J Am Coll Cardiol* no. 32 (7):1861-5.

Kempfert, J., F. Girrbach, M. Haensig, S. Subramanian, D. M. Holzhey, and F. W. Mohr. 2013. "Transapical Aortic Valve-in-Valve-in-Valve Implantation as a Procedural Rescue Option." *The Annals of Thoracic Surgery* no. 95 (1):325-328. doi: http://dx.doi.org/10.1016/j.athoracsur.2012.05.063.

Kim, H., J. Lu, M. Sacks, and K. Chandran. 2008. "Dynamic Simulation of Bioprosthetic Heart Valves Using a Stress Resultant Shell Model." *Annals of Biomedical Engineering* no. 36 (2):262-275. doi: 10.1007/s10439-007-9409-4.

Klaudija Bijuklic, M. T. T., MD; Reginald I. Low, MD; Eberhard Grube, MD;, and M. Joachim Schofer, PhD. 2012. "Direct Flow Medical valve." *Euro Intervention*.

Kuetting, M., A. Sedaghat, M. Utzenrath, J.-M. Sinning, C. Schmitz, J. Roggenkamp, N. Werner, T. Schmitz-Rode, and U. Steinseifer. 2014. "In vitro Assessment of the Influence of Aortic Annulus Ovality on the Hydrodynamic Performance of Self-expanding Transcatheter Heart Valve Prostheses." *Journal of Biomechanics* no. 47 (5):957-965. doi: http://dx.doi.org/10.1016/j.jbiomech.2014.01.024.

Kukucka, M., M. Pasic, S. Dreysse, A. Mladenow, H. Habazettl, R. Hetzer, and A. Unbehaun. 2012. "Patient–Prosthesis Mismatch After Transapical Aortic Valve Implantation: Incidence and Impact on Survival." *The Journal of Thoracic and Cardiovascular Surgery*. doi: 10.1016/j.jtcvs.2012.01.043.

Labrosse, M. R., K. Lobo, and C. J. Beller. 2010. "Structural Analysis of the Natural Aortic Valve in Dynamics: From Unpressurized to Physiologically Loaded." *Journal of Biomechanics* no. 43 (10):1916-1922. doi: http://dx.doi.org/10.1016/j.jbiomech.2010.03.020.

Latrobe. 2013. "MP35N Data Sheet." *www.latrobesteel.com*:4.

Leber, A. W., W. Eichinger, J. Rieber, M. Lieber, S. Schleger, U. Ebersberger, M. Deichstetter, J. Vogel, T. Helmberger, D. Antoni, G. Riess, E. Hoffmann, and A. M. Kasel. 2013. "MSCT guided sizing of the Edwards Sapien XT TAVI device: Impact of different degrees of oversizing on clinical outcome." *International Journal of Cardiology* (0). doi: http://dx.doi.org/10.1016/j.ijcard.2013.03.030.

Leon, M. B., C. R. Smith, M. Mack, D. C. Miller, J. W. Moses, L. G. Svensson, E. M. Tuzcu, J. G. Webb, G. P. Fontana, R. R. Makkar, D. L. Brown, P. C. Block, R. A. Guyton, A. D. Pichard, J. E. Bavaria, H. C. Herrmann, P. S. Douglas, J. L. Petersen, J. J. Akin, W. N. Anderson, D. Wang, and S. Pocock. 2010. "Transcatheter aortic-valve implantation for aortic stenosis in patients who cannot undergo surgery." *N Engl J Med* no. 363 (17):1597-607. doi: 10.1056/NEJMoa1008232.

Li, A. E., I. Kamel, F. Rando, M. Anderson, B. Kumbasar, J. A. C. Lima, and D. A. Bluemke. 2004. "Using MRI to Assess Aortic Wall Thickness in the Multiethnic Study of Atherosclerosis: Distribution by Race, Sex, and Age." *American Journal of Roentgenology* no. 182 (3):593-597. doi: 10.2214/ajr.182.3.1820593.

Li, K., and W. Sun. 2010. "Simulated Thin Pericardial Bioprosthetic Valve Leaflet Deformation Under Static Pressure-Only Loading Conditions: Implications for Percutaneous Valves." *Annals of Biomedical Engineering* no. 38 (8):2690-2701. doi: 10.1007/s10439-010-0009-3.

Lide, D. R. 1990. "Handbook of Chemistry and Physics." *CRC* no. 90th.

Lin, S., P. Akula, and L. Gu. 2013. "Mechanical Performance of Bovine Pericardial Bioprosthetic Valves." *Journal of Medical Devices* no. 7:926-926. doi: 10.1115/1.4024346.

Lindroos, M., M. Kupari, J. Heikkilä, and R. Tilvis. 1993. "Prevalence of aortic valve abnormalities in the elderly: An echocardiographic study of a random population sample." *Journal of the American College of Cardiology* no. 21 (5):1220-1225. doi: http://dx.doi.org/10.1016/0735-1097(93)90249-Z.

LSTC. 2013. "LS-DYNA." *http://www.lstc.com/*.

Mack, M. J., D. R. Holmes, J. Webb, A. Cribier, S. K. Kodali, M. R. Williams, and M. B. Leon. 2013. "Patient Selection for Transcatheter Aortic Valve Replacement." *Journal of the American College of Cardiology* no. 62 (17_S). doi: 10.1016/j.jacc.2013.08.707.

Mark, S. D., V. Prasanna, V. A. Ferrari, and H. C. Herrmann. 2015. "Percutaneous Ventricular Septal Defect Closure After Sapien 3 Transcatheter Aortic Valve Replacement." *JACC: Cardiovascular Interventions* no. 8 (7):e109-e110. doi: http://dx.doi.org/10.1016/j.jcin.2015.01.034.

Markus, H. S., and M. M. Brown. 1993. "Differentiation between different pathological cerebral embolic materials using transcranial Doppler in an in vitro model." *Stroke* no. 24 (1):1-5.

Martin, C., T. Pham, and W. Sun. 2011. "Significant differences in the material properties between aged human and porcine aortic tissues." *Eur J Cardiothorac Surg* no. 40 (1):28-34. doi: 10.1016/j.ejcts.2010.08.056.

McNeel, R. 2013. "Rhinoceros 3D v5." *http://www.rhino3d.com/*.

Medtronic. 2013a. "Medtronic CoreValve " *http://www.corevalve.com/intl/product/index.htm*.

Medtronic. 2013b. "Medtronic CoreValve Image." *http://cdn.medgadget.com/img/corevalve.jpg*.

Meredith, I., S. Worthley, R. Whitbourn, P. Antonis, J. Montarello, A. Newcomb, D. Allocco, and K. Dawkins. 2012. "TCT-104 Feasibility Study of the Repositionable Lotus Aortic Valve Replacement System: 3-Month Outcomes in 11 Patients at High Surgical Risk (REPRISE I)." *Journal of the American College of Cardiology* no. 60 (17, Supplement):B32-B33. doi: http://dx.doi.org/10.1016/j.jacc.2012.08.120.

Meredith, I. T., S. Worthley, R. Whitbourn, P. Antonis, J. Montarello, A. E. Newcomb, D. Allocco, and K. Dawkins. 2013. "The Repositionable Lotus Aortic Valve Replacment System: Six-Month Outcomes in the Reprise 1 Feasibility Study." *Journal of the American College of Cardiology* no. 61 (10, Supplement):E1868. doi: http://dx.doi.org/10.1016/S0735-1097(13)61868-9.

Moat, N. E., P. Ludman, M. A. de Belder, B. Bridgewater, A. D. Cunningham, C. P. Young, M. Thomas, J. Kovac, T. Spyt, P. A. MacCarthy, O. Wendler, D. Hildick-Smith, S. W. Davies, U. Trivedi, D. J. Blackman, R. D. Levy, S. J. Brecker, A. Baumbach, T. Daniel, H. Gray, and M. J. Mullen. 2011. "Long-term outcomes after transcatheter aortic valve implantation in high-risk patients with severe aortic stenosis: the U.K. TAVI (United Kingdom Transcatheter Aortic Valve Implantation) Registry." *J Am Coll Cardiol* no. 58 (20):2130-8. doi: 10.1016/j.jacc.2011.08.050.

Mohammadi, H., F. Bahramian, and W. Wan. 2009. "Advanced Modeling Strategy for the Analysis of Heart Valve Leaflet Tissue Mechanics Using High-Order Finite Element Method." *Medical Engineering & Physics* no. 31 (9):1110-1117. doi: http://dx.doi.org/10.1016/j.medengphy.2009.07.012.

Mohr, F. W., T. Walther, M. Baryalei, V. Falk, R. Autschbach, A. Scheidt, and H. Dalichau. 1995. "The Toronto SPV Bioprosthesis: One-Year Results in 100 Patients." *The Annals of Thoracic Surgery* no. 60 (1):171-175. doi: http://dx.doi.org/10.1016/S0003-4975(95)00388-6.

Morganti, S., F. Auricchio, M. Conti, A. Reali, S. Morganti, F. Auricchio, M. Conti, A. Reali, M. S., and et al. 2013. Patient-specific finite element analysis of transcatheter aortic valve implantation. In *2nd ECCOMAS Young Investigators Conference (YIC 2013)*.

Morganti, S., M. Conti, M. Aiello, A. Valentini, A. Mazzola, A. Reali, and F. Auricchio. 2014. "Simulation of transcatheter aortic valve implantation through patient-specific finite element analysis: Two clinical cases." *Journal of Biomechanics* no. 47 (11):2547-2555. doi: http://dx.doi.org/10.1016/j.jbiomech.2014.06.007.

Muñoz-García, A. J., J. H. Alonso-Briales, M. F. Jiménez-Navarro, J. Caballero-Borrego, A. J. Domínguez-Franco, I. Rodríguez-Bailón, M. Such-Martínez, J. M. Hernández-García, and E. de Teresa-Galván. 2011. "Mechanisms, Treatment and Course of Paravalvular Aortic Regurgitation After Percutaneous Implantation of the CoreValve Aortic Prosthesis." *International Journal of Cardiology* no. 149 (3):389-392. doi: 10.1016/j.ijcard.2011.03.011.

Mylotte, D., A. Andalib, P. Theriault-Lauzier, M. Dorfmeister, M. Girgis, W. Alharbi, M. Chetrit, C. Galatas, S. Mamane, I. Sebag, J. Buithieu, L. Bilodeau, B. de Varennes, K. Lachapelle, R. Lange, G. Martucci, R. Virmani, and N. Piazza. 2015. "Transcatheter heart valve failure: a systematic review." *Eur Heart J* no. 36 (21):1306-27. doi: 10.1093/eurheartj/ehu388.

Ngo, D. T., A. L. Sverdlov, and J. D. Horowitz. 2012. "Prevention of aortic valve stenosis: A realistic therapeutic target?" *Pharmacology & Therapeutics* no. 135 (1):78-93. doi: http://dx.doi.org/10.1016/j.pharmthera.2012.04.001.

NHS. 2014. "Southampton General Hospital " *http://www.uhs.nhs.uk/Ourhospitals/SGH/SouthamptonGeneralHospital.aspx*.

Nijhoff, F., P. Agostoni, H. Amrane, A. Latib, L. Testa, J. A. Oreglia, F. De Marco, M. Samim, F. Bedogni, F. Maisano, G. Bruschi, A. Colombo, A. J. Van Boven, and P. R. Stella. "Transcatheter Aortic Valve Implantation in Patients with Severe Aortic Valve Stenosis and Large Aortic Annulus, Using the Self-expanding 31-mm Medtronic CoreValve Prosthesis: First Clinical Experience." *The Journal of Thoracic and Cardiovascular Surgery* (0). doi: http://dx.doi.org/10.1016/j.jtcvs.2013.09.059.

Nikon. 2013. "XT H 225L uCT Scanner " *http://www.nikonmetrology.com/en_EU/Products/X-ray-and-CT-Inspection/Computed-Tomography/XT-H-225-Industrial-CT-Scanning*.

Nkomo, V. T., J. M. Gardin, T. N. Skelton, J. S. Gottdiener, C. G. Scott, and M. Enriquez-Sarano. 2006. "Burden of Valvular Heart Diseases: a Population-Based Study." *The Lancet* no. 368 (9540):1005-1011. doi: http://dx.doi.org/10.1016/S0140-6736(06)69208-8.

Nombela-Franco, L., J. Rodés-Cabau, R. DeLarochellière, E. Larose, D. Doyle, J. Villeneuve, S. Bergeron, M. Bernier, I. J. Amat-Santos, M. Mok, M. Urena, M. Rheault, J. Dumesnil, M. Côté, P. Pibarot, and E. Dumont. 2012. "Predictive Factors, Efficacy, and Safety of Balloon Post-Dilation After Transcatheter Aortic Valve Implantation With a Balloon-Expandable Valve." *JACC: Cardiovascular Interventions* no. 5 (5):499-512. doi: http://dx.doi.org/10.1016/j.jcin.2012.02.010.

Open-Source. 2014. "ImageJ." *http://imagej.net/Welcome*.

Otto, C. M. 2008. "Calcific Aortic Stenosis — Time to Look More Closely at the Valve." *New England Journal of Medicine* no. 359 (13):1395-1398. doi: doi:10.1056/NEJMe0807001.

Otto, C. M., B. K. Lind, D. W. Kitzman, B. J. Gersh, and D. S. Siscovick. 1999. "Association of Aortic-Valve Sclerosis with Cardiovascular Mortality and Morbidity in the Elderly." *New England Journal of Medicine* no. 341 (3):142-147. doi: doi:10.1056/NEJM199907153410302.

Pasic, M., S. Buz, S. Dreysse, T. Drews, A. Unbehaun, C. Klein, M. Kukucka, A. Mladenow, E. Ivanitskaia-Kuhn, and R. Hetzer. 2010. "Transapical Aortic Valve Implantation in 194 Patients: Problems, Complications, and Solutions." *Ann Thorac Surg* no. 90 (5):1463-9; discussion 1469-70. doi: 10.1016/j.athoracsur.2010.05.072.

Pasic, M., S. Dreysse, T. Drews, S. Buz, A. Unbehaun, M. Kukucka, A. Mladenow, and R. Hetzer. 2010. "Improved Technique of Transapical Aortic Valve Implantation: “The Berlin Addition”." *The Annals of Thoracic Surgery* no. 89 (6):2058-2060. doi: http://dx.doi.org/10.1016/j.athoracsur.2009.07.096.

Pasic, M., A. Unbehaun, S. Dreysse, T. Drews, S. Buz, M. Kukucka, A. Mladenow, T. Gromann, and R. Hetzer. 2010. "Transapical Aortic Valve Implantation in 175 Consecutive Patients: Excellent Outcome in Very High-Risk Patients." *J Am Coll Cardiol* no. 56 (10):813-20. doi: 10.1016/j.jacc.2010.02.065.

Piazza, N., S. Bleiziffer, G. Brockmann, R. Hendrick, M.-A. Deutsch, A. Opitz, D. Mazzitelli, P. Tassani-Prell, C. Schreiber, and R. Lange. 2011. "Transcatheter Aortic Valve Implantation for Failing Surgical Aortic Bioprosthetic Valve: From Concept to Clinical Application and Evaluation (Part 2)." *JACC: Cardiovascular Interventions* no. 4 (7):733-742. doi: 10.1016/j.jcin.2011.05.007.

Praz, F., and F. Nietlispach. 2013. "Cerebral protection devices for transcatheter aortic valve implantation: is better the enemy of good?" *EuroIntervention* no. 9 Suppl:S124-8. doi: 10.4244/eijv9ssa26.

Roberts, W. C. 1970. "The Congenitally Bicuspid Aortic Valve: A Study of 85 Autopsy Cases." *The American Journal of Cardiology* no. 26 (1):72-83. doi: http://dx.doi.org/10.1016/0002-9149(70)90761-7.

Roberts, W. C., and J. M. Ko. 2005. "Frequency by Decades of Unicuspid, Bicuspid, and Tricuspid Aortic Valves in Adults Having Isolated Aortic Valve Replacement for Aortic Stenosis, With or Without Associated Aortic Regurgitation." *Circulation* no. 111 (7):920-5. doi: 10.1161/01.cir.0000155623.48408.c5.

Rodes-Cabau, J. 2010. "Progress in Transcatheter Aortic Valve Implantation." *Rev Esp Cardiol* no. 63 (4):439-50.

Rodés-Cabau, J., E. Dumont, R. H. Boone, E. Larose, R. Bagur, R. Gurvitch, F. Bédard, D. Doyle, R. De Larochellière, C. Jayasuria, J. Villeneuve, A. Marrero, M. Côté, P. Pibarot, and J. G. Webb. 2011. "Cerebral Embolism Following Transcatheter Aortic Valve Implantation: Comparison of Transfemoral and Transapical Approaches." *Journal of the American College of Cardiology* no. 57 (1):18-28. doi: 10.1016/j.jacc.2010.07.036.

Rödler, S. M., A. Moritz, W. Schreiner, A. End, P. Dubsky, and E. Wolner. 1997. "Five-Year Follow-up After Heart Valve Replacement With the CarboMedics Bileaflet Prosthesis." *The Annals of Thoracic Surgery* no. 63 (4):1018-1025. doi: http://dx.doi.org/10.1016/S0003-4975(97)00174-4.

Ronald K. Binder, M. J. R.-C., MD; David A. Wood, MD; John G. Webb, MD. 2012. "Edwards SAPIEN 3 valve." *Euro Intervention* no. 8.

Rossi, M. L., G. Belli, P. Pagnotta, C. Lucarelli, and P. Presbitero. "Paravalvular Leak Leading to Severe Aortic Valve Regurgitation after TAVI: Percutaneous Closure Strategy." *Heart, Lung and Circulation*. doi: http://dx.doi.org/10.1016/j.hlc.2015.04.163.

Russ, C., R. Hopf, S. Hirsch, S. Sundermann, V. Falk, G. Szekely, and M. Gessat. 2013. "Simulation of Transcatheter Aortic Valve Implantation Under Consideration of Leaflet Calcification." *Conf Proc IEEE Eng Med Biol Soc* no. 2013:711-4. doi: 10.1109/embc.2013.6609599.

Russo, C. F., A. Cannata, M. Lanfranconi, E. Vitali, A. Garatti, and E. Bonacina. 2008. "Is Aortic Wall Degeneration Related to Bicuspid Aortic Valve Anatomy in Patients with Valvular Disease?" *The Journal of Thoracic and Cardiovascular Surgery* no. 136 (4):937-942. doi: http://dx.doi.org/10.1016/j.jtcvs.2007.11.072.

Sabaté, M., S. Cánovas, E. García, R. Hernández Antolín, L. Maroto, J. M. Hernández, J. H. Alonso Briales, A. J. Muñoz García, E. Gutiérrez-Ibañes, and J. Rodríguez-Roda. 2013. "In-hospital and Mid-term Predictors of Mortality After Transcatheter Aortic Valve Implantation: Data From the TAVI National Registry 2010-2011." *Revista Española de Cardiología (English Edition)* no. 66 (12):949-958. doi: http://dx.doi.org/10.1016/j.rec.2013.07.003.

Saikrishnan, N., C.-H. Yap, N. Milligan, N. Vasilyev, and A. Yoganathan. 2012a. "Erratum to: In Vitro Characterization of Bicuspid Aortic Valve Hemodynamics Using Particle Image Velocimetry." *Annals of Biomedical Engineering* no. 40 (8):1776-1776. doi: 10.1007/s10439-012-0582-8.

Saikrishnan, N., C. H. Yap, N. C. Milligan, N. V. Vasilyev, and A. P. Yoganathan. 2012b. "In Vitro Characterization of Bicuspid Aortic Valve Hemodynamics Using Particle Image Velocimetry." *Ann Biomed Eng* no. 40 (8):1760-75. doi: 10.1007/s10439-012-0527-2.

Saleeb, A. F., A. Kumar, and V. S. Thomas. 2013. "The Important Roles of Tissue Anisotropy and Tissue-to-Tissue Contact on the Dynamical Behavior of a Symmetric Tri-Leaflet Valve During Multiple Cardiac Pressure Cycles." *Medical Engineering & Physics* no. 35 (1):23-35. doi: http://dx.doi.org/10.1016/j.medengphy.2012.03.006.

Schaefer, U., C. Frerker, C. Busse, and K.-H. Kuck. 2012b. "Transjugular and Transseptal Treatment of a Degenerated Mitral Valve Prosthesis with a Balloon-expandable Biological Valve." *Heart, Lung and Circulation* no. 21 (12):836-840. doi: http://dx.doi.org/10.1016/j.hlc.2012.03.125.

Schaefer, U., C. Frerker, D. Schewel, T. Thielsen, F. Meincke, F. Kreidel, and K.-H. Kuck. 2012a. "Transfemoral and Transseptal Valve-in-Valve Implantation Into a Failing Mitral Xenograft With a Balloon-Expandable Biological Valve." *The Annals of Thoracic Surgery* no. 94 (6):2115-2118. doi: http://dx.doi.org/10.1016/j.athoracsur.2012.04.123.

Scharfschwerdt, M., R. Meyer-Saraei, C. Schmidtke, and H.-H. Sievers. 2013. "Hemodynamics of the Edwards Sapien XT Transcatheter Heart Valve in Noncircular Aortic Annuli." *The Journal of Thoracic and Cardiovascular Surgery*. doi: http://dx.doi.org/10.1016/j.jtcvs.2013.07.057.

Schoen, F. J., and R. J. Levy. 2005. "Calcification of Tissue Heart Valve Substitutes: Progress Toward Understanding and Prevention." *The Annals of Thoracic Surgery* no. 79 (3):1072-1080. doi: 10.1016/j.athoracsur.2004.06.033.

Schultz, C. J., A. Weustink, N. Piazza, A. Otten, N. Mollet, G. Krestin, R. J. van Geuns, P. de Feyter, P. W. J. Serruys, and P. de Jaegere. 2009. "Geometry and Degree of Apposition of the CoreValve ReValving System With Multislice Computed Tomography After Implantation in Patients With Aortic Stenosis." *Journal of the American College of Cardiology* no. 54 (10):911-918. doi: http://dx.doi.org/10.1016/j.jacc.2009.04.075.

Scientific, B. 2016. "Boston Scientific Lotus valve." *http://www.bostonscientific.com/en-EU/products/transcatheter-heart-valve/lotus-aortic-implantation.html*.

Shahmirzadi, D., and E. E. Konofagou. 2012. "Detection of Aortic Wall Inclusions Using Regional Pulse Wave Propagation and Velocity In Silico." *Artery Research* no. 6 (3):114-123. doi: http://dx.doi.org/10.1016/j.artres.2012.05.004.

Shoja, M. M., P. S. Agutter, M. Loukas, B. Benninger, G. Shokouhi, H. Namdar, K. Ghabili, M. Khalili, and R. S. Tubbs. 2012. "Leonardo da Vinci's Studies of the Heart." *International Journal of Cardiology*. doi: http://dx.doi.org/10.1016/j.ijcard.2012.09.078.

Siebenmann Md, R. P. 1997. "Implantation of the Toronto SPV Stentless Porcine Bioprosthesis in Dilated Ascending Aorta." *The Annals of Thoracic Surgery* no. 64 (4):1197-1200. doi: http://dx.doi.org/10.1016/S0003-4975(97)00827-8.

Sievers, H.-H., and C. Schmidtke. 2007. "A Classification System for the Bicuspid Aortic Valve from 304 Surgical Specimens." *The Journal of Thoracic and Cardiovascular Surgery* no. 133 (5):1226-1233. doi: http://dx.doi.org/10.1016/j.jtcvs.2007.01.039.

Simpleware. 2014. "ScanIP." *http://www.simpleware.com/software/scanip/*.

SIMULIA. 2013a. "Abaqus CAE, Explicit Dynamics." *Abaqys Analysis User's Manuel 6.3.3*.

SIMULIA. 2013b. "Abaqus CAE, Rayleigh Damping " *Abaus Analysis User's Manuel 26.1.1*.

SIMULIA. 2013c. "Abaqus v6.12.1." *http://www.3ds.com/products-services/simulia/portfolio/abaqus/latest-release/*.

SIMULIA. 2014a. "Abaqus CAE, Co-Simulation: Overview." *Abaqus Analysis User's Manual 17.1.1*.

SIMULIA. 2014b. "Abaqus CAE, Equation of State " *Abaqus Analysis User's Manuel 25.2.1*

SIMULIA. 2014c. "Abaqus CAE, Eulerian Analysis." *Abaqus Analysis User's Manual 14.1.1*.

Simulia. 2014d. "Abaqus CAE, Hyperelastic Behaviour of Rubber-like Materials." *Abaqus Analysis User's Manual 22.5.1*.

Sinning, J.-M., N. Werner, G. Nickenig, and E. Grube. 2013. "Medtronic CoreValve Evolut R with EnVeo R." *EuroIntervention* no. 9 (S):S95-S96. doi: 10.4244/EIJV9SSA18.

Smith, C. R., M. B. Leon, M. J. Mack, D. C. Miller, J. W. Moses, L. G. Svensson, E. M. Tuzcu, J. G. Webb, G. P. Fontana, R. R. Makkar, M. Williams, T. Dewey, S. Kapadia, V. Babaliaros, V. H. Thourani, P. Corso, A. D. Pichard, J. E. Bavaria, H. C. Herrmann, J. J. Akin, W. N. Anderson, D. Wang, and S. J. Pocock. 2011. "Transcatheter versus Surgical Aortic-Valve Replacement in High-Risk Patients." *New England Journal of Medicine* no. 364 (23):2187-2198. doi: doi:10.1056/NEJMoa1103510.

Smucker, M. L., C. L. Tedesco, S. B. Manning, R. M. Owen, and M. D. Feldman. 1988. "Demonstration of an Imbalance Between Coronary Perfusion and Excessive Load as a Mechanism of Ischemia During Stress in Patients with Aortic Stenosis." *Circulation* no. 78 (3):573-82.

Smuts, A. N., D. C. Blaine, C. Scheffer, H. Weich, A. F. Doubell, and K. H. Dellimore. 2011. "Application of Finite Element Analysis to the Design of Tissue Leaflets for a Percutaneous Aortic Valve." *Journal of the Mechanical Behavior of Biomedical Materials* no. 4 (1):85-98. doi: http://dx.doi.org/10.1016/j.jmbbm.2010.09.009.

Stewart, B. F., D. Siscovick, B. K. Lind, J. M. Gardin, J. S. Gottdiener, V. E. Smith, D. W. Kitzman, and C. M. Otto. 1997. "Clinical Factors Associated With Calcific Aortic Valve Disease fn1." *Journal of the American College of Cardiology* no. 29 (3):630-634. doi: http://dx.doi.org/10.1016/S0735-1097(96)00563-3.

Stockholders, T. 2013. "MP35N Data Sheet."1.

Sturla, F., E. Votta, M. Stevanella, C. A. Conti, and A. Redaelli. 2013. "Impact of modeling fluid–structure interaction in the computational analysis of aortic root biomechanics." *Medical Engineering & Physics* no. 35 (12):1721-1730. doi: http://dx.doi.org/10.1016/j.medengphy.2013.07.015.

Sun, W., A. Abad, and M. S. Sacks. 2005. "Simulated Bioprosthetic Heart Valve Deformation under Quasi-Static Loading." *Journal of Biomechanical Engineering* no. 127 (6):905-914. doi: 10.1115/1.2049337.

Sun, W., K. Li, and E. Sirois. 2010. "Simulated Elliptical Bioprosthetic Valve Deformation: Implications for Asymmetric Transcatheter Valve Deployment." *Journal of Biomechanics* no. 43 (16):3085-3090. doi: http://dx.doi.org/10.1016/j.jbiomech.2010.08.010.

Tamburino, C., D. Capodanno, A. Ramondo, A. S. Petronio, F. Ettori, G. Santoro, S. Klugmann, F. Bedogni, F. Maisano, A. Marzocchi, A. Poli, D. Antoniucci, M. Napodano, M. De Carlo, C. Fiorina, and G. P. Ussia. 2011. "Incidence and Predictors of Early and Late Mortality After Transcatheter Aortic Valve Implantation in 663 Patients with Severe Aortic Stenosis." *Circulation* no. 123 (3):299-308. doi: 10.1161/circulationaha.110.946533.

Tan, F. P. P., X. Y. Xu, R. Torii, N. B. Wood, N. Delahunty, M. Mullen, N. Moat, and R. Mohiaddin. 2012. "Comparison of Aortic Flow Patterns Before and After Transcatheter Aortic Valve Implantation." *Cardiovascular Engineering and Technology* no. 3 (1):123-135. doi: 10.1007/s13239-011-0073-3.

Thubrikar, M., W. C. Piepgrass, T. W. Shaner, and S. P. Nolan. 1981. *The design of the normal aortic valve*. Vol. 241.

Tzamtzis, S., J. Viquerat, J. Yap, M. J. Mullen, and G. Burriesci. 2013. "Numerical Analysis of the Radial Force Produced by the Medtronic-CoreValve and Edwards-SAPIEN After

Transcatheter Aortic Valve Implantation (TAVI)." *Medical Engineering & Physics* no. 35 (1):125-130. doi: http://dx.doi.org/10.1016/j.medengphy.2012.04.009.

UK-TIA. 1988. "United Kingdom transient ischaemic attack (UK-TIA) aspirin trial: interim results. UK-TIA Study Group." *Br Med J (Clin Res Ed)* no. 296 (6618):316-20.

Ulrich Gerckens, M., Luciano Pizzulli, MD, Konstantinos Raisakis, MD. 2013. "Alcohol Septal Ablation as a Bail-Out Procedure for Suicide Left Ventricle After Transcatheter Aortic Valve Implantation." *Journal of Invasive Cardiology* no. 25 (5).

Urena, M., D. Doyle, E. Dumont, H. B. Ribeiro, S. Bilodeau, and J. Rodés-Cabau. 2014. "Transcatheter Aortic Valve Replacement With a Balloon-expandable Valve for the Treatment of Noncalcified Bicuspid Aortic Valve Disease." *Revista Española de Cardiología (English Edition)* no. 67 (4):327-329. doi: http://dx.doi.org/10.1016/j.rec.2013.10.014.

Van Belle, E., F. Juthier, J. L. Auffray, M. Laskar, A. Leguerrier, B. Lung, M. Gilard, H. Eltchaninoff, C. Banfi, J. Fajadet, P. Leprince, A. Prat, and E. Teiger. 2012. "TCT-91 Peri-valvular Aortic Regurgitation in Balloon-expendable and Self-expendable TAVI Procedures: Predictors and Impact on Clinical Outcome - Insights from the FRANCE2 Registry." *Journal of the American College of Cardiology* no. 60 (17, Supplement):B28-B29. doi: http://dx.doi.org/10.1016/j.jacc.2012.08.106.

Van Belle, E., M. Samim, P. Stella, J. Kluin, F. Ramjankhan, G. Sieswerda, P. Agostoni, M. Hillaert, F. Juthier, A. Prat, L. Van Herwerden, and P. Doevendans. 2011. "147 TAVI with the Edwards-SAPIEN Endoprosthesis: Impact of a Systematic "Oversizing" Policy on Aortic Regurgitation." *Archives of Cardiovascular Diseases Supplements* no. 3 (1):48. doi: http://dx.doi.org/10.1016/S1878-6480(11)70149-5.

van Swieten, J. C., P. J. Koudstaal, M. C. Visser, H. J. Schouten, and J. van Gijn. 1988. "Interobserver agreement for the assessment of handicap in stroke patients." *Stroke* no. 19 (5):604-7.

VolumeGraphics. 2014. "VGStudio MAX 2.1." *http://www.volumegraphics.com/en/products/vgstudio-max/basic-functionality/*.

Walther, T., H. Möllmann, A. van Linden, and J. Kempfert. 2011. "Transcatheter Aortic Valve Implantation Transapical: Step by Step." *Seminars in Thoracic and Cardiovascular Surgery* no. 23 (1):55-61. doi: http://dx.doi.org/10.1053/j.semtcvs.2011.05.006.

Wang, Q., S. Kodali, C. Primiano, and W. Sun. 2014. "Simulations of transcatheter aortic valve implantation: implications for aortic root rupture." *Biomechanics and Modeling in Mechanobiology*:1-10. doi: 10.1007/s10237-014-0583-7.

Wang, Q., E. Sirois, and W. Sun. 2012. "Patient-Specific Modeling of Biomechanical Interaction in Transcatheter Aortic Valve Deployment." *Journal of Biomechanics* no. 45 (11):1965-1971. doi: http://dx.doi.org/10.1016/j.jbiomech.2012.05.008.

Watton, P. N., X. Y. Luo, X. Wang, G. M. Bernacca, P. Molloy, and D. J. Wheatley. 2007. "Dynamic Modelling of Prosthetic Chorded Mitral Valves Using the Immersed Boundary Method." *Journal of Biomechanics* no. 40 (3):613-626. doi: http://dx.doi.org/10.1016/j.jbiomech.2006.01.025.

Webb, J. G., L. Altwegg, R. H. Boone, A. Cheung, J. Ye, S. Lichtenstein, M. Lee, J. B. Masson, C. Thompson, R. Moss, R. Carere, B. Munt, F. Nietlispach, and K. Humphries. 2009. "Transcatheter Aortic Valve Implantation: Impact on Clinical and Valve-Related Outcomes." *Circulation* no. 119 (23):3009-16. doi: 10.1161/circulationaha.108.837807.

Webb, J. G., and R. K. Binder. 2012. "Transcatheter aortic valve implantation: The evolution of prostheses, delivery systems and approaches." *Archives of Cardiovascular Diseases* no. 105 (3):153-159. doi: http://dx.doi.org/10.1016/j.acvd.2012.02.001.

Webb, J. G., M. Chandavimol, C. R. Thompson, D. R. Ricci, R. G. Carere, B. I. Munt, C. E. Buller, S. Pasupati, and S. Lichtenstein. 2006. "Percutaneous Aortic Valve Implantation Retrograde From the Femoral Artery." *Circulation* no. 113 (6):842-850. doi: 10.1161/circulationaha.105.582882.

Wong, D. R., J. Ye, A. Cheung, J. G. Webb, R. G. Carere, and S. V. Lichtenstein. 2010. "Technical Considerations to Avoid Pitfalls During Transapical Aortic Valve Implantation." *The Journal of Thoracic and Cardiovascular Surgery* no. 140 (1):196-202. doi: http://dx.doi.org/10.1016/j.jtcvs.2009.07.081.

Xiong, F. L., W. A. Goetz, C. K. Chong, Y. L. Chua, S. Pfeifer, E. Wintermantel, and J. H. Yeo. 2010. "Finite element investigation of stentless pericardial aortic valves: relevance of leaflet geometry." *Ann Biomed Eng* no. 38 (5):1908-18. doi: 10.1007/s10439-010-9940-6.

Yun, B., J. Wu, H. Simon, S. Arjunon, F. Sotiropoulos, C. Aidun, and A. Yoganathan. 2012. "A Numerical Investigation of Blood Damage in the Hinge Area of Aortic Bileaflet Mechanical Heart Valves During the Leakage Phase." *Annals of Biomedical Engineering* no. 40 (7):1468-1485. doi: 10.1007/s10439-011-0502-3.

Zegdi, R., V. Ciobotaru, M. Noghin, G. Sleilaty, A. Lafont, C. Latrémouille, A. Deloche, and J.-N. Fabiani. 2008. "Is It Reasonable to Treat All Calcified Stenotic Aortic Valves With a Valved Stent?: Results From a Human Anatomic Study in Adults." *Journal of the American College of Cardiology* no. 51 (5):579-584. doi: http://dx.doi.org/10.1016/j.jacc.2007.10.023.

μ-VIS. 2013. "Multidisciplinary, Multiscale, Microtomographic Volume Imaging Centre." *The University of Southampton*.